Investigation of the Electron Donor P_{700} and the Electron Acceptor A_1 in Photosystem I of Oxygenic Photosynthesis Using EPR Spectroscopy

vorgelegt von
Diplom-Biologe
Jens Niklas
aus Hagen

Von der Fakultät II - Mathematik und Naturwissenschaften
der Technischen Universität Berlin
zur Erlangung des akademischen Grades
Doktor der Naturwissenschaften
Dr.rer.nat.

genehmigte Dissertation

Promotionsausschuss:

Vorsitzender: Prof. Dr. Thomas Friedrich
Berichter/Gutachter: Prof. Dr. Wolfgang Lubitz
Berichter/Gutachter: Prof. Dr. Peter Hildebrandt

Tag der wissenschaftlichen Aussprache: 18.10.2006

Berlin 2007

D 83

Abstract

Photosynthesis is one of the most important biological processes on earth. This work focuses on the investigation of two important organic cofactors which are involved in electron transfer in photosystem I of oxygenic photosynthesis. The first is P_{700}, the primary electron donor, and the other one is A_1, an intermediate electron acceptor. P_{700} is comprised of chlorophylls (Chl *a*/Chl *a*′ heterodimer) and A_1 is a quinone (phylloquinone, vitamin K_1). EPR spectroscopy is the major tool used in this work to investigate the electronic structure of the paramagnetic intermediates.

The intermediate $A_1^{\bullet-}$ was studied both as the stationary radical and as the light-induced spin-correlated radical pair $P_{700}^{\bullet+}A_1^{\bullet-}$. A detailed comparison with the quinone *in vitro* was performed to elucidate how the protein modifies the electronic structure of the cofactor. The dependence of the redox potential and the *g*-tensor on the solvent polarity was studied. From the comparison it can be concluded, that the very low redox potential and the high g_x-value of VK_1 ($VK_1^{\bullet-}$) in the A_1 binding site of PS I can be explained in terms of a apolar protein environment.

Advanced multiple resonance EPR techniques like ENDOR and TRIPLE at elevated magnetic fields (Q-band) were used to determine the proton hf tensors of the quinone radical anion *in vitro* and of $A_1^{\bullet-}$. The hf tensor principal components for all protons visible in the ENDOR spectra of the phylloquinone radical anion *in vitro* were determined. The combination of advanced EPR techniques with the knowledge of the hf tensors of the quinone radicals *in vitro* allowed for the first time to get comprehensive information about the spin density distribution in $A_1^{\bullet-}$. ENDOR lines of the α-protons of the second (benzene) ring were assigned. Previous ambiguous assignments of the single H-bond to $A_1^{\bullet-}$ were corrected. The H-bond was found to be quite strong, similar to the H-bond present in bacterial photosynthetic RCs.

The comparative study, with DFT calculations which utilize a simplified structural model, and high-resolution ENDOR spectroscopy indicates that the H-bond interaction is indeed the crucial factor for the explanation of the spin density distribution in $A_1^{\bullet-}$.

The triplet state of the primary donor P_{700} was investigated. The first ENDOR spectra of $^3P_{700}$ in PS I from *T. elongatus* were obtained and the monomeric nature of $^3P_{700}$ at low temperature was confirmed. The study of the temperature dependence of the zero field splitting tensor indicates that, similar to $^3P_{680}$ in PS II, the triplet exciton is located at low temperature on only one chlorophyll, while at high temperature the triplet exciton is delocalized over a pair of chlorophylls.

Abstract

Die Photosynthese ist einer der wichtigsten biologischen Prozesse. In dieser Arbeit wurden zwei essentielle organische Kofaktoren der Elektronentransportkette von Photosystem I, einem der beiden Photosysteme der oxygenen Photosynthese, untersucht. Einer der beiden Kofaktoren ist P_{700}, der primäre Elektronendonor, der andere ist A_1, ein intermediärer Elektronenakzeptor. P_{700} besteht aus Chlorophyllen (Chl *a*/Chl *a*′ Heterodimer) und A_1 ist ein Chinon (Phyllochinon, Vitamin K_1). Als Hauptuntersuchungsmethode wurde EPR-Spektroskopie eingesetzt, die eine sensitive Methode zur Untersuchung der elektronischen Struktur paramagnetischer Intermediate ist.

Das Intermediat $A_1^{\bullet-}$ wurde sowohl als stationäres Radikal als auch im licht-induzierten spin-korrelierten Radikalpaar $P_{700}^{\bullet+}A_1^{\bullet-}$ untersucht. Es wurden ausführliche Vergleiche mit dem Chinonradikal *in vitro* durchgeführt, um aufzuklären wie das Protein die elektronische Struktur des Kofaktors beeinflusst. Die Abhängigkeit des Redoxpotentials und des *g*-Tensors von der Polarität des Lösungsmittels wurden untersucht. Es konnte in Übereinstimmung mit früheren Untersuchungen festgestellt werden, dass das sehr niedrige Redoxpotential und der grosse g_x-Wert von VK_1 ($VK_1^{\bullet-}$) in der A_1 Bindestelle von PS I durch eine unpolare Proteinumgebung erklärt werden können.

Multiple Resonanzmethoden wie ENDOR und TRIPLE in höheren Magnetfeldern (Q-Band) wurden eingesetzt, um die Hyperfein-Tensoren der Protonen der Chinonradikale *in vitro* und in $A_1^{\bullet-}$ zu bestimmen. Die Hauptwerte der Hyperfein-Tensoren aller Protonen, die im ENDOR Spektrum des Chinonradikals *in vitro* beobachtet wurden, konnten bestimmt werden. Die Kombination moderner EPR-Techniken mit der Kenntnis der Hyperfein-Tensoren der Chinonradikale *in vitro* erlaubte zum ersten Mal, umfassende Informationen über die Spindichteverteilung in $A_1^{\bullet-}$ zu erhalten. ENDOR Signale konnten den α-Protonen des zweiten Chinonringes zugeordnet werden. Die bisherigen, zweifelhaften Zuordnungen von ENDOR Signalen zu dem Proton der Wasserstoffbrücke wurden korrigiert. Die Wasserstoffbrücke ist relativ stark, vergleichbar mit den Wasserstoffbrücken in bakteriellen photosynthetischen Reaktionszentren.

Der Vergleich mit DFT Rechnungen, in denen ein vereinfachtes Modell der A_1 Bindestelle verwendet wurde, zeigte, dass diese Wasserstoffbrücke der entscheidende Faktor zur Erklärung der spezifischen Spindichteverteilung in $A_1^{\bullet-}$ ist.

Der Triplett-Zustand des primären Elektronendonors P_{700} wurde untersucht. Im Zuge dieser Untersuchungen wurden die ersten ENDOR Spektren von $^3P_{700}$ in PS I von *T. elongatus* erhalten und die monomere Strukur von $^3P_{700}$ bei niedrigen Temperaturen bestätigt. Die Untersuchung der Temperaturabhängigkeit des Nullfeldaufspaltungs-Tensors zeigte, dass sich das Triplett-Exciton bei niedriger Temperatur auf einem Chlorophyll befindet, während es bei höheren Temperaturen über ein Chlorophyllpaar delokalisiert ist.

Table of Content

1. Introduction

Photosynthesis

Nearly all the free energy used by biological organisms is derived from sun light by a process called photosynthesis. Photosynthesis is the process of the conversion of light energy into chemical energy. It is the most important process of energy conversion found in nature. It is also outstanding from a quantitative point of view. In the following sections, a short introduction into the large field of photosynthesis will be given. For a more detailed view on photosynthesis, see refs. [1-4].

The basic chemical equation describing photosynthesis is as follows:

$$CO_2 + 2H_2(A) \xrightarrow{light} (CH_2O) + (2A) + H_2O\,. \qquad (1.1)$$

$H_2(A)$ is an oxidiziable substrate like water, molecular hydrogen, or simple organic molecules. CH_2O stands for carbohydrates, *e.g.* sucrose or starch. The process is ubiquitous for anoxygenic and oxygenic photosynthesis, the former one being the evolutionary older type. The quite different photosynthesis (without electron transport) performed by some archaea is not discussed here.

Organisms which are doing anoxygenic photosynthesis ($A \neq O$) possess just one type of photosystem.[5] Examples are purple bacteria, green sulfur bacteria and heliobacteria. They use molecular hydrogen, hydrogen sulfate or small organic molecules as electron donors.

Oxygenic photosynthesis ($A = O$) is the evolutionary younger process. It exists for less than 3.5 billion years. Organisms doing oxygenic photosynthesis possess two types of photosystems, called photosystem I and photosystem II (Figure 1.1). Higher plants, algae and

chlorophytes are capable of performing oxygenic photosynthesis. They use H_2O as direct electron donor and generate as a by-product molecular oxygen. Over millions of years it has accumulated in the atmosphere, and thus built the basis of all higher life on earth. The molecular mechanisms of photosynthesis are numerous and complicated. The first step is the absorption of light by chlorophylls (Chls), followed by energy transfer to the reaction center (RC) and subsequent electron transfer. The energy of light is used for generation of an electrochemical potential across the photosynthetic membrane. Photosystem II (PS II) transfers the electrons from water to a quinone and evolves O_2. Photoystem I (PS I) creates reduced intermediates that are used for the production of nicotinamide adenine dinucleotide phosphate (NADPH).

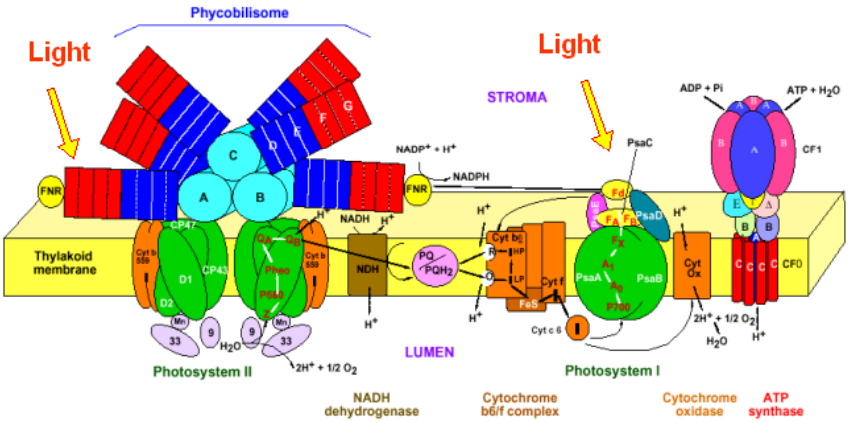

Figure 1.1: Schematic view on the photosynthetic membrane of cyanobacteria. Scheme is courtesy of D. Bryant. The photosynthetic membrane of higher plants is in general very similar, with differences concerning the light-harvesting and the cytochrome complex.

The electron flow between the two photosystems also generates a transmembrane proton gradient which is used to generate adenosine triphosphate (ATP). The generation of

transmembrane proton gradient is similar to respiration.[6;7] The main difference to respiration is the origin of the high energy electrons: in respiration they come from oxidation of molecules, in photosynthesis from light absorption by Chls. NADPH and ATP which are created in these light reactions are used for fixing the carbon by the reduction of CO_2, in the dark reactions of photosynthesis.

A short history of photosynthesis research

Photosynthesis has been an important topic of scientific research in the past four centuries. Since a large number of important investigations were carried out over this long period, the few examples mentioned here represent only a small and subjective view which is far from being complete. The focus of experiments presented here is on oxygenic photosynthesis. For a more detailed overview on the history of photosynthesis research, see refs. [8-10].

It was already in 1640s when Van Helmont observed that the soil was not primarily responsible for a plant's change in mass as it grew.[11] Hales proposed that plants extract some of their matter from the air.[12] Priestly discovered that plants could 'restore air which had been injured by the burning of candles', *i.e.* plants can produce oxygen.[13] It was Ingenhousz who showed that the plants are only able to 'purify air' when they are placed in light.[14] Senebier found in 1782 that 'fixed air' (CO_2) is essential for the plants to produce oxygen.[15] De Saussure found 1804 that also water is a necessary compound for photosynthesis[16].

In 1842 Mayer suggested the idea of the conversion of light energy into chemical energy.[17] Engelmann found at the end of the 19th century that chloroplasts are the site of photosynthesis and recorded the first action spectrum of photosynthesis.[18;19] Von Sachs proved the involvment of Chl in photosynthesis. Warburg discovered in 1919 that photosynthesis

consists of two different reactions, the so called light reaction and the dark reaction.[20;21] Wurmser presented the concept of redox reactions, and the general equation of photosynthesis in 1925.[22] In a more general way, including anoxygenic photosynthesis, van Niel derived equation (Eq. 1.1) in 1929.[23]. Both light and dark reactions take place in the chloroplast, as demonstrated by Hill in 1937.[24] Addtionally, he observed that the light dependent reactions take place in the thylakoid membrane of the chloroplast. Since the final products of the dark reactions are carbohydrates with six carbon atoms, this should read as follows:

$$6CO_2 + 12H_2O \rightarrow 6(CH_2O) + 6O_2 + 6H_2O \qquad (1.2)$$

In 1957, Emerson and coworkers discovered the so-called 'red drop effect' and showed, that oxygenic photosynthesis relies on the use of two different photosystems.[25;26] Hill and Bendall developed the Z-scheme (Figure 1.2),[27] which was confirmed experimentally by Witt and coworkers[28] as well as by Kok and Hoch.[29]

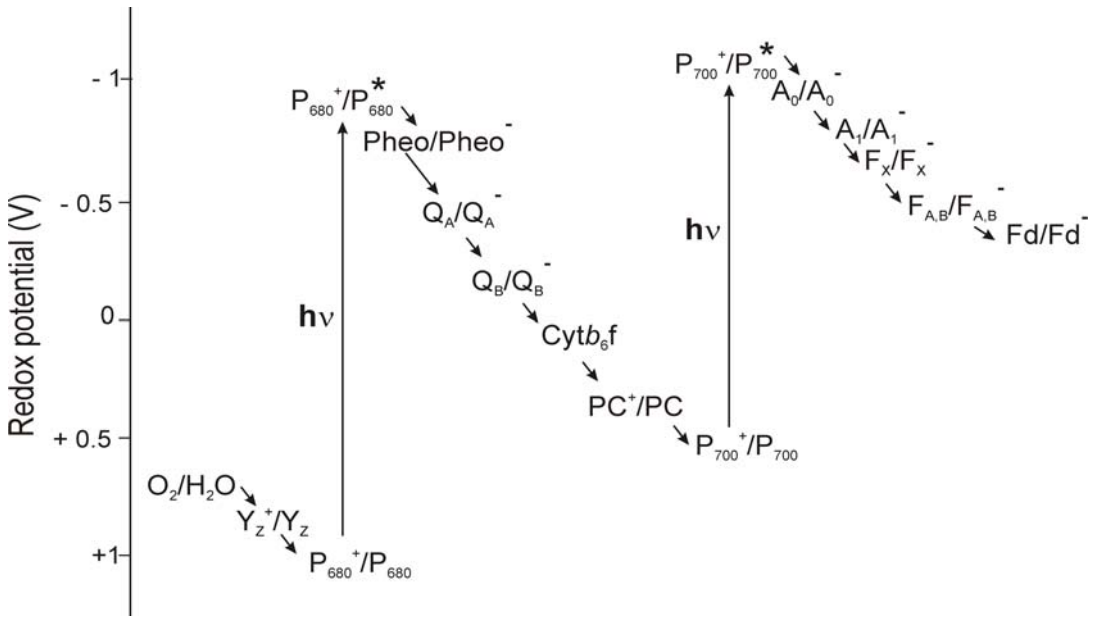

Figure 1.2: Energy scheme of linear electron transport in oxygenic photosynthesis ('Z-scheme').

A more recent milestone was the crysallization and subsequent X-ray structure determination of the bacterial RC from *Rb. sphaeroides* (previously *Rhodopseudomonas sphaeroides*) and *Blastochloris viridis* (previously *Rhodopseudomonas viridis*).[30;31] These were the first membrane proteins whose structure was solved at atomic resolution. For this achievement Michel, Deisenhofer and Huber received the Nobel Price in Chemistry in 1988 [http://nobelprize.org]. This discovery had a stimulating effect on the attempts to investigate structure-function relationships in photosynthesis. More recently, the three dimensional structures of photosytem I and II involved in oxygenic photosynthesis have also been elucidated.[32;33]

The light and dark reactions

The processes of oxygenic photosynthesis take place in the chloroplasts in case of higher plants and some algae or in the thylakoid membrane of cyanobacteria. Chloroplasts are specialized, membrane surrounded, semi-autonomous organells. Chloroplasts contain an outer membrane and an inner membrane. Between these a small intermembrane space is present. The inner membrane encloses the stroma, which is the place of the dark reactions. The chloroplast has its own genetic material (DNA), and contains the enzymes of the Calvin-cycle (dark reactions), and the complexes for protein synthesis. Inside the stroma, the thylakoid membrane is located. This is a single, folded membrane, which encloses the thylakoid lumen. Part of the membrane consists of disc like, stapeled structures, which are called grana. The connecting membrane parts are called stroma lamella. Here, the light driven reactions take place, which produce energy and reducing agents (ATP and NADPH, repectively), which are subsequently consumed in the dark reactions. The most important proteins of the photosynthetic apparatus are embedded in the thylakoid membrane: Photosystem I, Photosystem II, the cytochrome *bf* complex, the ATP synthase, and ferredoxin-NADPH

reductase (Figure 1.1). The thylakoid membrane is divided in appressed and nonappressed regions. Photosystem I and ATP synthase are mostly located in nonappressed regions,

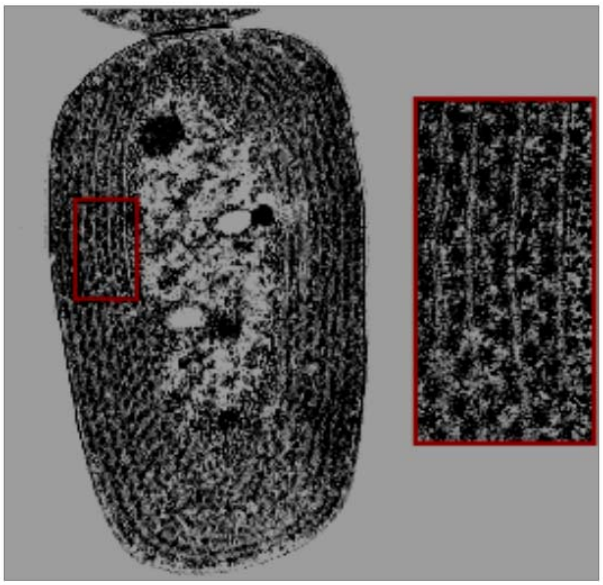

Figure 1.3: Cyanobacterial membrane. Pictue is courtesy of D. Bryant.

while PS II is mostly found in appressed regions. The cytochrome *bf* complex is distributed equally. Mobile electron carriers in the thylakoid lumen like plastoquinone, plastocyanin and ferredoxin connect the membrane embedded enzymes. Additionally, light harvesting complexes (LHC-1, LHC-2) collect the energy and funnel it into the two photosystems.

Cyanobacteria (prokaryotic organisms) are considered to be the precursors of chloroplasts.[2;34] The photosynthetic reactions in it are very similar to higher plants.[35;36] Since prokaryotic cyanobacteria do not have organells like chloroplasts (or mitochondria), photosynthesis takes place in the inner cell membrane.

Photosynthetic reaction centers

All known photosynthetic reaction centers share a few common structural features like the core structure and the arrangement of cofactors. They have two parallel branches of cofactors, related by a pseudo C_2-symmetry. The primary donor (consisting of two B(Chls)), two accessory B(Chls), two acceptor Chls or B(Pheos), and quinones are the cofactors. The names 'primary donor', 'primary acceptor' and 'secondary acceptor' for the oxygenic photosystems arise from structural comparisons with bacterial RCs. In PS I and PS II the individual electron transfer steps may occur in a slightly different way. The cofactors involved in electron transfer are bound by two homologous protein subunits (heterodimer); in some RCs by two identical (homodimeric) protein subunits. In both cases the subunits are related by pseudo C_2-symmetry.

Charge separation is initiated by absorption of a quantum of light by the RC or its surrounding antenna system. The excitation energy is then funnelled to the RC, and the electron transport starts from the excited singlet state of the primary donor. To prevent wasteful backreactions, the electron is subsequently transferred to more distant and energetically lower lying acceptors resulting in stable charge separation.

Photosynthetic reaction centers are divided in two classes: type I (*e.g.* PS I) and type II (*e.g.* PS II) RCs. Type I RCs employ FeS-clusters as terminal electron acceptors. In turn they reduce soluble ferredoxin on the stromal side of the membrane. Examples of type I RCs are PS I and the photosynthetic RCs of Heliobacteria. Type II RCs use the quinone of second branch as (mobile) terminal electron acceptor (Q_B). It receives two electrons, two protons and then leaves the binding pocket as hydroquinone. It migrates to the lipid membrane and is re-oxidized at the cytochrome *bf* complex. PS II and RCs of purple bacteria are examples of type II RCs.

Photosystem I

PS I is a large integral membrane multi protein complex (Figure 1.4). It catalyzes the light driven electron transfer from the soluble copper containing plastocyanin on the lumenal side to ferredoxin on the stromal side of the membrane. The heme containing soluble cytochrome c_6 can also act as an electron donor to PS I in cyanobacteria. In plants, algae and cyanobacteria flavodoxin can act as the electron acceptor instead of ferredoxin under iron-limiting conditions.[37] PS I consists of about 13 subunits, the exact number depending on the organism.[38;39] The major subunits PsaA, PsaB and PsaC, which carry the cofactors of the electron transfer chain and most of the antenna pigments are very similar in all organisms. The only high resolution X-ray structure (2.5 Å) is available for PS I from *Thermosynechococcus elongatus* (formerly *Synechococcus elongatus*).[32] The experiments described in this work have been performed on cyanobacterial PS I. Therefore the discussion is focussed on it.

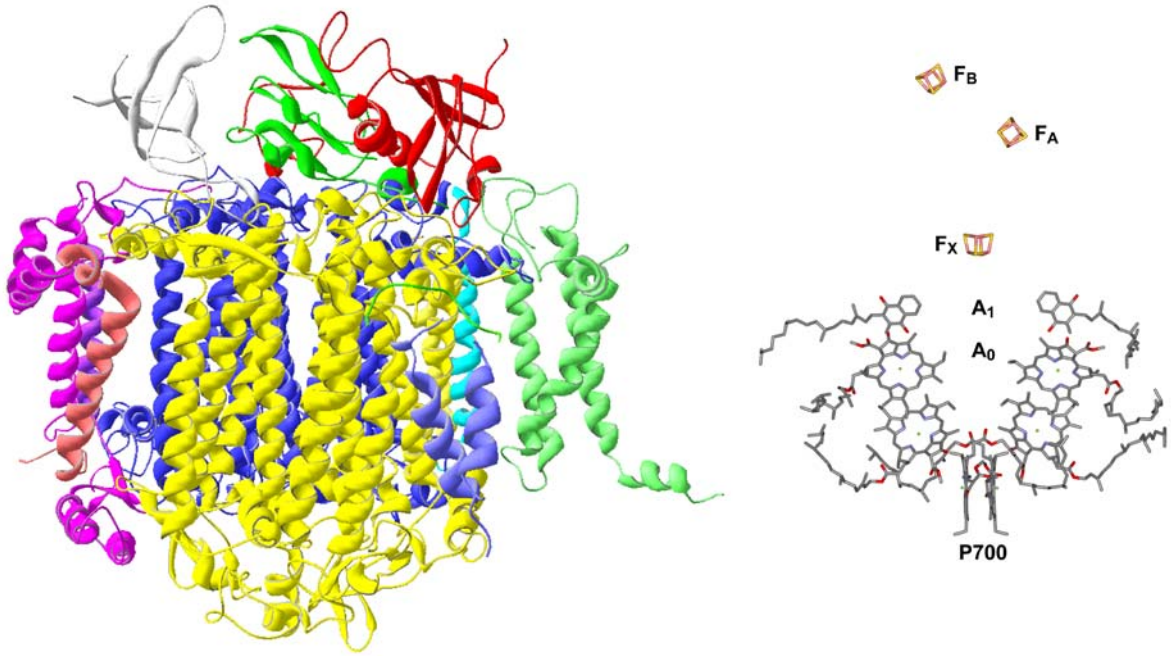

Figure 1.4: X-ray structure of cyanobacterial PS I (PDB entry 1JB0).[32] Left: View on a PS I monomer from the side. Right: View on the cofactors of the electron transfer chain in a PS I monomer.

Cyanobacterial PS I *in vivo* exists as a trimer with a molecular weight of 3x356,000 kDa.[40] It is the largest and most complex membrane protein for which the structure has been determined at atomic resolution. It binds 96 chlorophylls, 22 carotenoids, three [Fe_4S_4] clusters, two phylloquinones and four lipids. The electron transfer chain is located in the center of the protein. A pair of chlorophylls (P_{700}) are considered to be the primary donor in analogy to the bacterial photosynthetic RC. The primary electron acceptor is A_0, a monomeric chlorophyll. After A_0, the electron is transferred to A_1, a phylloquinone, and subsequently to the three FeS clusters F_X, F_A, and F_B. From the terminal cluster F_B, the electron is transferred to ferredoxin, which subsequently leaves the docking site. After the cycle is complete, $P_{700}^{\bullet+}$ has to be reduced to allow a repetition of electron transfer. A docking site for the soluble electron carriers is located on the lumenal side close to P_{700}. The two large subunits, PsaA and PsaB harbor most of the antenna system as well as most of the cofactors in the electron transfer chain. The 5 C-terminal helices of PsaA and PsaB are located at the center of PS I and surround the electron transfer chain (in homology the type II RCs), while the 6 N-terminal helices flank the inner core on both sites. Six smaller membrane-embedded proteins PsaF, PsaI, PsaJ, PsaK, PsaL and PsaX surround the core formed by the subunits PsaA and PsaB. Their main function is the stabilization of the antenna complex. Another function of the small subunits might be the interaction of PS I with external antenna complexes. PsaL has an additional structural role, since it is involved in the formation of the PS I trimer. In contrast to cynaobacteria, so far only monomeric PS I was found in eukaryotic organisms.[41;42;42] The three extrinsic subunits PsaC, PsaD, and PsaE, which do not contain any transmembrane helices, are located on the stromal site of PS I and form a stromal bridge that provides the docking site for the soluble electron carriers ferredoxin and flavodoxin. The central subunit PsaC carries the two electron acceptors F_A and F_B. The electron transfer chain is located in the center of one monomeric unit of PS I. The organic cofactors are arranged in two branches.

They are named A and B branches, since most (but not all) cofactors of the A-branch and B-branch are coordinated by the subunits PsaA and PsaB, respectively.

The primary donor

The pair of chemically different Chls constituting the 'primary donor' P_{700} are located close to the lumenal surface of PS I. The Chl of the B branch is a Chl *a* molecule, chemically identical to the other Chl molecules in PS I, whereas the Chl in the A branch is a Chl *a*′, the epimer at the C13 position of the chlorine ring system. This asymmetry is further enhanced due to a H-bonded network between the protein and the Chl *a*′ in the A branch, while the other P_{700} Chl *a* in the B branch does not form any hydrogen bonds to the protein.[40] This asymmetry can lead to significant differences in the redox potential of both chlorophylls, which may explain why the unpaired electron of the radical cation $P_{700}^{\bullet+}$ is located mostly on the B branch Chl.[43;44]

The early acceptor chlorophylls

From the primary donor the electron is transferred to the 'first stable' electron acceptor A_0. It is a matter of debate, if the accessory Chls are involved in the first electron transfer steps. In view of the quite large distance between the P_{700} Chls and A_0 in each respective branch, and the high speed of the electron transfer steps, their involvement is very likely. The central Mg atoms of the accessory Chls are not directly coordinated by the protein, but by a water molecule, which forms the second H-bond to an asparagine side chain. The discussion of the first fast steps of the electron transfer are controversial. Evidence is found that the very first step of charge separation starts from the accessory chlorophylls, and later the charge migrates to P_{700}.[45-47]

The two Chls located in the middle of the membrane region represent the spectroscopically identified electron acceptor A_0. Their coordination is unique to PS I. The sulfur atom of a methionine residue provides the axial ligand to the central Mg^{2+}. The interaction between sulfur as a weak Lewis acid and Mg^{2+} as a strong Lewis base is expected to be very weak. It has been suggested that this weak interaction hinders a stronger base like water from entering this site, thereby leading to a Chl which may behave as if it lacks a fifth ligand. This may be responsible for the extremely low redox potential of this cofactor (estimated to be ~ – 1 V). These structural features could be important for electron transport. It is reported that replacement of the methionine by histidine, which can provide a strong axial ligand to the Mg^{2+}, blocks electron transport at the level of A_0.[48] The second ligand to the A_0 Chls is provided by a tyrosine which forms a H-bond to the C12 keto group.

The phylloquinone electron acceptor (A_1)

From A_0 the electron is further transferred to the phylloquinone(s), which is the electron acceptor A_1. The quinone binding pockets on both sides of the PsaA/PsaB heterodimer are very similar. Both quinones are π-stacked with a tryptophane side chain and exhibit asymmetric hydrogen bonding. Only one of the two oxygen atoms forms a H-bond to the HN backbone group of a leucine, whereas the other oxygen atom is not hydrogen bonded. Like Chl in the A_0-site, also the protein bound phylloquinones exhibit an extremely low redox potential (estimated to be ~ – 0.8 V).[49;50] In fact, this is the most negative redox potential of all quinones found in nature, so far.

The FeS-cluster F_X

The electron proceeds from A_1 to the [4Fe4S] cluster F_X. It is a rare example fo an inter-protein FeS cluster, coordinated by four cysteines; two of them are provided by PsaA and two by PsaB. The loops of PsaA and PsaB which coordinate F_X, are highly conserved regiones in PS I. Like all components in the redox chain, its redox potential is very low, about – 700 mV.[51]

The FeS-clusters F_A and F_B

The [4Fe4S] clusters F_A and F_B are coordinated by the PsaC subunit. It is located in the center of the stromal rridge that provides the docking site for the soluble electron carrier ferredoxin. The cluster F_A is located closer to F_X, while F_B is the terminal FeS cluster (in terms of electron transfer) that transfers the electron to ferredoxin. Both FeS cluster have a similarly low redox potential.[51]

When looking at the very similar branches in PS I, the question arises if the electron transfer takes place in both branches or only in one. In type II reaction centers the use of only one branch (with exception of Q_B as terminal acceptor) is clearly a functional advantage. In contrast, this is not the case in type I RCs, since here electrons going through A- or B-branch finally end up at F_X. This topic is discussed until this date, see *e.g.* refs. [49;52]. Species dependent and/or temperature dependent electron transfer reactions have been discussed (many studies have been performed at cryogenic temperature.) Recently, there seems to be some basic agreement that at physiological temperature, both branches are active, but the electron transport *via* the B branch is faster. This could be the result of a higher activation energy barrier in the A-branch as compared to the B-branch. There are two lipids located

close to the pathway from A_1 to F_X that could account for this. A negatively charged phospholipid is located on the A branch and the electron has to be transferred against this negative charge, whereas on the B branch a neutral galactolipid is found. This could cause the higher activation energy barrier of the A branch.[35] On the other hand, charged amino acids in the environment of the two phylloquinones could also influence the branching of electron transfer, as proposed recently.[53] A recent discussion about the energetic of electron transfer to from A_0 to A_1, from A_1 to F_X, and the branching can be found in ref. [52].

Antenna system

The antenna system of PS I from *T. elongatus* contains 90 Chl molecules (plus the six RC Chls) and 22 carotenes. They capture light and transfer the excitation energy to the center of the complex, where the electron transfer chain is located. The Chls form a kind of network. Each of the Chls has several neighbors in a distance of less than 15 Å, so energy can be efficiently transferred in multiple pathways to the center of the complex where the electron transfer chain is located.[54] Carotenoids fulfill three functions in PS I.[55-57] First, they prevent the system from damage by over-excitation, caused by excess light (photoinhibition); second, they play a structural role; and third, they function as additional antenna pigments. Their photo-protective role is critical not only for PS I, but also for other photosynthetic reaction centers. Chlorophylls in excited states are highly reactive molecules. They can undergo conversion from excited singlet state to the triplet state (^{3}Chl), which can react with oxygen ($^3O_2$) to form singlet oxygen ($^1O_2^*$), a very dangerous poison for the cell. The ^{3}Chl triplet states are effectively quenched by energy transfer to carotenoids, which dissipate the excess energy by heat. In addition, already existing singlet oxygen can be converted to its ground state by carotenoids.

Aim of this work

The aim of this work is to understand the function of cofactors of the electron transfer chain in PS I. As the main tool, EPR spectroscopy is used, which is a sensitive probe of the electronic structure of the paramagnetic (functional) states of these cofactors.[58;59] 'Standard EPR methods' often do not provide sufficient resolution to disentangle the electronic structure. Hence, in this work advanced multiple resonance techniques like ENDOR and TRIPLE spectroscopy were applied (see chapter 2) to increase the resolution.[60;61] In addition, many experiments were conducted at higher frequency (34 GHz) to further increase the spectral resolution.

Model systems of the cofactors were extensively studied, allowing a detailed comparison of the protein bound cofactors and the cofactor *in vitro*. This allows to elucidate the role played by the protein environment in tuning the cofactor properties.

This investigation is focussed on two cofactors, the primary donor P_{700} and the phylloquinone electron acceptor A_1. The primary donor P_{700} exhibits two paramagnetic states, the radical cation $P_{700}^{\bullet+}$ and the triplet state $^3P_{700}$. The radical cation $P_{700}^{\bullet+}$ has already been investigated in detail previously.[44] Hence, the focus of this work is on the second paramagnetic state $^3P_{700}$, about which much less is known so far. This state is experimentally less accessible, since it is short-lived and has to be created *in situ* by light excitation. The radical anion $A_1^{\bullet-}$, the first stable electron acceptor in PS I, has already been studied extensively, since its redox potential is exceptional for a quinone.[49;50] However, definitive understanding of its electronic structure has not yet been achieved.

References

1. *Molecular to Global Photosynthesis,* Archer, M. D. and Barber, J. (Eds.), Photoconversion of Solar Energy Vol. 2, London, Imperial College Press **2004**

2. Blankenship, R. E., *Molecular Mechanisms of Photosynthesis*, Oxford, Blackwell Science Limited **2002**

3. Hall, D. O. and Rao, K., *Photosynthesis*, Cambridge, Cambridge University Press **1999**

4. Lawlor, D. W., *Photosynthesis*, New York, BIOS Scientific Publishers Limited **2001**

5. *Anoxygenic Photosynthetic Bacteria,* Blankenship, R. E., Madigan, M. T., and Bauer, C. E. (Eds.), Advances in Photosynthesis Vol. 2, Govindjee (Series Ed.), Dordrecht, Kluwer Academic Publishers **1995**

6. Voet, D. and Voet, J. G., *Biochemistry*, New York, John Wiley & Sons **2004**

7. *Energy Transduction in Biological Membranes: a Textbook of Bioenergetics,* Cramer, W. A. and Knaff, D. B. (Eds.), Springer Advanced Texts in Chemistry, New York, Springer **1990**

8. *Discoveries in Photosynthesis,* Govindjee, Beatty, J. T., Gest, H., and Allen, J. F. (Eds.), Advances in Photosynthesis and Respiration Vol. 20, Govindjee (Series Ed.), Dordrecht, Springer **2005**

9. Govindjee, in Yunus, M., Pathre, U., and Mohanty, P. (Eds.), *Probing Photosynthesis: Mechanisms, Regulation and Adaptation*, London, Taylor & Francis, 9-39 **2000**

10. Huzisige, H. and Ke, B., *Photosynthesis Research*, 38, 185-209 **1993**

11. van Helmont, J. B., *Ortus Medicinae* **1648**

12. Hales, S., *Vegetable staticks, or, an account of some statical experiments on the sap in vegetation,* Innys, W. (Ed.), London **1727**

13. Priestley, J., *Philosophical Transactions of the Royal Society of London Series B-Biological Sciences*, 62, 147-264 **1772**

14. Ingenhousz, J., London, Elmsley and Payne **1779**

15. Senebier, J., *Mémoires physicochimiques sur la l'influence de la lumière solaire pour modifier les êtres de trois règnes, surtout ceux du règne végétal*, Chirol (Ed.), Geneva **1782**

16. de Saussure, N. T., *Recheres chimique sure la Vegetation*, Paris **1804**

17. Mayer, J. R., *Die organische Bewegung in ihrem Zusammenhang mit dem Stoffwechsel*, Heilbronn **1845**

18. Engelmann, T. W., *Botanische Zeitung*, 40, 419-426 **1882**

19. Engelmann, T. W., *Botanische Zeitung*, 39, 441-448 **1881**

20. Warburg, O., *Biochemische Zeitschrift*, 103, 188-217 **1920**

21. Warburg, O., *Biochemische Zeitschrift*, 100, 230-270 **1919**

22. Wurmser, R., *Annales de physiologie et de physicochimique biologie*, 1, 47-63 **1925**

23. van Niel, C. B., Contribution to Marine Biology, Stanford, California, Stanford University Press, 161-169 **1929**

24. Hill, R., *Nature*, 139, 181-182 **1937**

25. Emerson, R. and Arnold, W., *Journal of General Physiology*, 15, 391-420 **1932**

26. Emerson, R. and Arnold, W., *Journal of General Physiology*, 16, 191-205 **1932**

27. Hill, R. and Bendall, F., *Nature*, 186, 136-137 **1960**

28. Witt, H. T., Müller, A., Rumberg, B., *Nature*, 191, 194-195 **1961**

29. Kok, B. and Hoch, G., in McElroy, W. D. and Glass, B. (Eds.), *Light and Life*, Baltimore, John Hopkins Press, 397-423 **1961**

30. Deisenhofer, J., Epp, O., Miki, K., Huber, R., Michel, H., *J. Mol. Biol.*, 180, 385-398 **1984**

31. Michel, H., *Journal of Molecular Biology*, 158, 567-572 **1982**

32. Jordan, P., Fromme, P., Witt, H. T., Klukas, O., Saenger, W., Krauss, N., *Nature*, 411, 909-917 **2001**

33. Loll, B., Kern, J., Saenger, W., Zouni, A., Biesiadka, J., *Nature*, 438, 1040-1044 **2005**

34. Olson, J. M. and Blankenship, R. E., *Photosynthesis Research*, 80, 373-386 **2004**

35. Grotjohann, I. and Fromme, P., *Photosynthesis Research*, 85, 51-72 **2005**

36. Golbeck, J. H., *Annual Review of Plant Physiology and Plant Molecular Biology*, 43, 293-324 **1992**

37. Fromme, P., Melkozernov, A., Jordan, P., Krauss, N., *FEBS Letters*, 555, 40-44 **2003**

38. Scheller, H. V., Jensen, P. E., Haldrup, A., Lunde, C., Knoetzel, J., *Biochimica et Biophysica Acta*, 1507, 41-60 **2001**

39. Xu, W., Tang, H. D., Wang, Y. C., Chitnis, P. R., *Biochimica et Biophysica Acta*, 1507, 32-40 **2001**

40. Fromme, P., Jordan, P., Krauss, N., *Biochimica et Biophysica Acta*, 1507, 5-31 **2001**

41. Sener, M. K., Jolley, C., Ben-Shem, A., Fromme, P., Nelson, N., Croce, R., Schulten, K., *Biophysical Journal*, 89, 1630-1642 **2005**

42. Ben Shem, A., Frolow, F., Nelson, N., *Nature*, 426, 630-635 **2003**

43. Krabben, L., Schlodder, E., Jordan, R., Carbonera, D., Giacometti, G., Lee, H., Webber, A. N., Lubitz, W., *Biochemistry*, 39, 13012-13025 **2000**

44. Webber, A. N. and Lubitz, W., *Biochimica et Biophysica Acta*, 1507, 61-79 **2001**

45. Müller, M., Niklas, J., Lubitz, W., Holzwarth, A. R., *Biophysical Journal*, **85**, **3899-3822 2003**

46. Holzwarth, A. R., Müller, M. G., Niklas, J., Lubitz, W., *Biophysical Journal*, 90, 552-565 **2006**

47. Holzwarth, A. R., Müller, M. G., Niklas, J., Lubitz, W., *Journal of Physical Chemistry B*, 109, 5903-5911 **2005**

48. Fairclough, W. V., Forsyth, A., Evans, M. C. W., Rigby, S. E. J., Purton, S., Heathcote, P., *Biochimica et Biophysica Acta*, 1606, 43-55 **2003**

49. Brettel, K. and Leibl, W., *Biochimica et Biophysica Acta*, 1507, 100-114 **2001**

50. Brettel, K., *Biochimica et Biophysica Acta*, 1318, 322-373 **1997**

51. Vassiliev, I. R., Antonkine, M. L., Golbeck, J. H., *Biochimica et Biophysica Acta*, 1507, 139-160 **2001**

52. Santabarbara, S., Heathcote, P., Evans, M. C. W., *Biochimica et Biophysica Acta*, 1708, 283-310 **2005**

53. Ishikita, H. and Knapp, E. W., *Journal of Biological Chemistry*, 278, 52002-52011 **2003**

54. Fromme, P., Schlodder, E., Jansson, S., in Green, B. R. and Parson, W. W. (Eds.), *Light-Harvesting Antennas in Photosynthesis*, Advances in Photosynthesis and Respiration Vol.13, Dordrecht, Kluwer Academic Publishers, 253-279 **2003**

55. *The Photochemistry of Carotenoids*, Frank, H. A., Young, A. J., Britton, G., and Cogdell, R. J. (Eds.), Advances in Photosynthesis Vol. 8, Govindjee (Series Ed.), Dordrecht, Springer **1999**

56. Frank, H. A. and Cogdell, R. J., *Photochemistry and Photobiology*, 63, 257-264 **1996**

57. Wang, Y. L., Mao, L. S., Hu, X. C., *Biophysical Journal*, 86, 3097-3111 **2004**

58. *Biophysical Techniques in Photosynthesis,* Amesz, J. and Hoff, A. J. (Eds.), Advances in Photosynthesis Vol. 3, Govindjee (Series Ed.), Dordrecht, Kluwer Academic Publishers **1996**

59. Lubitz, W., *Electron Paramagnetic Resonance*, A Specialist Periodical Report.Vol. 19, Gilbert, B. C., Davies, M., and Murphy, D., The Royal Society of Chemistry, 174-242 **2004**

60. Schweiger, A. and Jeschke, G., *Principles of pulse electron paramagnetic resonance*, New York, Oxford University Press **2001**

61. Kevan, L. and Kispert, L. D., *Electron Spin Double Resonance Spectroscopy*, New York, John Wiley & Sons **1976**

2. Electron Paramagnetic Resonance

Electron **p**aramagnetic **r**esonance (EPR) spectroscopy is like **n**uclear **m**agnetic **r**esonance (NMR) spectroscopy a magnetic resonance technique.[1] In contrast to NMR spectroscopy, where preferably diamagnetic molecules are investigated, the presence of an unpaired electron spin is an essential requirement in EPR spectroscopy. This limits the applicability of the method to paramagnetic substances. This restriction (or selectivity) to paramagnetic molecules is on the other hand an important advantage when investigating complex systems with only one or a few paramagnetic sites (surrounded by a diamagnetic environment). Hence, EPR spectroscopy has become an important technique in bioscience, see *e.g.* refs. [2;3]. In fact, in the field of photosynthesis research EPR spectroscopy is one of the most valuable tools.[4;5] Several important parameters that characterize the electronic structure of paramagnetic molecules, like the *g*-tensor and the hf tensors, can be obtained by EPR spectroscopy.

A comprehensive description of EPR spectroscopy is outside the scope of this work, and can be found elsewhere.[1;6-8] Here only a brief introduction is given which covers the special cases of radicals, radical pairs and triplet states investigated in this work, as well as the special methods applied here.

Spin Hamiltonian

An unpaired electron has a spin (S = ½) and thus a magnetic moment. The magnetic moment is proportional to the angular momentum $\vec{S}$ of the electron, so the magnetic moment operator is $\vec{\mu}_S = -g_e \mu_B \vec{S}$, where g_e is the *g*-value of the free electron (2.002319…), and μ_B is the Bohr magneton. The negative sign indicates that the electron spin

and magnetic moment have antiparallel orientation. Upon application of a static magnetic field**,** only two different orientations of the electron spin are allowed (n = 2S + 1; n = number of orientations), with the electron spin quantum number $m_S = – ½$ and $m_S = + ½$. The energies of these two electronic spin states are different, which is called the electron Zeeman effect. The state $m_S = – ½$ has lower energy, since the magnetic moment of the electron is aligned parallel to the magnetic field. The energies of these two electronic spin states are given by the spin Hamiltonian $H = \mu_B g_e \vec{B}_0 \vec{S}$.

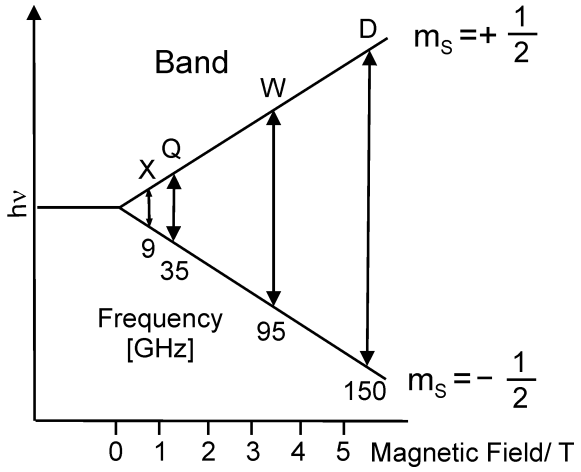

Figure 2.1: Energy of electronic spin states as a function of the magnetic field and frequency bands. m_S is the electron spin quantum number.

The energy difference between these two states depends linearly on the magnetic field and is given by $\Delta E = h\nu = \mu_B g_e B_0$. A transition between the two states can be induced by electromagnetic radiation, which is typically in the microwave (MW) frequency range at standard magnetic fields (Figure 2.1). The electron Zeeman interaction and hence the *g*-value of unpaired electrons in molecules is deviating from g_e and is anisotropic, *i.e.* dependent on the orientation of the molecule with respect to the static magnetic field and thus described by the *g*-tensor (Eq. 2.1):

$$H = \underbrace{\mu_B \vec{B}_0 \mathbf{g} \vec{S}}_{H_{EZ}} \tag{2.1}$$

In the organic radicals with planar π-systems like chlorophylls and quinones it is found that the *g*-tensor component normal to the molecular plane is close to the value of the free electron ($g_z \approx g_e$) , while the two other *g*-tensor components in the plane are shifted to higher values ($g_x, g_y > g_e$) due to spin orbit coupling of the ground state with excited states.[9-11]

The second type of interaction is the nuclear Zeeman interaction, analogue to the electron Zeeman interaction. Many nuclei have a nuclear spin $I \neq 0$ (if the numbers of protons and neutrons are not both even) like ^1H, ^2H, ^{13}C and ^{14}N and hence also a magnetic moment (the magnetic moments of the nuclei are much smaller than the one of the electron). The energy levels are thus further split (Eq. 2.2); see Figure 2.2 for an energy diagram of a system consisting of one electron spin and one nuclear spin I = ½.

$$H = H_{EZ} + \underbrace{\sum_{i=1}^{n} \left(- \mu_N^i g_N^i \vec{B}_0 \vec{I}_i \right)}_{H_{NZ}} \tag{2.2}$$

where μ_N and g_N are the nuclear magneton and *g*-factors of the corresponding nuclei (n is the number of nuclei). The small *g*-anisotropy of the nuclei is usually neglected in EPR spectroscopy. The internuclear spin coupling is so small that is it not resolved in EPR spectroscopy.

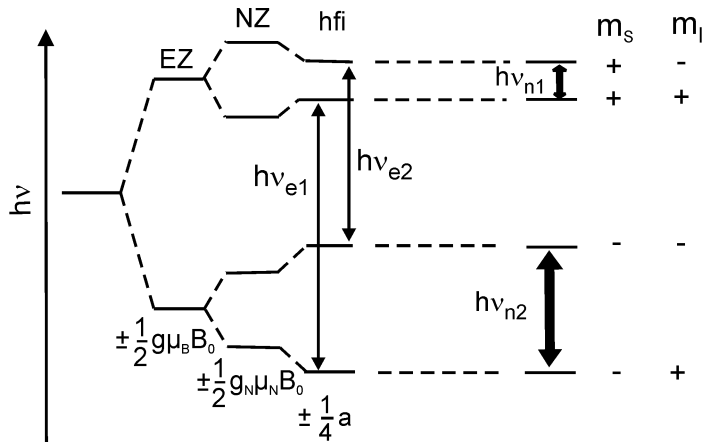

Figure 2.2: Energy diagram for one unpaired electron spin S = ½ (isotropic *g*-value) interacting with one nucleus with I = ½ (positive nuclear *g*-value, *e.g.* a proton), and isotropic hfcc (first order assumption; weak coupling case). EZ = electron zeeman interaction, NZ = nuclear zeeman interaction, hfi = hyperfine interaction. The two allowed EPR transitions are marked with thin arrows ($h\nu_e$), the two allowed NMR transition are marked with thick arrows ($h\nu_n$).

The third type of interaction is between the magnetic moments of the nuclei with the electron spin, called hyperfine interaction (hfi). This interaction does not further split the energy levels, but causes a shift (Figure 2.2). The hfi can be split in two different terms. The first is the isotropic Fermi contact term, which is proportional to the electron spin density at the nucleus. The second term is the anisotropic dipole-dipole interaction. This results in the following spin Hamiltonian (Eq. 2.3) for a single electron interacting with n nuclei with I = ½:

$$H = H_{EZ} + H_{NZ} + \sum_{i=1}^{n} \underbrace{\vec{S}\mathbf{A}_i\vec{I}_i}_{hfi} \tag{2.3}$$

where $\mathbf{A}_i$ is the hyperfine (hf) tensor of nucleus *i*.

A fourth type of interaction may occur if the nuclear spin I ≥ 1. This interaction is called the nuclear quadrupole interaction, which arises from an electric field gradient at the nucleus (Eq. 2.4):

$$H = H_{EZ} + H_{NZ} + H_{hfi} + \sum_{i=1}^{n} \underbrace{\vec{I}_i\mathbf{Q}_i\vec{I}_i}_{H_{nq}}, \tag{2.4}$$

where $\mathbf{Q}_i$ is the (traceless) nuclear quadrupole (nq) tensor of nucleus *i*.

In case of presence of a second unpaired electron spin in the system, as found for radical pairs or triplet states, an additional interaction is present. It can be split into the isotropic exchange term and the anisotropic dipolar interaction between the two unpaired electron spins. In this work, the radical pair (RP) $P_{700}^{\bullet+}A_1^{\bullet-}$ and the Chl triplet states $^3P_{680}$ and $^3P_{700}$ were investigated. For the RP investigated here, the exchange interaction is negligibly small. In the Chl triplet states EPR transitions from triplet to singlet states are forbidden. Thus, the exchange interaction term can be neglected. The dipolar interaction between the two electrons is described by the (traceless) zero field splitting (ZFS) tensor **D**:

$$\mathbf{D} = \begin{pmatrix} \frac{1}{3}D - E & 0 & 0 \\ 0 & \frac{1}{3}D + E & 0 \\ 0 & 0 & -\frac{2}{3}D \end{pmatrix} \tag{2.5}$$

This tensor can thus be described by the values D and E (in case of axial symmetry E = 0). The spin Hamiltonian for a system with S = 1 with n nuclei is then as follows (Eq. 2.6):

$$H = H_{EZ} + H_{EX} + \underbrace{\vec{S}\mathbf{D}\vec{S}}_{H_{DD}} + H_{NZ} + H_{hfi} + H_{nq} \tag{2.6}$$

EPR spectroscopy of biomolecules can in principle be performed on solutions or single crystals. For measurement on solutions, two limiting cases have to be distinguished: i) liquid solutions with fast tumbling of the paramagnetic molecules and ii) frozen solutions with random orientation of the molecules with respect to the external magnetic field. In the first case, all anisotropic parts of the interactions vanish due to motional averaging. This means that only the trace of the *g*-tensor and hf tensors is observed, *i.e.* only g_{iso}- and a_{iso}- values can be determined. Since the nq tensor is traceless, it can not be observed in liquid solutions. The

traceless dipolar interaction of two unpaired electrons is also averaged out. In frozen solution the sum of isotropic and anisotropic interactions can be observed. The random orientation of the molecules typically leads to the observation of powder patterns and dramatically reduced resolution as compared to liquid solution.

However, not all parameters of Eq. 2.6 can be obtained by the analysis of EPR spectra in liquid and frozen solution. Instead a variety of methods have to be applied to determine these parameters. The main methods used in this work are described below.

EPR spectroscopy

There exist two possibilities to record an EPR spectrum: i) either a constant magnetic field is applied and the frequency of the electromagnetic radiation is scanned, or, ii) the frequency of the electromagnetic radiation is kept constant and the magnetic field is scanned. The later method is experimentally by far more common and was used throughout this work. The measurements can be done using weak, continuous electromagnetic irradiation and detection (CW EPR). In CW EPR the static magnetic field is superimposed with a modulated (usually in kHz region) magnetic field to increase the sensitivity (phase-sensitive detection). This results in derivative-like EPR spectra. The other possibility is pulse EPR, where strong and short MW pulses are used to excite the spin system and to detect the **e**lectron **s**pin **e**cho (ESE) or the **f**ree **i**nduction **d**ecay (FID). Both CW and pulse EPR were used in this work. As mentioned above, EPR spectroscopy can be performed at various magnetic fields and frequency bands (Figure 2.1). Due to the linear dependence of the resonance frequency on the magnetic field, higher magnetic fields can be used to resolve the anisotropy of the *g*-tensor. In this work, the standard X-band and the higher frequency Q-band were used.

ENDOR spectroscopy

The limited resolution of EPR spectra often (especially in frozen solution) prevents the determination of hf tensors. Higher resolution can be obtained by application of advanced EPR techniques like **e**lectron-**n**uclear **do**uble **r**esonance (ENDOR) spectroscopy.[12-14] ENDOR is a double resonance technique, which uses RF radiation to drive NMR transitions and MW frequency radiation to drive EPR transitions (Figure 2.2). In an ENDOR experiment, the radio frequency is scanned, while other parameters are kept constant. Like EPR experiments, ENDOR experiments can be performed in CW[12;13] or pulse mode.[7;14] In a CW ENDOR experiment a partially saturated EPR transition is desaturated by the RF radiation. The change of the EPR signal intensity is the ENDOR signal. In order to increase the sensitivity, the RF is frequency modulated (usually in the kHz range) in a way analogous to the field modulation in an EPR experiment. The two main pulse ENDOR techniques are called Davies ENDOR[15] and Mims ENDOR[16] after their inventers. Davies ENDOR (Figure 2.3 A) is usually used to determine the hfccs of strongly coupled nuclei, while Mims ENDOR (Figure 2.3 B) is usually used to investigate intermediate to weakly coupled nuclei.[7;14] The ENDOR sequences can be separated into three periods: the inversion, mixing and detection period. In the Davies ENDOR experiment, the first microwave (MW) π-pulse selectively inverts the polarization of a particular EPR transition. The subsequent radio frequency (RF) π-pulse mixes the population of levels with different projections of nuclear spins. Then the detection sequence monitors the resulting populations of the electron spin levels. The Mims ENDOR starts with the preparation sequence of two non-selective $\pi/2$ MW pulses, spaced by τ, which creates a grated polarization pattern. During the mixing period, a RF π-pulse is applied which changes the polarization. The detection is done *via* the stimulated echo.

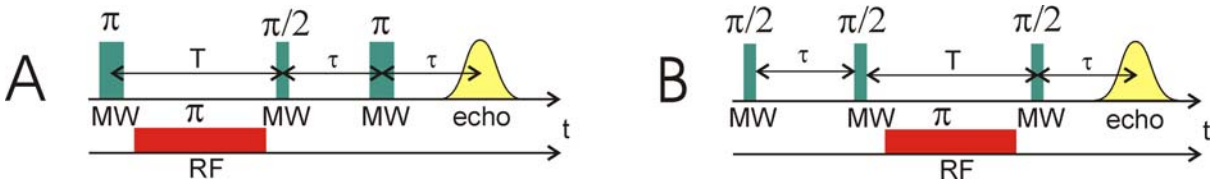

Figure 2.3: Pulse ENDOR techniques. MW denotes the microwave pulses (flip angles given above), RF the radio frequency pulses (π-pulses). Pulse lengths and interpulse delays are kept constant, the RF is scanned. **A** Davies ENDOR[15] **B** Mims ENDOR[16]

Both CW and pulse methods have specific advantages and are in some way complementary. CW ENDOR is the superior method for measurements in liquid solution[13], whereas in frozen solutions and powders pulse ENDOR is often the method of choice.[7;14]

ENDOR spectra of frozen solutions often consist of multiple overlapping powder patterns of different nuclei. To determine the angles of the hfccs with respect to the *g*-tensor or ZFS-tensor axes one has to selectively excite molecules that have different orientations with respect to the magnetic field. For a complete orientation selection all principal components of the *g*-tensor must be resolved.[7]For the quinone radicals investigated here, the *g*-tensor is not resolved at X-band frequency. The use of higher magnetic fields like Q-band leads in some cases to complete resolution of the *g*-tensor and to complete orientation selection in the ENDOR experiments.

TRIPLE spectroscopy

Depending on the interaction mechanism, nuclei can have different signs of hf couplings. Especially important is the sign of the isotropic coupling (a_{iso}), which depends on the mechanism leading to a non-zero electron spin density at the nucleus. The most important nucleus for EPR spectroscopy on organic radicals is the proton. In EPR spectroscopy, protons are often divided by their distance to the π-system. Protons directly bound to carbon atoms which are part of the π-system, are called α-protons. Protons, which are one bond further

away, are called β-protons and so on. For α–protons in π-radicals, which are coupled by the exchange mechanism (π-σ spin polarization), a negative sign of a_{iso} is typically found, while a positive sign is an indication of the hyper conjugation mechanism and characteristic for β–protons as found in methyl or methylene groups.[1;6] Hence the sign of the hfcc contains not only important information about the spin system, but also direct structural information. The ENDOR spectra provide only the magnitude of the hf coupling constants (hfcc) but do not directly give their signs. In rare cases it is possible to determine the sign of a hfcc by analysis of the temperature dependence of the ENDOR lines or by analysis of their line shape. There are several EPR techniques for the hfcc sign determination. Most commonly used is the electron-nuclear-nuclear general triple experiment (TRIPLE), which uses two different radio frequencies to drive different NMR transitions. In the CW general TRIPLE experiment an NMR transition of one nucleus is saturated by RF radiation, while the second radio frequency is scanned. The change of intensity of ENDOR lines as compared to the normal ENDOR experiment is the TRIPLE signal. This method is often successfully applied in liquids,[13] and delivers directly the sign of the isotropic hfcc.

In frozen solutions pulse general TRIPLE[7;14;17] (Figure 2.4) is often superior over CW general TRIPLE experiments, but it still suffers from lower sensitivity. In the one-dimensional (1D) pulse TRIPLE resonance experiment, an additional RF π-pulse is applied during the mixing time of the Davies ENDOR experiment. While the first RF pulse is set to one of the ENDOR transitions, the frequency of the second RF pulse is scanned to generate the TRIPLE spectrum. The difference between this spectrum and the ENDOR spectrum yields the difference TRIPLE spectrum, which exhibits only ENDOR lines that belong to the same m_S manifold as the one selected by the first RF pulse.

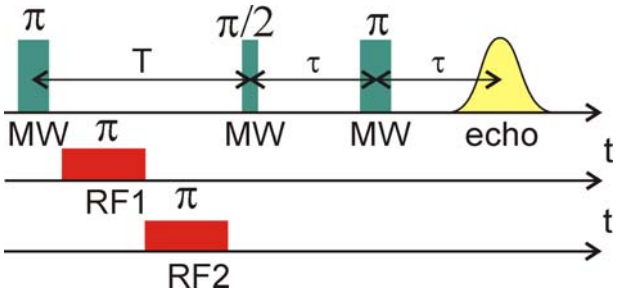

Figure 2.4: Pulse electron-nuclear-nuclear triple resonance technique based on Davies ENDOR. In the one-dimensional experiment, one RF is kept constant,[17] while in the two-dimensional experiment both RFs are scanned.[18;19]

This experiment can be extended to the second dimension by sweeping the frequencies of both RF pulses (two-dimensional (2D) pulse TRIPLE).[18] This can be used to disentangle an ENDOR spectrum, which is congested and consists of signals originating from different paramagnetic centers. It allows an assignment of the signals to their respective centers and electron spin manifolds. The application of the 2D TRIPLE experiment to orientationally disordered systems like frozen solutions[19] can resolve overlapping powder patterns. Moreover, it is highly dependent on the relative orientation of the hyperfine tensors of the nuclei with respect to each other. The information about the angles of the hfccs with respect to the *g*-tensor is only partially accessible to an ENDOR experiment; *e.g.* ENDOR spectra of two protons which have an A_z orientation collinear to the g_z component and are rotated one with a positive and one with a negative angle from g_x are identical. But in the 2D TRIPLE experiment they can be distinguished. Beside that, 2D TRIPLE spectra are more sensitive for the angles between hyperfine couplings than ENDOR spectra, which allows the determination of these angles more precisely.

EPR spectroscopy of short-lived species

Many paramagnetic states are short-lived. Hence, for the study of these states, two conditions have to be fulfilled. The first one is the (repetitive) creation of these radicals, radical pairs or triplet states in the EPR resonator. In case of photosynthetic reaction centers, this is often provided by excitation with light.[20-23] The second condition is the use of time-resolved techniques. This is usually no problem for pulse techniques, since they are inherently time-resolved. The pulse techniques can be used as in case of the stationary species. Only a Laser pulse is introduced before the pulse sequence.

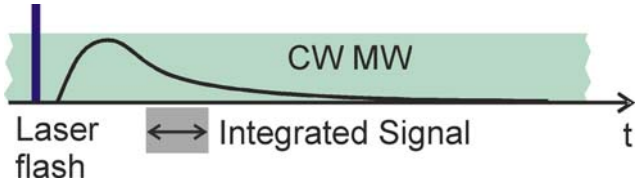

Figure 2.5: The principle of transient EPR using direct detection (no field modulation). The paramagnetic species is created by a short light pulse, *e.g.* by a Laser, and the absorbance changes are observed. A transient EPR spectrum is obtained by integration of the EPR signal over a certain period.

In contrast, for CW EPR it is more difficult to achieve time-resolution. Similar to normal CW EPR, low microwave power is used in time-resolved CW experiments to monitor the buildup and the decay of the paramagnetic species. The time resolution is limited by the frequency of the modulation (time resolution typically tens of µs). To improve the time resolution of the experiment, the EPR signal is often measured with direct detection of the EPR signal without modulation (Figure 2.5).[21;24;25] The concomitant loss of sensitivity is often dispensable due to the strong spin polarization in radical pairs and triplet states, which leads to strong signals.[26-28]The determination of the hfcc signs in the light-induced species is different for triplet states and radical pairs. If the sign of the ZFS tensor is known, the ENDOR spectrum of a triplet state reveals directly the sign of the hfccs.

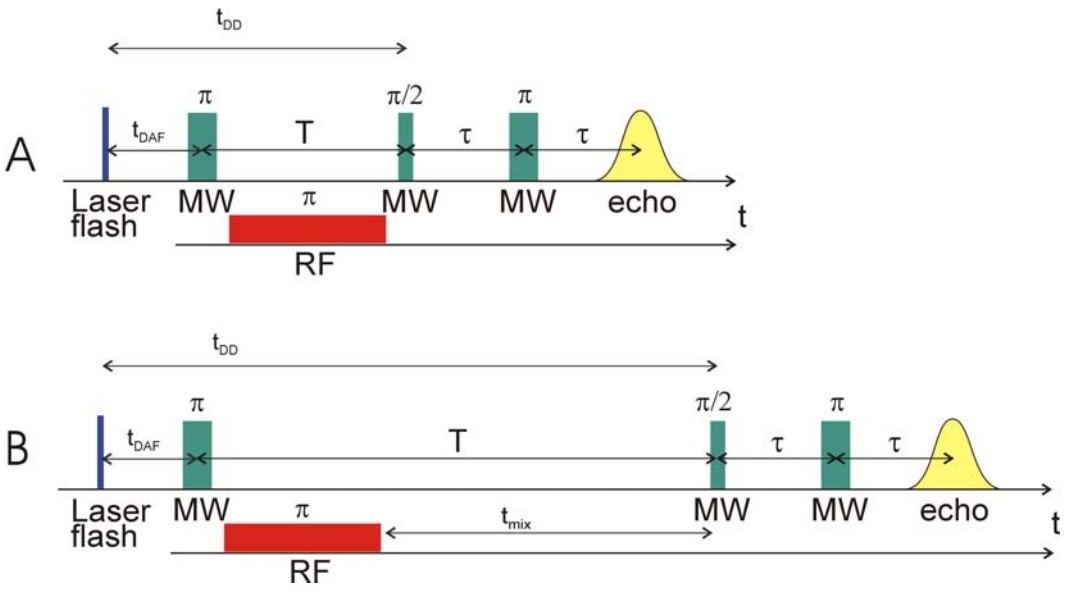

Figure 2.6: Pulse ENDOR of light-induced species. **A** Davies ENDOR on a light-induced paramagnetic species, *e.g.* a spin-polarized radical pair. **B** **V**ariable **mi**xing **t**ime (VMT) ENDOR on a light-induced spin-polarized radical pair.[29]

However, this does not apply to radical pairs. In principle, the TRIPLE experiment can be performed like on stationary radicals to determine the hfcc sign. But it was found in this work, that the efficiency of the TRIPLE experiment was too low to determine the hfcc sign in the radical pair $P_{700}^{\bullet+}A_1^{\bullet-}$. Another method applied by Fursman *et al.*[30] works only for very special cases. Hence, a different method was introduced to determine the hfcc sign in spin polarized radical pairs. A modification of the Davies ENDOR sequence, called **v**ariable **mi**xing **t**ime (VMT) ENDOR, which allows the determination of absolute signs of hfcc was recently proposed.[31;32] It was found that in the case of strong polarization of electron spin states (*e.g.* at high fields and low temperatures), the introduction of an additional delay time t_{mix} after the RF pulse (Figure 2.6), comparable with the electron spin lattice relaxation time, results in a change of the relative intensities of ENDOR lines originating from different electron spin manifolds. This change of intensities allows to assign the ENDOR lines to the electron spin manifold and in turn to determine the absolute sign of the hfcc (if the sign of the

nuclear *g*-value is known). Due to the strong non-equilibrium polarization of the electron spin states in the RP similar effects were observed for the radical pair.[29]

References

1. Carrington, A. and McLachlan, A. D., *Introduction to Magnetic Resonance*, New York, Harper & Row **1969**

2. Möbius, K. and Lubitz, W., in Berliner, L. J. and Reuben, J. (Eds.), *Biological Magnetic Resonance*.Vol. 7, New York, Plenum Press, 129-247 **1987**

3. *Advanced EPR - Applications in Biology and Biochemistry*, Hoff, A. J. (Ed.), Amsterdam, Elsevier **1989**

4. Lubitz, W. and Lendzian, F., *Advances in Photosynthesis. "Biophysical Techniques in Photosynthesis"*, Dordrecht, Kluwer, 255-275 **1996**

5. Lubitz, W., *Electron Paramagnetic Resonance*, A Specialist Periodical Report.Vol. 19, Gilbert, B. C., Davies, M., and Murphy, D., The Royal Society of Chemistry, 174-242 **2004**

6. Atherton, N. M., *Principles of Electron Spin Resonance*, New York, E. Horwood & PTR Prentice Hall **1993**

7. Schweiger, A. and Jeschke, G., *Principles of pulse electron paramagnetic resonance*, New York, Oxford University Press **2001**

8. Weil, J. A., Bolton, J. R., Wertz, J. E., *Electron Paramagnetic Resonance: Elementary Theory and Practical Applications*, Weil, J. A., Bolton, J. R., and Wertz, J. E. (Eds.), New York, John Wiley & Sons, Inc. **1994**

9. Stone, A. J., *Molecular Physics* , 7, 311-316 **1964**

10. Stone, A. J., *Proceedings of the Royal Society of London Series A-Mathematical and Physical Sciences*, 271, 424-424 **1963**

11. Stone, A. J., *Molecular Physics*, 6, 509-515 **1963**

12. Kevan, L. and Kispert, L. D., *Electron Spin Double Resonance Spectroscopy*, New York, John Wiley & Sons **1976**

13. Kurreck, H., Kirste, B., Lubitz, W., *Electron nuclear double resonance spectroscopy of radicals in solution - applications to organic and biological chemistry*, Marchand, A. P. (Ed.), Deerfield Beach, Florida, VCH Publishers, Inc. **1988**

14. Gemperle, C. and Schweiger, A., *Chemical Reviews*, 91, 1481-1505 **1991**

15. Davies, E. R., *Physics Letters A*, 47, 1-2 **1974**

16. Mims, W. B., *Proceedings of the Royal Society of London Series A-Mathematical and Physical Sciences*, 283, 452-& **1965**

17. Mehring, M., Höfer, P., Grupp, A., *Berichte der Bunsen-Gesellschaft-Physical Chemistry Chemical Physics*, 91, 1132-1137 **1987**

18. Epel, B. and Goldfarb, D., *Journal of Magnetic Resonance*, 146, 196-203 **2000**

19. Goldfarb, D., Epel, B., Zimmermann, H., Jeschke, G., *Journal of Magnetic Resonance*, 168, 75-87 **2004**

20. Möbius, K., *Molecular Crystals and Liquid Crystals*, 394, 1-17 **2003**

21. Levanon, H. and Möbius, K., *Annual Review of Biophysics and Biomolecular Structure*, 26, 495-540 **1997**

22. Stehlik, D. and Möbius, K., *Annual Review of Physical Chemistry*, 48, 745-784 **1997**

23. Stehlik, D., Bock, C. H., Thurnauer, M. C., in Hoff, A. J. (Ed.), *Advanced EPR - Applications in Biology and Biochemistry*, Amsterdam, Elsevier, 371-403 **1989**

24. Bittl, R. and Weber, S., *Biochimica et Biophysica Acta*, 1707, 117-126 **2005**

25. McLauchlan, K. A., in Hoff, A. J. (Ed.), *Advanced EPR - Applications in Biology and Biochemistry*, Amsterdam, Elsevier, 345-369 **1989**

26. Budil, D. E. and Thurnauer, M. C., *Biochimica et Biophysica Acta*, 1057, 1-41 **1991**

27. Angerhofer, A. and Bittl, R., *Photochemistry and Photobiology*, 63, 11-38 **1996**

28. Angerhofer, A., in Scheer, H. (Ed.), *Chlorophylls*, Boca Raton, CRC Press, 945-991 **1991**

29. Epel, B., Niklas, J., Antonkine, M. L., Lubitz, W., *Applied Magnetic Resonance*, 30, 311-327 **2006**

30. Fursman, C. E., Teutloff, C., Bittl, R., *Journal of Physical Chemistry B*, 106, 9679-9686 **2002**

31. Epel, B., Poppl, A., Manikandan, P., Vega, S., Goldfarb, D., *Journal of Magnetic Resonance*, 148, 388-397 **2001**

32. Epel, B., Manikandan, P., Kroneck, P. M. H., Goldfarb, D., *Applied Magnetic Resonance*, 21, 287-297 **2001**

3. Materials and Experimental Procedures

Chemicals

Quinones

1,4-Benzoquinone (BQ), 1,4-naphthoquinone (NQ), 2-methyl-1,4-naphthoquinone (VK_3) and 2-methyl-3-phytyl-1,4-naphthoquinone (VK_1) were obtained commercially (Aldrich).

The deuterated 1,4-benzoquinone (BQ-d_4) was prepared by I. Heise (MPI für Bioanorganische Chemie, Mülheim) as described previously by Zhao *et al.*[1] The degree of deuteration was checked with NMR and mass spectroscopy and was found to be higher than 95%.

Perdeuterated 2-methyl-1,4-naphthoquinone (VK_3-d_8) was a kind gift of H. Zimmermann (MPI für Medizinische Forschung, Heidelberg). It was prepared as follows: 5 g 2-methyl-naphthalene (Aldrich) was perdeuterated by heating with 100 ml D_2O (99.9%) and 200 mg Pt (Adams catalyst prereduced with deuterium gas) in a stainless steel high pressure vessel with metal-fittings for 8 days at 290°C. The exchange was repeated twice under the same conditions. The final product (9 g) was distilled in the bulb-tube. Mass spectroscopy delivered m/e = 152, and a degree of deuteration ~98%. The freezing point was 34-36 °C. To 3.75 g 2-methyl-naphthalene-d_{10} in 45 ml CH_3COOD (90%, in D_2O) were added drop wise while stirring within one hour 14.5 g CrO_3 in 25 ml diluted CH_3COOD (60%, in D_2O). The temperature during the addition was kept at 5-10 °C, followed by incubation at room temperature for 30 minutes, then by heating at 40°C for another hour. After cooling, the mixture was poured in 200 ml cold D_2O, filtered, washed with water and recrystallized from

ethanol/water. This yielded 1.5 g crystalline product. Mass spectroscopy delivered a m/e = 172, and the degree of deuteration ~98%. The melting point was determined to be 105-106 °C. The fully deuterated 1,4-naphthoquinone (NQ-d_6) was prepared from naphthalene-d_8 (Aldrich) as described above for 2-methyl-1,4-naphthoquinone.

Solvents

2-Propanol-h_8 (IP-d_8) and 2-Propanol-d_8 (IP-d_8) were obtained from Merck (Darmstadt) and 2-Propanol-d_1 (IP-d_1) from Roth (Karlsruhe (all z.A. quality)). All other solvents used were obtained from Merck (Darmstadt). Methanol-d_4, ethanol-d_6, *tert*-butanol, chloroform and tetrahydrofuran (THF) were z.A. quality. Dimethoxyethane (DME) and dimethylformamide (DMF) were z.S. quality, while acetonitrile was HPLC quality and dimethylsolfoxide (DMSO) was Uvasol quality. DMF and DMSO were dried, purified by fractional destillation and carefully dried again. All other solvents were thoroughly dried using standard methods.[2] Benzyl-trimethyl-ammonium-hydroxid [$C_{10}H_{17}ON$] in methanol was obtained from Lancaster (Newgate, Great Britain). Potassium-*tert*-butylate [C_4H_9KO] was obtained from Acros Organics (Geel, Belgium).

Preparation of quinone radical anions in vitro

Preparation using coulometry

The coulometry setup was connected to a high-vacuum line. It contained 4 electrodes. The reference was an $Ag/AgNO_3$ electrode. The concentration was 20 mM in acetonitrile with 0.2 M tetrabutylammonium-hexafluorophosphate ($TBAPF_6$) as supporting electrolyte. The second electrode was a Pt-wire, the third a Pt-net, and the fourth one was glassy carbon. The

salt bridge consisted of acetonitrile with a Pt-wire. The supporting electrolyte (either $TBAPF_6$ or tetrabutylammonium-tetrafluoroborate ($TBABF_4$) was added into the cell and degassed using an oil bath at 150°C for 60-90 minutes with the high vacuum line pumping. About 10 mL of solvent was distilled on the supporting electrolyte. Directly before use, all solvents were deoxygenated using three freeze-pump-thaw cycles. In N_2 (purified using an Oxisorb® gas purification cartridge) counter flow BQ/BQ-d_4 was added which was in a tiny glass capillary (under N_2 atmosphere), resulting in a 1 mM solution. A potentiostat EG&G 283 was used. Cyclovoltammetry was measured before performing coulometry to assure correct setup, and to check for the redox potential of the sample. In the cyclovoltammetry the Pt-net acted as counter electrode. For coulometry the Pt-wire was used as counter electrode, and the Pt-net as working electrode. The applied voltage was 100 mV more negative than the first reduction peak. Reduction was performed using 700 mC, which under ideal conditions yields 70 % singly reduced $BQ^{\bullet-}$. An EPR quartz tube with 3.0 mm o.d. was directly connected to the coulometry cell. About 40-100 µL of the solution were transferred to the EPR tube and frozen in liquid nitrogen. Subsequently, the tube was pumped and sealed.

Preparation using chemical methods

Liquid solution samples

The respective quinone was dissolved in IP-h_8 and filled in the capillary (o.d. 2 mm), equipped with a side bag. Potassium-*tert*-butylate was used as base and filled into the side arm. The tubing was connected to a high-vacuum line and pumped until all IP-h_8 was evaporated. The solvent was degassed by three freeze-pump-thaw cycles, and was distilled in the side arm with potassium-*tert*-butylate. Then the glass tubing was evacuated again and sealed under vacuum. The quinone was dissolved in the solution of potassium-*tert*-butylate in

IP (quinone concentration 0.2-0.5 mM). Generation of the semiquinone radical anion with benzyl-trimethyl-ammonium-hydroxide lead to samples with identical EPR and ENDOR spectra. The yield of the radical anion was superior, but sometimes degenerated products appeared after longer incubation times at ambient temperatures. All liquid solution EPR and ENDOR spectra were recorded on samples, where the quinone radical anion was generated with potassium-*tert*-butylate.

Frozen solution samples

The quinones were dissolved in IP-h_8, IP-d_1, IP-d_8, MeOH-d_4, EtOH-d_6, *tert*-butanol or D_2O, which was deoxygenated by bubbling with purified nitrogen in a quartz tube (o.d. 3 mm). A small amount of a solution of benzyl-trimethyl-ammonium-hydroxide in methanol was added to the deoxygenated solutions. For BQ and NQ, benzyl-trimethyl-ammonium-hydroxide was diluted in the respective IP. Then, the samples were rapidly frozen in liquid nitrogen. The sample was pumped and sealed afterwards. The initial concentration of the quinones in IP was below 0.5 mM in case of IP, 1 mM in case of EtOH and *tert*-butanol, 5 mM in case of MeOH and 50 mM in case of D_2O as solvents.

Cell growth and isolation of PS I

Growth of the thermophilic cyanobacterium *Thermosynechococcus elongatus* and the isolation of PS I is described in ref. [3]. The trimeric PS I complexes were a kind gift from P. Fromme, J. Frank and J. Kern (TU Berlin).

Growth of *Synechocystis* sp. PCC 6803 is described in ref. [4] The cells were a kind gift of H. Strauss and P. Schmieder (Leibniz-Institut für molekulare Pharmakologie, Berlin). Growth of the *menB*26 mutant strain is described in ref. [5]. It is a spontaneous light-tolerant mutant from the *menB*18 strain.[5;6] In *menB* strains, the biosynthetic pathway of VK_1 is interrupted by interposon mutagenesis of the *menB* genes in *Synechocystis* sp. PCC 6803.[6] The procedure used for the isolation of trimeric PS I complexes is a modification of the one used in ref. [7].

Cells were harvested by 15 minutes centrifugation at 8000 g, resuspended in small volume of ice-cold 50 mM Tris, pH 8.0 buffer (about 100 ml for 2 liter culture) and centrifuged again. The cells were thoroughly resuspended in the same buffer (1 gram of cell pellet per 10 ml buffer) using a homogenizer. All subsequent preparation steps were done on ice or in the cold room (4°C) and under green light. Pre-cooled buffers and solutions were used. Cells were broken by passing twice through French Pressure Cells (4°, 1200 psi pressure). Unbroken cells or cell debris was removed by a short centrifugation (15 minutes, 6000g). The thylakoid membranes in the supernatant were spun down by ultracentrifugation for 1 hour at 45000 rpm (Ti-70 rotor). The supernatant containing bilinprotein was discarded. The thylakoid pellet was resuspended in a very small volume (a few mL only) of 50 mM Tris, pH 8.0 buffer with a homogenizer. The volume of the sample was adjusted to a final Chl concentration of about 0.4-.5 mg/ml Chl (after addition of β-DM in the next step). To increase the yield of PS I trimers from the membranes, $CaCl_2$ stock solution was added to the membranes (final concentration 1 mM), and incubated for 30-40 min in the dark at 4°C with medium stirring. The membranes were solubilized with 1% β-DM for 45-60 minutes (20% stock solution, added drop wise while stirring). The unsolubilized material was removed by centrifugation at about 12000 rpm for 20 minutes (JA 20 rotor). The solubilized membranes were loaded on a continuous sucrose gradient (20%-5% w/v in 50 mM Tris pH 8.0 buffer with 0.05% β-DM), spun in an ultracentrifuge for about 14-17 hours (SW 28 rotor, 28000 rpm). The lower green

band containing mainly trimeric PS I was collected. Two methods were used to remove the sucrose and worked equally well:

(i) Dilution and subsequent concentration of the sample. The sample was diluted with 50 mM Tris buffer pH 8.0 with 0.02% β-DM and concentrated again. This procedure was applied twice. As concentrator, a 50 ml Amicon cell(Millipore, Bedford, MA), either with a YM100 or YM50 membrane was used.

(ii) Dialysis for 4 hours against 4.5 L of 50 mM Tris pH 8.0 buffer with 0.01% β-DM (or 2 times by 2 hours). A 50 kDa cut-off membrane (Spectra por pre-soaked membrane) was used. The sample was concentrated using the same cell and membrane as described above.

The samples were loaded onto a second gradient (5-20% sucrose in 50 mM Tris buffer pH 8.0 without detergent). The samples were spun in an ultracentrifuge for 14-17 hours (SW 28 rotor, 28000 rpm). The trimeric PS I was pelleted after centrifugation and was solubilized with a small volume of 20 mM Tris buffer pH 8.0 with 0.05% β-DM. The resuspended PS I was washed using a concentrator as mentioned above to remove sucrose. Glycerol was added to 20% (w/v) final concentration. Afterwards the sample was quickly frozen in liquid nitrogen and stored at -80^{o}C.

Preparation of biological samples

Quinone exchange in the A_1 binding site of PS I

A two hundred fold molar excess of either VK_3-h_8 or VK_3-d_8 (30 mM solution in ethanol) was added to a 6-12 µM trimeric PS I solution (50 mM Tris pH 8.0 with 0.05% β-DM) isolated from the *menB*26 mutant cells. Incubation was carried out at room temperature for about 4 h with intensive stirring under room light and continued overnight in the dark at 4°C.

Afterwards, the samples were washed twice with 2 mL of buffer to remove excess quinone using a 50 kDa Centricon to a final volume of about 50 µL.

To achieve a H/D exchange in *menB* PS I samples, the concentrated PS I solution (~1 mM Chl) was applied to a NAP-10 column equilibrated with D_2O-buffer (50 mM Tris, pD 8.3, 0.05% β-DM), and eluted with the same buffer. Then the quinone exchange against VK_3-h_8 was performed as described above, but using the D_2O-buffer (50 mM Tris, pD 8.3, 0.05% β-DM). The sample was stirred overnight in the dark at 4 °C to allow efficient exchange.

Preparation of $P_{700}^{\bullet+}$ samples for EPR spectroscopy

Samples with trimeric PS I from *T. elongatus* and *Synechocystis* sp. PCC 6803 contained between 12 and 20 mM Chl. $P_{700}^{\bullet+}$ was generated by continuous illumination at room temperature with two 150 W halogen lamps equipped with a water filter, cold glass filter and a concentrated $CuSO_4$ solution (used to minimize IR and UV irradiation) for a few seconds followed by rapid freezing under illumination.

Preparation of $A_1^{\bullet-}$ samples for EPR spectroscopy

All steps were done under anaerobic conditions. The buffers were degassed and purged by Argon. About 20 µL solution of trimeric PS I (> 10 mM Chl a) were mixed with 2.5 µL 1 M glycine buffer pH 10. Fresh sodium dithionite (Fluka, Neu-Ulm) was dissolved in 1 M glycine buffer pH 10 (final concentration 300 mM), and 2.5 µL added to the PS I solution. This was followed by a dark adaptation for 30 minutes at 4 °C to ensure good pre-reduction of the iron-sulfur centers, with subsequent freezing. Illumination was carried out at 200 K by two 150 W halogen lamps from two sides. A water filter, cold glass filter and a concentrated $CuSO_4$

solution were used to minimize IR and UV irradiation. Illumination time was 5 minutes. For *T. elongatus* PS I an additional illumination for 10 minutes at 240 K was done. This increased the amount of $A_1^{\bullet-}$ without yielding a significant amount of $A_0^{\bullet-}$.

Preparation of $A_0^{\bullet-}$ samples for EPR spectroscopy

All steps were done under anaerobic conditions. The buffers were degassed and purged by Argon. Samples with trimeric PS I from *T. elongatus* contained between 12 and 20 mM Chl. PS I samples from *Synechocystis* sp. PCC 6803 whose VK_1 molecules were extracted by treatment with organic solvents[8] contained about 4 mM Chl. The latter ones were prepared in the group of A. van der Est (St. Catharines, Canada). About 20 µL solution of PS I were mixed with 2.5 µL 1 M glycine buffer pH 10. Fresh sodium dithionite (Fluka, Neu-Ulm) was dissolved in the same buffer (final concentration 300 mM), and 2.5 µL added to the PS I solution. This was followed by a dark adaptation of 30 minutes at 4 °C to ensure good prereduction of the iron-sulfur centres, and subsequent freezing. Illumination was carried out at 240 K by two 150 W halogen lamps from two sides. A water filter was used. Illumination time was 20 minutes.

Preparation of PS I samples for EPR spectroscopy on $P_{700}^{\bullet+}$ $A_1^{\bullet-}$

Samples with trimeric PS I from *T. elongatus* and *Synechocystis* sp. PCC 6803 contained between 12 and 20 mM Chls. Samples were reduced by adding sodium ascorbate solution (to a final concentration of 5 mM), relaxed 5 minutes in the dark at 4°C, and afterwards quickly frozen in liquid nitrogen in the dark.

Preparation of PS I samples for EPR spectroscopy on $^3P_{700}$

The $^3P_{700}$ EPR samples were prepared similar to the one used for generation of the stationary radical anion $A_1^{\bullet-}$:

(i) For low temperature measurements (10-220 K) the protein was concentrated to about 12-15 mM Chl. Sodium dithionite was added to a final concentration of 30 mM in 0.2 M glycine buffer (pH 10.0). The sample was incubated 30 minutes anaerobically at 4°C in the dark. Illumination was done with the setup described above at 0°C anaerobically for 15 min (in case of X-band samples), followed by rapid freezing. In case of Q-band samples, the illumination was done at 240 K for 30 minutes.

ii) For high temperature measurements (240-295 K) the protein was concentrated to about 20 mM Chl. Treatment with sodium dithionite was performed as described above. Quartz capillaries with an outer diameter of 4 mm and an inner diameter of 1.2 mm (255 K) and 0.8 mm (≥ 265 K) have been used. The illumination after the 30 min prereduction was omitted, because excitation of these type of samples creates the secondary radical pair, which recombines to the triplet state of P_{700} with high yield at higher temperatures.

Preparation of PS II samples for EPR spectroscopy on $^3P_{680}$

D_1D_2*cytb*559-complexes[9] were a kind gift of the AG of Prof. A. Holzwarth (MPI für Bioanorganische Chemie, Mülheim). They were prepared from market spinach as described in ref. [10], with the exception that the incubation with Triton X-100 was done three times. The complexes obtained by this method contain six Chl *a*, two pheophytin *a*, one or two *β*-carotene molecules. The samples contained no quinones, and have most probably no non-heme iron. The complexes were concentrated to an OD_{676} ~ 200 using a YM-30 Centricon and afterwards quickly frozen in liquid nitrogen.

Uv/vis spectroscpopy

Uv/vis spectra were measured in two channel spectrometers, either a Cary 05E (Varian) or a UV2-300 (Unicam). Reference was the same solvent/buffer. The Chl concentration in the sample was determined in the following way: A small amount of buffer containing PS I or PS II was mixed with 80% (v/v) buffered (Na_2CO_3) acetone, thoroughly mixed and spun down. A spectrum of the supernatant was recorded and the Chl concentration calculated using the absorption coefficients determined by Porra *et al.*[11]

Cyclovoltammetry and square wave voltammetry

An $Ag/AgNO_3$ electrode was used as reference electrode, which was 20 mM in Acetonitrile with 0.2 M Tetrabutylammonium-hexafluorophosphate ($TBAPF_6$) as supporting electrolyte. Both working and counter electrode were glassy carbon. The salt bridge consisted of acetonitrile with a Pt-wire. A potentiostat type EG&G 273 A was used. Supporting electrolytes were $TBAPF_6$ and $TBABF_4$. The supporting electrolyte was dissolved in 5 mL of the respective solvent. BQ-h_4/BQ-d_4 was added in counter flow of Argon 4.0, further purified with an Oxisorb® gas purification cartridge, to a final concentration of 1 mM. Cyclovoltammetry was performed with different scan speeds in the range of 25-800 mV/s. Square wave voltammetry was done with 6-24 kHz. Afterwards, Ferrocen was added in purified Argon counter flow and the voltammetry was repeated with a larger scanning range. It is assumed to be independent from the respective solvent. All preparative steps were done under Argon (grade 4.0), which was further purified using an Oxisorb® gas purification cartridge.

EPR spectroscopy

CW EPR, ENDOR, general and special TRIPLE measurements at X-band were performed on a Bruker ESP 300E X-band EPR spectrometer with home-built ENDOR accessories, consisting of a Rhode & Schwarz RF signal generator (type SMT 02) and an ENI A-500 (500W) RF amplifier. A TM_{110}-type microwave cavity similar to the one described previously was used.[12] The sample temperature was controlled using a Bruker ER4111 VT nitrogen flow system. A PC with home-written software was used for data acquisition in multiple resonance experiments (ENDOR, general TRIPLE, special TRIPLE). The stationary magnetic field, which is monitored by a Hall probe, was additionally checked by an ER 035 M-1000 NMR Gaussmeter and subsequently corrected for an offset and by a linear correction with the factor of 1.0045 (a field sweep of 1.000 mT according to the Hall controller corresponds to a 'real' field sweep of 1.0045 mT).

CW EPR Q-band experiments were carried out on a Bruker ER200E spectrometer equipped with a DR051 QG microwave bridge. The MW frequency was monitored by a frequency counter of the type HP 5352B. The magnetic field was – in addition to the Hall controller – checked by an ER 035 M-1000 NMR Gaussmeter. The resonator was of similar type as the one described in ref. [13], but with graphite as cavity material. Phosphorus-doped silicon (PSi) was mounted in the resonator as internal *g*-standard.[14] It was calibrated with a LiF:Li crystal in an EPR tube, which *g*-value is known to a high precision.[15]

Transient EPR, pulse EPR and ENDOR X-band measurements were performed on a Bruker ESP 380E FT-EPR spectrometer with an ER 4118 SPT resonator or 1052 DLQ-H resonator placed in an Oxford CF935 helium cryostat. Direct detection EPR without field modulation was done and data analysis were performed as described in ref.[16], using a laboratory written

acquisition module. Data were recorded with a Lecroy 9540A digital storage oscilloscope triggered by a photodiode. Samples were excited by 532 nm flashes from a frequency doubled Nd:YAG laser (Spectra Physics, GCR 130) with 8 ns duration. The repetion rate was 10 Hz. Incident light energy at the sample was 10 mJ per pulse at low temperatures (below 180 K), 7 mJ from 180 K to 240 K and 2 mJ above 240 K. Temperature calibration was performed with a thermocouple at the sample position under laser illumination. For pulse EPR and ENDOR measurements a travelling wave tube (TWT) amplifier was used. A ENI A-500 (500W) RF amplifier was used for the ENDOR measurements.

Transient EPR, pulse EPR, ENDOR and TRIPLE Q-band measurements were done on a Bruker ELEXSYS E580-Q spectrometer with a Super Q-FT microwave bridge equipped with a home-built resonator similar to the one described in ref. [13]. Field-sweep echo-detected (FSE) EPR spectra were recorded using the two-pulse echo sequence ($\pi/2$-τ-π-τ-echo), in which the echo intensity was registered as a function of the external magnetic field. Microwave (MW) pulses of 40 ns ($\pi/2$) and 80 ns (π pulse) and τ = 340 ns were used. The ^{1}H ENDOR was recorded using the Davies ENDOR sequence.[17] (π-t-$\pi/2$-τ-π-τ-echo) with an inversion π pulse of 200 ns, t = 21 μs, and radiofrequency (RF) π-pulse of 17 μs and the detection sequence similar to the FSE EPR experiment The ^{2}H ENDOR was recorded using the Mims ENDOR sequence[18] ($\pi/2$-τ-$\pi/2$-t-$\pi/2$-τ-echo) with 44 ns $\pi/2$ pulses, τ = 268 ns and an RF π-pulse of 40 μs. An ENI 3200L (300W) RF amplifier was used for ^{1}H ENDOR measurements and an ENI A-500 (500W) RF amplifier with a Trilithic^{TM} high power low-pass filter H4LE35-3-AA ('cut off' frequency ~35 MHz) for ^{2}H ENDOR measurements. One- and two-dimensional TRIPLE experiments[19-21] were performed using the same ENDOR sequence as described above with the introduction of a second RF pulse of same length between first RF pulse and detection sequence.

For measurements of the light-induced radical pair $P_{700}^{\bullet+}$ $A_1^{\bullet-}$ and the light-induced triplet states $^3P_{680}$ and $^3P_{700}$ a resonator of same design was used which contained 12 slits of 0.3 mm width to allow *in situ* light excitation of the sample. Light excitation at 532 nm was achieved with the Brilliant Laser system from Quantel. It consists of an OPO, type Vibrant 355 II, pumped by short (~ 8 ns) light pulses at 355 nm provided by a Nd:YAG Laser. The light was coupled into the cavity by an optical fibre with an output energy of ~ 12 mJ. Transient EPR was done using the direct detection method. Field-sweep echo-detected EPR (FSE EPR) spectra were recorded using the two-pulse echo sequence ($\pi/2$-τ-π-τ-echo), where the echo intensity was registered as a function of the magnetic field. The delay after laser flash (DAF) was 1 µs, unless explicitly stated differently. Microwave (MW) pulses of $t_{\pi/2}$ = 40 ns, t_{π} = 80 ns and τ = 400 ns were used. ^{1}H ENDOR was recorded using the Davies ENDOR sequence (π-t-$\pi/2$-τ-π-τ-echo) with an inversion pulse t_{π} = 200 ns, t = 21 µs, radiofrequency (RF) π-pulse of 17 µs and detection sequence similar to EDEPR experiment[17]. For ^{1}H ENDOR measurements of the RP the generation of RF pulses and the detection was done by an external PC equipped with the SpecMan program[22] and an Agilent E4420B RF synthesizer. The sequence of MW and RF pulses and detection was repeated twice after 10 ms and 20 ms, respectively, and subtracted to account for stationary background. An ENI 3200L 300W RF amplifier was used for most measurements.

The VMT (**v**ariable **m**ixing **t**ime) ENDOR experiment[23] on the RP was similar to the Davies type ENDOR experiment, but using a 9 µs RF pulse. Here, a type AR2500L RF amplifier (Amplifier Research) was used. All pulse EPR and ENDOR spectra were corrected for the 'dark' background spectra recorded 10 ms after the Laser flash.

Spectral simulations

Stationary radicals ($P_{700}^{\bullet+}$, $A_1^{\bullet-}$, $Q^{\bullet-}$)

The frequencies and probabilities of EPR and ENDOR transitions were derived from Eq. 2.4 by application of the selection rules $\Delta m_S = 1$ and $\Delta m_I = 0$, and $\Delta m_S = 0$ and $\Delta m_I = 1$ for allowed EPR and ENDOR transitions, respectively. Since paramagnetic centers of a frozen solution sample are randomly oriented, the EPR spectra are obtained by summation of signals from all orientations. For the correct calculation of EPR spectra the strongly coupled protons were included. The ENDOR experiments are performed at a specific magnetic field. Due to the finite width of the microwave pulses, only part of the EPR spectrum is excited. This effect (orientation selection) has to be taken into account to correctly estimate the impact of different transitions on the final ENDOR spectra. The orientation selectivity of MW pulses in ENDOR was accounted for by i) inclusion of the strongly coupled protons in the spin Hamiltonian, ii) manual specification of the excitation width of pulses, comparable with the EPR linewidth. All data processing routines and simulations were done in Matlab™ environment.[24] EPR spectra were simulated using the EasySpin software package (version 2.2.0).[25] For ENDOR and TRIPLE simulations the EasySpin package together with home-written routines was used. The EasySpin software directly evaluates the spin Hamiltonian without using any approximations. Both EPR and ENDOR simulations were done simultaneously to increase the precision of the determination parameters. The ENDOR signatures of every nucleus were obtained separately and then summed with appropriate weight coefficients. A manual fit of experimental data was used in all cases. The effect of microwave pulse selectivity in Davies ENDOR experiments was taken into account by multiplication of the calculated ENDOR spectra with a frequency dependent profile (self-ELDOR hole[26]) approximated by a Lorentzian function. The width (FWHH) of the profile was taken equal to $\Gamma_{ELDOR}/2\pi = 1/2t_{inv} = 2.5$ MHz. The efficiency of Mims ENDOR is hf

coupling-dependent (blind spots) and was calculated according to the simplified formula: $F(\nu-\nu_L) = \frac{1}{2}\sin^2(2\pi(\nu-\nu_L)\tau)$, where ν_L is the nuclear Larmor frequency and τ = 268 ns.[18;26]

Spin-correlated radical pair $P_{700}^{\bullet+}A_1^{\bullet-}$

The simulations of the EPR spectra of the spin-correlated radical pair $P_{700}^{\bullet+}A_1^{\bullet-}$ were done with the program of Salikhov and coworkers[27-29] (in Matlab™ environment[24]). The protons of the methyl group (the only strongly coupled protons in $A_1^{\bullet-}$) were included in the simulation.

Since no program for the simulation of the ENDOR spectra of the spin-correlated radical pair $P_{700}^{\bullet+}A_1^{\bullet-}$ was available, the same program was used as for the stationary radicals.

Spin-polarized triplet states $^3P_{680}$ and $^3P_{700}$

The EPR spectra of the spin-polarized triplet state of the donor Chl(s) $^3P_{680}$ and $^3P_{700}$ were simulated using a home written program (by E. Reijerse) in Matlab™ environment,[24] which calculates the two positions of the triplet state transitions in the first order approximation for the zero field splitting (ZFS). It is assumed that exclusively the T_0 state is populated and that *g*- and ZFS-tensors are collinear.

DFT calculations of the quinone radical anions

Phylloquinone and other quinones *in vitro*

Complete geometry optimizations were performed for $BQ^{\bullet-}$, $NQ^{\bullet-}$, $VK_3^{\bullet-}$, and $VK_1^{\bullet-}$, in coordination with two to four IP molecules. For $VK_1^{\bullet-}$ a reduced model system was employed, truncated after the fifth carbon of the phytyl chain (Figure 3.1). In each system,

one or two H-bonds to each carbonyl oxygen atom were assumed in the starting structures. For $VK_3^{\bullet-}$ and $VK_1^{\bullet-}$, additional calculations were performed. For these, a special geometry optimization with H-bonds restricted to the quinone plane was done. In all cases, B3LYP density functional[30-32] was used in combination with the Dunning-Huzinaga basis sets, which

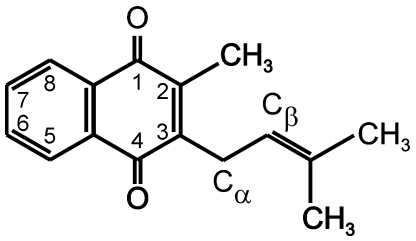

Figure 3.1: Molecular structure of the truncated model system of VK_1 used in the DFT calculations. C_α and C_β denote the first and second carbon atom of the phytyl chain.

were augmented by polarization and diffuse functions from the same authors.[33] The Gaussian 03 program was used for the geometry optimizations.[34] The spectroscopic data were computed in additional single point calculations employing the optimized geometries. For this purpose the B3LYP functional was used in combination with the EPR-II basis set, which was developed for an accurate calculation of magnetic properties.[35] The *g*-values were calculated employing the coupled-perturbed Kohn-Sham equations,[36] in conjunction with a parameterized one electron spin-orbit operator.[37] Magnetic hfcc were calculated for all hydrogen and deuterium atoms, including the isotropic Fermi contact terms and the dipolar hfcc. All property calculations were performed in gas phase and employing the COSMO continuum method,[38] using the dielectric constant of $\varepsilon = 18.3$ for IP. All spectroscopic data were calculated with the program package ORCA.[39]

Phylloquinone in the A_1 binding site of PS I

The smallest feasible model system was chosen, containing the phylloquinone with a truncated phytyl chain (Figure 3.1) and the -truncated- two amino acids leucine (LeuA722)

and alanine (AlaA721). The peptide nitrogen of leucine forms the H-bond to the quinone oxygen. The coordinates were taken from the x-ray structure of the pdb file 1JB0[40] and a restricted geometry optimization was performed. Hereby, the orientation of the phytyl chain was fixed (the dihedral angle C_β-C_α-C_3-C_2 was kept constant), and the orientation of the leucine with respect to the quinone was frozen, while the H-bond length was not fixed. This was realized by fixing i) the distance between the carbonyl oxygen O_4 and the leucine nitrogen atom, ii) the angle between C_4, O_4, and the leucine nitrogen atom, and iii) the dihedral angle between C_3, C_4, O_4, and the leucine nitrogen atom. All other geometrical parameters were fully optimized.

The B3LYP density functional[30-32] was used in combination with the Dunning-Huzinaga basis sets, which were augmented by polarization and diffuse functions from the same authors.[33] The Gaussian 03 program was used for the geometry optimizations.[34] The spectroscopic data were computed in additional single point calculations employing the optimized geometries. For this purpose the B3LYP functional was used in combination with the EPR-II basis set, which was developed for an accurate calculation of magnetic properties.[35] The *g*-values were calculated employing the coupled-perturbed Kohn-Sham equations,[36] in conjunction with a parameterized one electron spin-orbit operator.[37;41;42] Magnetic hfcc were calculated for all hydrogen atoms, including the isotropic Fermi contact terms and the dipolar hfcc. The property calculations were performed in gas phase. All spectroscopic data were calculated with the program package ORCA.[39]

References

1. Zhao, J. D., Warren, P. V., Li, N., Bryant, D. A., Golbeck, J. H., *FEBS Letters*, 276, 175-180 **1990**

2. Perrin, D. D., Armarego, W. L. F., Perrin, D. R., *Purification of laboratory chemicals*, Pergamon Press **1980**

3. Fromme, P. and Witt, H. T., *Biochimica et Biophysica Acta*, 1365, 175-184 **1998**

4. Strauss, H. M., Hughes, J., Schmieder, P., *Biochemistry*, 44, 8244-8250 **2005**

5. Johnson, T. W., Zybailov, B., Jones, A. D., Bittl, R., Zech, S., Stehlik, D., Golbeck, J. H., Chitnis, P. R., *Journal of Biological Chemistry*, 276, 39512-39521 **2001**

6. Zybailov, B., van der Est, A., Zech, S. G., Teutloff, C., Johnson, T. W., Shen, G. Z., Bittl, R., Stehlik, D., Chitnis, P. R., Golbeck, J. H., *Journal of Biological Chemistry*, 275, 8531-8539 **2000**

7. Shen, G. Z., Zhao, J. D., Reimer, S. K., Antonkine, M. L., Cai, Q., Weiland, S. M., Golbeck, J. H., Bryant, D. A., *Journal of Biological Chemistry*, 277, 20343-20354 **2002**

8. Rustandi, R. R., Snyder, S. W., Biggins, J., Norris, J. R., Thurnauer, M. C., *Biochimica et Biophysica Acta*, 1101, 311-320 **1992**

9. Nanba, O. and Satoh, K., *Proceedings of the National Academy of Sciences of the United States of America*, 84, 109-112 **1987**

10. van Leeuwen, P. J., Nieveen, M. C., van de Meent, E. J., Dekker, J. P., van Gorkom, H. J., *Photosynthesis Research*, 28, 149-153 **1991**

11. Porra, R. J., Thompson, W. A., Kriedemann, P. E., *Biochimica et Biophysica Acta*, 975, 384-394 **1989**

12. Zweygart, W., Thanner, R., Lubitz, W., *Journal of Magnetic Resonance Series A*, 109, 172-176 **1994**

13. Sienkiewicz, A., Smith, B. G., Veselov, A., Scholes, C. P., *Review of Scientific Instruments*, 67, 2134-2138 **1996**

14. Stesmans, A. and Devos, G., *Physical Review B*, 34, 6499-6502 **1986**

15. Stesmans, A. and VanGorp, G., *Review of Scientific Instruments*, 60, 2949-2952 **1989**

16. Bittl, R., Schlodder, E., Geisenheimer, I., Lubitz, W., Cogdell, R. J., *Journal of Physical Chemistry B*, 105, 5525-5535 **2001**

17. Davies, E. R., *Physics Letters A*, 47, 1-2 **1974**

18. Mims, W. B., *Proceedings of the Royal Society of London Series A-Mathematical and Physical Sciences*, 283, 452-& **1965**

19. Goldfarb, D., Epel, B., Zimmermann, H., Jeschke, G., *Journal of Magnetic Resonance*, 168, 75-87 **2004**

20. Epel, B. and Goldfarb, D., *Journal of Magnetic Resonance*, 146, 196-203 **2000**

21. Mehring, M., Höfer, P., Grupp, A., *Berichte der Bunsen-Gesellschaft-Physical Chemistry Chemical Physics*, 91, 1132-1137 **1987**

22. Epel, B., Gromov, I., Stoll, S., Schweiger, A., Goldfarb, D., *Concepts in Magnetic Resonance Part B-Magnetic Resonance Engineering*, 26B, 36-45 **2005**

23. Epel, B., Niklas, J., Antonkine, M. L., Lubitz, W., *Applied Magnetic Resonance*, 30, 311-327 **2006**

24. Matlab™, Natick, MA, The Mathworks, Inc., **2004**

25. Stoll, S. and Schweiger, A., *Journal of Magnetic Resonance*, 177, 390-403 **2005**

26. Gemperle, C. and Schweiger, A., *Chemical Reviews*, 91, 1481-1505 **1991**

27. Kandrashkin, Y. E., Salikhov, K. M., van der Est, A., Stehlik, D., *Applied Magnetic Resonance*, 15, 417-447 **1998**

28. Salikhov, K. M., Schlüpmann, J., Plato, M., Möbius, K., *Chemical Physics*, 215, 23-35 **1997**

29. Kandrashkin, Y. E., Salikhov, K. M., Stehlik, D., *Applied Magnetic Resonance*, 12, 141-166 **1997**

30. Lee, C. T., Yang, W. T., Parr, R. G., *Physical Review B*, 37, 785-789 **1988**

31. Becke, A. D., *Journal of Chemical Physics*, 98, 5648-5652 **1993**

32. Stephens, P. J., Devlin, F. J., Chabalowski, C. F., Frisch, M. J., *Journal of Physical Chemistry*, 98, 11623-11627 **1994**

33. Dunning, T. H., *Journal of Chemical Physics*, 53, 2823-2833 **1970**

34. Frisch, M. J., Trucks, G. W., Schlegel, H. B., Scuseria, G. E., Robb, M. A., Cheeseman, J. R., Montgomery, J., Vreven, T., Kudin, K. N., Burant, J. C., Millam, J. M., Iyengar, S. S., Tomasi, J., Barone, V., Mennucci, B., Cossi, M., Scalmani, G., Rega, N., Petersson, G. A., Nakatsuji, H., Hada, M., Ehara, M., Toyata, K., Fukuda, R., Hasegawa, J., Ishida, T., Nakajima, T., Honda, Y., Kitao, O., Nakai, H., Klene, M., Li, X., Knox, J. E., Hratchian, H. P., Cross, J. B., Adamo, C., Jaramillo, J., Gomperts, R., Stratmann, R. E., Yazyev, O., Austin, A. J., Cammi, R., Pomelli, C., Ochterski, J. W., Ayala, P. Y., Morokuma, K., Voth, G. A., Salvador, P., Dannenberg, J. J., Zakrzewski, V. G., Dapprich, S., Daniels, A. D., Strain, M. C., Farkas, O., Malick, D. K., Rabuck, A. D., Raghavachari, K., Foresman, J. B., Ortiz, J. V., Cui, Q., Baboul, A. G., Clifford, S., Cioslowski, J., Stefanov, B. B., Liu, G., Liashenko, A., Piskorz, P., Komaromi, I., Martin, R. L., Fox, D. J., Keith, T., Al Laham, M. A., Peng, C. Y., Nanayakkara, A., Challacombe, M., Gill, P. M. W., Johnson, B., Chen, W., Wong, M. W., Gonzalez, C., Pople, J. A., Gaussian 03, Revision B.01, Pittsburgh PA, Gaussian, Inc., **2003**

35. Barone, V., *Recent Advances in Density Functional Methods*, Chong, D. P. (Ed.), World Scientific Publ. Co.: Singapore **1996**

36. Neese, F., *Journal of Chemical Physics*, 115, 11080-11096 **2001**

37. Koseki, S., Schmidt, M. W., Gordon, M. S., *Journal of Physical Chemistry A*, 102, 10430-10435 **1998**

38. Klamt, A. and Schüürmann, G., *Journal of the Chemical Society-Perkin Transactions 2*, 5, 799-805 **1993**

39. Neese, F., ORCA. An *ab initio*, Density Functional and Semiempirical Program Package, Mülheim an der Ruhr, Germany, Max-Planck-Institut für Bioanorganische Chemie, **2004**

40. Jordan, P., Fromme, P., Witt, H. T., Klukas, O., Saenger, W., Krauss, N., *Nature*, 411, 909-917 **2001**

41. Koseki, S., Gordon, M. S., Schmidt, M. W., Matsunaga, N., *Journal of Physical Chemistry*, 99, 12764-12772 **1995**

42. Koseki, S., Schmidt, M. W., Gordon, M. S., *Journal of Physical Chemistry*, 96, 10768-10772 **1992**

4. Studies on Quinone Model Systems

Quinones are important organic cofactors involved in many electron transfer processes in nature.[1-3] They can exist in different redox and protonation states, *e.g.* in the oxidized state Q, in the singly reduced radical anion state $Q^{\bullet -}$, and as hydroquinone QH_2 (Figure 4.1). In the electron transport chain in PS I the quinone vitamin K_1 (VK_1, phylloquinone) serves as an intermediate electron acceptor (named A_1). During the electron transfer this quinone becomes singly reduced and its radical anion is formed.[4-6]

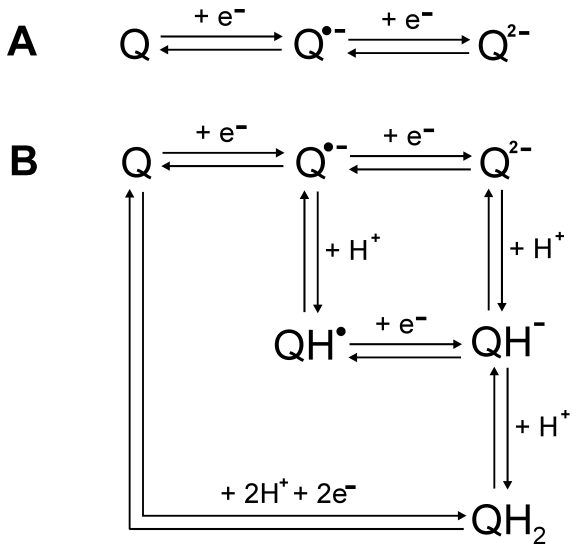

Figure 4.1: Quinone redox and protonation states. Adapted from ref. [3] **A** In an aprotic solvent. **B** In a protic solvent.

The most important property of A_1 is its ability to undergo oxidation/reduction. There is a energetic difference between its neutral state A_1 and the (paramagnetic) radical anion $A_1^{\bullet -}$. The oxidation/reduction potential has to be adjusted between the redox potentials of its electron donor A_0 and its electron acceptor F_X. The specific interaction between the quinone and the protein modifies its electronic structure and properties. The redox potential of A_1 is found to be several hundreds millivolt more negative than the potential of VK_1 in water.[4;5]

VK_1 in the protein binding site represents a very complicated system with several amino acids in a specific spatial arrangement. It is very difficult to understand the electronic structure of the protein bound cofactor without a comparison with the cofactor *in vitro*. The factors affecting the electronic properties of the protein bound cofactor can not be easily extracted; even if a high resolution X-ray structure is available. Advanced quantum mechanical calculations are necessary to obtain information about the electronic structure from the nuclear coordinates. Hence, the use of model compounds, which mimic the properties of their biological counterparts, is often the prerequisite or a first step in the understanding of the function of protein bound cofactors and to deconvolute the variety of influences of the protein on the cofactor. The '*in vitro* system' is simpler and different effects can be separated, *e.g.* by chosing solvents with different properties, or by use of selectively labeled solvents and/or models.

Here, for the investigation of model quinones, two experimental methods were applied: electrochemistry (to determine the redox potential) and EPR/ENDOR spectroscopy (to determine the *g*- and hf tensors).

In the first part of this chapter, the influence of the polarity of the surrounding of the quinone *in vitro* upon its redox potential is studied. The influence of the surrounding on the *g*-tensor of the quinone radical anion was also studied. It was shown previously experimentally and theoretically, that the *g*-tensor is a sensitive probe for the environment of the quinone radical anion.[7-11] The aim is to achieve a correlation between the redox potential and the *g*-tensor. This is especially interesting, since the redox potential of protein bound cofactors is often difficult to determine, whereas the *g*-tensor is more easily accessible from a simple EPR experiment.

The second part of this chapter deals with the characterization of the electron spin distribution in the quinone radical anions *in vitro*. Advanced EPR techniques like ENDOR

and TRIPLE were applied to determine the proton hf tensors, from which the spin density distribution can be extracted. To support the determination of the hf tensors and the molecular assignment, DFT calculation were performed. The comparison of the experimentally determined results and the results from DFT calculations also allows an estimation of the precision of the DFT approach, which is mandatory for the combined ENDOR and DFT study of $VK_1^{\bullet-}$ in PS I ($A_1^{\bullet-}$) in chapter 5.

The influence of the polarity of the surrounding on the quinone properties

The influence of the surrounding on the quinone properties may be separated into two contributions: the general polarity of the surrounding, which in some way also includes H-bonding, and site-specific effects of the protein (*e.g.* asymmetric H-bonding as found in PS I[12]). Protein-specific effects are hard to model. But a general and overall description of the protein binding pocket in terms of a more polar or apolar environment can be achieved in (isotropic) solutions.

At this point two important questions arise: what is polarity and how can it be quantified? There have been numerous studies on the measurement of polarity of a solvent and its influence on chemical properties on the dissolved molecules (solute), that are cited in refs. [13-15]. For a basic classification of solvents several different schemes exist.[15] For an (quantitative) investigation of the dependence of a parameter, *e.g.* the redox potential, on the polarity a quantitative description is necessary.

In some simplified theories, the dielectric constant (*i.e.* the relative permittivity) is often predicted to serve as a good quantitative measure of the polarity of the solvent. These theories regard solvents as a non-structured continuum not composed of individual solvent molecules

with their own solvent/solvent interactions, and they do not take into account specific solute/solvent interactions such as hydrogen-bonding and EPD/EPA (electron pair donor/electron pair acceptor) interactions.

The dipole moments of individual solvent molecules are also inadequate measures of solvent polarity. The charge distribution in a solvent molecule may not only be given by its dipole moment but also by its quadrupole or even higher multipole moments. This leads to dipolar, quadrupolar, etc. solvent molecules.[13]

The polarity of a solvent is determined by its solvation capability (or solvation power) for reactants and activated complexes as well as for molecules in their ground and excited states.[13] This depends on the action of all specific and nonspecific, intermolecular forces between ions, directional interactions between dipoles, inductive, dispersion, hydrogen bonding, and charge-transfer forces as well as solvophobic interactions. Only those interactions leading to definite chemical alteration of the solute molecules are excluded. No single macroscopic physical parameter could account for the variety of solute/solvent interactions. Hence, empirical scales of solvent polarity were introduced, based on convenient solvent sensitive reference processes. Since they reflect the complete picture of all the intermolecular forces acting in solution, these empirical parameters constitute a more comprehensive measure of the polarity of a solvent than any other single physical constant. Any empirical solvent scale is based on a particular reference process. Hence, it is not expected to be universal and useful for all kinds of reactions and absorptions.

The most comprehensive scales (more than 30 different solvent scales are known) are the ones derived from spectroscopic reference processes, which are easiest to measure for a large set of organic solvents. In the following, three main solvent polarity scales derived from spectroscopic reference processes are discussed which appear to be most suited for this study.

1. Dimroth and Reichardt have proposed a solvent polarity parameter, $E_T(30)$, based on the transition energy for the longest-wavelength solvatochromic absorption band of the pryridinium N-phenolate betaine dye.[13] The $E_T(30)$ value for a solvent is defined as the transition energy of the dissolved betaine dye, measured in kcal/mol. E_T^N presents the so-called normalised value of $E_T(30)$. Water (1.000) and tetramethylsilane (TMS; 0) are defined as the extreme reference solvents.

2. In another approach, Kosower took the longest-wavelength intermolecular charge-transfer (CT) of 1-ethyl-4-(methoxycarbonyl)pyridinium iodide as a model process.[16;17] He defined his polarity parameter, Z, as the molar transition energy, E_T, expressed in kcal/mol, for the CT absorption band. A high Z value corresponds to high solvent polarity.

One potential problem of these scales is, that no clear distinction between nucleophilic and electrophilic contributions to solute-solvent interaction can be made in determining solvent parameters. This is different in the following approach:

3. Gutmann realized that many chemical reaction are influenced primarily by coordination interactions between an electron pair acceptor substrate and electron pair donor solvent. He put as an empirical measure of the Lewis basicity of solvent, using the so-called donor number DN (or donicity).[18] It is defined as negative enthalpy ΔH for creation of a 1:1 adduct of $SbCl_5$ and the respective solvent in diluted solution of the non coordinating solvent 1,2-dichlorethane. Thus, donor numbers are considered as semiquantitative measures of solute/EPD solvent interactions. Complementary to the donor number, the acceptor number AN by Mayer and Gutmann[19;20] is a measure of the Lewis acidity or EPA properties of organic solvents. The solvent-dependent ^{31}P chemical shift of triethylphosphine oxide is observed. The AN values represent dimensionless numbers, with reference solvents for n-Hexane (AN = 0) and $SbCl_5$

(AN = 100). The chemical shift results mainly from the polarization of the dipolar P=O group, induced by the interaction with electrophilic solvents, particularly hydrogen-bonding solvents.

Most of the existing empirical solvent scales agree with each other very well qualitatively and sometimes even quantitatively.[13] An excellent linear correlation between $E_T(30)$ values and Kosower's Z values is found. There exists an approximately linear relationship between acceptor numbers and Z-values for solvents with dielectric constants above 10. For solvents with lower dielectric constants the Z-values generally exhibit negative deviations indicating that dielectric polarization effects become important owing to the highly polar character of the ground state complex (Kosower complex). Similar relationships are found if the $E_T(30)$ values are plotted versus the acceptor number. The fairly good linear relationships of AN with the other two scales ($E_T(30)$, Z-values) reveal that both measure to a large extent the electrophilic properties of the solvents. In both cases, already for intermediate polarity, the solvents $CHCl_3$ and CH_2Cl_2 show stronger deviations. Due to the considerations mentioned above, the AN scale and the $E_T(30)/E_T^N$ scale were used in this work.

A broad range of solvents (Figure 4.2) with different polarity were used, ranging from very apolar solvents like DME and THF to highly polar solvents like water and methanol. These selected solvents were found to stabilize the quinone radical anion sufficiently, whereas in some solvents which where initially used no stable quinone radical anion could be generated.

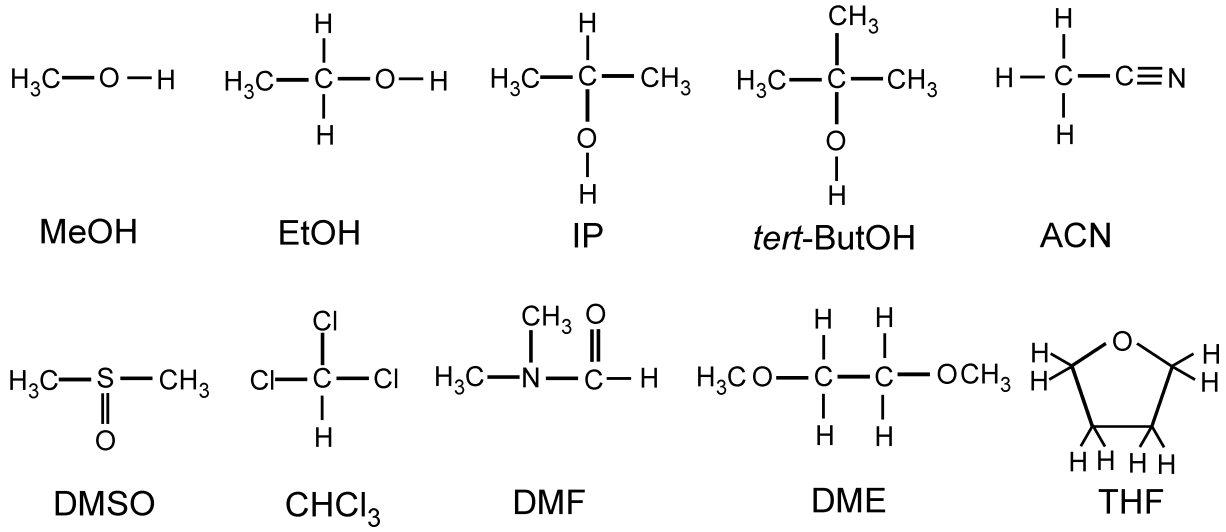

Figure 4.2: Molecular structures of the solvents used in this work. Methanol (MeOH), ethanol (EtOH), 2-propanol/*iso*-propanol (IP), *tert*-butanol (*tert*-ButOH), acetonitrile (ACN), dimethylsulfoxide (DMSO), chloroform ($CHCl_3$), *N*,*N*-dimethylformamide (DMF), dimethoxyethane (DME) and tetrahydorfuran (THF). Water is not depicted.

The redox potential of the first reduction step of the quinone was determined using cyclovoltammetry and square wave voltammetry. In addition, CW EPR measurements at Q-band were performed on the quinone radical anion in frozen solution of these solvents in order to determine the *g*-tensor. Instead of VK_1, the native quinone in PS I, the simpler and smaller 1,4-benzoquinone (BQ) and its quinone anion radical $BQ^{\bullet-}$ (both fully protonated BQ-h_4 and fully deuterated BQ-d_4) were used (Figure 4.3). This was done for the following reasons:

(i) due to its lack of shielding substituents it is best exposed to the solvent and expected to show more pronounced effects than better shielded quinones,

(ii) it exhibits a larger *g*-anisotropy than $VK_1^{\bullet-}$, which is in case of fully deuterated BQ already resolved at Q-band frequencies, and

(iii) it dissolves both in very apolar solvents like ethers and also in very polar solvents like water, allowing investigation of a full scale of solvents with different polarity.

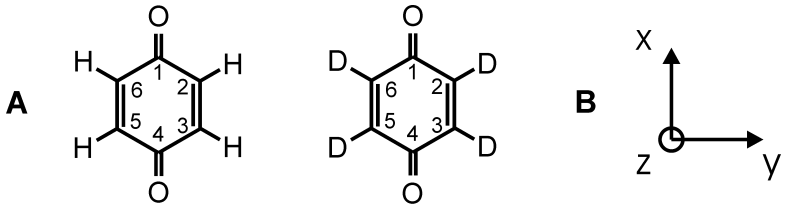

Figure 4.3: A Molecular structures of fully protonated and deuterated 1,4-benzoquinone (BQ-h_4 and BQ-d_4). **B** Molecular axes system of 1,4-benzoquinone. The x- and y-axes lie in the quinone plane, while the z-axis is perpendicular to the quinone plane. The principal axes of the *g*-tensor are collinear with the molecular axes.[7;21]

Results and Discussion

Redox potential of the quinones as determined by cyclovoltammetry and square wave voltammetry

A set of cyclovoltammograms of BQ in DME with different scanning rates are depicted in Figure 4.4, which is typical for aprotic solvents (Figure 4.1). In the potential range used in this work, BQ becomes singly reduced when lowering the potential, generating $BQ^{\bullet-}$. Afterwards $BQ^{\bullet-}$ is reoxidized when the potential is raised again. The peak amplitude ratios of reduction and oxidation are of the same intensity. The peaks are separated by 58 mV (one-electron step) and the separation is independent of the scanning rate. From this, it can be concluded that the steps are reversible and no subsequent chemical reactions occur. This is a necessity for coulometry. The second reduction step, which generates the dianion BQ^{2-} (Figure 4.1), can be only observed if the potential range is extended to lower potentials (data not shown). In the protic solvents IP and ethanol the potentials of the first and the second reduction are only separated by less than 100 mV. In methanol only a two electron transition was observed, while in water the cyclovoltammetry was not successful, probably due to fast generation of the benzohydroquinone (Figure 4.1). Cyclovoltammetry and square wave voltammetry yielded essentially the same redox potentials (data not shown). All measurements were done both with BQ-h_4 and BQ-d_4, but no significant differences were found (Table 4.1). As can be

seen from Table 4.1, the E_m values for the first reduction step of the quinone to its semiquinone radical anion vary considerably with the nature of the solvent. In aprotic solvents the redox potential is lower than in the protic solvents. This means that the reduced benzoquinone molecules are more strongly affected (stabilized) by the interactions with the solvent than the neutral form.

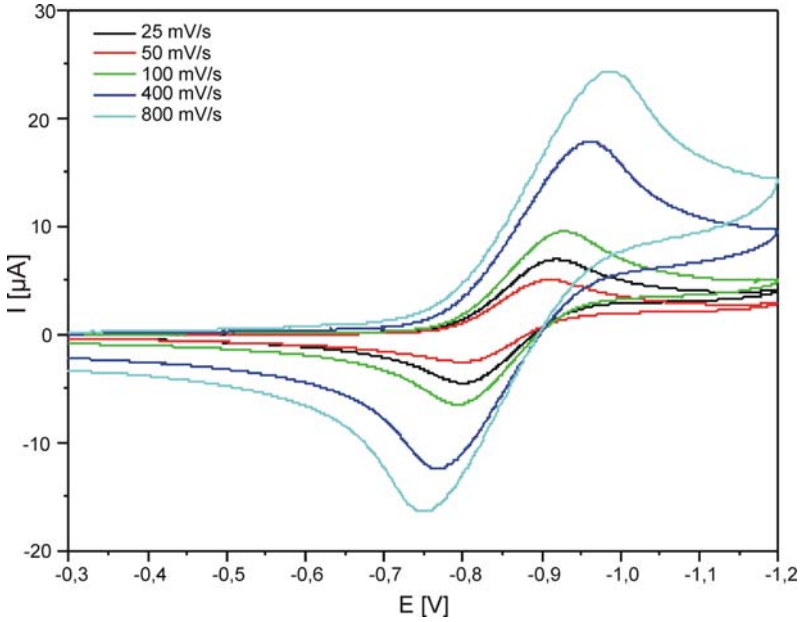

Figure 4.4: Cyclovoltammetry of 1 mM BQ (first reduction/re-oxidation step) in DME without ferrocen using different scanning rates.

Plots of the E_m *vs*. the reciprocal of dielectric permittivities ($1/\varepsilon_r$) and the dipole moment μ showed no correlation (plots not shown, for values see Table 4.1), whereas a good correlation was obtained with the AN proposed by Mayer/Gutmann for solute-solvent interactions (Figure 4.5). An almost linear dependence of E_m with the acceptor number is observed. The parameters of the fit with a linear function delivered a slope of 13 mV/AN and a value of –697 mV for a AN = 0. When using the E_T^N number by Dimroth and Reichardt, also a linear dependence was found, but more pronounced deviations were observed (Figure 4.6). The linear fit delivered a slope of 726 mV/E_T^N and a value of –709 mV for E_T^N = 0. A study using

VK_1[22] provided similar results: a linear dependence between E_m and AN and E_m and E_T^N. In that study, a better agreement of the redox potential change with AN, was found.

The redox potential of quinones is obviously linearly dependent on the polarity of the solvents. The use of the acceptor number scale, which measures electrophilic properties of the solvents gives superior agreement as compared to the E_T^N scale.

Table 4.1: Solvent polarity parameters, redox potential of BQ($BQ^{\bullet-}$) *(vs.* ferrocen) as determined by cyclovoltammetry and principal components of *g*-tensors of $BQ^{\bullet-}$ derived from CW EPR experiments at Q-band at T = 80 K

	ε_r	μ	E_T^N	AN	$E_m(Q/Q^{\bullet-})$ [mV]		g_x	g_y	g_z	g_{iso}
					BQ-h_4	BQ-d_4				
water	78.36	6.2	1.000	54.8	n.d.	n.d.	2.00648	2.00525	2.00223	2.00465
methanol	32.66	9.6	0.762	41.3	– 161[a]	– 166[a]	2.00647	2.00531	2.00228	2.00469
ethanol	24.55	5.5	0.654	37.1	– 232	– 232	2.00644	2.00527	2.00226	2.00466
2-propanol/ IP	19.92	5.5	0.546	33.5	– 178	– 183	2.00648	2.00527	2.00228	2.00468
tert-butanol	12.47	5.5	0.389	27.1	n.d.	n.d.	2.00663	2.00528	2.00225	2.00472
chloroform	4.89	3.8	0.259	23.1	– 388	– 399	2.00742	2.00530	2.00215	2.00496
DMSO	46.45	13.5	0.444	19.3	– 429	– 431	2.00776	2.00548	2.00225	2.00516
acetonitrile	35.94	13.0	0.460	18.9	– 476	– 484	2.00733	2.00538	2.00223	2.00498
DMF	36.71	12.7	0.386	16.0	– 481	– 485	2.00789	2.00549	2.00224	2.00521
DME	7.20	5.7	0.231	10.2	– 595	– 603	2.00779	2.00553	2.00225	2.00519
THF	7.58	5.8	0.207	8.0	– 557	– 570	2.00785	2.00548	2.00225	2.00519

Solvent abbreviations: 2-propanol/*iso*-propanol (IP), dimethylsulfoxide (DMSO), *N*,*N*-dimethylformamide (DMF), dimethoxyethane (DME) and tetrahydorfuran (THF).
The errors of the determination of the redox potential are ± 5 mV, and ± 0.00008 for the principal *g*-values. For conversion of the redox potentials, the following formula can be applied: $E_m(NHE) = E_m(Fc/Fc^+) + 630$ mV [a] $E_m(Q/Q^{\bullet-})$ & $E_m(Q/Q^{2\bullet-})$, since both reduction steps were not separated. n.d. : not determined

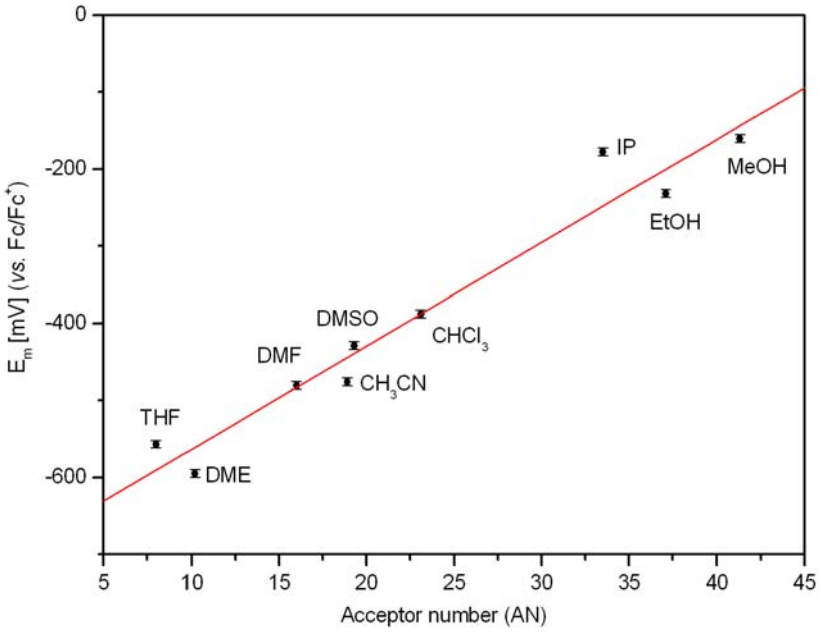

Figure 4.5: Plot of $E_m(BQ/BQ^{\bullet-})$ *vs.* the acceptor number (AN) of the respective solvent and a linear fit (red line) (fit parameters: slope = 13 mV/ AN; –697 mV for a AN = 0)

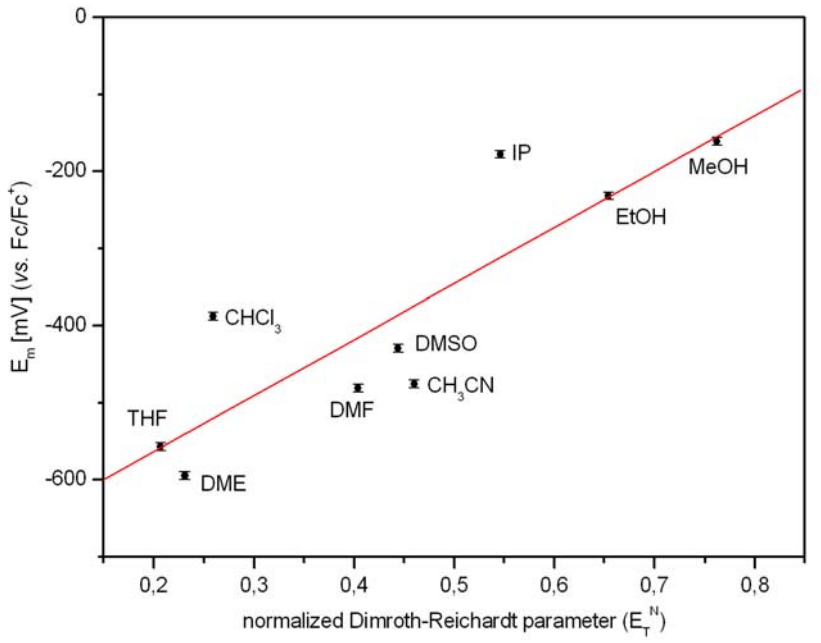

Figure 4.6: Plot of $E_m(BQ/BQ^{\bullet-})$ *vs.* the normalized Dimroth-Reichardt parameter (E_T^N) of the respective solvent and a linear fit (red line) (fit parameters: slope = 726 mV/ E_T^N; –709 mV for $E_T^N = 0$)

EPR measurements

A selected set of EPR spectra of BQ-$d_4^{\bullet-}$ is presented in Figure 4.7. The principal *g*-values were obtained by simulation of the spectra and are summarized in Table 4.1. The *g*-values in the solvents water, methanol, ethanol and IP agree well with those determined in previous studies.[7;23] It can be seen from Figure 4.7 and Table 4.1, that the three principal values of the *g*-tensor depend to a different extent on the solvent polarity.

The g_z component does not change, irrespective whether a polar or apolar solvent is used. Only for $BQ^{\bullet-}$ in chloroform the g_z component is found to be slightly lower than in the other solvents studied. Chloroform is the only solvent molecule in this study with a heavy atom (chlorine). Hence, the close contact of the chlorine atoms to $BQ^{\bullet-}$ might be an explanation for this effect. To test this idea, the same experiment was attempted with bromoform as solvent, since bromine is even heavier than chlorine. Unfortunately, a stable radical anion of BQ in this solvent could not be obtained.

The g_y component shows a weak dependence on the polarity of the solvent. It decreases with increasing solvent polarity. The g_x component also decreases with increasing solvent polarity, but it is more strongly influenced than the g_y component. The different dependence of the three *g*-values on the solvent polarity is expected:[24] in planar π-radicals like $BQ^{\bullet-}$ the *g*-tensor component normal to the molecular plane (g_z) is close to the value of the free electron. The *g*-tensor components in the plane are shifted to higher values due to spin orbit mixing of the ground state with higher lying excited states. In quinone anion radicals, the excitation of the electron from nominally non-binding orbitals of the oxygen into the half-occupied π*-orbital presents the dominating contribution. Other excitations are less important (see refs. [10;11] for discussion of contributions relevant for the *g*-tensor). Since the g_z-value is not affected by spin orbit mixing, no change is expected upon a change in the solvent.

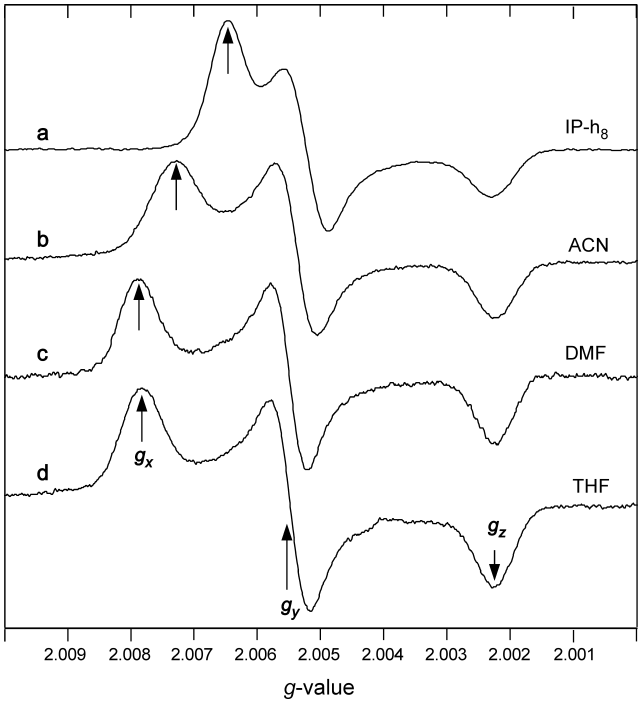

Figure 4.7: Selected CW EPR spectra of BQ-$d_4^{\bullet-}$ in different organic solvents recorded at Q-band frequency (34.0 GHz) at T = 80 K. Trace **a** BQ-$d_4^{\bullet-}$ in 2-propanol (IP-h_8), **b** BQ-$d_4^{\bullet-}$ in acetonitrile (ACN), **c** BQ-$d_4^{\bullet-}$ in *N*,*N*-dimethylformamide (DMF), **d** BQ-$d_4^{\bullet-}$ in tetrahydrofuran (THF). The principal *g*-values are indicated by arrows. Experimental conditions: P_{MW} = 2 μW, 12.5 kHz modulation frequency, modulation amplitude 0.2 mT, single scan (160 s).

The g_x-value was found to show the most pronounced deviation from the free electron g-value. The discussion will focus on g_x which shows the most prominent effect on the solvent polarity. Plots of the g_x-value *vs*. the reciprocal of dielectric permittivities ($1/\varepsilon_r$) and the dipole moment μ showed no correlation (plots not shown, for values see Table 4.1). In Figure 4.8 and Figure 4.9 the g_x-values are plotted *vs*. AN and E_T^N, respectively. No linear correlation, as observed for the redox potential, can be found, but it is obvious that g_x can be better correlated with AN. In all hydrogen bond donor solvents, the g_x-value remains the same, with only *tert*-butanol slightly increased. In the aprotic solvents, the g_x-values are significantly higher. Obviously, if H-bonds are present, they are have a dominating influence on g_x. This was also found in a recent theoretical study.[25]

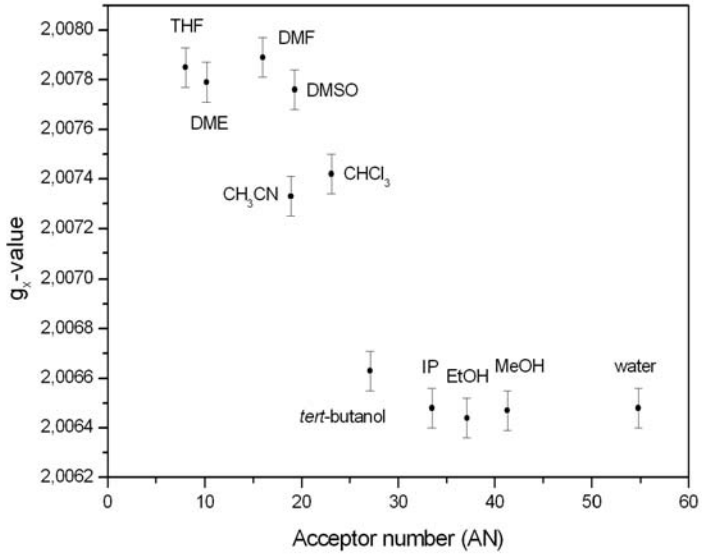

Figure 4.8: Plot of the g_x -values of $BQ^{\bullet-}$ *vs*. the Acceptor Number (AN)

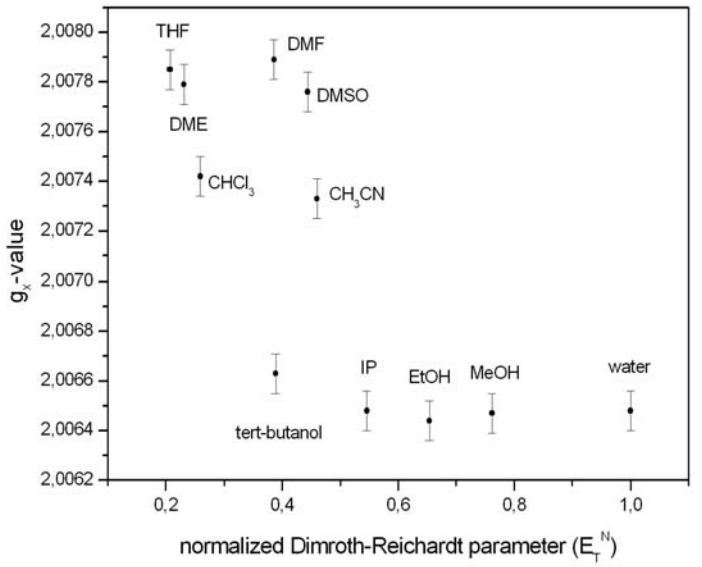

Figure 4.9: Plot of the g_x -values of $BQ^{\bullet-}$ *vs.* the normalized Dimroth-Reichard parameter(E_T^N)

For the aprotic solvents no linear dependence is observed as well. If acetonitrile is neglected, the dependence could be described as sigmoidal. In Figure 4.10 the g_x-values are

plotted against the redox potential. The dependence of the g_x-value from the redox potential is similar to the dependence of the g_x-value from the polarity.

In a theoretical study using the conductor-like polarizable continuum model (CPCM), but without taking the solvent molecules explicitly into account, the *g*-tensors were calculated for $BQ^{\bullet-}$ in THF ($g_x = 2.00860$), ACN ($g_x = 2.00856$) and DMSO ($g_x = 2.00858$).[10] The three computed g_x-values are higher than the experimentally determined g_x-values. The deviation between theory and experiment could be on the one hand due to deficiences in the DFT theory (see *e.g.* ref. [11] for a discussion) and/or the neglected of the environment in the calculations. On the other hand, the reason for the deviation between experimentally determined and calculated *g*-values could be due to not absolutely pure solvents. This would preclude the

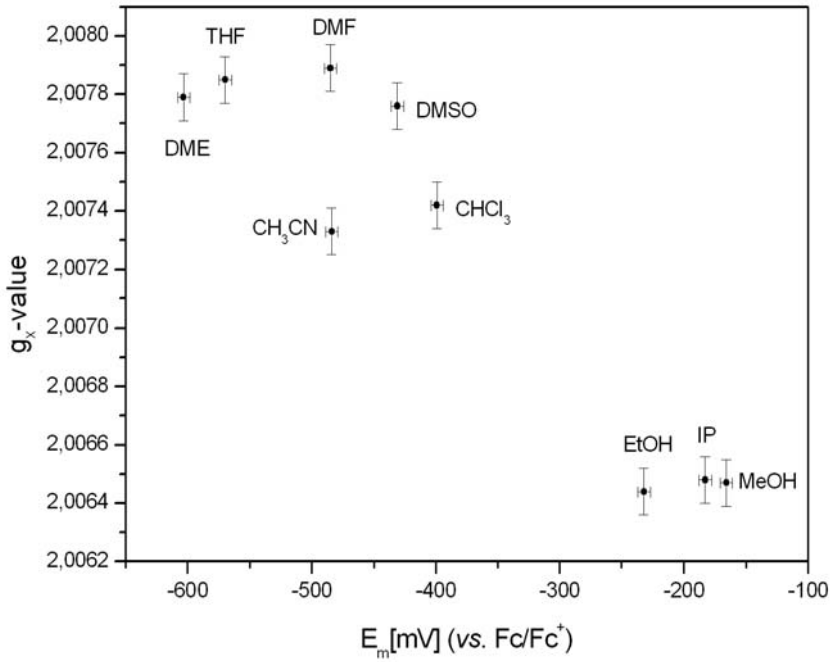

Figure 4.10: Plot of the g_x -values of $BQ^{\bullet-}$ *vs*. the the redox potential $E_m(BQ/BQ^{\bullet-})$

determination of the 'real' *g*-tensor of $BQ^{\bullet-}$ in a certain solvent. There might be 'contaminations' in the solvents, which could influence their polarity, or even exhibit specific

interactions with the $BQ^{\bullet-}$ anion. A high concentration of the supporting electrolyte is present to assure sufficient conductivity (up to several hundred mM in some aprotic solvents). This changes the polarity of the solvent. In addition, it exists in the solution an equilibrium between solvated ion pairs (ion pairs are defined as pairs of oppositely charged ions with a common solvation shell[13]) and single, dissociated and solvated cations and anions. Only the free ions contribute to the electrical conductivity of the solution. Solvents with sufficiently high relative permittivities and polarity (these solvents are called dissociating solvents) reduce the electrostatic attraction between oppositely charged ions to such an extent that ion pairs dissociate into free solvated ions. Therefore, an ion is completely solvated and shielded from the counterion in such solvents. In less polar solvents a significant amount of solvated ions pairs will be present. Since the $BQ^{\bullet-}$ anion is negatively charged, it might be associated with ions from the supporting electrolyte. To check if the ions of the supporting electrolyte are in close contact to $BQ^{\bullet-}$, ENDOR experiments were performed on some samples of $BQ^{\bullet-}$ in the apolar solvents. In these experiments a ^{19}F matrix ENDOR line was detected (one spectrum is shown in Figure 4.26 and discussed in a separate section below). This ENDOR line can only arise from a closely anion of the electrolyte. Since $BQ^{\bullet-}$ is also negatively charged, the presence of one or more cation of electrolyte in close contact to $BQ^{\bullet-}$ is very likely. In a theoretical study, Knüpling *et al.* demonstrated that the presence of positive charges close to the quinone radical anion decreases the g_x-value.[24] The cation of the supporting electrolyte is in principle well-shielded due to the bulky substituents, but small effects may occur. In cases of smaller counter cations like Na^+ significant interactions have been observed, see *e.g.* refs. [26;27]. Another important factor is a possible contamination with traces of polar and hydrogen-bonding molecules like water. All solvents were thoroughly dried, but the presence of very small amounts of such molecules can not be excluded. (The starting concentration of (oxidized) BQ is 1 mM in the solution.) If the presence of these molecules in the first solvent

shell is thermodynamically strongly favored, they can influence the micropolarity of the $BQ^{\bullet-}$ surrounding or even establish hydrogen bonds to the quinone anion. Solvents with different degrees of water content were used (DMF, chloroform) and chemical reduction in some of the organic solvents (DME, chloroform) by use of the base benzyl-trimethyl-ammonium-hydroxide in methanol. Already small amounts of water or methanol (less than 1%) had very strong effects on the *g*-tensor (data not shown). From this it has to be concluded, that the experimentally determined g_x-values of $BQ^{\bullet-}$ in the aprotic and apolar solvents might be incorrect. An interesting future approach would be to perfrom extended DFT calculations of the *g*-tensor of $BQ^{\bullet-}$ in different aprotic environments. In these calculations, at least the solvents molecules of the first solvation shell should be included.

ENDOR and TRIPLE spectroscopy on $VK_1^{\bullet-}$ and related quinone radical anions

The *g*-tensor is a global property of a paramagnetic molecule. It is determined by a variety of influences in the molecule and its environment. Detailed knowledge of the local electron spin distribution in the quinone radical anions is not accessible by the *g*-tensor. The spin density distribution of a molecule can be obtained from the hf tensors. The resolution of the EPR spectra (especially in frozen solution) is often too low for the determination of hfccs. The application of advanced EPR techniques like ENDOR and TRIPLE can reveal the hfccs (see also chapter 2). In liquid solution, CW ENDOR experiments[27] were done to directly determine the isotropic hfcc due to motional averaging of the dipolar part of the hf interaction in solution. This allows an estimation of the spin density on the respective nucleus. On the other hand information on the dipolar interaction is not available from liquid solution ENDOR. The information of the dipolar interaction is also required, since important interactions of the protein with the cofactor are often mostly dipolar in nature (*e.g.* H-bonds). In addition, it is impossible to perform 'liquid solution' measurements on PS I due to slow tumbling which prevents motional averaging of the anisotropic part of the hf interaction. ENDOR experiments on PS I thus always yield 'frozen solution ENDOR spectra'.[28;29] For a comparison and analysis of the ENDOR spectra, frozen solution ENDOR measurements on the quinone radical anion *in vitro* are needed. Pulse ENDOR was used for this measurements, since it is less dependent on meeting certain relaxation conditions.[30;31] To increase the resolution and determine the angles of the hfcc with respect to the *g*-tensor axes, molecules that have different orientations with respect to the magnetic field have to be selectively excited (orientation selected ENDOR; see also chapter 2).[31] For the small *g*-anisotropy found in the quinone radical anions, at least Q-band EPR is necessary to resolve the *g*-tensor

components. For the isolated quinone radical anions studied here only X-band (~9 GHz) ENDOR studies were available so far.[22;32;33] This left many hf tensors unassigned or only tentatively assigned.

IP was chosen as solvent for this study, since it was found to stabilize the quinone radical anion better than the other alcohols (methanol, ethanol, *tert*-butanol) and water. Another important consideration about IP is that it was available with different degrees of deuteration (Figure 4.11 B). This allows to study exclusively the quinone radical anions in case of the combination with fully deuterated IP. In contrast, fully protonated IP allows also the study of the solute-solvent interactions like H-bonding (only in frozen solution). Not only the radical anion $VK_1^{\bullet-}$ was studied, but also the radical anions of naphthoquinone ($NQ^{\bullet-}$) and vitamin K_3 ($VK_3^{\bullet-}$) were studied. NQ is a simple structural analogue of VK_1 without substituents. VK_3 differs from VK_1 by the lack of the phytyl tail (Figure 4.11 A). The use and understanding of the more symmetric NQ and the more asymmetric VK_3 is expected to be helpful in the assignment of the hf tensors to molecular positions. In addition, VK_3 has been incorporated into the A_1 binding site of PS I.[6;34;35] This makes a *in vitro* reference like in the case of VK_1 necessary.

Often isotropic hfccs determined in liquid solution are assumed to be identical to the one determined in frozen solution. This is not necessarily the case as shown previously for the hfccs of some benzoquinone-type radical anions, which clearly exhibit a temperature dependence.[33;36] Thus, the temperature dependence of the hfccs was studied to allow a reasonable comparison of the hfccs obtained in liquid solution with those obtained from the trace of the hf tensor in frozen solution.

DFT calculations on the three quinone radical anions were performed. The effect of solvation of the quinone radical anions was modeled in the calculations by using (i) the supermolecule approach to describe short range interactions like hydrogen bonding, and (ii)

the conductor like screening approach (COSMO) to treat long range solvation effects at low computational cost.[37]

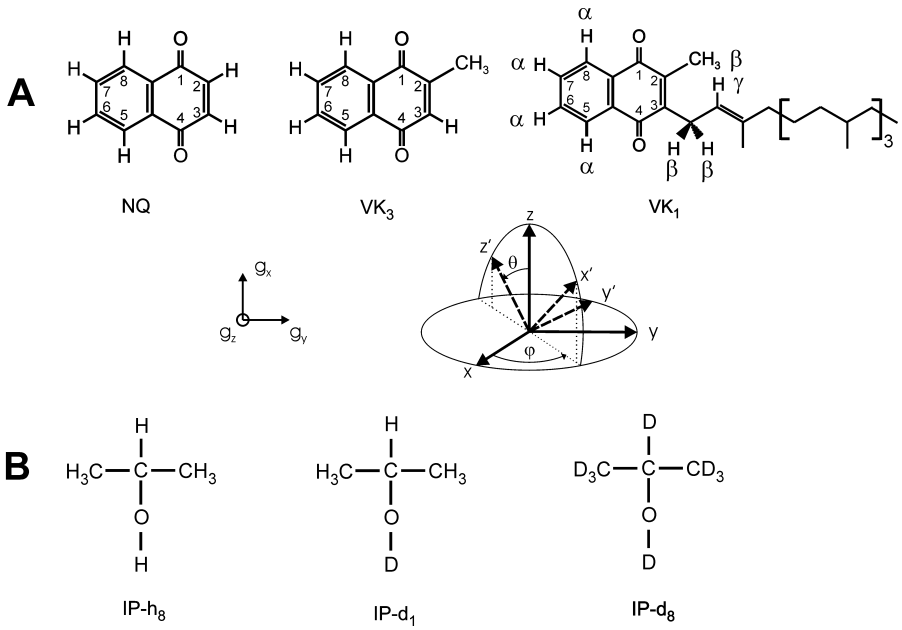

Figure 4.11: A Molecular structures of naphthoquinone (NQ), vitamin K_3 (VK_3) and vitamin K_1 (VK_1). In case of VK_1, α-, β- and γ-proton(s) are marked. The principal axes of the *g*-tensor are shown. The x and y principal components lie in the quinone plane, while the z component is perpendicular to the quinone plane. The x-direction is parallel to the C-O bond direction.[7;21] Hyperfine tensor angles are given with respect to the g-frame; the definitions of the spherical angles φ and θ are shown. **B** Molecular structures of fully protonated IP ($IP\text{-}h_8$), selectively deuterated IP ($IP\text{-}d_1$) and fully deuterated IP ($IP\text{-}d_8$).

Results and Discussion

The ENDOR spectra of quinone radical anions in frozen solution contain spectral features from a number of protons. They can be separated into three distinct groups:

i) Quinone protons, which include α-protons, directly attached to the π-system, and β-protons, separated by one bond from the π-system (Figure 4.11 A),

ii) Protons hydrogen bonded to the quinone oxygens,

iii) Solvent protons weakly coupled to the quinone.

Hfccs of the quinone protons

The hfi of the first group of protons can be observed both in liquid solution and frozen solution. To avoid signals from the solvent protons, completely deuterated 2-propanol (IP-d_8; Figure 4.11 B) was used for the measurements in frozen solution.

Naphthoquinone

Naphthoquinone (Figure 4.11 A) is the simplest of the three quinones investigated here. It contains only six protons. The protons at the positions 2 and 3, 5 and 8, and 6 and 7 are equivalent due to the symmetry of the molecule. Thus three hfccs and correspondingly 27 lines in the liquid solution EPR spectrum (a triplet of triplets of triplets) are expected. In the EPR spectrum of $NQ^{\bullet-}$ at 280 K all 27 lines are resolved (Figure 4.12). In the corresponding ENDOR spectrum (Figure 4.13) signals from three different hyperfine couplings are observed: one large hfcc (line pair 1/1') and two smaller hfccs (line pairs 2/2' and 3/3') of nearly the same size. Very weak signals from hfccs around 2.5 MHz are observed (marked with asterisk). They were found in various samples with different intensity, while the intensity

ratio of the lines 1/1', 2/2' and 3/3' was unaffected. Hence, these low intensity lines are attributed to a small amount of by-product(s) in the sample and not discussed further. The hfccs of the lines 1 to 3 are in very good agreement with previous EPR and ENDOR measurements (Table 4.2).[22;33]

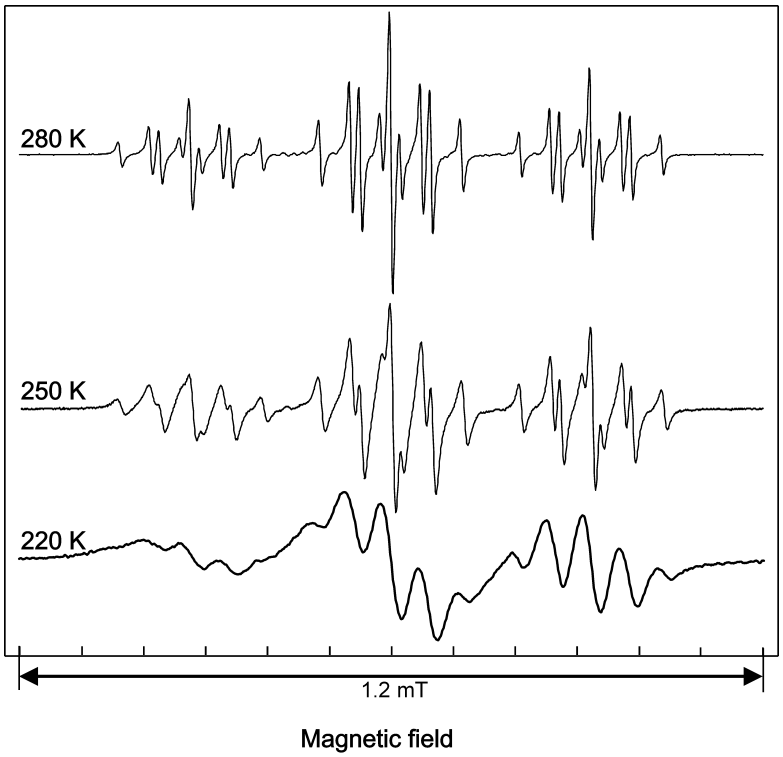

Figure 4.12: Liquid solution CW EPR spectra of chemically generated $NQ^{\bullet-}$ in IP-h_8 recorded at X-band (9.61 GHz) at three different temperatures. Experimental conditions: non-saturating microwave power, 12.5 kHz modulation frequency, modulation amplitude 5 μT, at 220 K 10 μT.

On the basis of the DFT calculations (see Figure 4.14) the larger hfcc is assigned to the protons in the positions 2/3 in the quinone ring and the hfcc of –1.75 MHz can be assigned to the protons in the positions 6/7 and the hfcc of –1.47 MHz belongs to the protons in the positions 5/8 (Table 4.2). There is excellent agreement between the experimentally determined hfccs and the DFT results, especially when using COSMO. This assignment is in complete agreement with previous calculations, see *e.g.* [38-41].

In the temperature range where sufficiently resolved EPR and ENDOR spectra were obtained, only the hfccs of protons 5 and 8 (close to carbonyl oxygens) showed a slight temperature dependence while the others stayed the same.

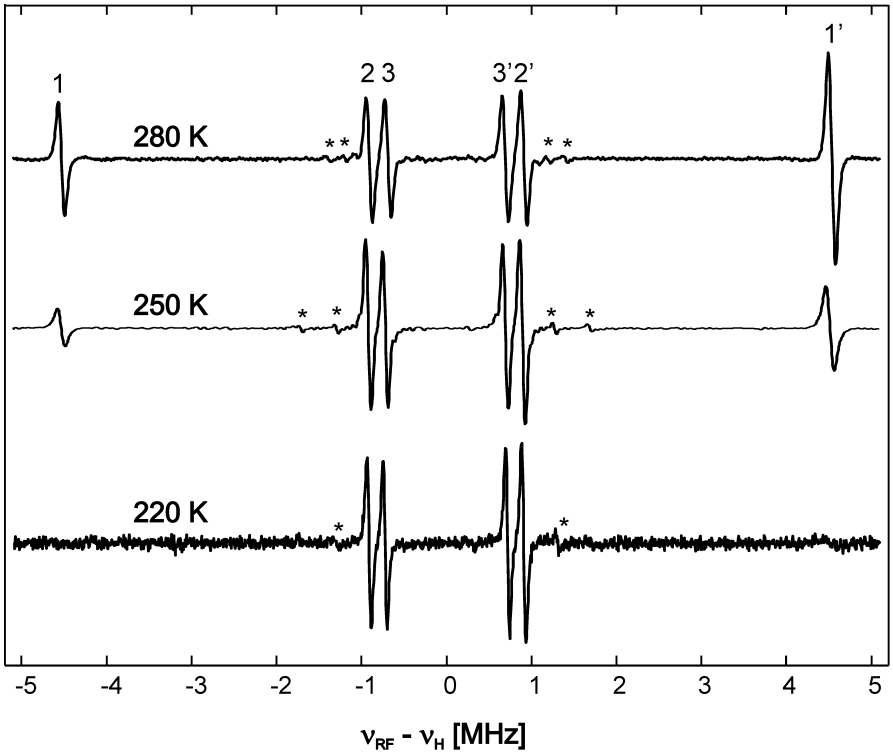

Figure 4.13: Liquid solution CW ENDOR spectra of chemically generated $NQ^{\bullet-}$ in IP-h_8 recorded at X-band (9.61 GHz) at three different temperatures. Experimental conditions: P_{MW} = from 2 to 8 mW, P_{RF} = 10 to 25 W, 12.5 kHz modulation, modulation depth ± 25 kHz.

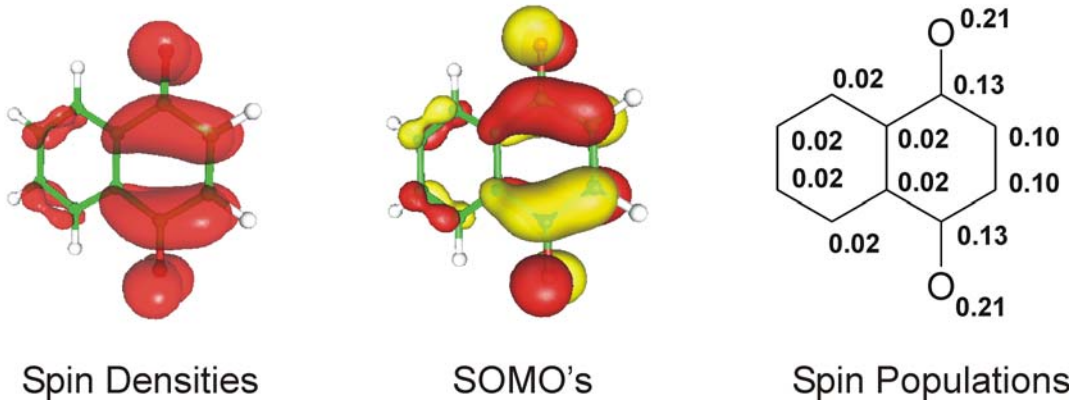

Figure 4.14: Spin densities, semi occupied molecular orbitals (SOMO's) and spin populations, obtained for $NQ^{\bullet-}$. While the spin density is the difference between the total α and β spin densities and therefore depends on all orbitals, the SOMO is the orbital of the unpaired electron. Spin populations were obtained from a Mulliken analysis, which attributes fractional amounts of electrons to every nucleus.

The intensity of line pair 1/1' exhibits a strong temperature dependence. While at 280 K all line pairs have similar intensity, at 250 K the line pair 1/1' is already significantly decreased in intensity. At 220 K the line pair is not observed anymore within this signal to noise ratio. This is due to the large anisotropy of this hf tensor, which strongly influences the relaxation at lower temperature.

Table 4.2: Hyperfine coupling parameters used in the fitting of the CW EPR and the CW ^{1}H ENDOR spectra of chemically generated $NQ^{\bullet-}$ in IP-h_8 at different temperatures and results of DFT calculations. Hyperfine couplings (a_{iso}) are given in MHz. The precision of the hfcc determination is estimated to be around ± 15 kHz (depending on the respective linewidth).

	Position [a]		
	2/3	**5/8**	**6/7**
Line pair	1/1'	3/3'	2/2'
$\mathbf{a_{iso}}$ **(280 K)**	– 9.07	– 1.38	– 1.82
$\mathbf{a_{iso}}$ **(250 K)**	– 9.07	– 1.42	– 1.82
$\mathbf{a_{iso}}$ **(220 K)**	– 9.07	– 1.45	– 1.82
$\mathbf{a_{iso}}$ **(263 K)**[b]	– 9.091	– 1.408	– 1.825
$\mathbf{a_{iso}}$ **(270 K)**[c]	– 9.05	– 1.42	– 1.78
$\mathbf{a_{iso}}$ **(DFT)**[d]	– 8.88 (– 8.68)	– 1.47 (– 1.22)	– 1.75 (– 1.87)

[a] positions 2 and 3, 5 and 8, 6 and 7 are equivalent
[b] from ref. [33]
[c] from ref. [22]
[d] for the DFT calculations, two solvent molecules were coordinated to each carbonyl oxygen. Geometry optimization was performed without restrictions. Hf tensor calculations were performed employing the COSMO continuum method (without brackets) and without the COSMO continuum method (in brackets). For details, see chapter 3.

The Q-band EPR and orientation-selected ^{1}H ENDOR spectra of $NQ^{\bullet-}$ in IP-d_8 are presented in Figure 4.15. The three field positions (close to the canonical orientations of the *g*-tensor), at which the respective ENDOR spectra were measured (a, b and c), are marked in the EPR spectrum. A number of additional experiments (a total of 9) were performed at other field positions to investigate in detail the angular dependence of the hfccs (data not shown). The simulations of the corresponding EPR and ENDOR spectra are represented by red lines.

The simulated *g*-factors of the $NQ^{\bullet-}$ radical in IP-d_8 are given in Table 4.3. No difference was observed between *g*-factors of deuterated and non-deuterated compounds and for the differently deuterated solvents. The *g*-factors for $NQ^{\bullet-}$ are in agreement with earlier high field EPR studies of non deuterated $NQ^{\bullet-}$.[7]

Table 4.3: Principal components of the *g*-tensor of $NQ^{\bullet-}$ in IP-d_8 derived from pulse EPR experiments at Q-band at T = 80 K and values from DFT calculations.[a]

	g_x	g_y	g_z	
$NQ^{\bullet-}$	2.00590(5)	2.00511(5)	2.00229(5)	this work[b]
	2.00582(5)	2.00505(5)	2.00228(5)	[c]
	2.00658	2.00530	2.00219	DFT

[a] for the DFT calculations, two solvent molecules were coordinated to each carbonyl oxygen. Geometry optimization was performed without restrictions. G-tensor calculations were performed employing the COSMO continuum method. For details, see chapter 3.

[b] The g-tensor was obtained from fully deuterated quinones.

[c] From a W-band EPR study.[7]

Table 4.3 also presents the results of *g*-tensor calculations using DFT. All data from DFT calculations, unless otherwise stated, are taken from the corresponding models with four H-bonds, which were optimized without restrictions. A detailed discussion of differences between the model systems with different H-bonds will be given below. While the g_y and g_z values are well predicted by the DFT calculations, the typical overestimation of the g_x component of quinone radicals was found. This discrepancy is partially the result of deficiencies in the density functionals.[11] It was also shown that at least part of this discrepancy is due to insufficient model systems in case of polar, protic solvents.[25] By increasing the amount of solvent molecules in the calculation and forming an extended solvent shell around the quinone, an improved prediction of the g_x values can be obtained.[10;25;42;43] However, since the accurate prediction of *g*-values is outside the scope of this work such time consuming calculations were not performed.

In case of $NQ^{\bullet-}$ in frozen solution, only three pairs of sharp lines are visible in the ENDOR spectra at 'single crystal like' orientations close to g_x and g_z (Table 4.4). The α-protons in positions 2 and 3 attached to the quinone ring have the largest hfcc (see discussion above). The A_x (-14.00 MHz) and A_z (-11.20 MHz) principal components of their hf tensors are completely resolved while the A_y component (-1.76 MHz) overlaps with signals from benzene ring α-protons of $NQ^{\bullet-}$. The previous pulse[22] and CW[33] X-band studies showed very similar results but were less accurate. The principal components of the hf tensors of the protons in positions 6/7 exhibit the relation $|A_x|>|A_z|>|A_y|$ which is typical for α-protons of π-radicals.[44;45]

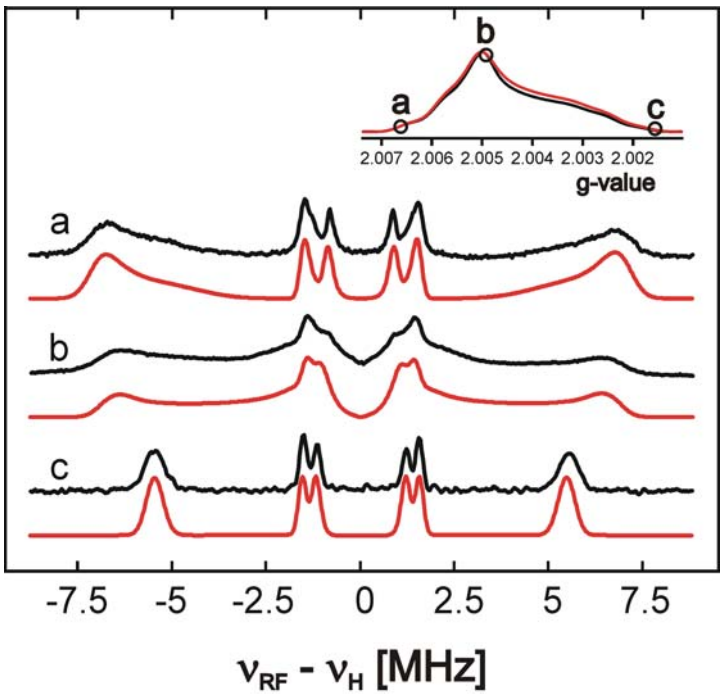

Figure 4.15 : Selected Q-band ^{1}H ENDOR spectra of $NQ^{\bullet-}$ in IP-d_8 recorded at T = 80 K and at different values of the magnetic field. ENDOR traces a, b and c correspond to spectral positions near g_x, g_y and g_z respectively. The black trace for each position presents experimental data and the red trace presents the simulation. The inserts in the right corner show the FSE EPR spectrum and its simulation. The field positions, at which the presented ENDOR spectra are measured, are marked with letters. The parameters of the ENDOR simulations are given in **Table 4.4.**

The presence of a large electron density on the carbonyl group strongly influences the hfcc of protons at positions 5/8. For them the A_z component of the hf tensor is the largest. The previous assignment of the larger isotropic hfcc of the benzene ring protons to the protons at position 6 and 7 is confirmed due to the orientation dependence of the ENDOR spectra. The DFT calculations show excellent agreement with the experimental data (Table 4.4).

Table 4.4: Parameters used for fitting of ^{1}H ENDOR spectra of $NQ^{\bullet-}$ in IP at T = 80 K (exp.) and results of DFT calculations[a] (DFT). Hyperfine couplings (A_i, a_{iso}) and linewidths (*lw*, full width at half height) are given in MHz. Angles (φ,θ) are given in degrees. The precision of the hfcc determination is estimated to be 25 % of the linewidth. The smallest component of the ring proton hfcc (A_y) exhibits a larger error.

	Position [a]							
	2/3		**5/8**		**6/7**		**H-bond(s)**	
	exp.	**DFT**	**exp.**	**DFT**	**exp.**	**DFT**	**exp.**	**DFT(av.)**
$\mathbf{A_x}$	– 14.00	– 13.59	– 1.69	– 1.57	– 3.12	– 3.03	+ 5.68	+ 5.86
$\mathbf{A_y}$	– 1.76	– 1.66	+ 0.36	+ 0.39	+ 0.19	+ 0.19	– 2.70	– 2.83
$\mathbf{A_z}$	– 11.15	– 11.39	– 3.17	– 3.24	– 2.40	– 2.41	– 2.70	– 2.58
$\mathbf{a_{iso}}$	– 8.97	– 8.88	– 1.50	– 1.47	– 1.78	– 1.75	< + 0.1	+ 0.15
$\mathbf{a_{iso}}$ [c]	– 9.07		– 1.38		– 1.82			
lw	0.6		0.22		0.24		0.5	
φ	± 17	± 17	± 8	± 8	± 15	± 15	±37,±53	±37, ±53
θ	0	< 2	0	< 2	0	< 2	< 15	< 4

[a] two solvent molecules were coordinated to each carbonyl oxygen. Geometry optimization was performed without restrictions. Hf tensor calculations were performed employing the COSMO continuum method.
[b] positions 2 and 3, 5 and 8, 6 and 7 are equivalent
[c] liquid solution data, see Table 4.2.

Vitamin K_3

In VK_3 the proton at position 2 is substituted with a methyl group (Figure 4.11A). The rotational motion of the methyl group completely averages the individual tensors of the methyl protons resulting in the observation of a single hfcc for all three protons. Thus, only two large couplings, from the methyl group protons and the α-proton at position 3, are observed in the ENDOR spectrum at 280 K (Figure 4.17). The simulation of the EPR spectrum (Figure 4.16) with the hfccs obtained in the ENDOR experiment allows the assignment of the largest hfcc (line pair 1/1') to the methyl group protons and the second largest hfcc (line pair 2/2') to the α-proton at position 3. This is confirmed by a general

TRIPLE experiment (data not shown). Since the substitution at position 2 lowers the symmetry of the quinone molecule, four different couplings of protons 5 to 8 in the benzene ring are expected. Indeed, 4 line pairs are found in the ENDOR spectrum. With help of the DFT calculations (Table 4.5, Figure 4.18), the hfccs are assigned as follows: line pair 3/3' to the α-proton at position 6, line pair 4/4' to the α-proton at position 8, line pair 5/5' to the α-proton at position 7, and line pair 6/6' to the α-proton at position 5. The experimentally determined hfccs and the results of the DFT calculations are summarized in Table 4.5.

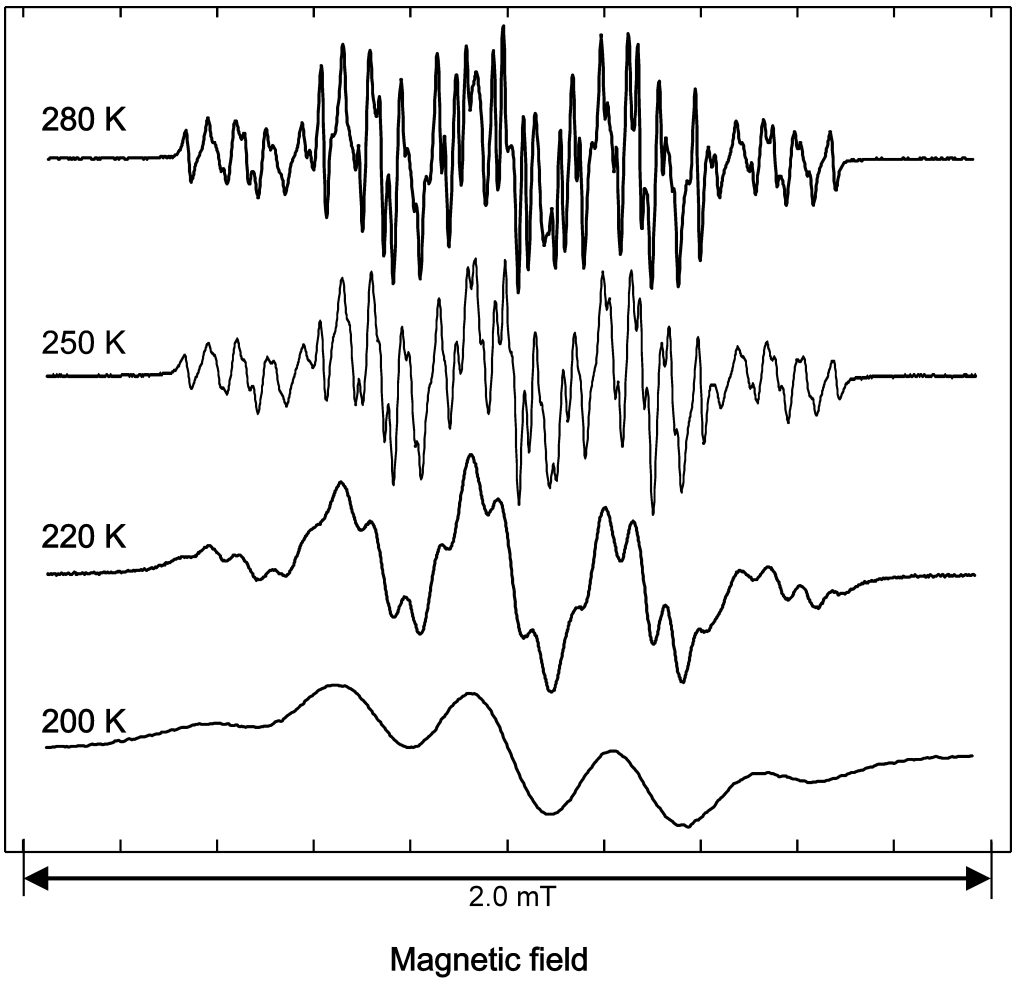

Figure 4.16: Liquid solution CW EPR spectra of chemically generated $VK_3^{\bullet-}$ in IP-h_8 recorded at X-band (9.61 GHz) at four different temperatures. Experimental conditions: non-saturating microwave power, 12.5 kHz modulation frequency, modulation amplitude 5 μT, at 200 K 10 μT.

The experimentally determined hfccs are in good agreement with previous EPR and ENDOR studies.[22;33] The rotational averaging of the hfccs of the methyl group was taken into account by averaging of the individual methyl proton tensors that were calculated in steps of 15 degrees.

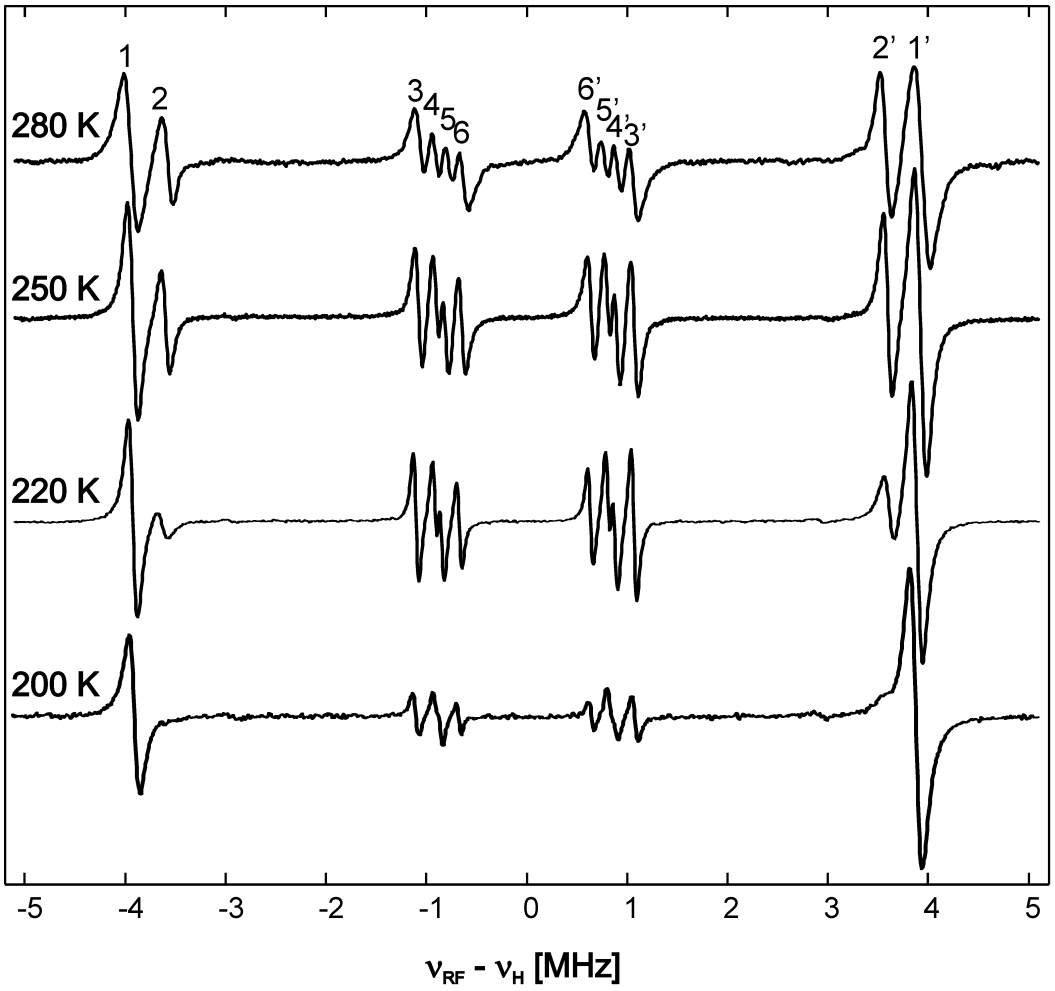

Figure 4.17: Liquid solution CW ENDOR spectra of chemically generated $VK_3^{\bullet-}$ in IP-h_8 recorded at X-band (9.61 GHz) at three different temperatures. Experimental conditions: P_{MW} = from 2 to 8 mW, P_{RF} = 10 to 25 W, 12.5 kHz modulation, modulation depth ± 25 kHz.

The assignment of the four small α-protons is in agreement with calculations from Das *et al.* [38] However, in the works of Grafton & Wheeler,[41] and Joela & Lehtovuori[46] two medium hfccs, which differ by less than 200 kHz, were assigned differently (line pairs 4/4' to the proton at position 7, and 5/5' to the proton at position 8). In contrast to the DFT calculations performed here, in their studies the solvent molecules hydrogen bonded to the carbonyl

oxygen were not included. It was shown before that they have a strong effect on the electronic structure, see *e.g.* refs.[10;25]. Hence, the assignment presented here seems to be more accurate. As for NQ, the agreement of the DFT calculations and the experimentally determined values is very good, especially when COSMO was used. However, the hfcc of the α-proton at position 3 shows a better agreement with the DFT calculation without the use of COSMO.

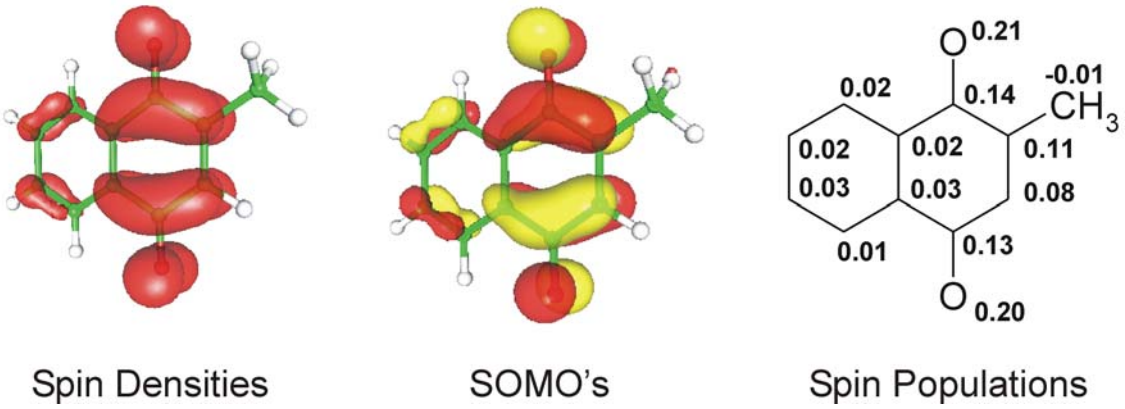

Figure 4.18: Spin densities, semi occupied molecular orbitals (SOMO's) and spin populations, obtained for $VK_3^{\bullet-}$. While the spin density is the difference between the total α and β spin densities and therefore depends on all orbitals, the SOMO is the orbital of the unpaired electron. Spin populations were obtained from a Mulliken analysis, which attributes fractional amounts of electrons to every nucleus.

The hfccs show some temperature dependence, which is more pronounced than for $NQ^{\bullet-}$. The introduction of the bulky methyl group may disturb the hydrogen bonding to the nearby carbonyl oxygen, which can slightly influence the spin density distribution.[33;36] For the line pair 2/2' the same temperature dependence of the intensity is observed as for line pair 1/1' in case of $NQ^{\bullet-}$ (Figure 4.13). This can be explained in the same way as for $NQ^{\bullet-}$. Namely, it is due to the large anisotropy of the hf tensor of this proton. The Q-band EPR and orientation-selected ^{1}H ENDOR spectra of $VK_3^{\bullet-}$ in IP-d_8 are presented in Figure 4.19. The three field positions (close to the canonical orientations of the *g*-tensor), at which the respective ENDOR spectra were measured (a, b and c), are marked in the EPR spectrum. A number of additional experiments (a total of 9) were performed at other field positions in order to investigate in detail the angular dependence of the hfccs (data not shown). The simulations of the

corresponding EPR and ENDOR spectra are presented by red lines. The simulated *g*-values of $VK_3^{\bullet-}$ in IP-d_8 are given in Table 4.6. No difference was observed between *g*-factors of

Table 4.5: Hyperfine coupling parameters used in the fitting of the CW EPR and the CW ^{1}H ENDOR spectra of $VK_3^{\bullet-}$ in IP-h_8 at different temperatures and results of DFT calculations.[a] Hyperfine couplings (a_{iso}) are given in MHz. The precision of the hfcc determination is estimated to be around ± 15 kHz (depending on the respective linewidth).

	Position					
	2 (CH_3)	**3 (α)**	**5(α)**	**6 (α)**	**7 (α)**	**8 (α)**
Line pair	1/1'	2/2'	6/6'	3/3'	5/5'	4/4'
a_{iso} (280 K)	+ 7.88	– 7.16	– 1.27	– 2.10	– 1.55	– 1.81
a_{iso} (250 K)	+ 7.85	– 7.20	– 1.29	– 2.14	– 1.62	– 1.79
a_{iso} (220 K)	+ 7.81	– 7.24	– 1.30	– 2.17	– 1.66	– 1.79
a_{iso} (200 K)	+ 7.78	n.d.	– 1.32	– 2.18	– 1.68	– 1.79
a_{iso} (263 K)[b]	+ 7.862	– 7.192	– 1.272	– 2.148	– 1.596	– 1.812
a_{iso} (250 K)[c]	+ 7.86	– 7.20	– 1.27	– 2.15	– 1.61	– 1.83
a_{iso} (DFT)[a]	+ 7.57 (+ 6.64)	– 6.81 (– 7.44)	– 1.23 (– 0.90)	– 2.26 (– 2.48)	– 1.66 (– 1.61)	– 1.78 (– 1.71)

[a] for the DFT calculations, two solvent molecules were coordinated to each carbonyl oxygen. Geometry optimization was performed without restrictions. Hf tensor calculations were performed employing the COSMO continuum method (without brackets) and without the COSMO continuum method (in brackets). For details, see chapter 3.

[b] from ref. [33] For the ease of comparison, similar experimental values are listed in the same row, not considering different assignment by the author.

[c] from ref. [22] For the ease of comparison, similar experimental values are listed in the same row, not considering different assignment by the author.

deuterated and non-deuterated quinone and for the different deuterated solvents. The explanation of the deviation of the *g*-tensor obtained experimentally and by DFT calculation given above for $NQ^{\bullet-}$ also holds here.

Table 4.6: Principal components of the *g*-tensor of $VK_3^{\bullet-}$ in IP-d_8 derived from pulse EPR experiments at Q-band at T = 80 K and values from DFT calculations. [a]

	g_x	g_y	g_z	
$VK_3^{\bullet-}$	2.00581(8) 2.00638	2.00513(8) 2.00525	2.00229(8) 2.00215	this work[b] DFT

[a] for the DFT calculations, two solvent molecules were coordinated to each carbonyl oxygen. Geometry optimization was performed without restrictions. Hf tensor calculations were performed employing the COSMO continuum method (without brackets) and without the COSMO continuum method (in brackets). For details, see chapter 3.

[b] The *g*-tensor was obtained from fully deuterated quinone.

Only two large couplings, from the methyl group protons and the α-proton at position 3, are observed. Even at 80 K the rotational motion of the methyl group is fast enough to completely average the individual tensors of the methyl protons resulting in the observation of a single set for all 3 protons.[44] Four different couplings of the protons 5 to 8 in the benzene ring are observed (see discussion above). The results of spectral simulations for the large hfccs show good agreement with previous CW X-band studies,[33] while in other studies some hfccs of the α-proton at position 3 were significantly overestimated (see *e.g.*ref .[22]). The experimental data and results of the DFT calculations are summarized in Table 4.7. The hf tensors obtained in the DFT calculation is in excellent agreement with the experiment. The largest hfcc of the α-proton in position 3 is overestimated by approximately 10% (in this case the DFT calculations delivered better agreement with the experimental values if no COSMO was used). The other α-protons (benzene ring) are predicted with better precision.

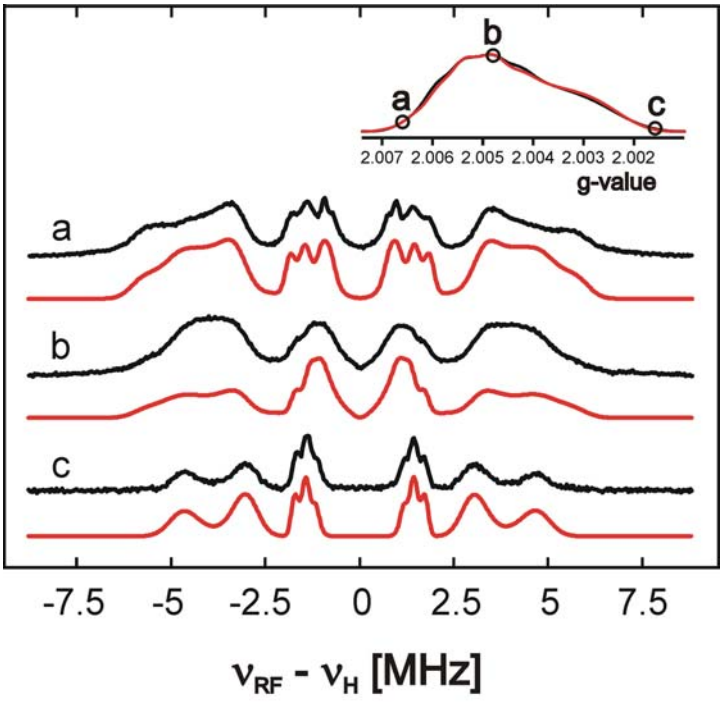

Figure 4.19: Selected Q-band ^{1}H ENDOR spectra of $VK_3^{\bullet-}$ in IP-d_8 recorded at T = 80 K and at different values of the magnetic field. ENDOR traces a, b and c correspond to spectral positions near g_x, g_y and g_z respectively. The black trace for each position represents experimental data and the red trace presents the simulation. The insert in the right corner show the FSE EPR spectrum and its simulation. The field positions, where the presented ENDOR spectra are measured, are marked with letters. The parameters of ENDOR simulations are given in **Table 4.7**

Table 4.7: Parameters used in the fitting of ^{1}H ENDOR spectra of $VK_3^{\bullet-}$ in IP at T = 80 K (exp.) and results of DFT calculations[a] (DFT). Hyperfine couplings (A_i, a_{iso}) and linewidths (*lw*, full width at half height) are given in MHz. Angles (φ,θ) are given in degrees. The precision of the hfcc determination is estimated to be 25 % of the linewidth. The smallest component of ring proton hfcc (A_y) exhibits a larger error.

	2 (CH_3)		**3 (α)**		**5 (α)**		**6 (α)**		**7 (α)**		**8 (α)**		**H-bonds**			
	exp.	**DFT**	**exp.**	**DFT**	**exp.**	**DFT**	**exp.**	**DFT**	**exp.**	**DFT**	**exp.**	**DFT**		**I**	**II**	**III**	**IV**
$\mathbf{A_x}$	+ 6.40	+ 6.63	–11.73	–10.42	– 1.48	– 1.31	– 3.80	– 3.80	– 3.01	– 2.90	– 1.99	– 1.76	exp.	+ 5.5	+ 5.9	+ 6.3	+ 6.4
													DFT	+ 5.5	+ 5.9	+ 6.5	+ 6.7
$\mathbf{A_y}$	+9.70	+10.10	– 1.00	– 0.78	+ 0.58	+ 0.60	+ 0.20	– 0.07	+ 0.37	+ 0.29	+ 0.16	+ 0.05	exp.	– 2.5	– 2.8	– 4.7	– 4.1
													DFT	– 2.5	– 2.8	– 4.7	– 4.6
$\mathbf{A_z}$	+ 5.80	+ 5.98	– 9.60	– 9.23	– 3.00	– 2.99	– 2.82	– 2.91	– 2.34	– 2.37	– 3.54	– 3.63	exp.	– 2.4	– 2.5	– 4.9	– 3.7
													DFT	– 2.8	– 2.5	– 5.1	– 4.5
$\mathbf{a_{iso}}$	+ 7.30	+ 7.57	– 7.44	– 6.81	– 1.30	– 1.23	– 2.14	– 2.26	– 1.66	– 1.66	– 1.79	– 1.78	exp.	+ 0.2	+ 0.2	– 1.1	– 0.5
													DFT	<0.1	+ 0.2	– 1.1	– 0.8
$\mathbf{a_{iso}}$[b]	+ 7.88		– 7.16		– 1.27		– 2.10		– 1.55		– 1.81		n.d.				
lw	1.3		0.7		0.2		0.2		0.2		0.2		0.5				
φ	+ 25	+ 20	– 21	– 21	+ 4	+ 4	+ 12	+ 12	– 20	– 20	– 14	– 14	DFT	+ 48	– 42	– 58	+ 44
θ	0	< 1	0	< 3	0	< 3	0	< 3	0	< 3	0	< 3	DFT	< 2	< 2	– 32	+ 21

[a] two solvent molecules were coordinated to each carbonyl oxygen. Geometry optimization was performed without restrictions. Hf tensor calculations were performed employing the COSMO continuum method.

[b] liquid solution data, see **Table 4.5.**

Vitamin K_1

VK_1 has even more substitutions than VK_3. It carries a phytyl chain at position 3 (Figure 4.11 A). The liquid solution EPR and ENDOR spectra are presented in Figure 4.20 and Figure 4.21, respectively. The ENDOR spectrum at 280 K exhibits seven line pairs. Simulation of the corresponding EPR spectrum and a general TRIPLE experiment (not shown) allow the assignment of the largest hfcc (line pair 1/1') to the methyl group protons at position 2 and the line pair 2/2' to the methylene protons of the phytyl tail. The line pairs 3/3' to 6/6' are assigned to the benzene ring protons. The line pair 7/7' is assigned to the γ-proton

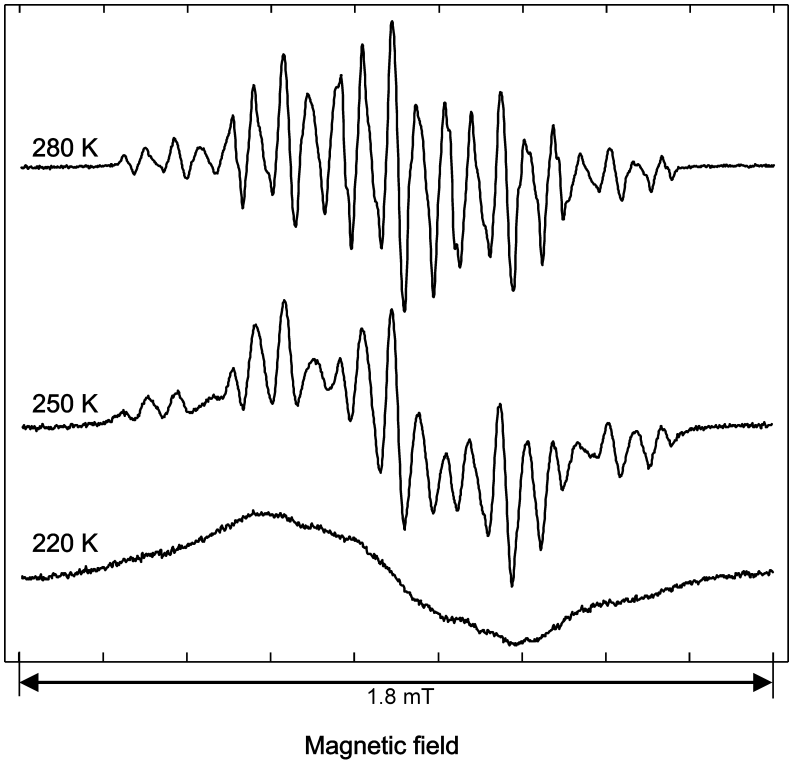

Figure 4.20: Liquid solution EPR spectra of chemically generated $VK_1^{\bullet-}$ in IP-h_8 recorded at X-band (9.61 GHz) at three different temperatures. Experimental conditions: non-saturating microwave power, 12.5 kHz modulation frequency, modulation amplitude 5 μT, at 200 K 10 μT.

of the phytyl tail.[22;33] The agreement of the experimentally determined values and the ones from previous studies is excellent.[22;33] DFT calculations show a similar precision of prediction

of the hfccs as in case of $VK_3^{\bullet-}$. In this case, the results obtained with COSMO are again closer to the experimentally determined values. The rotational averaging of hfccs of the methyl group was taken into account by averaging of the individual methyl proton tensors that were calculated in steps of 15 degrees.

The individual assignment of the hfccs to the benzene ring protons was done according to the DFT results.[22;33] A comparison with previous calculations demonstrates a good agreement with the assignment done here.[22;32] This indicates that the asymmetry of the hfccs of the benzene ring protons observed in $VK_3^{\bullet-}$ is reduced in $VK_1^{\bullet-}$. In some studies[38;40] the hfccs of the protons at positions 5 and 8, and 6 and 7 were found to be identical, which does not agree with the experimental findings of this work. The hfccs show some temperature dependence.

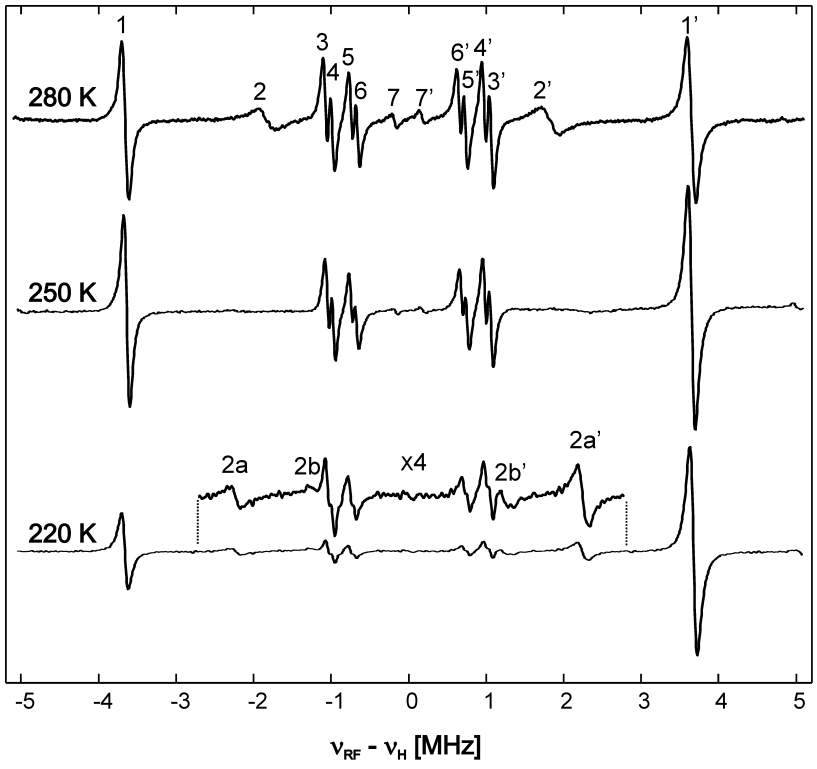

Figure 4.21: Liquid solution CW ENDOR spectra of chemically generated $VK_1^{\bullet-}$ in IP-h_8 recorded at X-band (9.61 GHz) at three different temperatures. Experimental conditions: P_{MW} = from 2 to 8 mW, P_{RF} = 10 to 25 W, 12.5 kHz modulation, modulation depth ± 25 kHz.

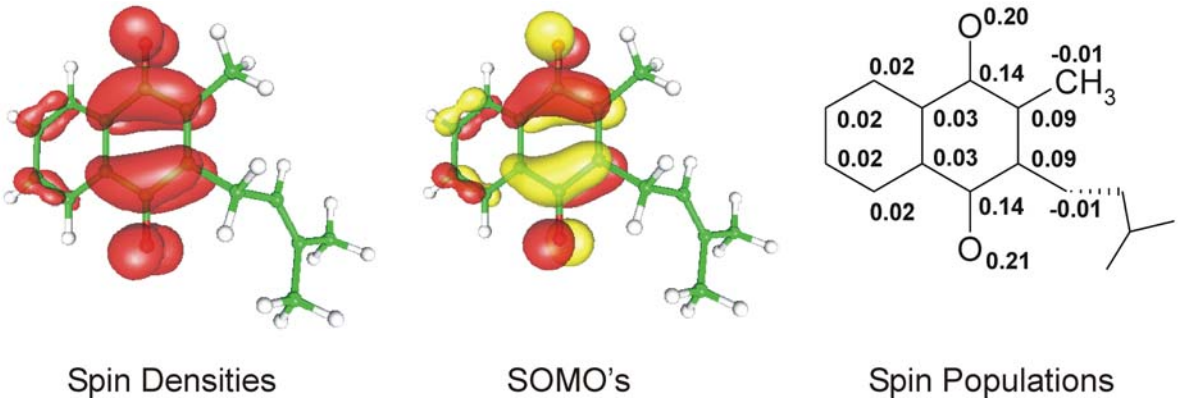

Figure 4.22: Spin densities, semi occupied molecular orbitals (SOMO's) and spin populations, obtained for $VK_1^{\bullet-}$(a model system with a reduced side chain). While the spin density is the difference between the total α and β spin densities and therefore depends on all orbitals, the SOMO is the orbital of the unpaired electron. Spin populations were obtained from a Mulliken analysis, which attributes fractional amounts of electrons to every nucleus.

Table 4.8: Hyperfine coupling parameters used for fitting of the CW EPR and the CW ^{1}H ENDOR spectra of $VK_1^{\bullet-}$ in IP-h_8 at different temperatures and results of DFT calculations.[a] Hyperfine couplings (a_{iso}) are given in MHz. The precision of the hfcc determination is estimated to be ± 15 kHz.

	Position						
	2 (CH_3)	**3 (CH_2)**	**3 (γ)**	**5 (α)**	**6 (α)**	**7 (α)**	**8 (α)**
Line pair	1/1'	2/2'	7/7'	6/6'	3/3'	4/4'	5/5'
a_{iso} (280 K)	+ 7.31	+ 3.67	– 0.36	– 1.31	– 2.14	– 1.96	– 1.48
a_{iso} (250 K)	+ 7.35	n.d.	– 0.36	– 1.36	– 2.13	– 1.97	– 1.52
a_{iso} (220 K)	+ 7.39	+ 4.50/+ 2.45	n.d.	– 1.41	– 2.12	– 1.99	– 1.54
a_{iso} (263 K)[b]	7.282	3.701	0.336	1.309	2.162	1.946	1.466
a_{iso} (280 K)[b]	+ 7.32	+ 3.65	– 0.38	– 1.29	– 2.15	– 1.96	– 1.48
a_{iso} (220K)[b]		4.52/2.47					
a_{iso} (280 K)[d]	7.32	3.7	0.38	1.27	2.17	1.96	1.48
a_{iso} (273 K)[e]	7.273	3.711	n.d.	1.135	2.124	1.993	1.528
a_{iso} (DFT)[a]	+ 7.13 (+ 7.15)	+ 4.11/+ 1.50 (+ 4.23/+ 1.45)	n.d.	– 1.39 (– 1.22)	– 2.08 (– 2.11)	– 2.01 (– 2.06)	– 1.47 (– 1.29)

[a] for the DFT calculations, two solvent molecules were coordinated to each carbonyl oxygen. Geometry optimization was performed without restrictions. Hf tensor calculations were performed employing the COSMO continuum method (without brackets) and without the COSMO continuum method (in brackets). For details, see chapter 3.

[b] from ref. [33] For the ease of comparison, similar experimental values are listed in the same row, disregarding different assignment by the author.

[c] from ref. [22] For the ease of comparison, similar experimental values are listed in the same row, disregarding different assignment by the author.

[d] from ref. [47] For the ease of comparison, similar experimental values are listed in the same row, disregarding different assignment by the author.

[e] from ref. [48] For the ease of comparison, similar experimental values are listed in the same row, disregarding different assignment by the author.

Especially interesting is the line pair 2/2', which is observed at 280 K and disappears at 250 K. At 220 K, two new line pairs 2a/2a' and 2b/2b' are found. This was observed previously for $VK_1^{\bullet-}$,[22;32;38] and a similar effect was found in case of the ubiquinone radical anion.[38;49] The fast rotation/motion of phytyl chain *vs.* the quinone rings at 280 K creates a motional averaging of the two methylene protons, which is not possible at lower temperature, where the rotation of the phytyl chain is partially blocked.[50]

The fairly good agreement of the hfccs determined at 220 K with the DFT results indicates that the geometry of the (truncated) phytyl chain is quite close to the average geometry present in IP solution.

The Q-band EPR and orientation-selected ^{1}H ENDOR spectra of $VK_1^{\bullet-}$ in IP-d_8 are presented in Figure 4.23. The three field positions (close to the canonical orientations of the *g*-tensor), at which the respective ENDOR spectra were measured (a, b and c), are marked in the EPR spectrum. A number of additional experiments (a total of 9) were performed at other field positions in order to investigate in detail the angular dependence of the hfccs (data not shown). The simulations of the corresponding EPR and ENDOR spectra are presented by red lines. The simulated *g*-factors of the quinone radical anion in IP-d_8 are given in Table 4.9. The *g*-factors for $VK_1^{\bullet-}$ are in agreement with earlier high field EPR studies.[7] The explanation of the deviation of the *g*-tensor obtained experimentally and by DFT calculation given above for $NQ^{\bullet-}$ also holds here. The ENDOR spectra of $VK_1^{\bullet-}$ exhibit only three main features from the methyl group protons in position 2 and the benzene ring protons. The lines of the α-protons in position 5 and 8, and 6 and 7, are not resolved. Signals from the methylene protons were not resolved in the frozen solution ENDOR spectra, in agreement with previous studies.[22] Since the energy differences for different degrees of rotation of the tail against the quinone ring are low (shallow energy minima),[50] the position of the phytyl tail will not be well defined in frozen solution. The hfccs of the methylene protons are strongly dependent on the dihedral

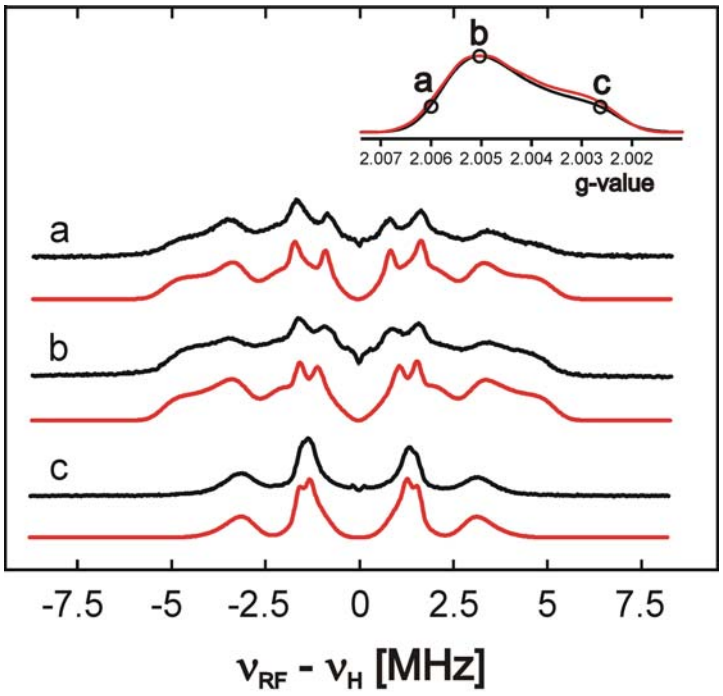

Figure 4.23: Selected Q-band ^{1}H ENDOR spectra of $VK_1^{\bullet-}$ in IP-d_8 recorded at T = 80 K and at different values of the magnetic field. ENDOR traces a, b and c correspond to spectral positions near g_x, g_y and g_z respectively. The black trace for each position represents experimental data and the red trace represents the simulation. The insert in the right corner shows the FSE EPR spectrum and its simulation. The field positions, at which the presented ENDOR spectra are measured, are marked with letters.

angle of these β-protons with respect to the quinone plane,[51] resulting in a distribution of hfccs and consequently in broad ENDOR lines. These weak and broad lines are buried under the ENDOR lines of the four weak to intermediate coupled α-protons of the benzene ring. However, they can be distinguished from the α-protons from the benzene ring by the sign of the hfcc, since the methylene protons are the only protons, beside the spectrally well separated methyl group protons, which are expected to show significant positive hfccs. Hence, the pulse TRIPLE method (see chapter 2) was applied in order to detect the signals of the methylene protons. Figure 4.24 presents the ENDOR and difference TRIPLE spectra of $VK_1^{\bullet-}$ in IP-d_8, recorded at two different spectral position. The low frequency ENDOR transition of methyl group protons (mark with an arrow) was used as the pumping frequency. Since the methyl group proton hfccs are positive, other positive hfccs are expected to be visible in the low

Table 4.9: Principal components of *g*-tensors of $VK_1^{\bullet-}$ in IP-d_8 derived from pulse Q-band EPR experiments at T = 80 K and values from DFT calculations. [a]

	g_x	g_y	g_z	
$VK_1^{\bullet-}$	2.0057(1)	2.0051(1)	2.0023(1)	this work
	2.00566(5)	2.00494(5)	2.00216(5)	[b]
	2.00640	2.00526	2.00217	DFT[a]

[a] for the DFT calculations, two solvent molecules were coordinated to each carbonyl oxygen. Geometry optimization was performed without restrictions. Hf tensor calculations were performed employing the COSMO continuum method (without brackets) and without the COSMO continuum method (in brackets). For details, see chapter 3.

[b] From a W-band EPR study (ref.[7]).

frequency region of the difference TRIPLE spectrum ($\nu_{RF} < \nu_H$), while negative hfccs will be observed in the high frequency region of the difference TRIPLE spectrum ($\nu_{RF} > \nu_H$). In both traces two clear signals from the *a*-protons of the benzene ring (negative hfccs) are observed (marked with a minus sign). In trace **a** clearly a very broad and unstructered line arising from positive hfccs (marked with a plus sign) can be seen, while in trace **b** no signals in the low frequency range are observed (beside the always prominent signal at the pumping frequency). It corresponds to hfccs of about 1 to 6.5 MHz. A precise determination of the upper limits of these hfccs is not possible due to the intense line at the pumping frequency. Surprisingly at the first glance, also some emissive line is observed in the difference TRIPLE spectra. The time necessary for the TRIPLE sequence is not longer negligibly shorter than the electronic and nuclear relaxation times, which causes this phenomena.[52;53] To assure that the broad signals in the difference TRIPLE spectra of $VK_1^{\bullet-}$ are no artifacts, the same experiment was performed with $VK_3^{\bullet-}$in IP-d_8 (Figure 4.25). The signals from the α-proton of the benzene ring and of the α-proton at position 3 indicate negative hfccs.

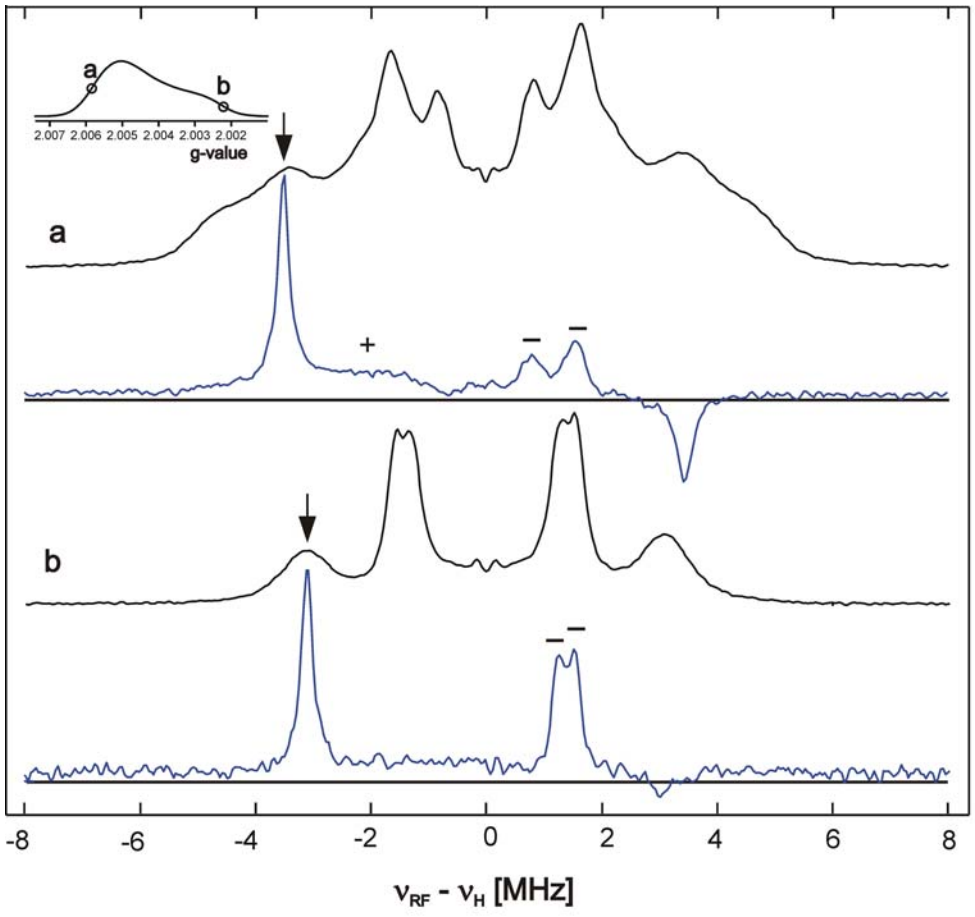

Figure 4.24: Pulse Q-band ^{1}H ENDOR spectra (black traces) and difference TRIPLE pectra (blue traces) of $VK_1^{\bullet-}$ in IP-d_8 , recorded at T = 80 K. The ENDOR/TRIPLE traces a and b correspond to spectral positions near g_x and g_z , respectively. The insert in the upper left corner shows the FSE EPR spectrum. The field positions, at which the presented ENDOR spectra were measured, are marked with letters. The arrows mark the frequency of the pumping RF pulse. The plus and minus signs denote the signs of the hfccs.

No broad signals from positive hfccs are observed. From this it can be concluded that i) the broad signal observed in the difference TRIPLE spectrum arises from the methylene protons (the γ-proton of the phytyl tail has a by far to large distance to the quinone ring to have hfccs in this range), and ii) the shape and width of the signal confirms a distribution of hfccs (and thus different orientations) of the methylene protons.

Table 4.10: Parameters used in the fitting of ^{1}H ENDOR spectra of $VK_1^{\bullet-}$ in IP at T = 80 K (exp.) and results of DFT calculations[a] (DFT). Hyperfine couplings (A_i, a_{iso}) and linewidths (*lw*, full width at half height) are given in MHz. Angles (φ,θ) are given in degrees. When not specified parameters for simulations are taken from DFT calculations. The precision of the hfcc determination is estimated to be 25 % of the linewidth. The smallest component of ring proton hfcc (A_y) exhibits a larger error.

	2 (CH_3)		**3 (CH_2)**		**5 (α)**		**6 (α)**		**7 (α)**		**8 (α)**		**H-bonds**			
	exp.	**DFT**	**exp.**	**DFT**	**exp.**	**DFT**	**exp.**	**DFT**	**exp.**	**DFT**	**exp.**	**DFT**		**I**	**II**	**III**	**IV**
$\mathbf{A_x}$	+ 6.40	+ 6.27		+0.41 +3.39	– 1.72	– 1.50	– 3.50	– 3.52	– 3.50	– 3.42	– 1.72	– 1.52	exp. DFT	+ 6.4 + 6.8	+ 6.1 + 6.6	+ 6.0 + 6.0	+ 5.5 + 6.0
$\mathbf{A_y}$	+10.20	+ 9.57		+4.85 +6.31	+ 0.50	+ 0.56	+ 0.04	+ 0.03	+ 0.04	+ 0.07	+ 0.50	+ 0.37	exp. DFT	– 5.2 – 5.2	– 5.1 – 5.1	– 4.0 – 4.0	– 2.5 – 3.7
$\mathbf{A_z}$	+ 6.05	+ 5.56		–0.76 +2.63	– 3.29	– 3.20	– 2.60	– 2.75	– 2.60	– 2.69	– 3.29	– 3.26	exp. DFT	– 5.4 – 5.4	– 5.3 – 5.3	– 3.9 – 4.2	– 2.2 – 3.6
$\mathbf{a_{iso}}$	+ 7.55	+ 7.13		+1.50 +4.11	– 1.50	– 1.39	– 2.02	– 2.08	– 2.02	– 2.01	– 1.50	– 1.47	exp. DFT	– 1.4 – 1.3	– 1.4 – 1.3	– 0.6 – 0.7	+ 0.3 – 0.4
$\mathbf{a_{iso}}$ [b]	+ 7.39		+2.45 +4.50		– 1.41		– 2.12		– 1.99		– 1.54		n.d.				
lw	0.7				0.2		0.2		0.2		0.2		0.5				
φ	+ 36	+ 34		–24 –8	+10	+ 8	+16	+ 16	– 17	– 17	– 10	– 10	DFT	+ 59	– 50	– 51	+ 53
θ	0	< 1		– 6 + 3	0	4	0	< 1	0	< 1	0	2	DFT	+ 57	– 36	– 26	+ 11

[a] two solvent molecules were coordinated to each carbonyl oxygen. Geometry optimization was performed without restrictions. Hf tensor calculations were performed employing the COSMO continuum method.
[b] liquid solution data, Table 4.8.

The comparison with the DFT calculations show a similar precision of prediction of the hfccs as in case of $VK_3^{\bullet-}$ (Table 4.7). Earlier X-band studies of $VK_1^{\bullet-}$ [22;33] and its close structural analog $MQ^{\bullet-}$[54] yielded similar results for the strongly coupled protons.

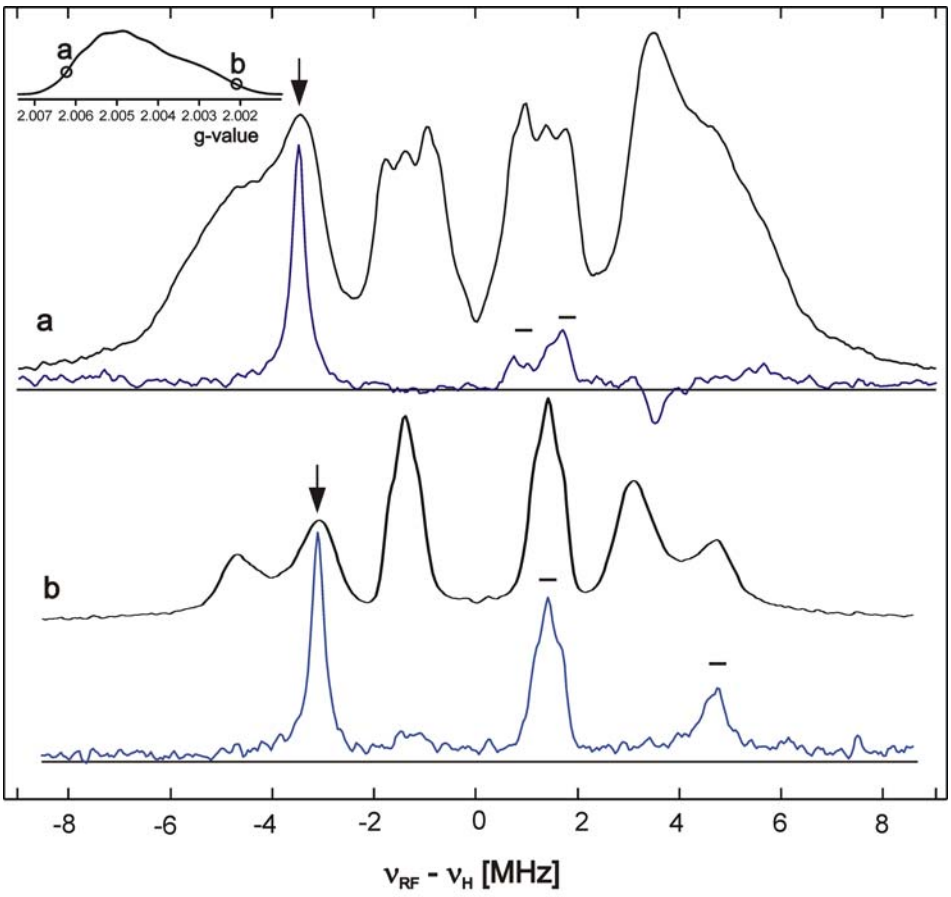

Figure 4.25: Pulse Q-band ^{1}H ENDOR spectra (black traces) and difference pulse TRIPLE pectra (blue traces) of $VK_3^{\bullet-}$ in IP-d_8 , recorded at T = 80. The ENDOR/TRIPLE traces a and b correspond to spectral positions near g_x and g_z , respectively. The insert in the upper left corner shows the FSE EPR spectrum. The field positions, at which the presented ENDOR spectra were measured, are marked with letters. The arrows mark the frequency of the pumping RF pulse. The plus and minus signs denote the signs of the hfccs.

Comparison between data obtained from ENDOR in liquid and frozen solution can be done by an analysis of the isotropic part of the hf tensor (obtained from the trace of this tensor ($a_{iso} = \frac{1}{3}\mathrm{Tr}(\mathbf{A}) = \frac{1}{3}(A_x + A_y + A_z)$). Table 4.2, Table 4.5, and Table 4.8 present the isotropic hfcc obtained in liquid solution at different temperatures, Table 4.4, Table 4.7, and Table 4.10 those obtained in frozen solutions. In general, good agreement is found. This indicates that no major spin redistribution occurs upon freezing of the samples.

Hyperfine couplings of the protons involved in hydrogen bonds

Information on the hfccs of protons involved in H-bonds can be obtained from ENDOR spectroscopy. ^{1}H-ENDOR spectroscopy can be done on quinones in protonated solvents, ^{2}H-ENDOR spectroscopy can be done on quinones in deuterated solvents. In the first case, the ^{1}H-ENDOR spectra contain signals from the protons of the quinone (if the quinone is protonated), signals from the H-bond protons and other solvent protons (*e.g.* first solvent shell). Hence, subtraction procedures are required to differentiate between these three different sets of proton signals. In earlier studies subtraction was typically done using ENDOR spectra of quinones in fully protonated and fully deuterated solvents. It was found in this work and in ref. [55] that protons of the solvent, which are not involved in H-bonds, also contribute to the spectra. Therefore, selectively deuterated (IP-d_1) solvent was used as a reference in the analysis here. In this case the difference of corresponding ENDOR spectra contains solely signals from the H-bonds. To minimize the subtraction artifacts deuterated quinones were used if available.

Figure 4.26 presents selected ^{1}H ENDOR spectra of fully deuterated benzoquinone (BQ-$d_4^{\bullet-}$), naphthoquinone (NQ-$d_6^{\bullet-}$), and vitamin K_3 (VK_3-$d_8^{\bullet-}$) in IP-d_1 (black traces) and difference spectra of the corresponding semiquinone radicals in IP-h_8 and IP-d_1 (blue traces). For $VK_1^{\bullet-}$ the ^{1}H ENDOR difference spectra of the semiquinone radicals in IP-d_1 and IP-d_8 (black trace), as well as IP-h_8 and IP-d_1 (blue trace) are shown. Overall up to 8 experiments at different field positions were performed for each quinone. The data for BQ-$d_4^{\bullet-}$ are included for comparison. The subtraction of ^{1}H ENDOR spectra of protonated quinones in IP-h_8 and IP-d_1 leads to comparable results (data not shown). However, it was found that difference spectra of deuterated compounds contain less subtraction artifacts.

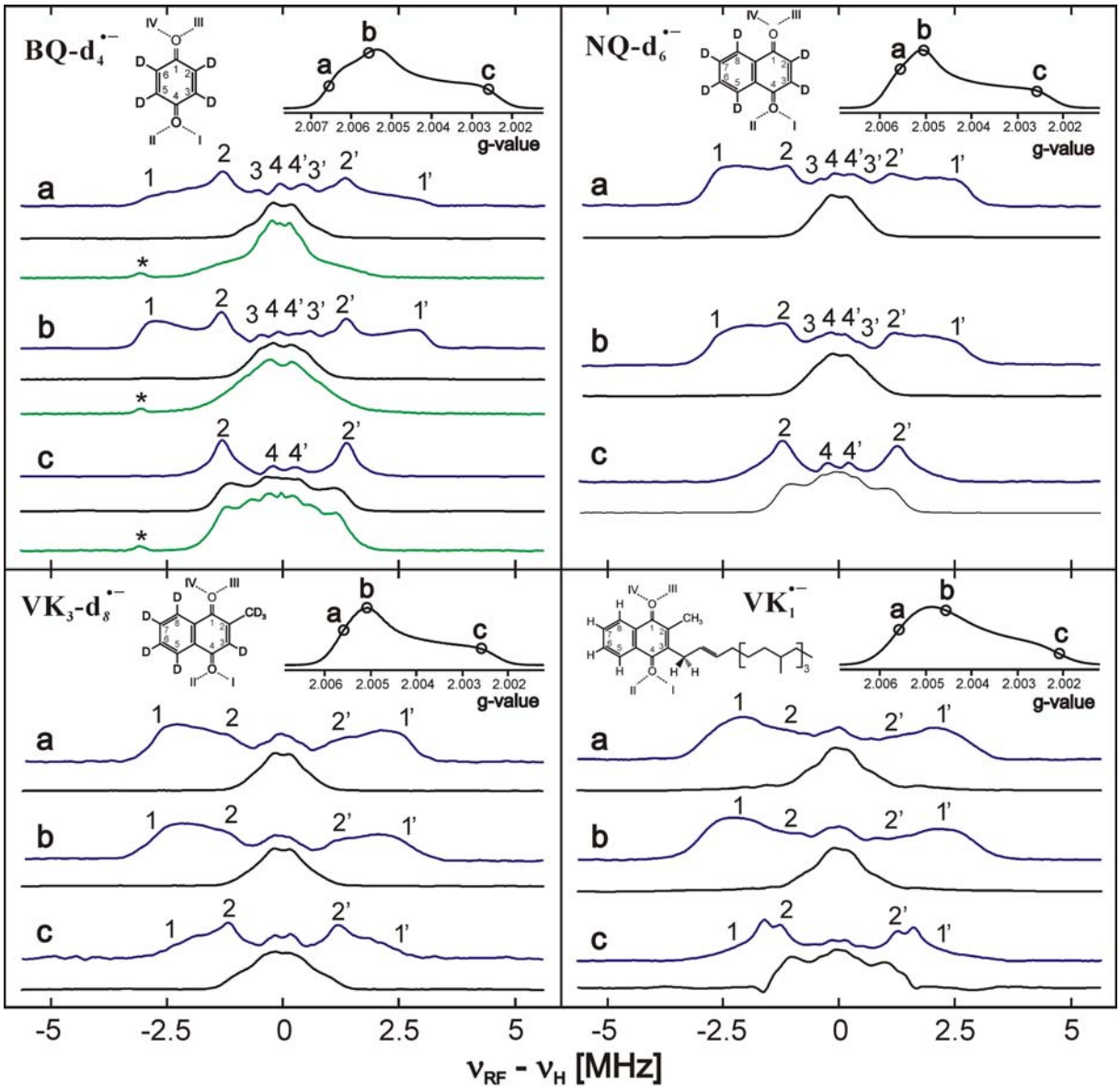

Figure 4.26: Selected pulse Q-band ^{1}H ENDOR difference spectra in IP-h_8 and IP-d_1 (blue trace for each field position) and ^{1}H ENDOR spectra in IP-d_1 (black trace for each field position) of chemically generated BQ-$d_4^{\bullet-}$ (upper left plot), NQ-$d_6^{\bullet-}$ (upper right plot), VK$_3$-$d_8^{\bullet-}$ (lower left plot) and VK$_1^{\bullet-}$(lower right plot) recorded at different values of the magnetic field. Additional ^{1}H ENDOR spectra are presented for coulometrically generated BQ-$d_4^{\bullet-}$ in DME (green trace). The asterisks marks the a ENDOR line from ^{19}F. The molecular structures with numbering scheme are given. Traces a, b and c correspond to spectral positions near g_x, g_y and g_z, respectively. The ^{1}H ENDOR difference spectra show signals that stem only from the exchangeable protons (these hydrogens form H-bonds in a first and second solvation shell). The spectra in IP-d_1 exhibit only non-exchangeable protons from the solvent. The insert in the right corner of each of the 4 panels shows the EPR spectrum. The field positions where the ENDOR experiments were done, are marked with black circles and letters (a,b,c). Specific spectral features (see text for the discussion) are marked with Arabic numbers.

The ^{1}H ENDOR difference spectra of BQ-$d_4^{\bullet-}$ are shown in Figure 4.26 (upper left plot, blue traces). A well resolved dipolar powder pattern is observed. The magnetic dipolar

interaction leads to an axially symmetric hf tensor. The largest component of the hf tensor lies along the H-bond direction. Previous studies found that for $BQ^{\bullet-}$ in alcohols the largest component of the dipolar tensor lies in the plane of the quinone and is directed approximately along the lone pair orbitals of oxygen (53.5° from the C–O bond direction).[56] Therefore, it manifests itself in ^{1}H ENDOR spectra recorded near the spectral positions g_x and g_y (see line pair 1/1', traces **a** and **b**), but not near g_z (trace **c**). The small components of the axial tensor can be found in all ENDOR spectra (line pair 2/2' traces **a**, **b** and **c**). Since only one dipolar pattern is observed it is concluded that all H-bonds to the quinone oxygens are equivalent. The simulation of the ENDOR spectra provides principal components of the H-bond tensor of + 6.25 ± 0.05 MHz, – 2.90 ± 0.05 MHz and –2.80 ± 0.05 MHz, and an angle φ = 55 ± 10°, while the out-of-plane angle is below 10° (linewidth 0.3 MHz). These data are in full agreement with results of previous experimental studies[25;56] as well as previously published DFT calculations.[25;57] The length of the H-bonds according to DFT calculations on $BQ^{\bullet-}$ is 1.76 Å.

In all ENDOR difference spectra additional weak signals of exchangeable protons with couplings up to 1 MHz are observed (line pairs 3/3' and 4/4'). These are not a subtraction artifacts, since they are also visible in the difference spectra of protonated quinones. They represent signals from H-bond protons of a second solvent shell. The principal components of their tensor are (+)1.06 MHz, (-)0.50 MHz, (-)0.50 MHz and the orientation of the tensor is similar to those of the H-bonds. Provided that the weak H-bonds are also established to the carbonyl oxygen, the length of the weak bond can be estimated to be approx. 1.8 times longer than those for the strong H-bond. This corresponds to a length of about 3.25 Å.

The ^{1}H ENDOR difference spectra of NQ-$d_6^{\bullet-}$ are similar to those of BQ-$d_4^{\bullet-}$. However, the linewidth of all spectral components is clearly increased (Figure 4.26, upper right panel). This indicates a certain distribution of H-bond parameters. The DFT calculations predict that the

in-plane angles of the two H-bonds on the side of the benzene ring are changed while the orientations of the other two bonds are similar to those in $BQ^{\bullet-}$. However, a distribution of the in-plane angle φ can not explain the loss of intensity of the A_y component in both ENDOR spectra recorded along the g_x and g_y direction. The simulation of the spectra (for simulation parameters see Table 4.4) shows that for the representation of spectral lineshapes at least two of the H-bonds should adopt an out-of-plane angle of up to 15°.

Kaupp *et al.* [11] have found that the results of structure optimization of the quinones in alcohols using DFT depend on the starting conditions. The optimizations lead to multiple conformers with similar energy. These conformers differ by their out-of-plane angles of the H-bonds between the quinone and solvent molecules. For example the $NQ^{\bullet-}$ structure reported by Kaupp *et al.* [11]has two H-bonds with an out of plane angle of about 12° and two H-bonds with 24°. The consequences of these flat potential surfaces are i) a distribution of H-bond angles, and ii) a limited accuracy of the computed out-of-plane H-bond angles in the calculation.

The optimization of the molecular structure becomes even more problematic for the quinones with bulky substituents like VK_3 (methyl group) and VK_1 (methyl group and phytyl tail). Here different geometry optimizations were performed:

i) without any restrictions and

ii) with H-bonds restricted to the plane of the quinone. The unrestricted structure optimization results in significant out-of-plane H-bonding to the oxygen close to the bulky substituent and

iii) without restrictions, but taking a reduced number of H-bonds due to the bulky substituents.

The unrestricted structure optimization with four H-bonds results in significant out-of-plane H-bonding to the oxygen close to the bulky substituent. The DFT calculations show that the

couplings of ring protons are only marginally dependent on the geometry of the H-bonds. In contrast, the H-bond hf tensors are strongly dependent on the H-bond out-of-plane angle and thus on the results of the geometry optimizations. The case of three H-bonds to VK_3 lead to severe changes of the ring proton hfccs, which do not agree with the experimental results. The case of H-bonds to $VK_1^{\bullet-}$ shows less pronounced deviations, but the hfccs are still further away from the experimentally determined hfccs (see Table 4.11 and Table 4.12).

Table 4.11: Comparison of the spin Hamiltonian parameters for $VK_3^{\bullet-}$ as determined experimentally and calculated using DFT [a] with the COSMO continuum method for different model systems.

		2 (CH_3)	3 (α)	5 (α)	6 (α)	7 (α)	8 (α)	H-bonds I,II,III,IV[a]			
experi-mental	A_x	+ 6.40	– 11.73	– 1.54	– 3.80	– 3.01	– 1.99	+ 5.5	+ 5.9	+ 6.3	+ 6.4
	A_y	+ 9.7	– 1.00	+ 0.60	– 0.07	+ 0.29	+ 0.05	– 2.5	– 2.8	– 4.7	– 4.1
	A_z	+ 5.80	– 9.60	– 3.00	– 2.82	– 2.34	– 3.54	– 2.4	– 2.5	– 4.9	– 3.7
	a_{iso}	+ 7.30	– 7.40	– 1.31	– 2.23	– 1.69	– 1.83	+ 0.2	+ 0.2	– 1.1	– 0.5
4IP [b]	A_x	+ 6.63	–10.42	– 1.31	– 3.80	– 2.90	– 1.76	+ 5.5	+ 5.9	+ 6.5	+ 6.7
	A_y	+ 10.10	– 0.78	+ 0.60	– 0.07	+ 0.29	+ 0.05	– 2.5	– 2.8	– 4.7	– 4.6
	A_z	+ 5.98	– 9.23	– 2.99	– 2.91	– 2.37	– 3.63	– 2.8	– 2.5	– 5.1	– 4.5
	a_{iso}	+ 7.57	– 6.81	– 1.23	– 2.26	– 1.66	– 1.78	< 0.1	+ 0.2	– 1.1	– 0.8
3IP [c]	A_x	+ 8.08	– 8.11	– 1.55	– 3.02	– 3.74	– 1.41	+ 5.5	+ 5.8	–	+ 6.7
	A_y	+ 11.50	+ 0.11	+ 0.13	– 0.21	+ 0.07	+ 1.09	– 2.5	– 2.5	–	– 2.8
	A_z	+ 7.38	– 7.75	– 3.31	– 2.43	– 2.89	– 2.96	– 2.7	– 2.8	–	– 3.4
	a_{iso}	+ 8.99	– 5.25	– 1.57	– 1.74	– 2.23	– 1.09	+ 0.1	+ 0.2	–	+ 0.2
4IP in plane [d]	A_x	+ 6.50	– 10.31	– 1.35	– 3.70	– 2.97	– 1.74	+ 5.4	+ 5.7	+ 5.7	+ 5.9
	A_y	+ 9.85	– 0.74	+ 0.58	– 0.04	+ 0.25	+ 0.06	– 2.4	– 2.4	– 2.4	– 2.5
	A_z	+ 5.83	– 9.17	– 3.03	– 2.85	– 2.41	– 3.54	– 2.7	– 2.8	– 2.6	– 2.7
	a_{iso}	+ 7.39	– 6.74	– 1.27	– 2.20	– 1.71	– 1.74	+ 0.1	+ 0.2	+ 0.2	+ 0.2

[a] For numbering of the H-bonds, see Figure 4.26, lower left panel.
[b] Two solvent molecules were coordinated to each carbonyl oxygen. Geometry optimization without restrictions.
[c] Coordination of one IP molecule to the carbonyl oxygen on the site of the methyl group and of two IP molecules to the opposite carbonyl oxygen.
[d] Similar to model system 4IP[b], but H-bonds were restricted to lie in the quinone plane. The model system 4IP[b] was found to be only 1.3 kJ/mol more stable than model system 4IP in plane[d].

Table 4.12: Comparison of the spin Hamiltonian parameters for $VK_1^{\bullet-}$ as determined experimentally and calculated using DFT with the COSMO continuum method for different model systems.

		2 (CH_3)	3 (CH_2)	5 (α)	6 (α)	7 (α)	8 (α)	H-bonds I,II,III,IV[a]			
experi-mental	A_x	+ 6.40		– 1.72	– 3.50	– 3.50	– 1.72	+ 6.4	+ 6.1	+ 6.0	+ 5.5
	A_y	+10.20	n.d.	+ 0.50	+ 0.04	+ 0.04	+ 0.50	– 5.2	– 5.1	– 4.0	– 2.5
	A_z	+ 6.05		– 3.29	– 2.60	– 2.60	– 3.29	– 5.4	– 5.3	– 3.9	– 2.2
	a_{iso}	+ 7.55		– 1.50	– 2.02	– 2.02	– 1.50	– 0.7	+ 0.8	– 0.6	+ 0.3
4IP[b]	A_x	+ 6.27	+ 0.41 + 3.39	– 1.50	– 3.52	– 3.42	– 1.52	+ 6.8	+ 6.6	+ 6.0	+ 6.0
	A_y	+ 9.57	+ 4.85 + 6.31	+ 0.56	+ 0.03	+ 0.07	+ 0.37	– 5.2	– 5.1	– 4.0	– 3.7
	A_z	+ 5.56	– 0.76 + 2.63	– 3.20	– 2.75	– 2.69	– 3.26	– 5.4	– 5.3	– 4.2	– 3.6
	a_{iso}	+ 7.10	+ 1.50 + 4.11	– 1.39	– 2.08	– 2.01	– 1.47	– 1.3	– 1.3	– 0.7	– 0.4
2IP[c]	A_x	+ 5.82	+ 0.27 + 4.09	– 1.35	– 3.70	– 3.44	– 1.43	–	+ 6.3	–	+ 6.3
	A_y	+ 9.01	+ 4.98 + 7.07	+ 1.07	– 0.07	+ 0.04	+ 0.78	–	– 2.6	–	– 2.6
	A_z	+ 5.08	– 0.99 + 3.36	– 2.90	– 2.85	– 2.70	– 3.04	–	– 3.3	–	– 3.1
	a_{iso}	+ 6.64	+ 1.42 + 4.84	– 1.06	– 2.21	– 2.04	– 1.23	–	+ 0.1	–	+ 0.2
4IP in plane[d]	A_x	+ 6.37	+ 0.62 + 2.98	– 1.49	– 3.58	– 3.34	– 1.57	+ 5.4	+ 5.5	+ 5.3	+ 5.6
	A_y	+ 9.56	+ 5.20 + 5.93	+ 0.56	+ 0.01	+ 0.10	+ 0.32	– 2.2	– 2.3	– 2.3	– 2.3
	A_z	+ 5.67	– 0.54 + 2.24	– 3.17	– 2.79	– 2.64	– 3.30	– 2.5	– 2.6	– 2.4	– 2.6
	a_{iso}	+ 7.20	+ 1.76 + 3.72	– 1.37	– 2.12	– 1.96	– 1.52	+ 0.2	+ 0.2	+ 0.2	+ 0.2

[a] For numbering of the H-bonds, see Figure 4.26, lower right panel.
[b] Two solvent molecules were coordinated to each carbonyl oxygen. Geometry optimization without restrictions.
[c] A single IP molecule was coordinated to each carbonyl oxygen.
[d] Similar to model system 4IP[b], but H-bonds were restricted to lie in the quinone plane. The model system 4IP[b] was found to be only 1.3 kJ/mol more stable than model system 4IP in plane[d].

The difference ^{1}H ENDOR spectra of VK_3-$d_8^{\bullet-}$ and $VK_1^{\bullet-}$ are presented in Figure 4.26 (bottom left and bottom right, respectively). The line pair 2/2' from the A_y component of the hf tensor becomes so broad that the two line almost disappear from the ENDOR spectra (traces **a** and **b**) and the wing of the large component of the dipolar coupling (line pair 1/1', trace **c**) becomes very prominent at the spectral position near g_z. Due to the poorly resolved spectra it is impossible to independently evaluate the hf parameters for each H-bond. However, using the parameters obtained from DFT calculations as starting values (see Table 4.11 and Table 4.12) a reasonable ENDOR lineshape simulation was achieved. Thereby, an indirect confirmation of the structure with non-planar H-bonds is obtained.

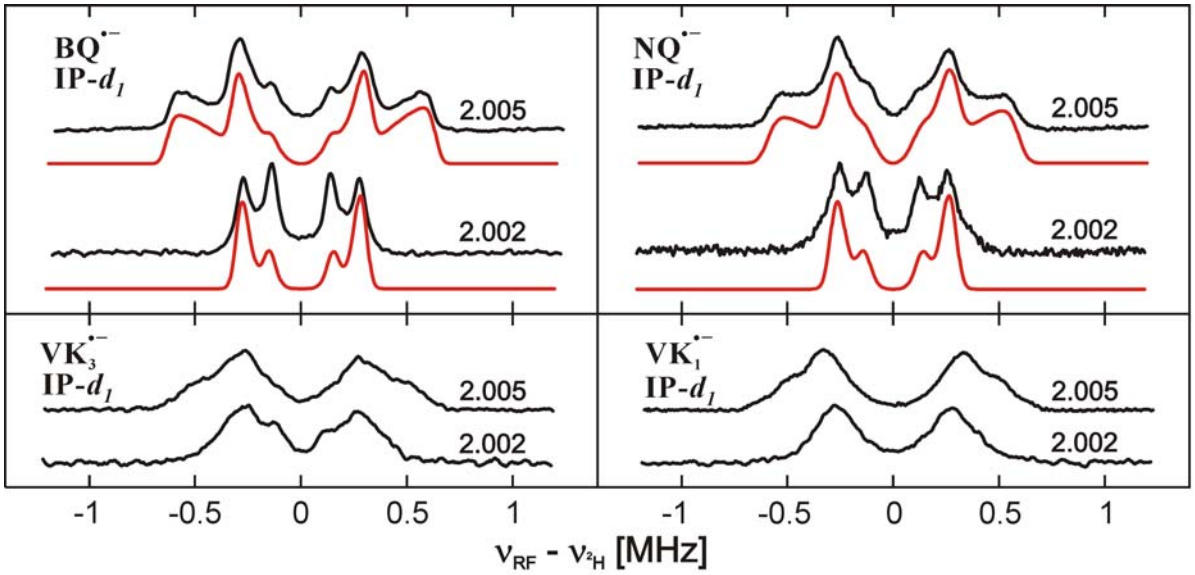

Figure 4.27: Pulse Q-band Deuterium Mims ENDOR spectra of chemically generated $BQ^{\bullet-}$, $NQ^{\bullet-}$, $VK_3^{\bullet-}$ and $VK_1^{\bullet-}$ in IP-d_1 recorded at the peak maximum ($g \sim 2.005$) and at the high field edge ($g \sim 2.002$) of the respective EPR spectra (shown in black). The simulations are shown in red. The simulation parameters for $BQ^{\bullet-}$ are: principal components of the hf tensor $A_x = +0.98 \pm 0.02$ MHz, $A_y = -0.47 \pm 0.02$ MHz, $A_z = -0.44 \pm 0.01$ MHz, and of the nq tensor $P_x = +102 \pm 10$ kHz, $P_y = -57 \pm 5$ kHz, $P_z = -45 \pm 5$ kHz, hf and nq tensors have the same orientation, $\varphi = 54 \pm 15^0$, $\theta = 0^0$ (see Figure 1 for the definition of angles). Simulation parameters for $NQ^{\bullet-}$ are: principal components of hf tensor $A_x = +0.88 \pm 0.03$ MHz, $A_y = -0.40 \pm 0.03$ MHz, $A_z = -0.40 \pm 0.01$ MHz, nq tensor $P_x = +102 \pm 12$ kHz, $P_y = -57 \pm 6$ kHz, $P_z = -45 \pm 6$ kHz, hf and nq tensors are collinear ($\varphi = 54 \pm 15^0$, $\theta = 0^0$).

The second way to investigate the hydrogen bond proton hf tensors is the use of ^{2}H ENDOR spectroscopy of 'normal' protonated quinones in deuterated solvents. The hfccs obtained for ^{2}H can be scaled by the ratio of two nuclear *g*-values to obtain also the ^{1}H hfccs. If selectively deuterated solvents like IP-d_1, where only the OH hydrogen is exchanged (Figure 4.11 B), are used, no subtraction procedures are necessary. (In principle, 1/8 of the solvent protons is deuterated, which might create low intensity signals close to the matrix line.)

Figure 4.27 shows Mims ^{2}H ENDOR spectra of $BQ^{\bullet-}$, $NQ^{\bullet-}$, $VK_3^{\bullet-}$ and $VK_1^{\bullet-}$ in IP-d_1. Even though these spectra contain only the lines from the deuterons of the 'hydrogen' bond they are significantly more complicated than the ^{1}H ENDOR spectra due to the presence of nuclear quadrupole (nq) splitting. Only $BQ^{\bullet-}$ and $NQ^{\bullet-}$ spectra are sufficiently resolved to allow reliable simulations. The parameters of the simulations are given in the caption of Figure 4.27. Scaling the hfcc of the deuterons by the factor g_{2H}/g_{1H} provided proton hfccs close to those derived from the ^{1}H ENDOR. Similar hfccs and nqc were recently experimentally determined for $BQ^{\bullet-}$.[25;56] The calculated nq couplings are somewhat larger (P_x = + 115 ± 2.5 kHz, P_y = – 68 ± 1 kHz, P_z = – 47 ± 1 kHz for $BQ^{\bullet-}$ and $NQ^{\bullet-}$). It was demonstrated for $BQ^{\bullet-}$ in H_2O that an increase of the solvation shell in the DFT calculations led to a slight reduction of the nqccs.[25]

As observed for the proton ENDOR spectra (Figure 4.26), the deuterium ENDOR spectra of higher substituted quinones exhibit a substantial broadening. Some splitting due to the nq interaction can still be observed in the ^{2}H ENDOR spectra of $VK_3^{\bullet-}$ at a field position close to g_z, while spectra of $VK_1^{\bullet-}$ do not show a resolved quadrupole splitting. This confirms that the hydrogen bonds are more disordered and thus the spin Hamiltonian parameters are distributed.

However, since the overall widths of the spectra do not change significantly upon addition of bulky substituents to the quinone molecule it can be concluded that the length of the H-

bond does not significantly change. This correlates with the results of the ^{1}H ENDOR where the distribution of hf parameters (primarily the out-of-plane angles) has been shown to be responsible for the ENDOR line broadening.

The length of the H-bonds to the quinone radical anions

In previous studies it was empirically established that the nq coupling constant $e^2qQ/h=2P_{max}$ shows a linear dependence on the inverse third power of the length of the H-bond:[58;59]

$$e^2qQ/h = a - \frac{b}{r^3}, \tag{4.1}$$

where a and b are empirical coefficients equal to 310 kHz and 572 kHz[58] and 328 kHz and 643 kHz,[59] respectively. P_{max} is the largest component of the nq coupling tensor (here P_x). The nq coupling constant is given in kilohertz (kHz) and the H-bond length in angstroms (Å). Using Eq. 4.1 and a nq coupling of $2P_{max}=2P_x=$ 204 kHz a distance of 1.75 Å or 1.73 Å is obtained both for $BQ^{\bullet-}$ and $NQ^{\bullet-}$ for the two different sets of coefficients. The DFT calculations with four solvent molecules showed that the H-bonds have a length of 1.76-1.78 Å. These results correlate well with values of 1.74 Å for $BQ^{\bullet-}$ and 1.76-1.77 Å for $NQ^{\bullet-}$ obtained by Kaupp *et al.* [11] using DFT calculations.

Another experimental approach for the evaluation of the length of H-bonds is based on the point-dipole model. From the dipolar part of the hf coupling the H-bond length can be calculated according to:

$$A_{dip} = \frac{g_e\beta_e g_N\beta_N}{hr^3}\rho_S\left(3\cos^2\delta - 1\right), \tag{4.2}$$

where g_e and g_N are the electron and nuclear *g*-values, β_e and β_n are the electron and nuclear magnetons, ρ_S is the spin density at the quinone oxygen, δ is the angle between the applied magnetic field and the direction of the H-bond, and *r* is the length of the H-bond in Å.[31] The disadvantage of this approach is, however, that the spin density on the oxygen must be known for this estimation. This can be determined experimentally using ^{17}O labeling of the quinone and subsequent analysis of the oxygen hf coupling obtained from EPR experiments. However, it should be noted that the error of such an analysis can be quite large since only the largest component of the ^{17}O hf coupling is typically determined and a localization of the unpaired electron in the p_z orbital of the oxygen is assumed. The spin densities determined from experimental data are 0.23[36] for $BQ^{\bullet-}$ in IP, 0.20[60] for $NQ^{\bullet-}$ in ethanol, and 0.19 for $VK_3^{\bullet-}$ in IP[61] (see Figure 4.14, Figure 4.18, and Figure 4.22 for a comparison with the calculated spin densities). ^{17}O hf couplings for $VK_1^{\bullet-}$ are not available, however, they should be very close to those of $VK_3^{\bullet-}$. Using Eq. 4.2 and the experimentally determined hfccs of the H-bond protons, distances of 1.82 Å, 1.78 Å and 1.78 Å are obtained for $BQ^{\bullet-}$, $NQ^{\bullet-}$ and for the in-plane H-bonds in $VK_3^{\bullet-}$. In view of the possible error margins of both methods, the agreement between the different methods of determination of H-bond length is considered to be satisfactory.

Hyperfine couplings of weakly coupled protons of the solvent

The presence of a so-called matrix line from distant nuclei is common for ENDOR spectra of frozen samples.[31;62;63] The matrix line is centered at the Larmor frequency and is typically unstructured or only weakly structured. However, in the ^1H ENDOR spectra of fully deuterated quinone radical anions in IP-d_1 a clearly resolved structure was found.

The ^{1}H ENDOR spectra of BQ-$d_4^{\bullet-}$, NQ-$d_6^{\bullet-}$ and VK_3-$d_8^{\bullet-}$ in IP-d_1 are presented in Figure 4.26, lower trace for each field position. The signals must be attributed to non-exchangeable bulk solvent protons. Extremely weak ENDOR signals were detected in the control sample of deuterated quinone in IP-d_8 (data not shown). In this way the contribution of protons from benzyl-trimethyl-ammonium-hydroxide, which was used to produce the radical anion, to the respective ENDOR spectra can be excluded. Several previous investigations in which a subtraction of quinone ENDOR spectra in IP-h_8 and IP-d_8 was used for the analysis of H-bonds, attributed these signals to a second set of weaker H-bonds. This in not supported by the results presented. It is easy to see that in contrast to the H-bond signals, which are presented in the same figures (see upper trace for each field position), the hf tensors of these solvent protons have a different orientation. While the largest component of the H-bond tensors lies in the plane of the quinone (at least for $BQ^{\bullet-}$ and $NQ^{\bullet-}$) the corresponding largest component of the bulk-solvent protons is oriented nearly perpendicular to this plane. It should be noted that at orientations close to g_z the lines from weakly coupled protons and H-bond protons overlap. The simulations give values of 2.1 to 2.4 MHz for the largest component of this hf tensor and 1.0 to 1.2 MHz for the smaller one.

Assuming a primarily dipolar nature of the interaction of these nuclei with the unpaired electron, the position of the proton must be above or below the quinone plane (carbonyl oxygens). In this case the largest component of the hyperfine tensor will be perpendicular to the π-plane, as observed in the experiment. The strength of a dipolar interaction is dependent on the distance between the nucleus and the unpaired electron (see Eq. 4.2). To estimate the maximum distance of the observed solvent shell protons, DFT was used. The dependence of the hyperfine coupling of a proton from a methane molecule, located right above the carbonyl oxygen, on the distance from the plane calculated. The oxygen carries the largest electron spin density, and thus the corresponding distance is the longest. According to these calculations a

proton that is located 3.1 Å above the carbonyl oxygen will have the strongest hf component of $A_{\|}$ = +2.3 MHz.

There are two possible assignments of the weak solvent couplings: i) to the protons of the H-bonded solvent molecules and ii) to the protons of other solvent molecules, which are located above (or below) the quinones plane. The optimized structures with 4 H-bonds give a closest distance to the methyl group protons of about 2.9 Å and an angle of the largest hf component from g_z of about 15°. However at 80 K we expect free rotation of the methyl groups, which leads to an averaging of hf couplings of the methyl group protons. Since the other protons of the methyl group are further away from the oxygen, the average hfcc is expected to be smaller than the one observed experimentally. In addition, similar hfccs from the solvent have been observed by us for $BQ^{\bullet-}$ in aprotic solvents, which are not forming H-bonds. The CH protons of H-bonded IPs are more than 3.3 Å away from the oxygen and their out-of-plane angles are about 50°. This suggests that the second assignment is more likely.

^{1}H ENDOR spectra were also recorded for coulometrically generated BQ-$d_4^{\bullet-}$ in some of the organic solvents used above. These are, in contrast to IP, no H-bond donor solvents. As an example, three ENDOR spectra of BQ-$d_4^{\bullet-}$ in DME recorded close to the orientations g_x, g_y and g_z are presented (Figure 4.26, upper left panel, green traces). They are similar to the ENDOR spectra of BQ-$d_4^{\bullet-}$ in IP-d_1. A difference is the presence of ENDOR signals of low intensity, which arise from larger hfccs, at g_y and especially g_x orientation. The similarity confirms that these lines are not specific to the H-bonding properties of the solvent. They can arise both from protons of the solvent molecules but also from protons of the supporting electrolyte. It is of note, that a weak and unstructered line at an RF frequency 3 MHz smaller than the proton Larmor frequency is observed (marked with an asterisk; ν_{RF} ~ 48.5-48.6 MHz, depending on the respective magnetic field). No corresponding line was detected in the high frequency range of the ENDOR spectrum. The line position was also found to be nearly

independent of the magnetic field. Thus, it is probably a matrix line from a nucleus different than proton. The inspection of the atoms present in the solvents and the supporting electrolyte showed that only the ^{19}F isotope (spin I = ½, natural abundance 100%) exhibits a corresponding nuclear *g*-value. Several ^{19}F atoms are present in the anion of the supporting electrolyte. The F atoms are obviously not too far away from the quinone radical anion, but also only weakly (dipolar) coupled, since no splitting of the line due to hf interaction is visible (lw ~ 0.25 MHz). Since BQ-$d_4^{\bullet-}$ is negatively charged, the presence of a positively charged counter ion close to the quinone is likely. The presence of larger hfccs than observed in IP-d_1, might indicate the the F atoms come close –in plane– to the carbonyl oxygens. This position is in case of IP-d_1 as solvent occupied by the 'H-bonding' deuterium. To clearly assign the ENDOR signal to the supporting electrolyte molecules and/or the solvent molecules, deuterated solvents and/or deuterated supporting electrolytes would be necessary.

Conclusions

The redox potential and electronic properties (^1H hf tensors and *g*-tensors) of quinone radical anions were investigated.

The redox potential of BQ/$BQ^{\bullet-}$ was determined in several solvents with different polarity and found to be exhibit a linear correlation with the empirical polarity scales, especially with the acceptor number (AN) from Mayer and Gutmann.[20] This is agreement with a previous study of VK_1.[22] The redox potential of a protein bound quinone, like A_1 in PS I, can be adjusted to the desired value by adjusting the overall polarity of its binding pocket. Thus, the very low redox potential of VK_1($VK_1^{\bullet-}$) in the A_1 binding site can be explained in terms of a apolar protein environment.

The *g*-tensor of $BQ^{\bullet-}$ in frozen solutions of the respective solvents was also determined. In protic solvents the *g*-tensor was found to be independent of polarity, in agreement with previous studies.[25;56] In aprotic solvents the g_x value was increased strongly as compared to the hydrogen-bonding solvents. for the aprotic solvents, not linear dependence was found as well. It has to be concluded that it not possible to precisely estimate the polarity of the quinone environment (*e.g.* in a protein) or the redox potential from the knowledge of the *g*-tensor. Only a rough estimate of the environment like polar and protic (H-bonding) or apolar and aprotic (no H-bonding) seems to be possible. In fact, even one, asymmetric H-bond as found for A_1 in PS I[64], provided *g*-tensor similar to the one observed for VK_1 in ether.[8] Furthermore, it was shown that the g-tensor is strongly influenced by the presence of only small amounts of H-bonding molecules in the solvent. This finding and the presence of ions of the supporting electrolyte close to the BQ radical anion raises some doubts about the reliability of the experimentally determined *g*-values of $BQ^{\bullet-}$ in the apolar solvents. An interesting future approach would be to perform extended DFT calculations of the *g*-tensor of $BQ^{\bullet-}$ in different aprotic environments, including at least the solvents molecules of the first solvation shell.

$VK_1^{\bullet-}$ and the related quinone radical anions $NQ^{\bullet-}$ and $VK_3^{\bullet-}$ in frozen 2-propanol solution were measured using CW X-band and pulse Q-band ENDOR spectroscopy. The use of a higher microwave frequency band (Q-band, 34 GHz) allowed a significant improvement, as compared to the standard X-band (9-10 GHz), with respect to the orientation selection and thus allowed the determination the hf tensor principal components for all protons visible in the ENDOR spectra. The methylene proton hfccs exhibit a distribution of values due to different orientations of the phytyl tail in frozen solution.

Hydrogen bonding to the quinone was studied in detail for all four quinones. In case of $BQ^{\bullet-}$ and $NQ^{\bullet-}$ the hydrogen bond were found to lie in plane of the quinone, in agreement with

previous studies on $BQ^{\bullet-}$.[25;56] For $VK_3^{\bullet-}$ and $VK_1^{\bullet-}$ it was shown that some of H-bonds do not lie in the plane of the quinone. This spread of H-bonds leads to a severe broadening of the ENDOR lines which precludes a comprehensive analysis of the H-bond proton hf tensors. Hydrogen bond lengths were estimated both from the dipolar couplings of the respective protons using the point dipolar model and from nqccs using the empirical formulas from Hunt & Mackay and Soda & Chiba.[58;59] The distances obtained by these two methods are very similar for all four quinone radical anions (1.77 ± 0.05 Å) and agree with the distances obtained by the DFT calculation.

Furthermore, ENDOR signals of weakly coupled non-exchangeable protons of the solvent were detected. The analysis of the respective hfccs suggests that these protons are located above and below the quinone plane, *i.e*. close to the carbonyl groups that carry the majority of the spin density. This can be useful for the understanding the coupling of protons from the direct protein environment of quinone radical anions. In particular, it will be helpful to understand weakly coupled protons close to$VK_1^{\bullet-}$ in the A_1 binding site, *e.g.* the tryptophan residue above the quinone plane.

The DFT calculations demonstrated the potential of the method in predicting the hf tensors of the quinone protons. The error of prediction increases with the complexity of the model but does not exceed 15%. Hf tensor orientations could also be predicted by the calculations and were found to be helpful in the spectral simulations. The combination with a COSMO continuum model for solvation further improved the agreement with the experimental results.

The accurate hyperfine data, obtained here for the VK_1 quinone radical anion *in vitro*, are very important for a solid comparison to the hfccs of $A_1^{\bullet-}$ in PS I. It can also be compared to the hfccs of the structurally very similar MQ found in bacterial photosynthetic RCs. In addition, the good prediction of hfccs by the DFT calculation provides confidence that the

DFT method using COSMO can also be applied to obtain the hfccs quinone radical anions in proteins, like $A_1^{\bullet-}$ in PS I (see chapter 5).

References

1. Voet, D. and Voet, J. G., *Biochemistry*, New York, John Wiley & Sons **2004**
2. *Energy Transduction in Biological Membranes: a Textbook of Bioenergetics,* Cramer, W. A. and Knaff, D. B. (Eds.), Springer Advanced Texts in Chemistry, New York, Springer **1990**
3. *Function of Quinones in Energy conserving systems*, Trumpower, B. L. (Ed.), New York, Academic Press, Inc. **1982**
4. Brettel, K. and Leibl, W., *Biochimica et Biophysica Acta*, 1507, 100-114 **2001**
5. Brettel, K., *Biochimica et Biophysica Acta*, 1318, 322-373 **1997**
6. van der Est, A., *Biochimica et Biophysica Acta*, 1507, 212-225 **2001**
7. Burghaus, O., Plato, M., Rohrer, M., Möbius, K., MacMillan, F., Lubitz, W., *Journal of Physical Chemistry*, 97, 7639-7647 **1993**
8. Teutloff, C., Hofbauer, W., Zech, S. G., Stein, M., Bittl, R., Lubitz, W., *Applied Magnetic Resonance*, 21, 363-379 **2001**
9. Yonezawa, T., Kawamura, T., Ushio, M., Nakao, Y., *Bulletin of the Chemical Society of Japan*, 43, 1022-1027 **1970**
10. Ciofini, I., Reviakine, R., Arbuznikov, A., Kaupp, M., *Theoretical Chemistry Accounts*, 111, 132-140 **2004**
11. Kaupp, M., Remenyi, C., Vaara, J., Malkina, O. L., Malkin, V. G., *Journal of the American Chemical Society*, 124, 2709-2722 **2002**
12. Jordan, P., Fromme, P., Witt, H. T., Klukas, O., Saenger, W., Krauss, N., *Nature*, 411, 909-917 **2001**
13. Reichardt, C., *Solvents and Solvent Effects in Organic Chemistry*, Weinheim, Wiley-VCH Verlag **2003**
14. Reichardt, C., *Chemical Reviews*, 94, 2319-2358 **1994**
15. Marcus, Y., *The Properties of Solvents,* Wiley series in solution chemistry Vol. 4, Fogg, P. G. T (Series Ed.), Chichester, John Wiley & Sons **1998**
16. Kosower, E. M., *An Introduction to Physical Organic Chemistry*, New York, Wiley **1968**
17. Kosower, E. M., *Journal of the American Chemical Society*, 80, 3253-3260 **1958**
18. Gutmann, V., *Coord. Chem. Rev.* , 18, 225-255 **1976**
19. Mayer, U., Gerger, W., Gutmann, V., *Monatshefte für Chemie*, 108, 489-498 **1977**

20. Mayer, U., Gutmann, V., Gerger, W., *Monatshefte für Chemie*, 106, 1235-1257 **1975**

21. Hales, B. J., *Journal of the American Chemical Society*, 97, 5993-5997 **1975**

22. Teutloff, C., Untersuchungen zur Bindung des sekundären Akzeptors in Photosystem I mit Methoden der EPR-Spektroskopie, Phd Thesis Technische Universität Berlin, **2004**

23. Lubitz, W., Isaacson, R., Flores, M., Sinnecker, S., Lendzian, F., Feher, G., *Biophysical Journal*, 82, 2333 **2002**

24. Knüpling, M., Torring, J. T., Un, S., *Chemical Physics*, 219, 291-304 **1997**

25. Sinnecker, S., Reijerse, E., Neese, F., Lubitz, W., *Journal of the American Chemical Society*, 126, 3280-3290 **2004**

26. Hales, B. J., *Journal of the American Chemical Society*, 98, 7350-7357 **1976**

27. Kurreck, H., Kirste, B., Lubitz, W., *Electron nuclear double resonance spectroscopy of radicals in solution - applications to organic and biological chemistry*, Marchand, A. P. (Ed.), Deerfield Beach, Florida, VCH Publishers, Inc. **1988**

28. Käss, H., Fromme, P., Witt, H. T., Lubitz, W., *Journal of Physical Chemistry B*, 105, 1225-1239 **2001**

29. Käss, H., Die Struktur des primären Donators P700 in Photosystem I: Untersuchungen mit Methoden der stationären und gepulsten Elektronspinresonanz, Phd Thesis Technische Universität Berlin, **1995**

30. Gemperle, C. and Schweiger, A., *Chemical Reviews*, 91, 1481-1505 **1991**

31. Schweiger, A. and Jeschke, G., *Principles of pulse electron paramagnetic resonance*, New York, Oxford University Press **2001**

32. Teutloff, C., Bittl, R., Lubitz, W., *Applied Magnetic Resonance*, 26, 5-21 **2004**

33. MacMillan, F., EPR and ENDOR investigation of the electron acceptor Q_A in plant photosystem II and related semiquinone anion radicals, Phd Thesis Freie Universität Berlin, **1993**

34. Pushkar, Y. N., Karyagina, I., Stehlik, D., Brown, S., van der Est, A., *Journal of Biological Chemistry*, 280, 12382-12390 **2005**

35. Pushkar, Y. N., Stehlik, D., van Gastel, M., Lubitz, W., *Journal of Molecular Structure*, 700, 233-241 **2004**

36. MacMillan, F., Lendzian, F., Lubitz, W., *Magnetic Resonance in Chemistry*, 33, S81-S93 **1995**

37. Klamt, A. and Schüürmann, G., *Journal of the Chemical Society-Perkin Transactions 2*, 5, 799-805 **1993**

38. Das, M. R., Connor, H. D., Leniart, D. S., Freed, J. H., *Journal of the American Chemical Society*, 92, 2258-2268 **1970**

39. Kirste, B., *Magnetic Resonance in Chemistry*, 25, 166-175 **1987**

40. O'Malley, P. J., *Biochimica et Biophysica Acta-Bioenergetics*, 1411, 101-113 **1999**

41. Grafton, A. K. and Wheeler, R. A., *Journal of Physical Chemistry A*, 101, 7154-7166 **1997**

42. Asher, J. R., Doltsinis, N. L., Kaupp, M., *Journal of the American Chemical Society*, 126, 9854-9861 **2004**

43. Asher, J. R., Doltsinis, N. L., Kaupp, M., *Magn. Reson. Chem.*, 43, S237-S247 **2005**

44. Bolton, J. R. and Carrington, A., *Molecular Physics*, 5, 161-167 **1962**

45. Atherton, N. M., *Principles of Electron Spin Resonance*, New York, E. Horwood & PTR Prentice Hall **1993**

46. Joela, H. and Lehtovuori, P., *Physical Chemistry Chemical Physics*, 1, 4003-4010 **1999**

47. Elsässer, C., EPR- und ENDOR-Untersuchungen an biologisch relevanten Chinonanionradikalen, Diploma Thesis Technische Universität Berlin, **2000**

48. Maly, T., EPR- und ENDOR-Untersuchungen an biologisch relevanten Semichinon-Radikalanionen, Diploma Thesis J.W.G Universität Frankfurt, **1999**

49. Feher, G., Isaacson, R., Okamura, M. Y., Lubitz, W., in Michel-Beyerle, M. E. (Ed.), *Antennas and Reaction Centers of Photosynthetic Bacteria*, Chemical Physics 42, Schäfer, F. P., Goldanskii, V. I., and Toennies, J. P., Berlin, Springer-Verlag, 174-189 **1985**

50. Himo, F., Babcock, G. T., Eriksson, L. A., *Journal of Physical Chemistry A*, 103, 3745-3749 **1999**

51. Heller, C. and Mcconnell, H. M., *Journal of Chemical Physics*, 32, 1535-1539 **1960**

52. Höfer, P., Entwicklung von Puls-ENDOR-Verfahren und Ihre Anwendung auf Polyazetylen, Universität Stuttgart, **1988**

53. Silakov, A. About the origin of emissive signals in pulse difference TRIPLE spectra. **2006**.

54. Gardiner, A. T., Zech, S. G., MacMillan, F., Käss, H., Bittl, R., Schlodder, E., Lendzian, F., Lubitz, W., *Biochemistry*, 38, 11773-11787 **1999**

55. O'Malley, P. J. and Babcock, G. T., *Journal of the American Chemical Society*, 108, 3995-4001 **1986**

56. Flores, M., Isaacson, R., Calvo, R., Feher, G., Lubitz, W., *Chemical Physics*, 294, 401-413 **2003**

57. O'Malley, P. J., *Journal of Physical Chemistry A*, 101, 9813-9817 **1997**

58. Soda, G. and Chiba, T., *Journal of Chemical Physics*, 50, 439-455 **1969**

59. Hunt, M. J. and Mackay, A. L., *Journal of Magnetic Resonance*, 15, 402-414 **1974**

60. Broze, M., Luz, Z., Silver, B. L., *Journal of Chemical Physics*, 46, 4891-4902 **1967**

61. Pushkar, Y. N., Ayzatulin, O., Stehlik, D., *Applied Magnetic Resonance*, 28, 195-211 **2005**

62. Kevan, L. and Kispert, L. D., *Electron Spin Double Resonance Spectroscopy*, New York, John Wiley & Sons **1976**

63. Astashkin, A. V. and Kawamori, A., *Journal of Magnetic Resonance*, 1411, 101-113 **1998**

64. Fromme, P., Jordan, P., Krauss, N., *Biochimica et Biophysica Acta*, 1507, 5-31 **2001**

5. The Electron Acceptor A_1

Introduction

The quinone VK_1 serves as an intermediate electron acceptor (named A_1) in the electron transport inside PS I. During the electron transfer this phylloquinone becomes singly reduced and the quinone radical anion $A_1^{\bullet-}$ is formed.[1;2] The protein bound VK_1 exhibits a variety of special properties. It has a very low redox potential; much lower than that of VK_1 in protic polar solvents (*e.g.* water).[2;3] It was found that this low redox potential is not specific for VK_1 in the A_1 binding site. Various analogues of VK_1 or even quinones of different type like plastoquinone-9 (PQ_9) or anthraquinone (AQ), see *e.g.*[1;4;5] can be incorporated into the A_1 binding site and experience a similar shift of their redox potentials. Thus, the generation of a low redox potential is a property of the A_1 binding site. Also the *g*-tensor of $A_1^{\bullet-}$ deviates strongly from the one of $VK_1^{\bullet-}$ in protic solvents.[6-8] In chapter 4 it was shown that both properties of $A_1^{\bullet-}$ can in principle be explained in terms of a apolar surrounding of the quinone radical anion, in agreement with previous studies.[7;9;10] In addition to the redox potential and the *g*-tensor, also the hfccs of the prominent methyl group protons are strongly different for $A_1^{\bullet-}$ as compared to $VK_1^{\bullet-}$ in polar protic solvents.[11;12] The change in spin density at this particular position can not be explained just by the low polarity of the binding site.[9;12] The spin density distribution in $A_1^{\bullet-}$ is only partially known so far. Hence, this chapter is devoted to the determination of the hfccs of $A_1^{\bullet-}$ and by this means also of the spin density distribution in $A_1^{\bullet-}$. Finally, the structure of the A_1 binding site in PS I must be correlated with the obtained spin density distribution to disentangle which effects are crucial for the change of spin density distribution in $A_1^{\bullet-}$ as compared to $VK_1^{\bullet-}$ *in vitro*.

First, the structure of the A_1 binding site(s) are described and second, the knowledge about hf tensors in $A_1^{\bullet-}$ obtained so far is discussed.

The structure and close environment of both VK_1 molecules of PS I (A-branch and B-branch, see chapter 1) within the 2.5 Å X-ray structure are shown in Figure 5.1 (PDB entry 1JB0).[13]

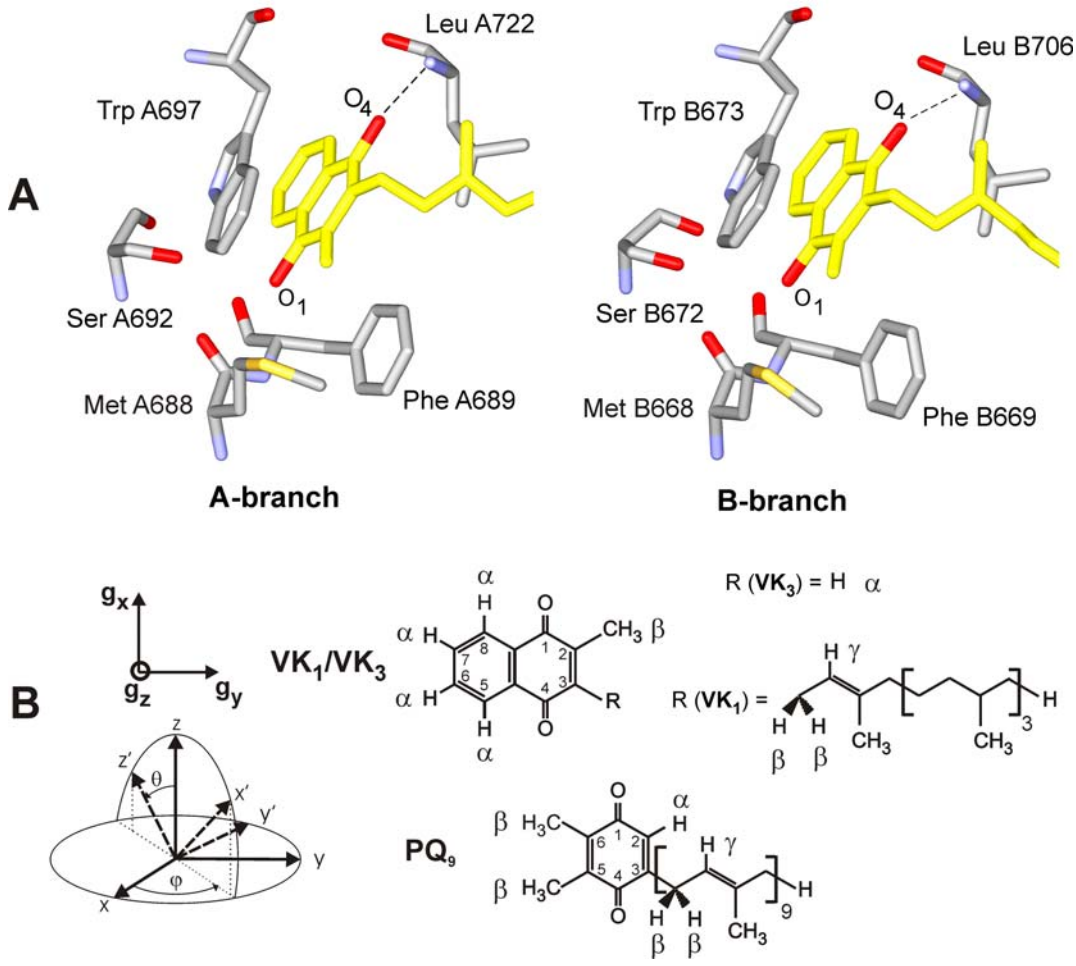

Figure 5.1: A Structure and close environment of VK_1 (yellow; phytyl tail truncated after the fifth carbon) in the A_1 binding site of the A-branch (left) and the B-branch (right) of PS I within the 2.5 Å X-ray structure (PDB entry 1JB0).[13] The two binding sites are very similar. The backbone amide proton of residue Leu A722/Leu A706 is in H-bonding distance to the C-O group at position 4 of VK_1, while in the symmetric position of the quinone (position 1) no H-bonding donor is present. The Trp A697/Trp A677 residue is π-stacked to the quinone with a plane-to-plane distance of 3.0-3.5 Å. Three other closeby residues, which are part of a H-bonding network, are also shown. **B** Molecular structures of VK_3, VK_1 and PQ_9 with numbering scheme. The α-, β- and γ-proton(s) of the quinones are marked. The principal axes of the *g*-tensor are shown. The x and y principal components lie in the quinone plane, with the x-direction parallel to the C-O bond, while the z component is perpendicular to the quinone plane.[14;15] Hf tensor angles are given with respect to the *g*-frame; the definitions of the spherical angles φ and θ are shown. Positive values refer to a counter-clockwise rotation.

The backbone amide proton of residue Leu A722/Leu B706 is in H-bonding distance to the C-O group at position 4 of VK_1, while in the symmetric position of the quinone no potential H-bonding donor is present. The Trp A697/Trp B677 residue is π-stacked to the quinone with a plane-to-plane distance of 3.0-3.5 Å. Both binding sites are nearly identical. Note, that the X-ray structure 1JB0 is obtained for the non-charge separated ground state of PS I, *i.e.* for A_1 and not $A_1^{\bullet-}$ (during electron transfer the quinone receives one electron and converts to the radical anion). X-ray crystallography can not provide information about the structure and dynamics of PS I in this state.

$A_1^{\bullet-}$ can be studied by EPR both during electron transfer (transient radical) and in the photochemically generated state (stationary radical).[1;11;16] In the first case the spin-correlated radical pair $P_{700}^{\bullet+}A_1^{\bullet-}$ is created.[1;16;17]

The spatial arrangement of the quinone in the charged state has been shown to be similar to the neutral quinone.[1;16;18] The interactions between the charged quinone and the protein are discussed controversially in the literature, *e.g.* with respect to the impact of the H-bond, and the π-stacked amino acid Trp A697/Trp B673.[11;12;19;20] The use of the two branches for electron transfer is also under discussion.[3;21] However, in cyanobacterial PS I only the A-branch A_1 is monitored by EPR spectroscopy. This refers both to the photoaccumulated $A_1^{\bullet-}$ and $A_1^{\bullet-}$ in the radical pair $P_{700}^{\bullet+}A_1^{\bullet-}$.[18;22] A more detailed discussion on the topic will be given below. The nuclei present in VK_1/A_1 are hydrogens, carbons and oxygens. While the magnetic isotope ^1H has a natural abundance of more than 99.9%, the magnetic isotopes of carbon and oxygen have a very low natural abundance. Thus, for determination of the ^{13}C or ^{17}O hf tensors the quinones have to be isotopically labeled and incorporated in the A_1 binding site.

Based on the structural information available at atomic resolution, there have been several DFT studies on $A_1^{\bullet-}$. The studies primarily focussed on the *g*-tensor,[23;24] which has been

determined with high precision using high frequency EPR.[6-8] Some preliminary DFT calculation of hfccs were done before the crystal structure was resolved.[25] Some other DFT studies reported only the isotropic hfccs.[9;26] A complete set of hf tensors is so far not available.

The low resolution in the frozen solution EPR spectra of $A_1^{\bullet-}$ allows the determination of hf tensors only in cases of large hfccs. The large hfccs of ^{13}C and ^{17}O have been determined earlier using transient EPR on specifically labeled VK_3 in the A_1 binding site. [19;27] However, the ^{13}C labeling was done only for two positions, and the estimation of spin density on the carbon atoms is complicated to achieve from the ^{13}C hf tensor. Both oxygens were uniformly ^{17}O labeled, thus no clear distinction between both oxygens could be made.

For the determination of ^{1}H hf tensors, no labeling techniques as in case of carbon or oxygen are needed. On the other hand, the ^{1}H hfccs are mostly too weak to be resolved in the EPR spectrum, demanding advanced techniques like ENDOR to increase the spectral resolution. ^{1}H ENDOR spectroscopy on the photoaccumulated radical $A_1^{\bullet-}$ was done by several groups, *e.g.* refs. [11;12;20], but only a few measurements on the radical pair $P_{700}^{\bullet-}A_1^{\bullet-}$ have been performed so far.[12;22;28-30] There are distinct advantages of the latter type of measurements: first, they are performed on PS I directly after charge separation, second, only reaction centers capable of charge separation are probed, and third, due to the transient nature of this phenomenon, the signal of the radical pair can easily be differentiated from stationary signals. Fourth, the full polarization of electron spin states provides strong signals. Note, however, that the analysis of the RP ENDOR spectra is rather complicated, thus a complete analysis of the spectra was not described yet.[29]

For $A_1^{\bullet-}$ only one large hf tensor of the methyl group protons has been determined and assigned definitively.[31;32] Other spectral features were differently assigned by several groups, see *e.g.* refs. [11;12]. A striking problem of nearly all previous ENDOR studies on $A_1^{\bullet-}$ is the poor

spectral resolution in the ENDOR spectra at X-band, where these studies were performed. At Q-band, which is used in this work, a better spectral resolution is available. However, even at this higher frequency the ENDOR spectra are still complicated due to the large number of protons which are coupled to the unpaired electron spin of $A_1^{\bullet -}$. This problem can be addressed in different ways. One way is the systematic modification of the protein environment by introducing (single point) mutations. Unfortunately, this method often alters the whole spatial arrangement of the cofactor in the protein environment.

Another method is isotopic labeling. Since isotopes have identical chemical properties, the system is not perturbed. The straightforward way to disentangle proton hfccs from the quinone and its protein environment is (selective) deuteration of either the quinone and/or its environment. Of special interest is the interaction of the protein environment with the quinone *via* hydrogen bonding. The selective exchange of this proton would allow a clear assignment of its ENDOR lines. However, until now the H/D exchange of the hydrogen bond proton in A_1 could not be achieved due the hydrophobicity of the binding site as reported previously.[9;12] To discriminate hfccs of quinone protons and protons of the protein environment, a protonated quinone can be substituted in the A_1 binding site of a deuterated PS I complex, or the quinone itself can be deuterated and substituted in the A_1 binding site of a protonated PS I complex. Selective deuteration of the quinone allows an easy assignment of hf tensor to molecular positions. The essential prerequisite of studies which use these labeling techniques is the effective exchange of the quinone in the A_1 site. The most gentle way is the use of PS I isolated from the *menB* mutant.[20;33] In *menB* strains, the biosynthetic pathway for production of VK_1 is interrupted by interposon mutagenesis of the *menB* genes in *Synechocystis* sp. PCC 6803.[30] This results in PS I complexes where PQ_9 (Figure 5.1B) instead of of VK_1 occupies the A_1 binding pocket. Its binding is much weaker than that of the native VK_1 and it can be replaced by other quinones with higher affinity to the A_1 binding site (*e.g.* VK_1 or VK_3). This

replacement strategy has been successfully used both *in vivo* and *in vitro*.[20;33] In the present study, VK_3 (VK_3-h_8 and VK_3-d_8) was used for the substitution, which is a close analog of VK_1 (Figure 5.1B; fully deuterated VK_1 or selectively deuterated VK_1/VK_3 were not available). Previous time resolved EPR measurements have shown that the substituted quinone occupies a position and orientation identical to native VK_1.[1;16]

In the previous chapter, Q-band EPR, ENDOR and TRIPLE spectroscopy and DFT calculations of quinone radical anions *in vitro* were described and yielded thus so far the most comprehensive assignment of proton hf tensors to molecular positions (see also ref. [34]). The hf tensor principal components for all protons visible in the ENDOR spectra were determined. The strength and geometry of hydrogen bonds formed between the quinone radical anion and specific solvent molecules were evaluated. In addition to the strong H-bonds, signals from the weaker coupled protons from the solvation shell were identified. The results of the DFT calculations showed a very good agreement with the experimental findings. Based on these results, a combination of orientation selective Q-band pulse EPR spectroscopy and DFT calculations were applied to also address the corresponding problem of the quinone radical anion $A_1^{\bullet-}$ in PS I. Measurements were performed both on the spin-correlated radical pair $P_{700}^{\bullet+}A_1^{\bullet-}$ and on the stationary radical anion $A_1^{\bullet-}$. This is the first ENDOR study on the radical pair $P_{700}^{\bullet+}$ $A_1^{\bullet-}$ and the second one on the stationary radical anion $A_1^{\bullet-}$ in PS I at a frequency higher than X-band.[20] Additionally, novel EPR techniques were used to obtain the signs of hfccs and the orientation of hf tensors. The proton hf tensors obtained for $VK_1^{\bullet-}$ and $VK_3^{\bullet-}$ in the A_1 binding site of PS I are compared to the proton hf tensors obtained for $VK_1^{\bullet-}$ and $VK_3^{\bullet-}$ *in vitro*, to investigate the influence of the protein on the hf tensors.

Results and Discussion

This section is divided in several parts. In the first part, the effective replacement of PQ_9 by VK_3 in the A_1 binding site of PS I isolated from the *menB* mutant is checked by transient EPR. In the second part, the results of pulse ENDOR spectroscopy on the RP and on the stationary radical anion $A_1^{\bullet-}$ are presented. This method was used for the determination of the magnitude of the hfccs. In the third part, the signs of the hfccs were determined by two different methods for the RP and stationary radical anion $A_1^{\bullet-}$, which are described in more detail in chapter 2. A novel EPR technique named **v**ariable **m**ixing **t**ime (VMT) ENDOR[35] was used to investigate the spin-correlated radical pair $P_{700}^{\bullet+}A_1^{\bullet-}$. For the sign determination of the hfccs in the stationary radical anion $A_1^{\bullet-}$, one- and two-dimensional TRIPLE spectroscopy was used.[36-38] The two-dimensional TRIPLE experiment not only delivers the signs of the hfccs, but also provides important information of the relative orientations of proton hf tensors with respect to each other. In the fourth part, the results of the DFT calculations are presented. On the basis of these results, the simulation parameters of the ENDOR spectra and the two-dimensional difference TRIPLE spectrum are given and compared with the hf tensors obtained for $VK_1^{\bullet-}$ and $VK_3^{\bullet-}$ in IP. Finally, several important topics, like the assignment of the H-bond proton, are separately discussed in detail and compared with results and interpretations of previous studies.

Transient EPR of the radical pair $P_{700}^{\bullet+}A_1^{\bullet-}$ of the PS I samples – Quinone replacement identified by transient EPR

Figure 5.2 shows the transient Q-band EPR spectra of the RP $P_{700}^{\bullet+}A_1^{\bullet-}$ in *T. elongatus* PS I (spectrum **a**) and the *menB* mutant PS I with VK_3-h_8 (spectrum **d**), VK_3-d_8 (spectrum **e**) and PQ_9 (spectrum **f**) in the A_1 binding site.

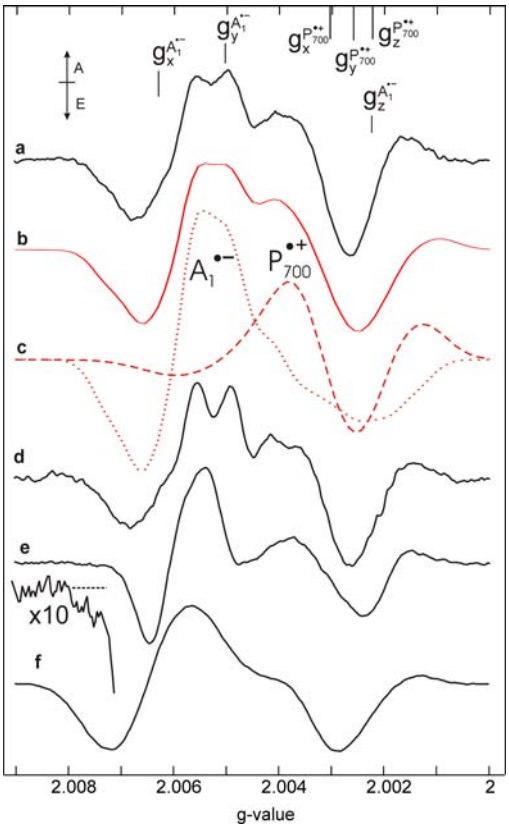

Figure 5.2: Transient Q-band EPR spectra of the $P_{700}^{\bullet+}A_1^{\bullet-}$ RP in PS I from *T. elongatus* and *Synechocystis menB* 26 mutant at 80 K.
a *T. elongatus* PS I.
b Simulation of spectrum **a**. The scale is different as compared to spectrum **c**.
c Individual contributions of $P_{700}^{\bullet+}$ (dashed line) and $A_1^{\bullet-}$ (dotted line) radicals to the simulated EPR spectrum presented in spectrum **b**.
d *menB* mutant PS I with VK_3-h_8 in the A_1 binding site.
e *menB* mutant PS I with VK_3-d_8 in the A_1 binding site.
f *menB* mutant PS I with PQ_9 in the A_1 binding site (as isolated).
The principal values of the *g*-tensor of the individual radicals $P_{700}^{\bullet+}$ and $A_1^{\bullet-}$ are given for PS I from *T. elongatus*. Insert: Enlarged view (x10) of spectrum **e**. E = emission and A = absorption.

The RP EPR spectra can be described as a superposition of emissive (E) and absorptive (A) spectra of $A_1^{\bullet-}$ and $P_{700}^{\bullet+}$ (see the simulated spectra **b** and **c**).[16;17;39] The signal of $P_{700}^{\bullet+}$ dominates the central and high field regions of the spectra, while the low field region of the EPR spectra contains a significant contribution of $A_1^{\bullet-}$ signal exhibiting a larger *g*-anisotropy. The *g*-values of $A_1^{\bullet-}$ are presented in Table 5.1, while the g-values of $P_{700}^{\bullet+}$ were taken from ref. [18]. Due to the small *g*-anisotropy of $P_{700}^{\bullet+}$, the absorptive EPR spectrum of stationary $P_{700}^{\bullet+}$ exhibits at Q-band only a single line (data not shown). The interaction tensor is taken from ref. [18].

Table 5.1: Principal *g*-values of the stationary radical anion $A_1^{\bullet-}$ (values in brackets) and $A_1^{\bullet-}$ in the RP $P_{700}^{\bullet+}A_1^{\bullet-}$.

	Quinone	g_x	g_y	g_z	g_{iso}
T. elongatus	**VK_1**	(2.0063) 2.0062	(2.0050) 2.0051	(2.0023) 2.0022	(2.0045) 2.0045
DFT on A_1	**VK_1**	2.0073	2.0055	2.0022	2.0050
***menB* mutant**	**PQ_9**	2.0067	2.0051	2.0022	2.0047
***menB* mutant**	**VK_3-d_8**	2.0063	2.0051	2.0024	2.0046
***menB* mutant**	**VK_3-h_8**	2.0063	2.0051	2.0024	2.0046

The error in the determination of the principal *g*-values is ± 0.0001. The *g*-values of $P_{700}^{\bullet+}$ and the interaction tensor are the same as determined in ref. [18].

The quantitative quinone replacement is of crucial importance for this work, since partial quinone exchange will result in a mixture of signals from PS I complexes with VK_3 or PQ_9 in their A_1 binding site. A serious contamination with PQ_9 would preclude accurate assignment of the lines in the ENDOR spectra. The evaluation of the degree of quinone exchange was done by inspection of the low field wing of the transient EPR spectra of the RP.[20] In the RP EPR spectrum of *menB* PS I with PQ_9 –as isolated– (spectrum **f**) signals are observed at lower field (higher *g*-value) as compared to the EPR spectra from PS I substituted with VK_3, especially for VK_3-d_8, where the linewidth is considerably smaller (Figure 5.2, spectrum **e**). Thus, the contribution of PQ_9 signals to the spectra of VK_3-d_8 substituted samples can easily be identified. In the spectra only a very small signal is visible in the low field region (see insert with the enlarged low field wing of spectrum **e**), thus the exchange is estimated to be nearly quantitative (better than 95%). It is important to note, that part of the low field signal can also be due to incomplete deuteration of VK_3-d_8 (~ 98%). In case of exchange against VK_3-h_8, the exact quantification of the PQ_9 exchange is more difficult due to the overlap of low field parts of the spectra of VK_3-$h_8^{\bullet-}$ and $PQ_9^{\bullet-}$. Since all the steps of sample preparation were done in parallel with the exchange against VK_3-d_8, using the identical procedure, the efficiency of the quinone replacement is expected to be identical.

The Q-band RP transient EPR spectra of *menB* mutant PS I substituted with VK_3-h_8 and VK_3-d_8 have been measured previously.[20;40] The EPR spectra presented here are very similar.

Thus, using the same argumentation as Pushkar *et al*., it can be concluded that the quinone molecules in samples of *menB* PS I, where PQ_9 was replaced with VK_3, occupy the same position as VK_1 in native PS I.

Pulse EPR and ENDOR measurements

Figure 5.3 presents the pulse Q-band EPR spectra of the RP $P_{700}^{\bullet+}A_1^{\bullet-}$and the stationary radical anion $A_1^{\bullet-}$. They are very similar to those obtained from transient EPR, except some intensity deviations in the high field region. The reason for these deviations is the interaction between the two radicals, which affects the spin echo amplitude in the region where the signals of $P_{700}^{\bullet+}$ and $A_1^{\bullet-}$ overlap.

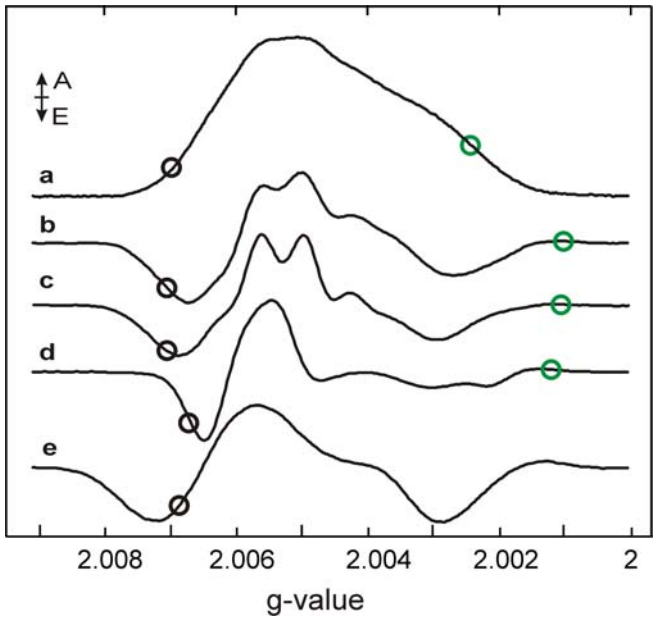

Figure 5.3: Pulse Q-band EPR spectra of stationary $A_1^{\bullet-}$ and $P_{700}^{\bullet+}A_1^{\bullet-}$ RP in PS I from *T. elongatus* and *Synechocystis menB* mutant at 80 K.
a Stationary $A_1^{\bullet-}$ in *T. elongatus* PS I (absorptive EPR).
b RP in *T. elongatus* PS I.
c RP in *menB* mutant PS I with VK_3-h_8 in the A_1 binding site.
d RP in *menB* mutant PS I with VK_3-d_8 in the A_1 binding site.
e RP in *menB* mutant PS I with PQ_9 in the A_1 binding site (as isolated).
The black circles represent the spectral positions where the ENDOR spectra presented in **Figure 5.5** were recorded, the green circles represent the spectral positions where the ENDOR spectra presented in **Figure 5.6** were recorded. E = emission and A = absorption.

Comparison of ENDOR spectra of $A_1^{\bullet-}$ in PS I from different species

The PS I complexes used are isolated from two different cyanobacterial organisms, the thermophilic *T. elongatus* and the mesophilic *Synechocystis* sp. PCC 6803. It is vital for a sound comparison of the ENDOR spectra to know if differences in the spectra are due to the different quinones VK_1 and VK_3 in the A_1 binding sites or due to the different binding sites in the two species. Two selected ENDOR spectra of stationary $A_1^{\bullet-}$ in PS I from wild type *Synechocystis* sp. PCC 6803 and the respective ENDOR spectra of PS I from *T. elongatus* are shown in Figure 5.4. They were found to be identical. This demonstrates the high degree of conservation in the A_1 binding site in both organisms and shows that differences between $VK_1^{\bullet-}$ and $VK_3^{\bullet-}$ are solely responsible for differences in the ENDOR spectra of $A_1^{\bullet-}$.

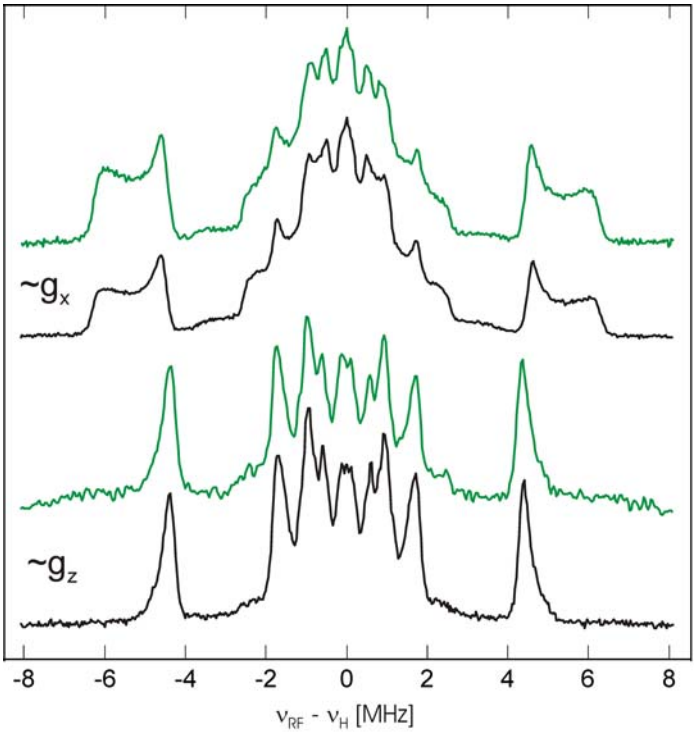

Figure 5.4: Comparison of two selected pulse Q-band ^{1}H ENDOR spectra of stationary $A_1^{\bullet-}$ in *T. elongatus* PS I (black spectra) and *Synechocystis* sp. PCC 6803 (green spectra) at 80 K. The spectra are recorded close to two canonical orientations.

Properties of the orientation selected ENDOR spectra

The X-band ^{1}H ENDOR spectra of $A_1^{\bullet-}$ consist of overlapping powder patterns of non equivalent nuclei, see refs. [12;31;41;42]. To determine the angles of the hf tensors with respect to the *g*-tensor axes and to increase the spectral resolution, molecules that have different orientations with respect to the magnetic field have to be excited. For a complete orientation selection all principal components of the *g*-tensor must be resolved. In the Q-band EPR spectrum of the stationary radical $A_1^{\bullet-}$ (Figure 5.3, spectrum **a**), the g_x and g_y components are not completely resolved, while the g_z component is well separated from the other *g*-tensor components (see Table 5.1 for the *g*-values). This means, that in the ENDOR spectra recorded close to g_z spectral position (high field edge), single crystal-like ENDOR spectra are obtained. ENDOR spectra recorded at the low field edge (close to g_x) will be close to single crystal-like, but still contain also signals from molecules with their x-axis (parallel to the C-O bond) slightly tilted with respect to the static magnetic field. In intermediate field positions the ENDOR spectra show powder patterns.

As mentioned above, the RP EPR spectra can be described as a superposition of emissive (E) and absorptive (A) spectra of $A_1^{\bullet-}$ and $P_{700}^{\bullet+}$. This results in a severe overlap from emissive and absorptive ENDOR signals from $A_1^{\bullet-}$ and $P_{700}^{\bullet+}$ (essentially an overlap of four ENDOR spectra). Furthermore, due to the coupling of the two electron spins (mixture of the singlet and triplet states) additional ENDOR signals may appear, which are not present in isolated radicals.[29] The polarization of the two main ENDOR lines of a nucleus can be different (*e.g.* low frequency ENDOR transition absorptive, high frequency ENDOR transition emissive), and depend on the sign of the hfcc.[29] This results in very congested ENDOR spectra, which are hard to analyze. However, as it can be seen from the simulation in Figure 5.2, the low field edge of the EPR spectrum contains a significant contribution only of the $A_1^{\bullet-}$ signal. It was observed here and in ref. [35], that the ENDOR spectra recorded at this spectral position i) show only

ENDOR lines from $A_1^{\bullet-}$, and ii) both ENDOR lines of a nucleus have the same polarization (emissive). At the high field edge, the situation is worse, since the g_z-values of $P_{700}^{\bullet+}$ and $A_1^{\bullet-}$ are close to each other. However, since this is a single-crystal like orientation for $A_1^{\bullet-}$, a basic analysis of the ENDOR spectra can be performed. At intermediate field position the ENDOR spectra are so congested due to the overlapping powder patterns (data not shown), that only the hfccs of the spectrally well separated methyl group protons could be determined.

Therefore, in the following the ENDOR spectra recorded at the low field edge and at the high field edge are compared and discussed. These field positions correspond to g_x and g_z spectral positions of $A_1^{\bullet-}$ (subsequently – unless displayed differently – g-values and orientations with respect to the g-tensor refer to $A_1^{\bullet-}$ (not to $P_{700}^{\bullet+}$).

At this point, an important issue concerning the determination of hfccs from ENDOR spectra has to be mentioned. There is a difference between the hfccs directly read from the spectra and the correct values obtained by simulation of the spectra. In the first case one observes the projections of hf tensors. Since there is no indication for different orientations of the hf tensors in the RP and in stationary $A_1^{\bullet-}$ (photoaccumulated samples), and for the simplicity of the comparison, only the hfccs obtained by simulation are provided. The projection values are only given when i) the ENDOR could not be simulated and ii) the results obtained here are compared with results from previous studies, where the hfccs were not obtained by simulation. The simulations of the RP ENDOR spectra were done with the same program as used for the stationary radical, since no simulation program for RP ENDOR spectra was available. This might lead to a larger error in the determination of the hfccs.

ENDOR at the low field edge

As mentioned above, the low field wing of RP EPR spectra constitutes exclusively of the emissive spectrum of $A_1^{\bullet-}$. Consequently, ENDOR spectra of the RP and stationary $A_1^{\bullet-}$ recorded at this position (close to g_x orientation of the $A_1^{\bullet-}$ *g*-tensor) are similar, but the ENDOR spectra of the RP are emissive. In Figure 5.5 the ENDOR spectra of $A_1^{\bullet-}$ (spectrum **a**) and the RP (spectrum **b**) in *T. elongatus* PS I, and the RP in *menB* mutant PS I with VK_3-h_8 (spectrum **c**), VK_3-d_8 (spectrum **d**) and PQ_9 (spectrum **e**) in the A_1 binding site, recorded at this orientation are presented. Note, that all ENDOR lines of the RP are emissive and are only for comparison presented like absorptive ENDOR spectra. Only spectrum **e** exhibits some absorptive lines. This spectrum was measured not at the low field edge, but at a spectral orientation close to the one where spectrum **d** was recorded (see Figure 5.3, spectrum **e** for spectral position). This was done to facilitate a comparison of spectra **d** and **e** with the intention to identify possible ENDOR lines of PQ_9 in spectrum **d**. A serious presence of PQ_9 in the two samples of *menB* PS I substituted with VK_3 was already excluded above on the basis of the analysis of the transient EPR spectra. However, even a minor contribution (< 5%) of PQ_9 might disturb the ENDOR spectra of *menB* PS I substituted with VK_3-d_8.

It is important to consider, which signals can be expected in the ENDOR spectra of the corresponding samples. In the ENDOR spectra of stationary $A_1^{\bullet-}$ (spectrum **a**) and the RP (spectrum **b**) in *T. elongatus* PS I signals from protons of VK_1 and the protein environment (including the H-bond proton) will be present. Differences between the two spectra must be due to the slightly different orientation selection (see Figure 5.3) and different binding of the negatively charged quinone in the two samples. In the RP ENDOR spectrum of *menB* mutant PS I with VK_3-h_8, signals from the protons of VK_3 and the protein environment (including the H-bond proton) will be present. The orientation selection is similar to the one in spectrum **b**. Differences between the spectra **b** and **c** are due to the presence of the α-proton at position 3 in

the quinone ring and the absence of the methylene protons of the phytyl tail of VK_1 (Figure 5.1). Further differences could be due to the slightly hf tensors of $VK_1^{\bullet-}$ and $VK_3^{\bullet-}$ (see chapter 4). In the *menB* sample substituted with VK_3-d_8 (spectrum **d**) only signals from protons of the protein are expected in the ^{1}H ENDOR spectrum. Specifically, signals from the backbone proton of the leucine residue H-bonded to the quinone are assumed to be most prominent (although signals of low intensity of not fully deuterated VK_3 or not-exchanged PQ_9 might be present).

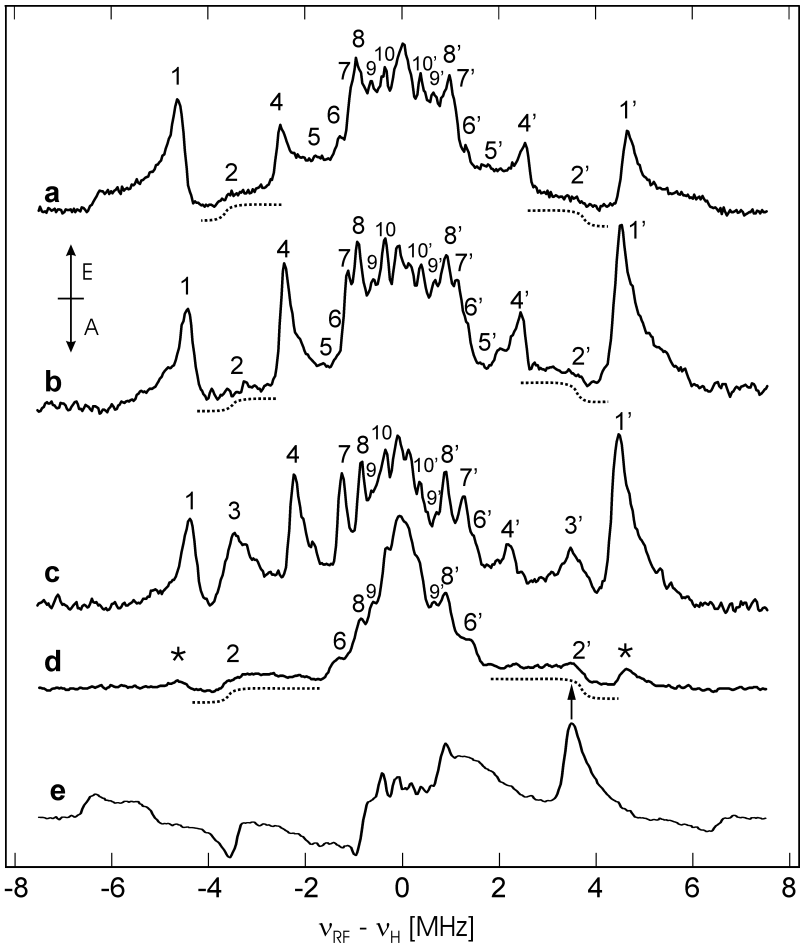

Figure 5.5: Pulse Q-band ^{1}H ENDOR spectra recorded at the low field edge of the EPR spectrum of $A_1^{\bullet-}$ and the RP in PS I from *T. elongatus* and the *menB* mutant. See **Figure 5.3** for exact spectral positions.
a Stationary $A_1^{\bullet-}$ in *T. elongatus* PS I (absorptive ENDOR).
b RP in *T. elongatus* PS I.
c RP in *menB* mutant PS I with VK_3-h_8 in the A_1 binding site.
d RP in *menB* mutant PS I with VK_3-d_8 in the A_1 binding site.
e RP in *menB* mutant PS I with PQ_9 in the A_1 binding site (as isolated).
The largest component of the H-bond proton signal ($A_{||}$) is underlined for better visualization. The signal of the impurity from non-deuterated VK_3 is marked with an asterisk (spectrum **d**). The signal of the impurity of PQ_9 is marked with an arrow. E = emission and A = absorption.

The spectra **a** to **c**, with protonated VK_1/VK_3 in the A_1 binding pocket, show a number of narrow lines (spectrum **a** exhibits a slightly different orientation selection). This indicates that in all cases a well-defined binding of the quinone to the protein is provided and that no heterogeneity is present. Some of these lines can be assigned straightforwardly. In the following section only the assignment of these lines will discussed, while the assignment of the other signals is described later.

The spectrum of $A_1^{\bullet-}$ from *T. elongatus* PS I shows a intense line pair 1/1' with a large hfcc of 9.1 MHz (Figure 5.5, spectrum **a**). In the RP ENDOR spectra this line pair has a hfcc of 8.8 MHz (spectrum **b**). A virtually identical hfcc of 8.7 MHz was determined for the RP in *menB* substituted with VK_3-h_8 (spectrum **c**). This line pair was previously attributed to the methyl group in position 2 of the quinone ring, see *e.g.* refs. [11;12;31;32] In complete agreement with these studies, this line pair is assigned to the methyl group at position 2. Traces of line pair 1/1' are visible in the spectrum of the PS I sample substituted with VK_3-d_8 (spectrum **d**, marked with the asterisk), which indicates that a small impurity of non-protonated quinone is present. Scaling the VK_3-d_8 and VK_3-h_8 spectra according to their matrix signal(s) the intensity of this signal can be estimated to be about 2-3%. This agrees with the degree of deuteration of the methyl group (see chapter 3). The ENDOR lines of $PQ_9^{\bullet-}$ (Figure 5.5, spectrum **e**) are hardly visible in spectrum **d**. Only a shoulder at line 2' in spectrum **d**, marked with arrow, is visible, thus its contribution to the ENDOR spectrum of *menB* PS I substituted with VK_3-d_8 is assumed to be even smaller than the 2-3% of not fully deuterated VK_3.

In the ENDOR spectra from *T. elongatus* PS I (spectrum **a** and **b**) and *menB* PS I substituted with VK_3-d_8 (spectrum **d**) a broad signal with a hfcc of 7.4 MHz is observed (line pair 2/2', shoulders are underlined with dashed lines for better visualization). In the ENDOR spectrum of *menB* PS I substituted with VK_3-h_8 (spectrum **c**) this line pair is not visible due to

strong overlap with another, more intense line pair (3/3'). The same signal was also observed by Teutloff *et al.* for $A_1^{\bullet-}$ in *T. elongatus* PS I, but not assigned.[12] A similar signal was observed by Pushkar *et al*. in the stationary $A_1^{\bullet-}$ in *menB* PS I substituted with VK_3-d_8, and assigned to the $A_{\|}$ component of the H-bond proton.[20] This line pair is assigned to the H-bond proton ($A_{\|}$ component). A detailed explanation and discussion of the assignment of this hfcc will be given later (see below).

The intense line pair 3/3' (hfcc of 7.2 MHz) is visible only in the sample substituted with VK_3-h_8 (spectrum **c**). Considering the similar methyl group hfccs in spectra **b** and **c**, and the overall similarity of the ENDOR spectra, there is no indication for a significantly different spin distribution in $VK_3^{\bullet-}$ as compared to $VK_1^{\bullet-}$. This leads to the conclusion that line pair 3/3' must arise from a non-protein proton existing in VK_3, and not in VK_1. The only candidate is the α-proton in position 3 of the quinone ring (Figure 5.1B). Thus, this hfcc is assigned to this proton.

The intense line pair 4/4' is observed in the RP and stationary $A_1^{\bullet-}$ ENDOR spectra of *T. elongatus* PS I (hfccs of 5.0 MHz and 5.2 MHz, respectively), and in the ENDOR spectra of *menB* PS I substituted with VK_3-h_8 (hfcc of 4.6 MHz). However, it is not visible in the spectrum of *menB* PS I substituted with VK_3-d_8 substituted (spectrum **d**), therefore it must arise from a α-proton belonging to the second (benzene) ring.

The analysis and assignment of the inner ENDOR lines is less straightforward and will be done later in the section about the spectral simulations.

ENDOR at the high field edge

It was mentioned above, that at this spectral position (close to g_z orientation of the $A_1^{\bullet-}$ *g*-tensor) single-crystal like ENDOR spectra can be obtained for the stationary radical anion $A_1^{\bullet-}$. However, in the RP EPR spectra a strong overlap of the $A_1^{\bullet-}$ and $P_{700}^{\bullet+}$ signals is present

(see Figure 5.2). Therefore, the ENDOR spectra recorded at this spectral position exhibit an overlap of the ENDOR signals from both radicals. Since the *g*-tensor of $P_{700}^{\bullet+}$ is not resolved at Q-band, power-type ENDOR signals are expected from this radical. Figure 5.6 presents the ENDOR spectra of the stationary radical anion $A_1^{\bullet-}$ and the RP in *T. elongatus* PS I (spectrum **a** and **b**, respectively), the *menB* mutant PS I substituted with VK_3-h_8 (spectrum **c**) and VK_3-d_8 (spectrum **d**) recorded at the high field edge of the EPR spectra. For a comparison the ENDOR

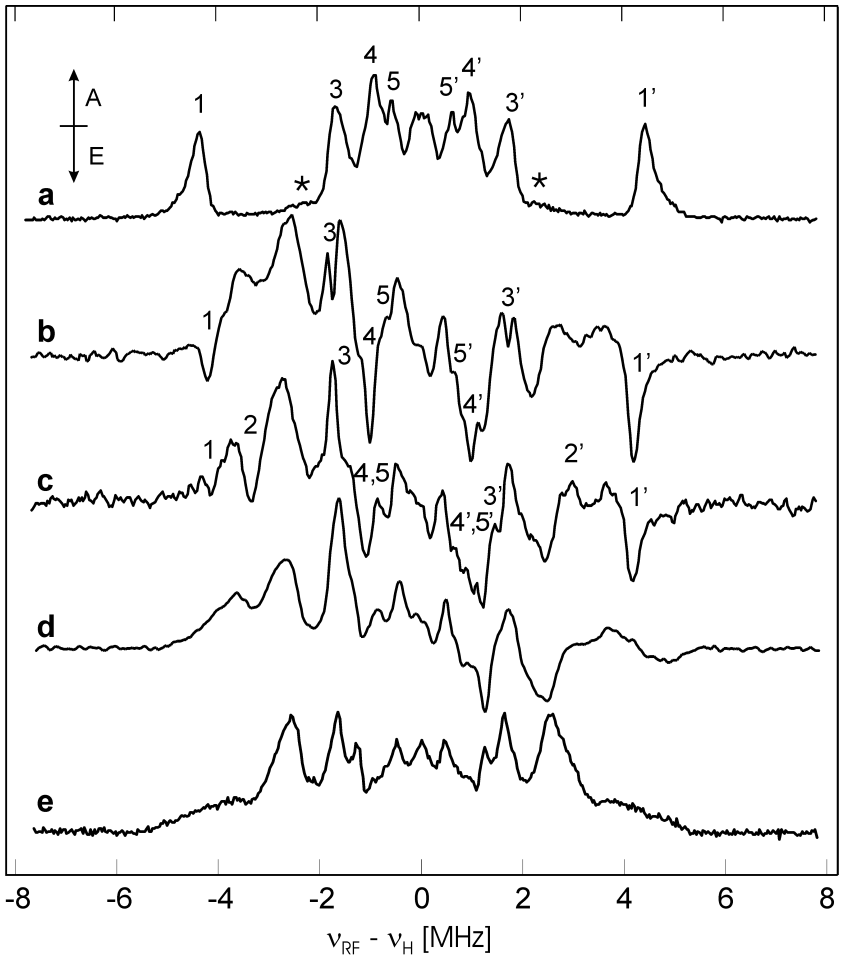

Figure 5.6: Pulse Q-band ^{1}H ENDOR spectra recorded at the high field edge of the EPR spectrum of $A_1^{\bullet-}$ and the RP in PS I from *T. elongatus* and the *menB* mutant (close to g_z orientation of $A_1^{\bullet-}$). See **Figure 5.3** for exact spectral positions.

a Stationary $A_1^{\bullet-}$ in *T. elongatus* PS I (absorptive ENDOR).

b RP in *T. elongatus* PS I.

c RP in *menB* mutant PS I with VK_3-h_8.

d RP in *menB* mutant PS I with VK_3-d_8.

e Stationary $P_{700}^{\bullet+}$ (t_{DAF} = 20 ms) in *menB* mutant PS I with VK_3-d_8 (absorptive ENDOR). The signal of the impurity $A_0^{\bullet-}$ is marked with an asterisk (spectrum **a**). E = emission and A = absorption.

spectrum of the stationary radical $P_{700}^{\bullet+}$ is presented in spectrum **e** (recorded with a t_{DAF} of 20 ms on *menB* mutant PS I substituted with VK_3-d_8). One can see that there is a strong similarity between RP and stationary ENDOR signals of $P_{700}^{\bullet+}$. In fact, $P_{700}^{\bullet+}$ has a larger contribution to the ENDOR spectra than $A_1^{\bullet-}$ at this spectral position. Due to the complex overlap of signals from emissive and absorptive ENDOR lines the contribution of $P_{700}^{\bullet+}$ can not be straightforwardly subtracted from the radical pair spectrum using the stationary $P_{700}^{\bullet+}$ ENDOR signal as a reference (compare spectra **d** and **e**). Hence, the analysis of the RP ENDOR spectra of $A_1^{\bullet-}$ at this field positions is rather complicated.

Careful examination of the RP spectra – in comparison to the ENDOR spectra of stationary $A_1^{\bullet-}$– shows that the $A_1^{\bullet-}$ signals are mostly emissive, in agreement with previous X-band studies.[9;12;29] All quinone proton ENDOR line pairs observed in the spectra show a characteristic asymmetry in their intensity due to the overlap of emissive and absorptive lines. $A_1^{\bullet-}$ ENDOR lines associated with positive hfccs (*e.g.* of the methyl group, line pair 1/1') exhibit a more intense high frequency component, while lines with negative hfccs (*e.g.* line pair 3/3') show the opposite behavior.

The spectrum of $A_1^{\bullet-}$ from *T. elongatus* shows a intense line pair 1/1' with a large hfcc of 8.6 MHz (Figure 5.5, spectrum **a**). In the RP ENDOR spectra this line pair has a hfcc of 8.3 MHz (spectrum **b**). A similar hfcc of 8.2 MHz was determined for the RP in *menB* PS I substituted with VK_3-h_8 (spectrum **c**). In the spectrum of the RP in *menB* PS I substituted with VK_3-d_8 (spectrum **d**) this line pair is not observed. In agreement with previous studies,[11;12;31;32] this line pair is assigned to the methyl group at position 2.

The weak and broad signal with a hfcc of about 4.8 MHz (marked with asterisk in spectrum **a**) belongs to a very small amount of $A_0^{\bullet-}$ present in the sample (see discussion below). Only in spectrum **c** the line pair 2,2' is observed (hfcc of 6.7 MHz). In the other spectra, no line pair

with similar hfcc and intensities is found. The magnitude of the hfcc is in the range which is expected for a strongly coupled α-proton with A_x = 7.2 MHz (see chapter 4). Line 2 is quite pronounced, while line 2' is hardly visible. This intensity ratio of the lines 2 and 2' is in agreement with a negative hfcc sign of a A_1 proton. Hence, the line pair is assigned to the α-proton at position 3 in VK_3 (Figure 5.1 B).

Exchange of the H-bond proton against deuterium (H/D exchange)

A direct approach to investigate exclusively the H-bonding to $A_1^{\bullet-}$ is the exchange of the H-bond proton against deuterium. As mentioned above, previous attempts to perform H/D exchange using PS I from *T. elongatus* were not successful.[9;12] In this work, PS I from the *menB* mutant was used for the exchange experiment. PQ_9 was replaced with VK_3-h_8 in a 99% D_2O buffer. The 'opening' of the A_1 binding site to allow exchange of the quinone could facilitate the exchange of the H-bond proton. In case of a successful exchange the ^1H ENDOR lines of the H-bond should disappear and the corresponding ^2H ENDOR lines will become visible in the ^2H ENDOR spectrum. This experiment was attempted. After the exchange experiment, the ^1H ENDOR spectrum showed the characteristic lines of VK_3-h_8, indicating a successful exchange of PQ_9 against VK_3-h_8. No differences were observed in the ^1H ENDOR spectra as compared to the ENDOR spectra of those samples where the quinone exchange was done in protonated buffer (identical to the spectra in Figure 5.5, spectrum **c** and Figure 5.6, spectrum **c**). No ^2H ENDOR signals were detected by Mims-type ENDOR spectroscopy (data not shown). ^2H Davies ENDOR experiments were not performed, since they are less efficient than Mims ENDOR experiments to detect the 'hydrogen bonded' deuterons when investigating the quinone model system *in vitro* (chapter 4). Thus, it has to be concluded that no H/D exchange occurred in the binding pocket despite the successful quinone exchange.

ENDOR on the chlorophyll radical anion $A_0^{\bullet-}$

As described in chapter 3, the stationary radical anion $A_1^{\bullet-}$ is generated by the photoaccumulation procedure. The PS I complexes are treated with sodium dithionite (a reducing agent), incubated for 30 minutes at 4°C in the dark, and subsequently frozen. This treatment leads to reduction of the FeS-clusters, but not of A_1, since the redox potential of A_1 is lower than the one of dithionite. The illumination of the frozen sample results in charge separation; in the charge separated state, the radical cation $P_{700}^{\bullet+}$ can be reduced by the reductant, if the temperature is not too low (≥ 200 K). This leads to the generation of a stable radical anion $A_1^{\bullet-}$. To obtain a sufficient amount of $A_1^{\bullet-}$ in the sample, the illumination takes several minutes. The charge separation in PS I complexes, where already a stable radical anion $A_1^{\bullet-}$ is present, can lead to the generation of the Chl radical anion $A_0^{\bullet-}$, which is located before A_1 in the electron transfer chain.[43;44] Hence, it is vital for a thorough analysis of ENDOR spectra of stationary $A_1^{\bullet-}$, to i) identify ENDOR lines that belong to the Chl radical anion $A_0^{\bullet-}$, and ii) to minimize the amount of $A_0^{\bullet-}$ in the $A_1^{\bullet-}$ samples.

There are previous ENDOR studies on $A_0^{\bullet-}$, which found that some hfccs of $A_0^{\bullet-}$ are larger than any of the hfccs of $A_1^{\bullet-}$.[45-48] These lines can therefore be considered as a marker for $A_0^{\bullet-}$. A variety of ENDOR lines arising from protons with smaller hfcc, which overlap with the ENDOR lines of $A_1^{\bullet-}$, has been reported.[45-48] The CW ENDOR method, which was used in these studies, may lead to different lineshapes and intensities as compared to the pulse Q-band ENDOR spectroscopy used in this work. Hence, it was necessary to perform ENDOR measurements on $A_0^{\bullet-}$ under the same experimental conditions which were used for the ENDOR experiments on $A_1^{\bullet-}$.

ENDOR spectra were recorded on two samples of *T. elongatus* PS I with different photoaccumulation conditions. The first sample is the one on which the EPR and ENDOR

spectra presented above were recorded (illuminated 5 minutes at 200 K, then 10 minutes at 240 K with the standard setup).

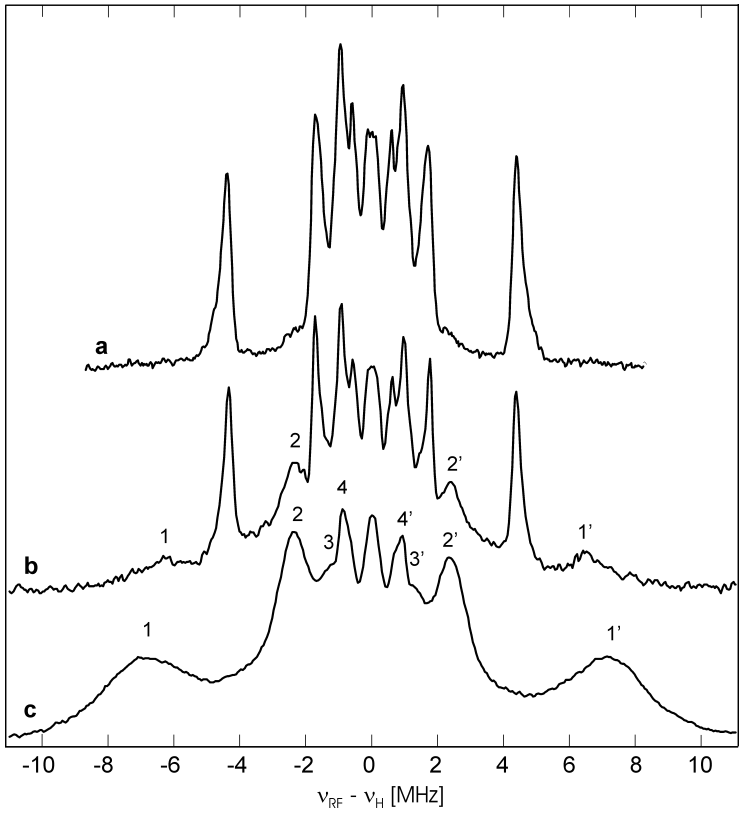

Figure 5.7: Comparison of pulse Q-band ^{1}H ENDOR spectra recorded on different PS I samples at 80 K.
a $A_1^{\bullet-}$ in *T. elongatus* PS I (recorded close to g_z spectral orientation).
b $A_1^{\bullet-}$ /$A_0^{\bullet-}$ mixture in *T. elongatus* PS I (recorded close to g_z spectral orientation).
c $A_0^{\bullet-}$ in *Synechocystis* sp. PCC 6803 PS I, VK_1 extracted (recorded on center of the $A_0^{\bullet-}$ EPR spectrum).

The ENDOR spectrum recorded close to the g_z spectral position is shown in Figure 5.7, spectrum **a**. The second sample was chemically treated identically but illuminated without glass filters (higher light intensity) at 240 K for 20 minutes (Figure 5.7, spectrum **b** for ENDOR spectrum recorded at the same spectral position). Under these conditions an additional accumulation of $A_0^{\bullet-}$ is likely.[43;44] A PS I sample from *Synechocystis* sp. PCC 6803 whose VK_1 molecules were extracted by treatment with orgnanic solvents, was treated chemically identically as the samples from *T. elongatus* PS I and illuminated 20 minutes at 240 K without glass filters. Spectrum **c** presents the ENDOR spectrum of this sample. This spectrum should represent a ENDOR spectrum of pure $A_0^{\bullet-}$. It exhibits four line pairs. Line pair 1/1' is very

broad, with hfccs of about 14 MHz, and two more narrow and intense line pairs (2/2' and 4/4') from hfccs about 4.8 - 4.9 MHz and 2.2 MHz are observed. The amplitude ratios of line pairs 2/2' and 4/4' to line pair 1/1' are approximately 3:1. Line pair 3/3' shows only low intensity.

Line pair 1/1' is also detected in spectrum **b**, but with slightly smaller hfccs, whereas it hardly can be seen in spectrum **a**. The different hfccs could be either due to the harsh treatment with organic solvent to extract VK_1 from the PS I complexes or due to species differences in the A_0 binding site of PS I. The line pair 2/2' is clearly visible in spectrum **b**, and to a small amount also in spectrum **a**. The line pairs 3/3' and 4/4' are not visible in spectrum **b**, due to the severe overlap with the more intense ENDOR signals from $A_1^{\bullet-}$. From this it can be concluded, that

i) $A_0^{\bullet-}$ contamination in *T. elongatus* PS I manifests itself with a broad line pair with hfccs of about 13 MHz, and at least one more narrow and intense line pair (2/2') with hfccs about 4.8 MHz, and

ii) the $A_1^{\bullet-}$ sample from *T. elongatus* PS I used in this work contains a negligible amount of $A_0^{\bullet-}$.

The attempts to prepare pure $A_1^{\bullet-}$ samples from *menB* PS I substituted with VK_3-h_8 and VK_3-d_8 were not successful. A severe contribution of $A_0^{\bullet-}$ was always observed (data not shown). In fact, even photoaccumulated samples of PS I isolated from *Synechocystis* sp. PCC 6803 wild type also contained a small amount of $A_0^{\bullet-}$ (Figure 5.4). Only from PS I isolated from *T. elongatus*, $A_1^{\bullet-}$ samples could be prepared with a negligible amount of $A_0^{\bullet-}$. This apparent problem with quinone substituted samples could only be circumvented by use of RP samples. In several previous ENDOR studies of stationary (photoaccumulated) $A_1^{\bullet-}$, low intensity signals with hfccs of about 12-14 MHz and 4.8 MHz were assigned to the H-bond proton in

$A_1^{\bullet-}$.[9;12;20;31;41;42;49] In view of the findings presented here, these assignments have to be critically re-considered. This is discussed in the section about the H-bond.

Determination of the signs of hyperfine coupling constants

The signs of hfccs are an essential information about the spin system. Especially important is the sign of the isotropic coupling (a_{iso}), which depends on the mechanism of the hf interaction. For α-protons in π-radicals, which are coupled by the exchange mechanism (π-σ spin polarization), a negative sign of A_{iso} is typically found, while a positive sign is an indication of the hyperconjugation mechanism and characteristic for β–protons as found in methyl or methylene groups. Hence, the sign of the hfcc does not only contain important information for an in-depth analysis of the ENDOR spectra, it gives important structural information.

Variable mixing time (VMT) ENDOR measurements on the RP

To determine the hfccs of the two radicals constituting a radical pair, the TRIPLE experiment can be performed. But it was found in this work, that the efficiency of the TRIPLE experiment was too low to determine the signs of the hfcc in the RP $P_{700}^{\bullet+}A_1^{\bullet-}$. Another method to determine the sign of hfccs was found by Fursman *et al.*[29] Unfortunately, this methods works only for very particular cases. At those spectral positions where this is possible, the ENDOR spectra are severely congested due to the overlap of emissive and absorptive ENDOR lines. Only for spectrally well separated lines (here only the methyl group protons of $A_1^{\bullet-}$ fulfill this condition), the determination of the hfccs is possible. A method which can be used at spectral position where only $A_1^{\bullet-}$ is observed with a good orientation selection, is of larger importance. At the low field wing ENDOR spectra close to single crystal-like are observed (Figure 5.5). Therefore, a different method which is called **v**ariable **m**ixing **t**ime (VMT) ENDOR was

invented and used to determine the hfcc sign at such spectral positions.[35] This method is based on the strong non-Boltzmann population of the electronic levels in the spin-correlated RP and the different life times of the electronic levels. Directly after charge separation only the electronic states that carry some singlet character are populated.[16;17] These levels decay faster than the electronic states with have only triplet character.[50;51] This relaxation based method is described in detail in ref. [35]. In a VMT ENDOR experiment (in the following paragraphs called VMT experiment), the detection part of the Davies ENDOR sequence is shifted away from the RF pulse (Figure 5.8) by a time t_{mix}, which is in the order of the decay of the fast decaying RP states (some tens of μs). As a result ENDOR transitions of a nucleus in the fast decaying electronic state become less intense as compared to ENDOR transitions in the slow relaxing electronic state. At Q-band and in case of the RP $P_{700}^{\bullet+}A_1^{\bullet-}$, this approximation is only valid for the low field edge. This means for a proton ($g_N > 0$) in the weak hyperfine coupling limit ($|A/2| < \nu_H$): i) the ENDOR spectrum is symmetric around ν_H, and ii) all ENDOR lines exhibit the same polarization (emissive). In a VMT experiment the low frequency ENDOR transition of a proton with a positive hfcc will be more diminished in amplitude than the high frequency ENDOR transition. For a proton with a negative hfcc the ENDOR amplitude will behave in the opposite fashion. A RP VMT ENDOR experiment on *T. elongatus* PS I is shown in Figure 5.8 (sequences are shown in the insert). The magnetic field was set at the low field edge of the emissive transition (same spectral position as in Figure 5.5). At this spectral position mainly one EPR transition, corresponding to the flip of the electron spin of $A_1^{\bullet-}$, is excited. t_{DAF} is the **d**elay **a**fter Laser **f**lash to the begin of the sequence, while t_{DD} refers to the **d**elay after the Laser flash to the beginning of the **d**etection sequence.[35] Spectrum **a** shows a 'standard' Davies ENDOR spectrum obtained with a delay of 3 μs between the end of the RF pulse and the detection

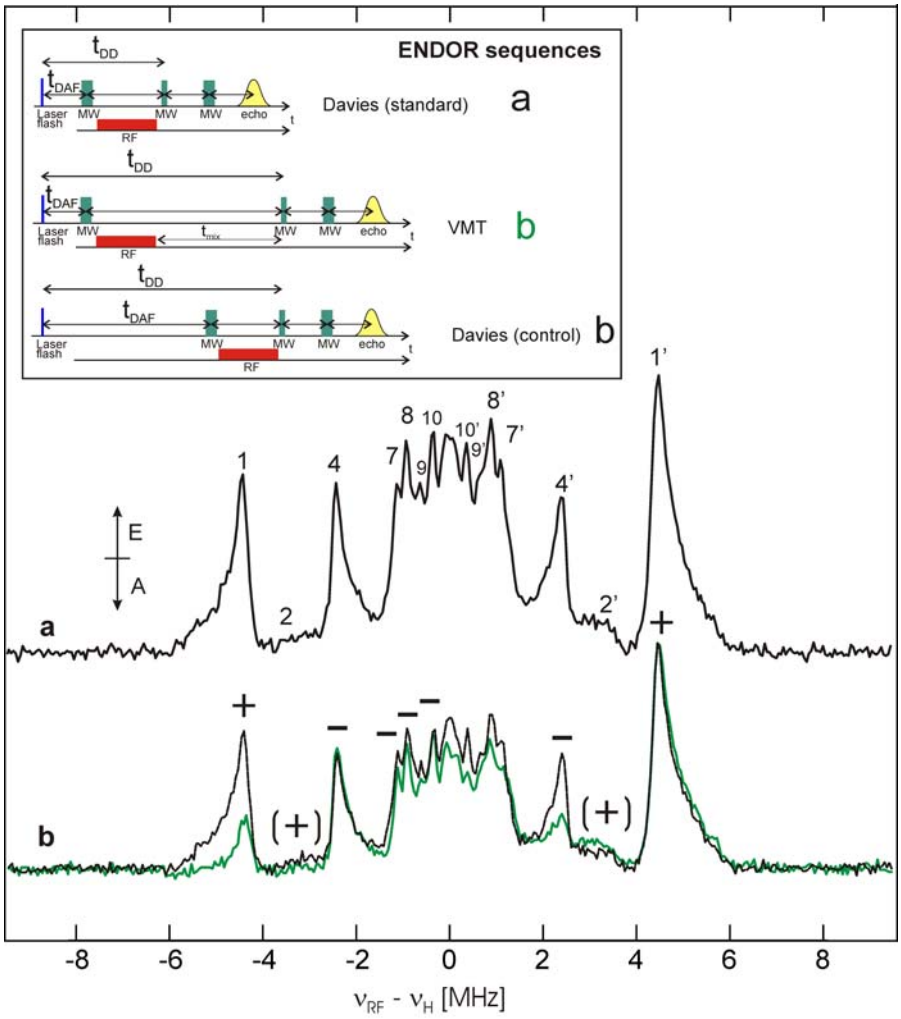

Figure 5.8: Variable **m**ixing **t**ime (VMT) pulse Q-band ^{1}H ENDOR spectra recorded at the low field edge on the RP in *T. elongatus* PS I at 80 K (same spectral position as in **Figure 5.5**). t_{DAF} = **d**elay **a**fter Laser **f**lash, t_{DD} = **d**elay after the Laser Flash to the beginning of the **d**etection sequence, t_{mix} = time after the end of the RF pulse to the beginning of the detection sequence.
a Standard Davies ENDOR spectrum recorded with t_{DAF} = 1 µs and a delay of 3 µs between the end of the RF pulse and the detection sequence (t_{DD} = 14 µs).
b **Green spectrum:** VMT ENDOR spectrum recorded with t_{DAF} = 1 µs and a delay of 43 µs (t_{mix}) between the end of the RF pulse and detection sequence (t_{DD} = 54 µs).
Black spectrum: Davies ENDOR spectrum recorded with 41 µs DAF and a delay of 3 µs between the end of the RF pulse and detection sequence (t_{DD} = 54 µs).
The numbering of the lines is the same as in spectrum **a** of **Figure 5.5**. The signs of the hfccs of selected lines are given on spectrum **b**. The insert shows schematically the three sequences used to obtain the spectra. For details, see chapter 2 and ref. [35]. E = emission, A = absorption.

sequence (t_{DAF} = 1 µs, t_{DD} = 14 µs). The black spectrum **b** (control) was recorded with the same sequence as in spectrum **a**, but t_{DAF} is increased from 1µs to 41 µs (t_{DAF} = 41 µs, t_{DD} = 54 µs). In case of the green spectrum **b** the 3 µs delay is increased to 43 µs (t_{DAF} = 1 µs, t_{DD} = 54 µs). All other parameters like MW and RF pulses were kept identical for all measurements.

The spectra **a** and **b** show essentially the same spectrum. The hfccs in the ENDOR spectra are independent of t_{DD} (this was found for all PS I samples investigated here). This shows, that possible spin redistribution processes (*e.g.* due to reorientation of the charged cofactor as compared with its neutral state) in the RP as discussed for the RP in bacterial photosynthetic RCs [52] do not occur in PS I at 80 K. This may be due to different timescales accessible: in bRC the RP can be monitored up to several ms, while in PS I the spin polarization decays nearly completely within a few hundred μs at 80 K. The A_1 binding site in PS I may also be more 'rigid' than the Q_A binding site in bacterial photosynthetic RCs.

A kinetic model to explain quantitatively the observed behavior was developed with the help of further VMT ENDOR experiments and additional experiments like inversion recovery (data not shown). A more thorough methodological discussion can be found in ref. [35].

Spectrum **b** shows marked intensity changes. Line pair 1/1' shows the VMT induced asymmetry characteristic for protons with positive hfcc (less intense low-frequency line). In case of line pair 2/2' only a weak effect is observed. This may be due to different relaxation times. The opposite behavior as for the line pair 1/1' is found for the line pair 4/4', which indicates a negative sign. This corroborates the assignment of this hfcc to an α-proton of the benzene ring. The inner lines show less pronounced effects. The overlap with signals from protons with different signs of hfcc probably causes this problem. However, a careful analysis reveals that the hfccs of the protons associated with the (narrow) signals 7/7', 8/8' and 10/10' have negative signs. A closer inspection of spectrum **a** shows already here some intensity asymmetry for signals originating from hfccs with different signs. It can be concluded that the relatively long time of the RF pulse (9 μs) already induces a VMT-type intensity asymmetry in the 'normal' ENDOR spectrum. This is even more prominent for the all other ENDOR spectra which were recorded with longer (17 μs) RF pulses (Figure 5.5).

VMT ENDOR experiments were also performed on the low field edge of the RP of *menB* PS I substituted with VK_3-h_8 and VK_3-d_8 as well (Figure 5.9 and Figure 5.10).

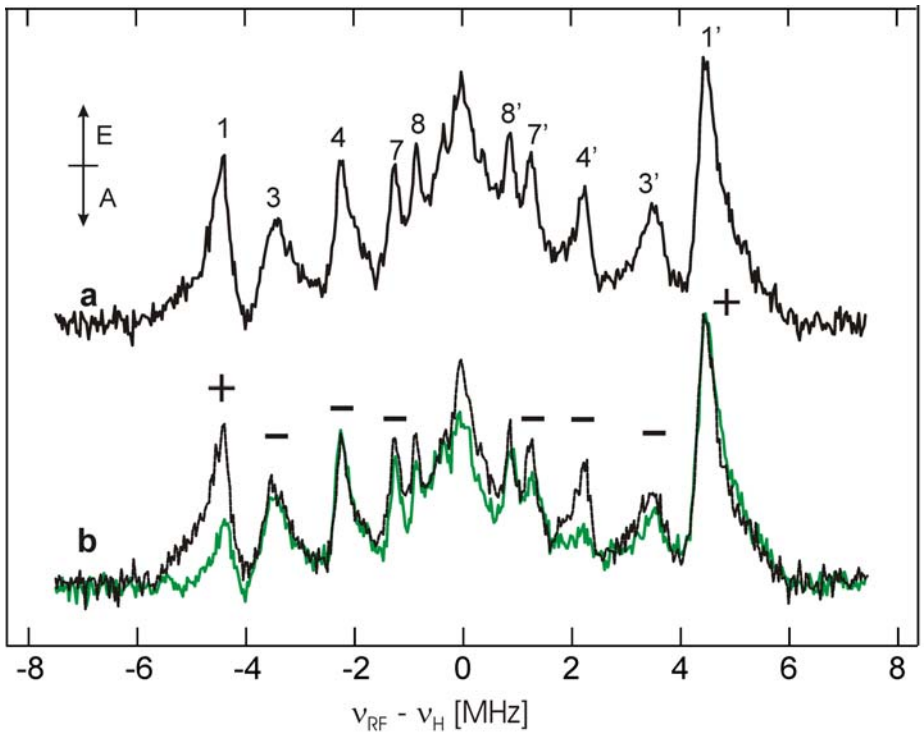

Figure 5.9: Variable **m**ixing **t**ime (VMT) pulse Q-band ^{1}H ENDOR spectra recorded at the low field edge (close to g_x spectral orientation) on the RP in *menB* mutant PS I substituted with VK_3-h_8 (80 K).
a Standard Davies ENDOR spectrum recorded with t_{DAF} = 1 µs and a delay of 3 µs between the end of the RF pulse and the detection sequence (t_{DD} = 14 µs).
b **Green spectrum:** VMT ENDOR spectrum recorded with t_{DAF} = 1 µs and a delay of 43 µs (t_{mix}) between the end of the RF pulse and detection sequence (t_{DD} = 54 µs).
Black spectrum: Davies ENDOR spectrum recorded with 41 µs DAF and a delay of 3 µs between the end of the RF pulse and detection sequence (t_{DD} = 54 µs).
The numbering of the lines is the same as in spectrum **c** of **Figure 5.5**. The signs of hfccs of selected lines are given on spectrum **b**.

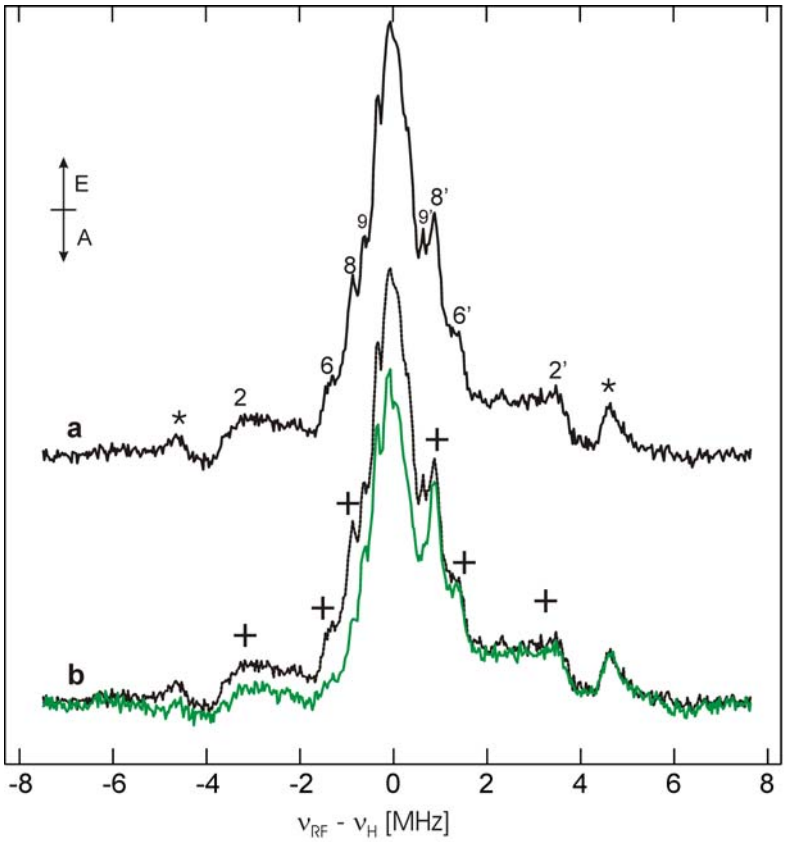

Figure 5.10: Variable **m**ixing **t**ime (VMT) pulse ^{1}H ENDOR spectra recorded at Q-band (80 K) at the low field edge (close to g_x spectral orientation) on the RP in *menB* mutant PS I substituted with VK_3-d_8.
a Standard Davies ENDOR spectrum recorded with t_{DAF} = 1 µs and a delay of 3 µs between the end of the RF pulse and the detection sequence (t_{DD} = 14 µs).
b **Green spectrum:** VMT ENDOR spectrum recorded with t_{DAF} = 1 µs and a delay of 43 µs (t_{mix}) between the end of the RF pulse and detection sequence (t_{DD} = 54 µs).
Black spectrum: Overlay of spectrum **a**.
The numbering of the lines is the same as in spectrum **d** of **Figure 5.5**. The signs of hfccs of selected lines are given on spectrum **b**.

It was confirmed for VK_3-h_8 substituted in *menB* PS I the line pair 1/1' assigned to the methyl group protons has a positive hfcc. The line pair 3/3' arises from a hfcc with a negative sign, but the response it quite weak. This might be due to different relaxation times. The line pair 4/4' shows a strong reponse, with its behavior typical for a negative hfcc. The hfcc associated with line pair 7/7' is negative, too. For the signals associated with smaller hfccs no clear effect was observed.

In *menB* PS I substituted with VK_3-d_8 the line pair 2, 2' was found to arise from a proton with positive hfcc. The VMT ENDOR effect of the line pairs 6/6' and 8/8' indicates for both a

positive sign. It can be concluded, that line pair 8/8' in the samples with protonated quinone is composed of overlapping ENDOR lines. One ENDOR line arises from a protein proton and has a positive hfcc, while the other arises from a proton of VK_1/VK_3, which has a negative sign. The analysis of the inner hfcc is complicated due to the small effect.

TRIPLE measurements

Figure 5.11 presents the ENDOR and one-dimensional (1D) TRIPLE difference TRIPLE spectra of the stationary radical anion $A_1^{\bullet-}$, recorded at two different spectral positions. The low frequency ENDOR transition of methyl group protons was used in both cases as the pumping frequency (marked with an arrow), since it is well separated from the other ENDOR lines and its hfcc sign is known. Because the methyl group proton hfccs are positive, signals from other positive hfccs are expected to be visible in the low frequency region of the ENDOR spectrum ($\nu_{RF} < \nu_H$), while negative hfccs will be observed in the high frequency region of the ENDOR spectrum ($\nu_{RF} > \nu_H$). At g_z spectral position, a single crystal type ENDOR spectrum is observed (ENDOR spectrum **d**, difference TRIPLE spectrum **e**). The two lines 3' and 4' show a strong response in the high frequency region, hence it is concluded that both hfccs have negative signs. In the low frequency part of the spectrum a broad signal ($\sim \pm$ 0.5 MHz) with a hfcc of $\sim$ +1.6 MHz is observed. Surprisingly at first glance, two emissive features are observed. This is not a special feature of the difference TRIPLE spectra of $A_1^{\bullet-}$, but has been also observed for the quinone radical anions *in vitro* (see chapter 3) and in other systems. It has been explained in terms of relaxation processes during the long time interval used between inversion and detection sequence (here 40 μs).[53;54]

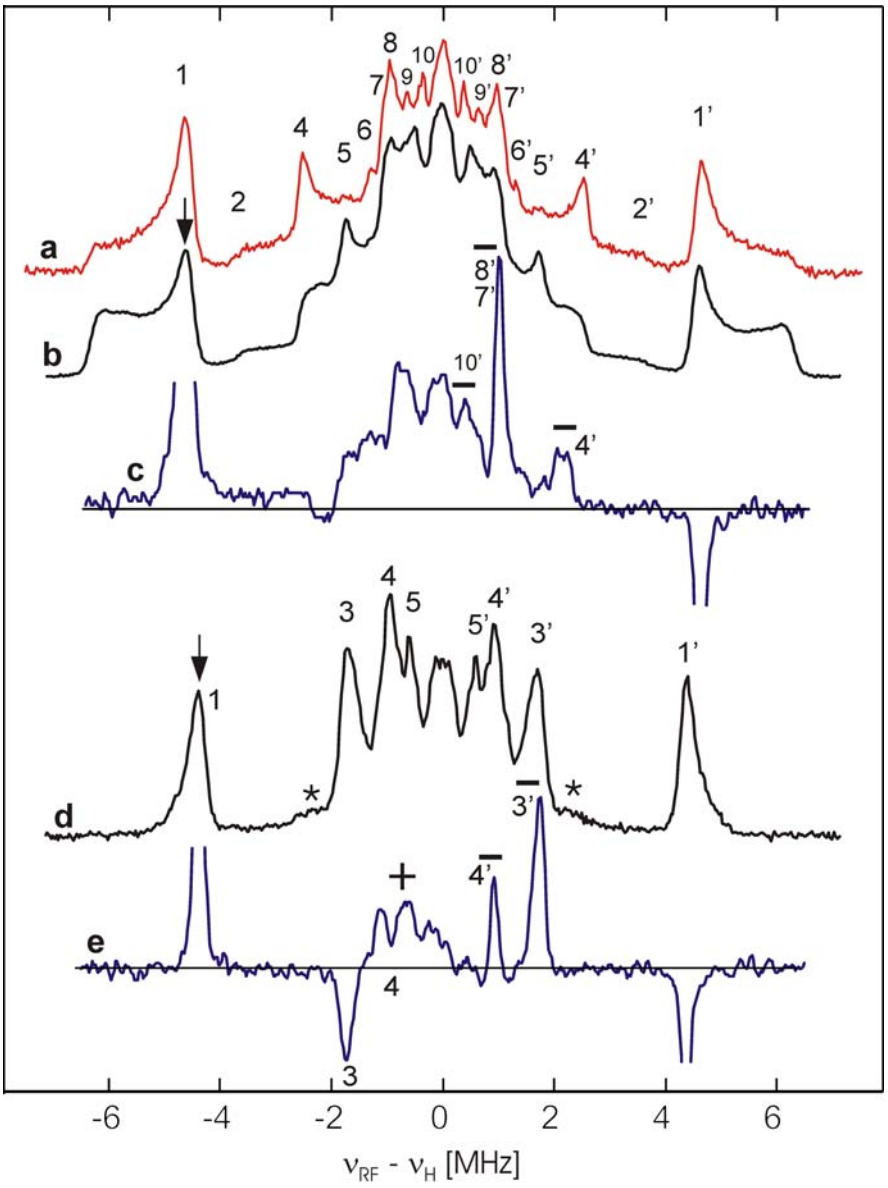

Figure 5.11: Pulse Q-band ^{1}H ENDOR (black spectra) and one-dimensional difference TRIPLE spectra (blue spectra) recorded on $A_1^{\bullet-}$ in *T. elongatus* PS I at two different spectral orientations, close to g_x (spectra **b** and **c**) and close to g_z (spectra **d** and **e**) at 80 K. The pulse ENDOR spectrum recorded at the low field edge (red spectrum a) is also shown. The arrows mark the RF pumping frequency (low frequency transition of the methyl group protons).

In the difference TRIPLE spectrum recorded close to g_x orientation (spectrum **c**), the orientation selection in the EPR spectrum is worse, as can be seen from the powder pattern of the methyl group hf tensor. However, a further orientation selection is achieved in the TRIPLE spectrum, since the narrow (~ 50 kHz) RF pumping pulse excites more molecules with g_x spectral position (since g-tensor and the hf tensor of the methyl group are not collinear, this

presents a simplification). Hence, an ENDOR spectrum recorded further on the low field wing (spectrum **a**) is shown to facilitate the comparison.

The broad line pair 2/2' shows no clear response, while line pair 4/4' shows the behaviour typical for negative hfccs. A very strong response is observed from the sum of the line pairs 7/7' and 8/8'. Both have negative hfcc. Line pair 10/10' arises from a proton with a negative hfcc.

In Figure 5.12 a two-dimensional (2D) pulse difference TRIPLE spectrum recorded at g_y spectral position on $A_1^{\bullet-}$ from *T. elongatus* PS I and the simulation of the most prominent features are shown. A detailed introduction in 2D TRIPLE spectroscopy is given in refs. [38;55]. The 2D TRIPLE spectrum is mirror-symmetric to its diagonals (assuming that third order corrections to the Hamiltonian are negligible), thus only the two lower quadrants are presented in the simulation. The correlation ridges of the protons with the same sign of hfcc are located in the left quadrant (see *e.g.* the correlation of methyl group protons (1') with the line 2, marked in Figure 5.12, while correlations of the protons with different signs are located on the right quadrant (the correlations between lines 2' and 4' is marked on the same figure). The intense signals on the diagonal (left quadrant) present, in principle, the ENDOR spectrum, while the signals on the anti-diagonal (right quadrant) are due to relaxation processes within the long time interval of the TRIPLE sequence (this was discussed for one-dimensional TRIPLE before and in chapter 4). The most prominent ridges located in the bottom part of the Figure 5.12 are due to the correlations with methyl group protons. Since the orientation of methyl group tensor is well known, the angles of the hf tensors of other protons can be determined. The information gathered from these experiments is presented in the section on the spectral simulation.

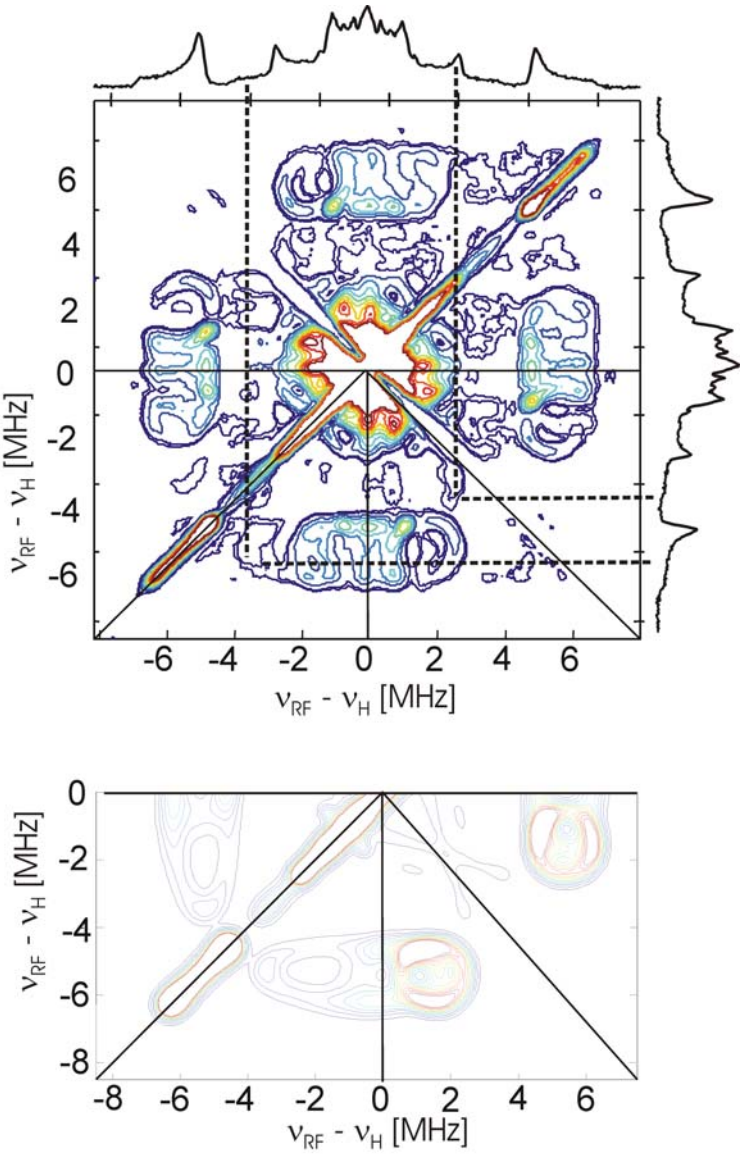

Figure 5.12: Two-dimensional pulse Q-band ^{1}H difference TRIPLE spectra of stationary $A_1^{\bullet-}$ in PS I from *T. elongatus*, recorded at ~ g_y orientation (80 K). Top: experiment. Bottom: simulation of the to lower quadrants. The correlation ridges of the protons with the same sign of hfcc are located in the left quadrant (see *e.g.* the correlation of methyl group protons (1') with the line 2), while correlations of protons with different signs are located on the right quadrant (see *e.g.* the correlations between lines 2' and 4'). On the top and at the right edge the ENDOR spectra recorded at this spectral orientation are given.

DFT calculations

The structural assignment of the hfccs to molecular positions of such a complicated system as $A_1^{\bullet-}$ is nearly impossible without proper quantum chemical calculations. For the starting

structure of the DFT calculations the coordinates of the A_1 site (VK_1 and protein environment of the A-branch) from the 2.5 Å X-ray structure (PDB entry 1JB0)[13] were used. The smallest feasible system was chosen and restricted geometry optimization was performed. The long phytyl chain of VK_1 has been truncated after the fifth carbon. The presence of H-bond(s) to the quinone oxygens are crucial for the electronic structure. Therefore, the – truncated - residues Ala A721 and Leu A722 were included. The peptide nitrogen of leucine is the H-bond donor to the C-O group at position 4 of VK_1 (see Figure 5.1). Other nearby residues were not included, since the interactions between them and the quinone are assumed to be of less importance.

In the geometry optimization, the orientation of the truncated phytyl chain and the orientation of the leucine with respect to the quinone were kept fixed, while the H-bond length was optimized (for a detailed description of the parameters used for the geometry optimization, see chapter 3). The geometry optimization of the charged quinone resulted in a short H-bond length of 1.66 Å, comparable to that of $Q_A^{\bullet -}$ in photosynthetic reaction centers from *Rb. sphaeroides*.[56-58] This leads to an elongation of the carbonyl C-O bond (1.285 Å in comparison to 1.270 Å at the opposite site). While the symmetry of the ring is already slightly distorted due to the side chain substitutions, an additional asymmetric influence is present due to this single H-bond.

The asymmetric H-bonding due to leucine has a drastic effect on the calculated spin populations on the carbon and oxygen atoms as compared to a symmetric H-bonding (Figure 5.13). Spin populations are defined as the fractional amount of the unpaired electron which can be attributed to a certain atom. This is not linearly connected with the polarized spin density on the respective proton which is probed by EPR/ENDOR (see Table 5.2). It provides important insight in the distribution of the unpaired electron over the whole molecule.

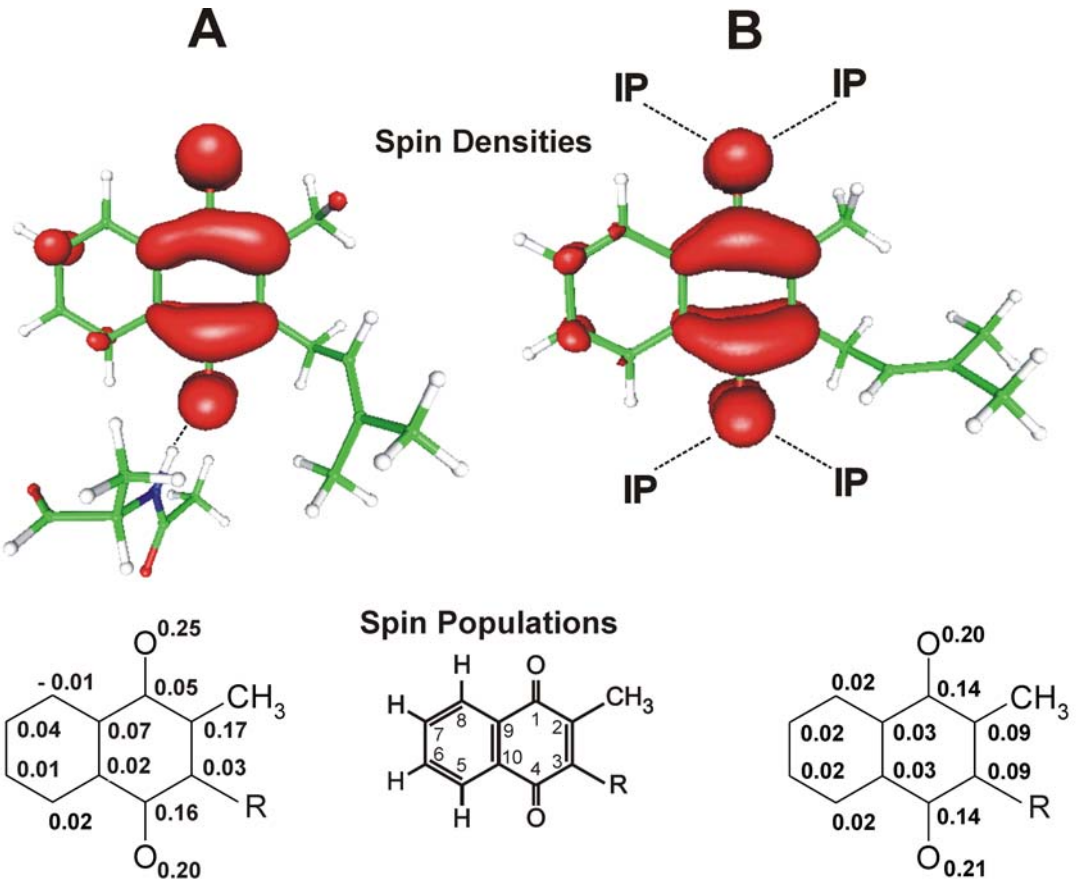

Figure 5.13: Comparison of calculated spin densities and spin populations of carbon and oxygen in $VK_1^{\bullet-}$ (with truncated phytyl chain, R) in different environments. The spin density is the difference between the total α and β spin densities. Spin populations were obtained from a Mulliken analysis, which attributes fractional amounts of electrons to every nucleus.
A $VK_1^{\bullet-}$ in the A_1 binding site, hydrogen bonded (dashed line) by the leucine peptide nitrogen.
B $VK_1^{\bullet-}$ *in vitro*, hydrogen bonded (dashed lines) by four IP molecules (see chapter 4 and ref. [34]).

An alternation of the spin populations is introduced into the system. It can be seen that the spin is shifted to the carbonyl oxygen O_1, which is not involved in the H-bond, while the spin on O_4 is hardly effected. Strong effects are also observed for the carbons C_1-C_3: The spin population at the carbon C_2 is increased, while the opposite holds for C_1 and C_3. The majority of the unpaired electron is now located at O_1, O_4, C_2 and C_4 and not at O_1, O_4, C_1 and C_4 as found for the symmetrically hydrogen-bonded $VK_1^{\bullet-}$ in IP. The spin populations in the second (benzene) ring are found to be in general small. Only C_7 shows a significant spin population for $VK_1^{\bullet-}$ in the A_1 site.

The proton hfccs and the angles of their principal orientations are given in Table 5.2. For comparison, the values for $VK_1^{\bullet-}$ symmetrically H-bonded by four IP molecules are also given. The isotropic hfccs, which depend on the polarized spin density on the nucleus, show the same trends. They are higher for the protons covalently bound by the carbons C_2, C_5 and C_7 and smaller for those protons bound by the carbons C_3, C_6 and C_8. The largest hf component of the H-bond proton tensor, A_x is pointing to a good approximation along the H-bond. The hf tensor of the H-bond proton is close to axial symmetry.

The molecular g-values were also calculated. The following values were obtained in the calculations: g_x = 2.0073, g_y = 2.0055, and g_z = 2.0022 (see Table 5.1 for a comparison with the experimentally determined *g*-values). Especially g_x is overestimated due to the neglect of the environment and inherent errors in the approximate DFT approach.[23;24]

Table 5.2: Comparison of calculated hfccs of $VK_1^{\bullet-}$ (truncated phytyl tail) in the A_1 binding site and $VK_1^{\bullet-}$ (truncated phytyl tail) *in vitro*, symmetrically hydrogen bonded by four IP molecules (in brackets). Angles (φ,θ) are given in degrees. For definition of the angles, see Figure 5.1.

	2 (CH_3)	**3 (CH_2)-1**	**3 (CH_2)-2**	**5 (α)**	**6 (α)**	**7 (α)**	**8 (α)**	**H-bond proton**
A_x	+9.67 (+6.27)	-0.85 (+0.41)	+2.53 (+3.39)	-1.84 (-1.50)	-1.74 (-3.52)	-5.19 (-3.42)	-0.65 (-1.52)	+7.27
A_y	+13.15 (+9.57)	+3.72 (+4.85)	+5.16 (+6.31)	-0.07 (+0.56)	+0.66 (+0.03)	-0.68 (+0.07)	+3.56 (+0.37)	-4.31
A_z	+8.84 (+5.56)	-2.01 (-0.76)	+1.68 (+2.63)	-3.56 (-3.20)	-1.59 (-2.75)	-3.72 (-2.69)	-1.55 (-3.26)	-3.78
a_{iso}	+10.55 (+7.10)	+0.29 (+1.50)	+3.12 (+4.11)	-1.82 (-1.39)	-0.89 (-2.08)	-3.19 (-2.01)	+0.46 (-1.47)	-0.28
φ	+33 (+34)	-22 (-24)	-13 (-8)	+12 (+8)	+10 (+16)	-22 (-17)	-5 (-10)	- 12
θ	0 (+1)	+4 (-6)	-3 (+3)	-2 (-4)	-2 (+1)	-1 (+1)	+1 (+2)	-30

There have been previous DFT calculations on the quinone in the A_1 binding site which also reported the (proton) hfccs.[9;25] Unfortunately, in one reference only the isotropic hfccs are given[9], while the calculation of O'Malley[25] was done before crystal structure of PS I was

resolved. Thus, in the work of O'Malley a different orientation of the phytyl chain was chosen and methyl imidazole has been selected as H-bond donor. He also found that an asymmetric H-bond produces an odd alternant distribution of the π-spin density with the O_1 spin population larger than the one of O_4, the spin population in C_1 lower than in C_4, and so on. These effects were also recovered in the calculated proton hfccs. Furthermore, an increased isotropic hfcc was found for the methyl group in case of asymmetric H-bonding. The results obtained in this work are qualitatively fully in line with the results presented here. While similar methods were used for the calculation of hfccs (B3LYP functional, EPR-II basis set), it is expected that the geometry optimization performed here will yield more accurate results due to the use of DFT in combination with a sophisticated basis set, while O'Malley used a semiempirical Hamiltonian (PM3).

Spectral simulations

The results of the DFT calculation were taken as starting parameters for the simulations (this refers only to the hf tensors, not to the *g*-tensor). The signs were taken from the TRIPLE experiments and the VMT ENDOR experiments. The same hfccs and angles were used for the simulation of the EPR, ENDOR and 2D TRIPLE spectra. The values are summarized in Table 5.4, Table 5.5 and Table 5.6. The simulations of the orientation selected ENDOR of stationary $A_1^{\bullet -}$ are presented in Figure 5.15 and the 2D TRIPLE simulation is shown in Figure 5.12. The error of the determination of the hfccs is typically in the order of 100 kHz, but may be in some cases of broad or overlapping lines larger. The precision of the determination of the angles of the hf tensors with respect to the *g*-tensor is < 10° for the methyl group protons, the strongly coupled α-proton of the benzene ring, and the H-bond proton. This is especially due to the sensitivity of the 2D TRIPLE spectrum on the angles between the hf tensors. For the weaker

coupled protons, the errors are larger. For the simulation of the RP ENDOR spectra, the same angles as for the stationary radical anion were taken. In case of the *menB* PS I samples, where only RP spectra could be obtained, the angles were taken from the measurement of VK_3 in IP. This is reasonable, since the DFT calculations and the experimentally determined angles for VK_1 in IP solution and in the A_1 site did not show any strong deviations of the orientation of the hf tensors.

The methyl group at position 2

The methyl group hfccs are in case of *T. elongatus* PS I 9.1 MHz (A_x), 12.7 MHz (A_y) and 8.6 MHz (A_z) for the stationary radical $A_1^{\bullet-}$ and 8.8 MHz, 12.4 MHz and 8.3 MHz for $A_1^{\bullet-}$ in the RP. The angle of the largest component of the methyl group hf tensor with the axis along g_y has been determined to be 30°. In case of the RP in PS I from *menB* substituted with VK_3-h_8 the hfccs are 8.7 MHz, 12.3 MHz and 8.2 MHz. The hfccs of methyl group protons obtained in this work agree well with previously published results.[11;12;29-31] The angle of 30° obtained here of the largest component of the methyl group hf tensor with the axis along g_y is in very good agreement to the angle obtained by EPR studies at W-band and single crystal studies.[7;18]

The α-proton at position 7 (benzene ring)

The hfccs of the prominent α-proton of the benzene ring are in case of PS I from *T. elongatus* – 5.2 MHz (A_x), – 0.7 MHz (A_y) and – 3.4 MHz (A_z) for stationary $A_1^{\bullet-}$, and – 5.0 MHz (A_x) and – 3.5 MHz (A_z) for $A_1^{\bullet-}$ in the RP. The angle of the axis along the largest component of the hf tensor (A_x) with the axis along g_x has been determined to be – 22°. In case of the RP in PS I from *menB* substituted with VK_3-h_8 the hfccs are – 4.6 MHz (A_x) and – 3.1 MHz (A_z). This hf tensor is assigned to the α-proton at position 7 in the second (benzene) ring. The analysis of the

field dependence of the hfccs in the orientation selected ENDOR spectra excludes the possilibity the this hf tensor could belong to the protons at position 5 or 8. The analysis of the 2D TRIPLE spectrum (which allows a distinction of the sign of a rotation of a hf tensor with respect to the *g*-tensor, see chapter 2 and ref. [38]) excludes the possibility that this hf tensor belongs to the proton at position 6. In addition, the assignment is strongly supported by the DFT results (see also ref. [25]).

The hydrogen bond proton (H-bond to oxygen O_4)

According to the X-ray structure, there is only one H-bond present in A_1.[13] Hydrogen bond protons exhibit mostly dipolar interactions with the unpaired electron. An axial symmetric tensor (nearly traceless) with principal values close to the ratio -1: -1: +2 is expected in case of an in-plane H-bond. In case of out-of-plane hydrogen bonding (small) rhombicity may appear. The largest component lies along the hydrogen bond direction and it is referred to as $A_{\|}$ while the other two components are named $A_{\perp}$. For a detailed discussion of H-bonding to quinone radical anions, see chapter 4.

The simulations of the H-bond proton tensor with the orientation from the X-ray structure shows an ENDOR pattern non typical for protons which establish a H-bond to quinone radical anions *in vitro* (chapter 4). It was found, that around g_x orientation the $A_{\perp}$ component becomes nearly invisible, while around g_y orientation the $A_{\|}$ component is less prominent. At g_z orientation solely the $A_{\perp}$ component is observed, which results in a defined pattern with relative high intensity.

On the basis of the ENDOR spectra recorded at g_x spectral position, the hfcc of + 7.4 MHz (line pair 2/2', Figure 5.5) can clearly be assigned to the H-bond proton ($A_{\|}$ component). This is in excellent agreement with the DFT calculation ($A_{\|}$ = + 7.27 MHz).

The $A_{\perp}$ component is typically close to $-A_{\parallel}/2$. The hfcc of – 3.5 MHz (line pair 3/3' at g_z position, Figure 5.6 and Figure 5.15) was assigned to the H-bond proton hf tensor. This assignment is less obvious than for the $A_{\parallel}$ component, since several other protons with similar couplings have significant contributions to the ENDOR spectra. The field dependence of the spectral lines corresponding to the hfcc of – 3.5 MHz fits to the H-bond proton (Figure 5.15), but not to other protons *e.g.* α-protons of the benzene ring or methylene protons of the phytyl tail. The analysis of the correlations in the 2D TRIPLE spectrum supports this assignment. In particular, the line belonging to the hfcc of – 5.2 MHz (line pair 4/4' at g_x orientation, Figure 5.5) shows a correlation with the line belonging to the H-bond proton (line pair 2/2', $A_{\parallel}$ = + 7.4 MHz). This excludes that both hfccs arise from the same proton.

Since all three components of the hf tensor of the H-bond proton are known, and the isotropic hfcc is very small, the length of H-bonds length can be estimated from the dipolar interaction according to:

$$A_{dip} = \frac{g_e \beta_e g_N \beta_N}{hr^3} \rho_S \left(3\cos^2\delta - 1\right), \qquad (5.1)$$

where g_e and g_N are the electron and nuclear *g*-values, β_e and β_n are the electron and nuclear magneton, ρ_S is the spin density at the quinone oxygen, δ is the angle between the applied magnetic field and the direction of the H-bond, and *r* is the length of the H-bond in Å.[59] The spin density on the oxygen at position 4 was taken from the DFT calculation (0.20), since no experimentally determined spin density of this oxygen in $A_1^{\bullet -}$ was available. However, it was found in the previous chapter and ref. [34], that the agreement of experimentally determined spin densities on the oxygen of quinone radical anions *in vitro* is very good. Using Eq. 5.1 and the experimentally determined hfccs of the H-bond protons from Table 5.4, a distance of 1.64 Å is

obtained. This is in excellent agreement with the distance obtained by the DFT calculation (1.66 Å).

Table 5.4: ^{1}H hfccs of $VK_1^{\bullet-}$ in the A_1 binding site of PS I from *T. elongatus* (MHz) and proposed assignment. Values given in brackets refer to the stationary $A_1^{\bullet-}$. The hfccs of $VK_1^{\bullet-}$ in IP are given as reference. See also ref. [34] and chapter 4. All measurements at T = 80 K. Angles (φ, θ) are given in degrees. Angles are assumed to be identical in the RP and the stationary radical anion. For definition of the angles, see Figure 5.1. For discussion of errors in the precision of the hf tensors, see text.

	2 (CH_3)		**3(CH_2)-2**	**5 (α)**		**6 (α)**		**7 (α)**		**8 (α)**		**H-bond**
	$A_1^{\bullet-}$	**$VK_1^{\bullet-}$(IP)**	**$A_1^{\bullet-}$**	**$A_1^{\bullet-}$**	**$VK_1^{\bullet-}$(IP)**	**$A_1^{\bullet-}$**	**$VK_1^{\bullet-}$(IP)**	**$A_1^{\bullet-}$**	**$VK_1^{\bullet-}$(IP)**	**$A_1^{\bullet-}$**	**$VK_1^{\bullet-}$(IP)**	**$A_1^{\bullet-}$**
A_x	+ 8.8 (+ 9.1)	+ 6.27		– 1.9 (– 1.9)	– 1.72	– 2.1 (– 2.0)	– 3.50	– 5.0 (– 5.2)	– 3.50	– 0.8 (– 0.8)	– 1.72	+ 7.4 (+ 7.4)
A_y	+ 12.4 (+ 12.7)	+ 10.20		(– 0.3)	+ 0.50	(+ 0.5)	+ 0.04	(– 0.7)	+ 0.04	(+ 3.5)	+ 0.50	(– 3.5)
A_z	+ 8.3 (+ 8.6)	+ 6.05	(+ 1.6)	(– 3.6)	– 3.29	(– 1.9)	– 2.60	– 3.50 (– 3.40)	– 2.60	(– 1.3)	– 3.29	(– 3.5)
a_{iso}	+ 9.8 (+ 10.1)	+ 7.55		(– 1.9)	– 1.50	(– 1.1)	– 2.02	– 3.1	– 2.02	(+ 0.5)	– 1.50	(+ 0.1)
φ	+ 30	+ 36		+ 12	+ 10	+ 10	+ 16	– 22	– 17	– 5	– 10	– 20
θ	0	0		0	0	0	0	0	0	0	0	– 30

Table 5.5: Comparison of ^{1}H hfccs of $VK_1^{\bullet-}$ in the A_1 binding site of PS I from *T. elongatus* determined experimentally and results from DFT calculation (MHz). Values given in brackets refer to the stationary $A_1^{\bullet-}$. All measurements at T = 80 K. Angles (φ, θ) are given in degrees. Angles are assumed to be identical in the RP and the stationary radical anion. For definition of the angles, see Figure 5.1. For discussion of errors in the precision of the hf tensors, see text.

	2 (CH_3)		**3(CH_2)-2**		**5 (α)**		**6 (α)**		**7 (α)**		**8 (α)**		**H-bond**	
	exp.	**DFT**	**exp.**	**DFT**	**exp.**	**DFT**	**exp.**	**DFT**	**exp.**	**DFT**	**exp.**	**DFT**	**exp.**	**DFT**
A_x	+ 8.8 (+ 9.1)	+ 9.67		+ 2.53	– 1.9 (– 1.9)	– 1.84	– 2.1 (– 2.0)	– 1.74	– 5.0 (– 5.2)	– 5.19	– 0.8 (– 0.8)	– 0.65	+ 7.4 (+ 7.4)	+ 7.27
A_y	+ 12.4 (+ 12.7)	+ 13.15		+ 5.16	(– 0.3)	– 0.07	(+ 0.5)	+ 0.66	(– 0.7)	– 0.68	(+ 3.5)	+ 3.56	(– 3.5)	– 4.31
A_z	+ 8.3 (+ 8.6)	+ 8.84	(+ 1.6)	+ 1.68	(– 3.6)	– 3.56	(– 1.9)	– 1.59	– 3.50 (– 3.40)	– 3.72	(– 1.3)	– 1.55	(– 3.5)	– 3.78
a_{iso}	+ 9.8 (+ 10.1)	+ 10.55		+ 3.12	(– 1.9)	– 1.82	(– 1.1)	– 0.89	(– 3.1)	– 3.19	(+ 0.5)	+ 0.46	(+ 0.1)	– 0.28
φ	+ 30	+ 33		– 13	+ 12	+ 12	+ 10	+ 10	– 22	– 22	– 5	– 5	– 20	– 12
θ	0	0		– 3	0	-2	0	– 2	0	– 1	0	+ 1	– 30	– 30

Table 5.6: Hfccs of $VK_3^{\bullet-}$ in the A_1 binding site of PS I from the *menB* mutant (MHz) and proposed assignment. Values given in brackets refer to the stationary $A_1^{\bullet-}$. The hfccs of $VK_3^{\bullet-}$ in IP are given as reference. See also ref. [34] and chapter 4. All measurements at T = 80 K. Angles (φ, θ) are given in degrees. For definition of the angles, see Figure 5.1. For discussion of errors in the precision of the hf tensors, see text.

	2 (CH_3)		**3 (α)**		**5 (α)**		**6 (α)**		**7 (α)**		**8 (α)**		**H-bond**
	$A_1^{\bullet-}$	**$VK_3^{\bullet-}$(IP)**	**$A_1^{\bullet-}$**	**$VK_3^{\bullet-}$(IP)**	**$A_1^{\bullet-}$**	**$VK_3^{\bullet-}$(IP)**	**$A_1^{\bullet-}$**	**$VK_3^{\bullet-}$(IP)**	**$A_1^{\bullet-}$**	**$VK_3^{\bullet-}$(IP)**	**$A_1^{\bullet-}$**	**$VK_3^{\bullet-}$(IP)**	**$A_1^{\bullet-}$**
A_x	+ 8.7	+ 6.40	– 7.6	– 11.73	– 1.8	– 1.48	– 2.5	– 3.80	– 4.6	– 3.01	– 0.8	–1.99	+ 7.4
A_y	+ 12.3	+ 9.70		– 1.00		+ 0.58		– 0.20		+ 0.37		+ 0.16	
A_z	+ 8.2	+ 5.80	– 6.7	– 9.60		– 3.00		– 2.82	– 3.1	– 2.34		– 3.54	
a_{iso}	+ 9.7	+ 7.30		– 7.40		– 1.30		– 2.14		– 1.66		– 1.79	
φ	+ 25	+ 25	– 15	– 21	+ 4	+ 4	+12	+ 12	– 20	– 20	– 14	– 14	– 20
θ	0	0	0	0	0	0	0	0	0	0	0	0	– 30

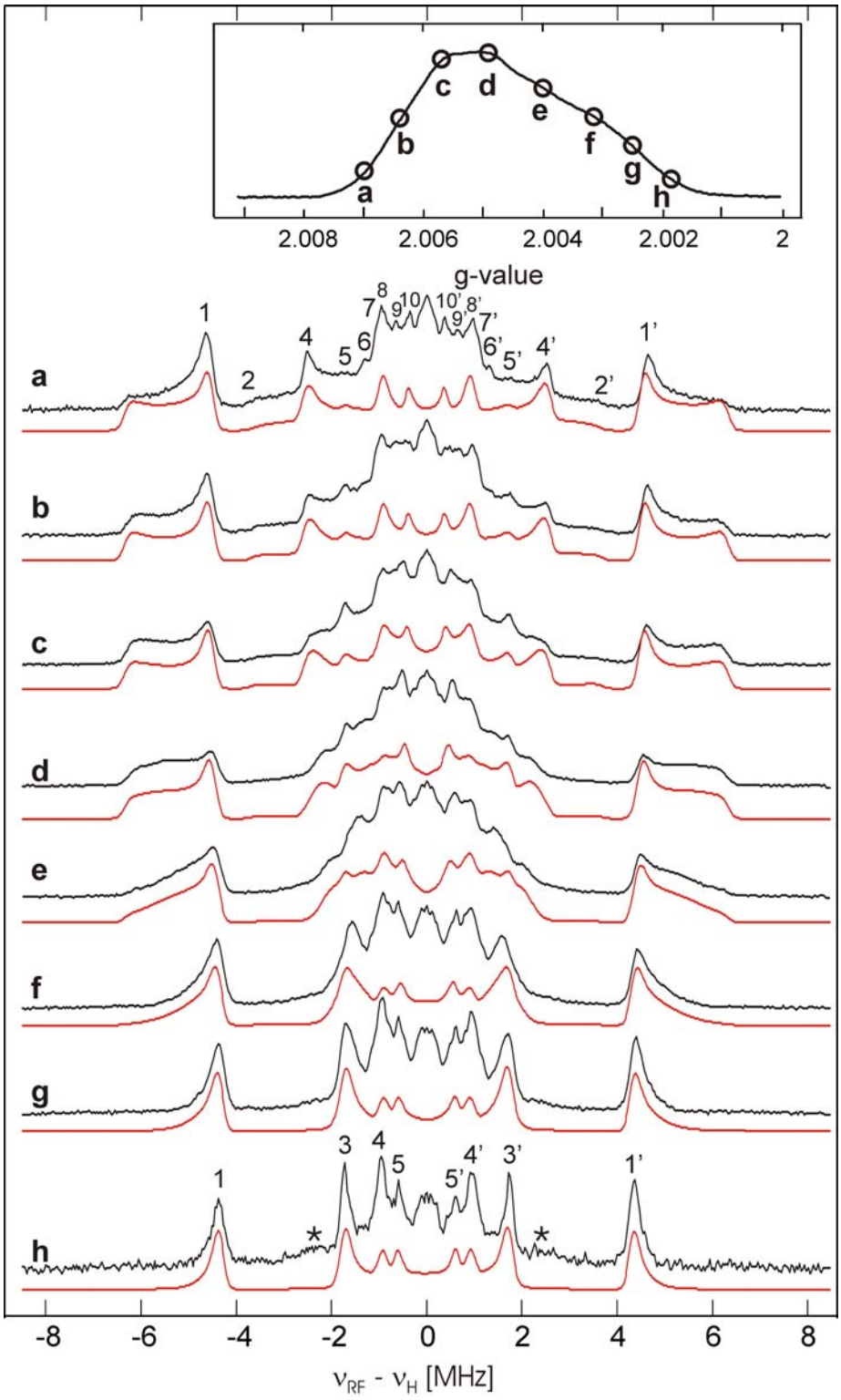

Figure 5.15: Selected pulse Q-band ^{1}H ENDOR spectra of the stationary radical anion $A_1^{\bullet-}$ in *T. elongatus* PS I recorded at T = 80 K at different values of the magnetic field. The inserts in the right corner show the reference FSE EPR spectrum. The field positions, at which the presented ENDOR spectra are measured, are marked with letters. The black spectrum for each position presents experimental spectrum and the red spectrum presents the simulation. The numbering of the ENDOR lines is identical to **Figure 5.5** and **Figure 5.6** and does not refer to molecular positions. The hf tensors of the methyl group protons, the H-bond proton and the four α-protons from the benzene ring are included in the simulation.

The other α-protons of the benzene ring

The assignment of hfccs of the several weakly to intermediate coupled protons, among them the three other α-protons of the benzene ring (5, 6 and 8), is more difficult than for for the stronger coupled protons. For these smaller hfccs, an unique assignment is on the current basis of the results not possible, due to the severe overlap of signals. However, the comparison with the DFT results and the hf tensors of $VK_1^{\bullet-}$ and $VK_3^{\bullet-}$ *in vitro* (hydrogen bonded by four IP molecules) allowed to achieve a very good simulation. The overall agreement of the parameter obtained by the simulation with the results of the DFT calculation are good.

The methylene protons

For the two methylene protons of the phytyl tail no reasonable simulation was obtained. In the RP ENDOR spectrum with VK_1 in the A_1 binding site of PS I no intense line was detected which is not present in the RP ENDOR spectrum with VK_3 in the A_1 binding site (VK_3 lacks the methylene protons, see Figure 5.1). No positive hfccs were determined at g_x orientation which would fit to the methylene protons. The broad signal with a positive hfcc (+ 1.6 MHz) observed in the 1D TRIPLE spectrum recorded at g_z spectral position could be from one of the methylene protons. This would in good agreement with the DFT results. The large line width might indicate that the hfcc shows a distribution, probably due to small variations of the dihedral angle (see also chapter 4).

The protons of the protein

The line pairs 6/6' and 8/8' detected at g_x orientation are at least partially from protons of the protein. This is the only orientation where analyzebable ENDOR signals from $A_1^{\bullet-}$ were

detected in PS I from the *menB* mutant substituted with VK_3-d_8. An assignment of these two hfccs to specific protons is impossible. However, assuming only a dipolar coupling of the protein protons to the electron spin, a hfcc of + 2.6 MHz would correspond to a small distance (in the range of 3.0-3.5 Å) to the high density positions of the quinone (see chapter 4). Since this is similar to the distance of the tryptophan residue to A_1, it might be speculated that the protons are from the tryptophan residue.

The remaining gaps in the assignment can be addressed in different ways. One way is to incorporate specifically deuterated VK_1 or VK_3 into the A_1 binding site. Another possibility is the use of completely deuterated PS I. The substitution of the deuterated quinone by protonated VK_1 or VK_3 would abondon all ^{1}H ENDOR signals from the protein, including the H-bond proton. The would significantly simplify the ENDOR spectra and allow to detected even broad lines of low intensity, *e.g.* of the methylene protons.

Number and location of phylloquinones involved in electron transfer

One matter of controversial discussion is if both phylloquinones are involved in electron transfer.[3;21;60] The use of only one branch is not a functional advantage as it is in type II reaction centers, since here electrons passing through A- or B-branch finally end up at F_X. Recently, there seems to be some basic agreement that at physiological temperature, both branches are active, but the electron transport *via* the B- branch is faster. To provide a final answer to these questions is outside the scope of this work. But it is of course important to know, which phylloquinones are observed under the experimental conditions used here. Upon illumination at cryogenic temperatures a fraction of the PS I complexes undergoes cyclic electron transfer, while the other fraction undergoes a ‘stable’ charge separation, with the negative charge located at the FeS-clusters.[61] It has been shown that the phylloquinone radical

anion involved in the cyclic electron transfer at low temperature –which is also the one observed by transient EPR spectroscopy as the RP $P_{700}^{\bullet+}A_1^{\bullet-}$ – is the one from the A-branch.[18;22;28]

Another more complicated issue is the localization of the phylloquinone radical anion in the –artificial– photoaccumulation procedure. Photoaccumulation of the phylloquinone radical anion on the A-branch, on the B-branch, and on both branches, depending on the experimental conditions have been reported.[12;18;28;41;42;49] The narrow and defined ENDOR signals which were observed in this work, including the number of ENDOR lines, showed no indication for a second reduced phylloquinone. In the TRIPLE experiments no signals arising from a second phylloquinone were found. Photoaccumulation was performed with illumination of different intensities, duration and at different temperatures with PS I from *T. elongatus* and *Synechocystis* sp. PCC 6803. In these samples, the determination of the distance between two phylloquinone radical anions in one PS I complex was attempted with advanced pulsed EPR measurements, PELDOR and RIDME.[59;62;63] No modulation arising from electron-electron interaction was detected (data not shown). Even though the absence of this modulation can not be taken as a proof of absence of a second reduced quinone, it is a further indication that only one phylloquinone radical anion was accumulated. In addition, Q-band EPR and ENDOR investigations on photoaccumulated $A_1^{\bullet-}$ in point mutants of *Synechocystis* sp. PCC 6803 were carried out, where the π-stacked tryptophan was replaced by phenylalanin (data not shown). Significant changes in the ENDOR spectra as compared to wild type PS I were only found in the A-branch mutant. The number of ENDOR lines of $A_1^{\bullet-}$ remained unchanged, indicating that only the A-branch phylloquinone was reduced.

From this it is concluded that under the experimental conditions used in this work exclusively only the A-branch phylloquinone is monitored. This holds both for the radical pair and photoaccumulated $A_1^{\bullet-}$.

Comparison of the hfccs observed in the stationary $A_1^{\bullet-}$ and in the radical pair $P_{700}^{\bullet+}A_1^{\bullet-}$

In this section proton hfccs of the stationary $A_1^{\bullet-}$ and in the radical pair $P_{700}^{\bullet+}A_1^{\bullet-}$ are compared. It is assumed that the orientations of hyperfine tensors are the same in both cases, thus, the difference between the values will be solely due to the changes of the magnitude of the hfccs. The methyl group proton hfccs in the RP are decreased by about 300 kHz as compared to the stationary radical (Table 5.4). A similar difference between RP and stationary radical was also observed within the lower resolution at X-band.[29] Some of the other proton hfccs like one for the α-proton 7 in the second ring show also small shifts, but they are close to the error of the hfccs determination. The interaction of the two unpaired electrons in the radical pair as a reason for the difference of the hfccs in the radical pair as compared to the stationary radical has been excluded in the previous work by Fursman *et al.*[29] Two other explanations may be suggested, which in principle follow previous ideas: either the binding situation may be slightly different, due to structural relaxation in the stationary anion radical. In case of the RP measurements, the ENDOR spectrum is recorded shortly after creation of the RP at low temperature (t_{DAF} = 1 µs, t_{DD} = 14 µs or t_{DD} = 22 µs). The RP ENDOR spectrum has also been measured with significantly longer delay after creation of the RP (up to t_{DAF} = 241 µs and t_{DD} = 254 µs) and the hfccs found to be identical to the one obtained with a DAF of 1 µs (data not shown). The stationary radical is created at higher temperature (200 K and above) and has several minutes too relax. An influence of the different charges in the environment ($P_{700}^{\bullet+}$ in case of the RP, reduced iron sulfur clusters FeS^- in case of the stationary radical) which causes a different electrostatic situation, may be a reason. However, it is important to keep in mind, that the changes of the hfccs of the methyl group protons are

below 3%, and thus represent just a minor effect. For the discussion of the specific influence of the A_1 binding site on the electronic structure of the quinone radical anion, this can be neglected.

Comparison of the proton hf tensors in $VK_1^{\bullet-}$ and $VK_3^{\bullet-}$ in the A_1 binding site

Position 2 : The methyl group protons

The methyl group hfccs are found to be nearly identical in $VK_1^{\bullet-}$ and $VK_3^{\bullet-}$ in the A_1 binding site (Table 5.4 and Table 5.6). The same holds for both radical anions in frozen isopropanol, see chapter 4 and [34].

Position 3: The α-proton/ the methylene protons

At position 3 VK_3 and VK_1 are structurally different (Figure 5.1). For $VK_3^{\bullet-}$ in IP the complete hf tensor was obtaind. In case of VK_3 in the A_1 site only two principal values were obtained. The determination of the hf tensors of the methylene protons of VK_1 was not successful in any case. A comparison is thus not possible.

Positions 5-8: The α-protons in the benzene ring

In all these cases, the A_1 binding pocket provides for both quinones a similar shift of hfccs as compared to the symmetric hydrogen bonded situation found in frozen IP solution. This holds for both rings of the quinones.

Since in both cases an identical $A_{\|}$ component of the H-bond proton has been determined, it may be concluded that the also the $A_{\perp}$ component is similar.

The spin density distribution in $A_1^{\bullet-}$ compared to $VK_1^{\bullet-}$/ $VK_3^{\bullet-}$ *in vitro* – Influence of different surrounding

In this section, the differences in the electronic structure of the quinone radical anions *in vivo* and *in vitro* will be discussed and subsequently the reasons for this effect evaluated. The experimental problem in frozen solutions is that one needs to determine all three components of the hf tensor to determine the isotropic hfcc, which is in many cases not possible. In contrast, DFT calculations deliver the complete tensors and spin densities, but severe deviations from the experimentally determined hfccs are sometimes observed. Therefore, it is of crucial importance to compare the results of the DFT calculations with experimentally determined values to decide if the DFT results can be trusted for such radical in a certain environment (*e.g.* organic solvents, protein).

The DFT calculations demonstrated the potential of the method in predicting the hf tensors of the quinone protons correctly with small deviations from the experimentally determined hf tensors in case of quinones *in vitro* (see chapter 4 and [34]). The calculation of proton hf tensors involved in in-plane hydrogen bonding delivered values very close to the ones determined experimentally. The prediction of the hf tensors from protons involved in out-of-plane hydrogen bonding were still quite close to the experiment, but showed somewhat larger deviations. The presence of two or four H-bonds to the quinone radical anions showed small, but significant changes of the ring proton hfccs. The presence of an odd number (3) of H-bonds induced strong changes in the ring proton hfccs. Whether the H-bonds were out-of-plane or in the plane of the quinone radical anion, had a negligible influence on the hfccs of the ring protons. In sharp contrast to this, the H-bond proton hf tensors were strongly affected.

An alternating effect of the spin density distribution upon asymmetric H-bonding was observed: An increase of the isotropic hfccs of the protons at the positions 2, 5 and 7 was found, while the isotropic hfccs of the protons at the positions 3, 6 and 8 were decreased as

compared to the symmetrically hydrogen bonded species. A similar effect was observed in the calculation of $VK_1^{\bullet-}$ in the (simplified) A_1 binding site. The DFT calculation with such a simple model of the protein binding pocket already delivers quite good predictions of the hfccs. In previous studies (see also chapter 4), an apolar and aprotic environment was discussed to explain the extremely low redox potential of A_1 and the high g_x value as compared to protic solvents as environment. The apolar environment of the quinone in the A_1 binding site was modeled by using a DME-MTHF (both are apolar and aprotic solvents) mixture as solvent. Indeed, this shifted the redox potential of VK_1 and the *g*-tensor to values very close to what was found for A_1.[7;9] The isotropic hfccs of VK_1 protons in a liquid solution of a DME-MTHF mixture and 2-proponal, where both oxygens are involved in symmetric H-bonds were also compared.[12] The methyl group and methylene proton hfccs changed only marginally. The hfccs of the protons in the positions 6 and 7 did not respond much on the change of solvent, while the smaller hfccs of the protons at positions 5 and 8 further decreased. No asymmetry was induced by the use of the apolar solvent mixture. Thus, the low polarizability can not account for the spin density distribution observed here. The asymmetric H-bonding is obviously the key factor to understand the spin density distribution in A_1.

Previous assignments of the H-bond proton

The determination of the H-bond proton hf tensor has previously been attempted several times, and the different (and controversial) assignments will be discussed in the following in relation to the assignment provided here.

Teutloff *et al.* assigned in a pulse X-band ^{1}H ENDOR study of the stationary radical anion $A_1^{\bullet-}$ and the radical pair in *T. elongatus* PS I one axial tensor with an $A_{\|}$ component of (+)14.8 MHz and an $A_{\perp}$ component of (-)4.9 MHz to the H-bond proton.[9] Such a hf tensor

would be an indication of an unusual short and strong H-bond. It is important to note, that the 14.8 MHz component was not detected in the radical pair ENDOR spectra. In a later work by the same authors, the large component of the hf tensor was assigned only tentatively to the H-bond proton, due to the possibility that this hfcc could arise from a contribution of $A_0^{\bullet-}$ in the photoaccumulated samples.[12].

In the Heathcote group the stationary radical anion $A_1^{\bullet-}$ was investigated using CW X-band ENDOR and special TRIPLE spectroscopy.[31;41;42;49] Their analysis was based on the assumption that the two phylloquinones in either the A- or B-branch can be photoaccumulated selectively. They proposed two strong H-bonds per $A_1^{\bullet-}$ radical anion, with different hfccs depending on the species where the PS I complexes were isolated from.[31;49;64] They assigned a hfcc of about (+)12 MHz to the large component of the H-bond proton hf tensor, close to the hfcc reported by Teutloff *et al.* in ref. [9].

An approach similar to the one presented in this study was used recently, wherein the stationary radical anion of VK_3-d_8 in the A_1 binding site of *menB* mutant PS I was investigated by ENDOR spectroscopy, using the increased spectral resolution at Q-band.[20] The authors determined hfccs of (+)7.7 MHz for the $A_{\|}$ component and (-)4.9 MHz for the $A_{\perp}$ component of one H-bond proton.

On the basis of the DFT calculations presented here and previous DFT calculations,[9;12;25;26] only strongly asymmetric H-bonding can induce the peculiar asymmetric spin density distribution observed experimentally in $A_1^{\bullet-}$. The presence of only one H-bond is also strongly supported by the high resolution X-ray structure.[13] Furthermore, under the experimental conditions used in this study, only one of the two phylloquinones is reduced (A-branch for both radical pair and stationary radical) and thus observed by EPR spectroscopy. Considering the powder-type ENDOR due to the low resolution at X-band, and possible contaminations with other radicals (*e.g.* $A_0^{\bullet-}$), it seems that the ENDOR spectra by the

Heathcote group were severely overinterpreted. Therefore, in the following only the case of one H-bond is discussed.

A serious problem that was encountered in this study is the presence of $A_0^{\bullet-}$ in photoaccumulated samples (see discussion above). Since the α- and β-protons of the Chl radical anion $A_0^{\bullet-}$ provide intense ENDOR signals, already quite small contributions of $A_0^{\bullet-}$ (a few percent) obscure the broad and weak ENDOR lines of the H-bond proton. At the low resolution of the X-band every ENDOR spectrum of the stationary radical anion $A_1^{\bullet-}$ contains also signals from $A_0^{\bullet-}$, if this radical is present in the sample. At Q-band the situation is slightly different: due to the larger *g*-anisotropy of $A_1^{\bullet-}$ compared to $A_0^{\bullet-}$, ENDOR spectra of pure $A_1^{\bullet-}$ can be obtained at spectral positions around g_x. This holds of course only for a small amount of $A_0^{\bullet-}$ in the sample.

The large hfccs of $A_0^{\bullet-}$ are in exactly the range where the large hfccs were detected by Teutloff *et al.* and the Heathcote group and assigned to the H-bond proton.[9;11;31;41] It was clearly shown here on stationary $A_1^{\bullet-}$ samples, that no signals from hfccs larger than the methyl group were discovered at orientations between g_x and g_y. In the radical pair samples $A_0^{\bullet-}$ is not present. Despite the excellent signal-to-noise ratio in the ENDOR spectra, these large hfccs in the radical pair ENDOR spectra were not observed. From this it is obvious, that these large hfccs can not arise from the proton H-bonded to $A_1^{\bullet-}$, but are due to $A_0^{\bullet-}$ protons, and that the assignments by Teutloff *et al.*[9] and the Heathcote group[11;31;41;42;65] are erroneous.

As mentioned above, also for the $A_\perp$ component, a variety of hfccs have been proposed. Especially the (-)4.9 MHz component is discussed, which was suggested in some previous studies.[9;12;20] The broad variety of hfccs suggested by the Heathcote group are not discussed in detail. As a general remark, no signals in the range of a hfccs of 6 MHz which could be due to the H-bond proton were observed in this work. The largest hfccs observed

come from the spectrally well separated methyl group protons, the + 7.4 MHz hfcc (which was assigned to the $A_{\|}$ component of the H-bond proton hf tensor) and next largest hfcc of about 5 MHz (line 4/4'). In this study, line pair 4/4' (hfcc directly read from the ENDOR spectrum is 4.9 MHz) is assigned to the α-proton at position 7 in the benzene ring. This is based on the comparison of the radical pair ENDOR spectra of the different PS I samples, the orientation dependence observed in the ENDOR spectra of stationary $A_1^{\bullet-}$(see discussion above), and the DFT calculation. The absence of this line pair in the RP ENDOR spectra of menB PS I substituted with VK_3-d_8 clearly demonstrates, that this line pair does not arise from the H-bond proton. When the field position is moved from g_x spectral position towards g_y spectral position on the stationary $A_1^{\bullet-}$ in *T. elongatus* PS I, this ENDOR line becomes much broader, due to the large anisotropy of this α-proton. In X-band, where the orientation selection is much more poor, this line is broad and exhibits a relative low intensity, thus the general appearance fits to an $A_{\perp}$ component of a dipolar tensor. As even explicitly mentioned in their work, Teutloff *et al.* just assigned this line pair to the H-bond proton, since they did not think that an α-proton from the second ring could have such a large hfcc.[12] This explanation can not account for the results of Pushkar *et al.*, since they used a fully deuterated quinone (VK_3-d_8) in the A_1 binding site of menB mutant PS I. A weak point of their study is that they used only photoaccumulated samples, which carry the risk of an $A_0^{\bullet-}$ contamination. Indeed, already in the EPR spectrum a strong contribution of $A_0^{\bullet-}$ is visible.[20] Thus a contribution of $A_0^{\bullet-}$ to the ENDOR spectra is expected at least at field positions higher than g_y spectral position, as stated by the authors. A closer inspection of the ENDOR spectra shows the presence of lines with large hfccs, which are indicative for $A_0^{\bullet-}$. The spectra at g_y and g_z spectral position show the strongest contribution of $A_0^{\bullet-}$, however, even at g_x spectral position the contamination is not negligible. It has to be concluded that a mixture of signals arising from $A_0^{\bullet-}$ and $A_1^{\bullet-}$ were observed in the ENDOR spectra recorded at all three

orientations and the contribution of $A_0^{\bullet-}$ was severely underestimated. The ENDOR spectrum of pure $A_0^{\bullet-}$ exhibits an intense line arising from a hfcc of about 4.8 MHz (Figure 5.7). Thus the assignment of the 4.9 MHz (line pair 4/4') hfcc to the $A_\perp$ component of the H-bond proton hf tensor, based on the ENDOR spectra of the stationary radical anion,[20] can not be correct. The analysis of relative intensities of the ENDOR signals from $A_0^{\bullet-}$ and $A_1^{\bullet-}$ presented by Pushkar *et al.* leaves the possibility that the hfcc observed at g_x spectral position by Pushkar *et al.*, may still be attributed to the parallel component of H-bond hf tensor. This would be in agreement with the ENDOR data presented in this work.

Conclusions

An extended Q-band EPR, ENDOR and TRIPLE investigation of both the stationary radical $A_1^{\bullet-}$ and the spin-correlated radical pair $P_{700}^{\bullet+}A_1^{\bullet-}$ of cyanobacterial PS I from *T. elongatus* was performed. In addition, PS I from the *menB* mutant substituted with VK_3 (VK_3-h_8 and VK_3-d_8) in the A_1 binding site was investigated. DFT calculations were performed, using a simple model of a VK_1 molecule hydrogen bonded to a leucine residue.

It was clearly shown, that under the experimental condition used in this work, only the A-branch A_1 is reduced. This holds both for stationary (photoaccumulated) $A_1^{\bullet-}$ and for $A_1^{\bullet-}$ in the RP $P_{700}^{\bullet+}A_1^{\bullet-}$. The hf tensor of the methyl group protons was determined with high precision for $A_1^{\bullet-}$ in PS I from *T. elongatus* and in *menB* mutant PS I, which was substituted with VK_3. For the first time, ENDOR lines of the α-protons of the second (benzene) ring were assigned. It was shown, that the α-proton at position 7 show a strongly increased hf tensor.

The hf tensor of the H-bond proton was identified. The comparative analysis of $A_1^{\bullet-}$ and $P_{700}^{\bullet+}A_1^{\bullet-}$ ENDOR spectra of PS I from *T. elongatus* and from the *menB* mutant with fully

deuterated and fully protonated VK_3 in combination with the DFT results allows to confirm the presence of only one strong H-bond. It was shown that previous ENDOR studies addressing the H-bond suffered from contributions of the contaminating Chl radical anion $A_0^{\bullet-}$, which is generated by the photoaccumulation procedure, and underestimated the strength of the coupling of the α-proton at position 7 in the benzene ring. The length of the H-bond was calculated using the point-dipolar approximation, delivered a length of 1.64 Å, which corresponds to a short and strong H-bond. This is quite similar to what is found for bacterial photosynthetic RCs.[56-58]

The hfcc of protons determined for the stationary radical anion and for the radical pair turned out to be nearly identical, indicating a similar binding situation. The small differences of the hfccs of the methyl group (< 3%) might indicate that the spin density asymmetry is slightly stronger in the stationary $A_1^{\bullet-}$.

The results further demonstrate that the spin density distribution in the protein bound phylloquinone $A_1^{\bullet-}$ exhibits a significant difference as compared to the spin density distribution found in protic solvents. The holds true for both VK_1 and VK_3.

The DFT calculations showed that the presence of only one strong H-bond can account for the significant asymmetry in spin density distribution. It was demonstrated further that DFT calculations using the simplified structural model with only the H-bond interaction can explain the ENDOR spectra. This indicates that H-bond interaction is the crucial factor for the explanation of the spin density distribution in $A_1^{\bullet-}$.

The change of the ENDOR line position (change of hfcc) with an increase of the time after the Laser flash, which was reported for the RP in bacterial photosynthetic RC, was not observed. A redistribution of the unpaired electron spin does not take place. This may be due to different timescales accessible: in bRC the RP can be monitored up to several ms, while in

PS I the spin polarization decays nearly completely within a few hundred µs at 80 K. The A_1 binding site in PS I may also be more 'rigid' than the Q_A binding site in bacterial photosynthetic RCs.

References

1. van der Est, A., *Biochimica et Biophysica Acta*, 1507, 212-225 **2001**
2. Brettel, K., *Biochimica et Biophysica Acta*, 1318, 322-373 **1997**
3. Brettel, K. and Leibl, W., *Biochimica et Biophysica Acta*, 1507, 100-114 **2001**
4. Pushkar, Y. N., Karyagina, I., Stehlik, D., Brown, S., van der Est, A., *Journal of Biological Chemistry*, 280, 12382-12390 **2005**
5. Semenov, A. Y., Vassiliev, I. R., van der Est, A., Mamedov, M. D., Zybailov, B., Shen, G. Z., Stehlik, D., Diner, B. A., Chitnis, P. R., Golbeck, J. H., *Journal of Biological Chemistry*, 275, 23429-23438 **2000**
6. MacMillan, F., Hanley, J., van der Weerd, L., Knüpling, M., Un, S., Rutherford, A. W., *Biochemistry*, 36, 9297-9303 **1997**
7. Teutloff, C., Hofbauer, W., Zech, S. G., Stein, M., Bittl, R., Lubitz, W., *Applied Magnetic Resonance*, 21, 363-379 **2001**
8. van der Est, A., Prisner, T., Bittl, R., Fromme, P., Lubitz, W., Möbius, K., Stehlik, D., *Journal of Physical Chemistry B*, 101, 1437-1443 **1997**
9. Teutloff, C., Untersuchungen zur Bindung des sekundären Akzeptors in Photosystem I mit Methoden der EPR-Spektroskopie, Phd Thesis Technische Universität Berlin, **2004**
10. Iwaki, M. and Itoh, S., *Plant Cell Physiol.*, 35, 983-993 **1994**
11. Rigby, S. E. J., Evans, M. C. W., Heathcote, P., *Biochimica et Biophysica Acta-Bioenergetics*, 1507, 247-259 **2001**
12. Teutloff, C., Bittl, R., Lubitz, W., *Applied Magnetic Resonance*, 26, 5-21 **2004**
13. Jordan, P., Fromme, P., Witt, H. T., Klukas, O., Saenger, W., Krauss, N., *Nature*, 411, 909-917 **2001**
14. Hales, B. J., *Journal of the American Chemical Society*, 97, 5993-5997 **1975**
15. Burghaus, O., Plato, M., Rohrer, M., Möbius, K., MacMillan, F., Lubitz, W., *Journal of Physical Chemistry*, 97, 7639-7647 **1993**
16. Bittl, R. and Zech, S. G., *Biochimica et Biophysica Acta*, 1507, 194-211 **2001**

17. Hore, P. J., in Hoff, A. J. (Ed.), *Advanced EPR - Applications in Biology and Biochemistry*, Amsterdam, Elsevier, 405-440 **1989**

18. Zech, S., Hofbauer, W., Kamlowski, A., Fromme, P., Stehlik, D., Lubitz, W., Bittl, R., *Journal of Physical Chemistry B*, 104, 9728-9739 **2000**

19. Pushkar, Y. N., Ayzatulin, O., Stehlik, D., *Applied Magnetic Resonance*, 28, 195-211 **2005**

20. Pushkar, Y. N., Stehlik, D., van Gastel, M., Lubitz, W., *Journal of Molecular Structure*, 700, 233-241 **2004**

21. Santabarbara, S., Heathcote, P., Evans, M. C. W., *Biochimica et Biophysica Acta*, 1708, 283-310 **2005**

22. Xu, W., Chitnis, P., Valieva, A., van der Est, A., Pushkar, Y. N., Krzystyniak, M., Teutloff, C., Zech, S. G., Bittl, R., Stehlik, D., Zybailov, B., Shen, G. Z., Golbeck, J. H., *Journal of Biological Chemistry*, 278, 27864-27875 **2003**

23. Kacprzak, S. and Kaupp, M., *Journal of Physical Chemistry B*, 108, 2464-2469 **2004**

24. Kaupp, M., *Biochemistry*, 41, 2895-2900 **2002**

25. O'Malley, P. J., *Biochimica et Biophysica Acta-Bioenergetics*, 1411, 101-113 **1999**

26. Teutloff, C., Bittl, R., Stein, M., Jordan, P., Fromme, P., Krauss, N., Lubitz, W. Structure based analysis of the magnetic resonance parameters of the phylloquinone acceptor A1 in PS I, [Proceedings of the 12th International Congress on Photosynthesis], S6-030Brisbane, Australia, CSIRO Publishing. **2001**

27. Pushkar, Y. N., Golbeck, J. H., Stehlik, D., Zimmermann, H., *Journal of Physical Chemistry B*, 108, 9439-9448 **2004**

28. Boudreaux, B., MacMillan, F., Teutloff, C., Agalarov, R., Gu, F. F., Grimaldi, S., Bittl, R., Brettel, K., Redding, K., *Journal of Biological Chemistry*, 276, 37299-37306 **2001**

29. Fursman, C. E., Teutloff, C., Bittl, R., *Journal of Physical Chemistry B*, 106, 9679-9686 **2002**

30. Zybailov, B., van der Est, A., Zech, S. G., Teutloff, C., Johnson, T. W., Shen, G. Z., Bittl, R., Stehlik, D., Chitnis, P. R., Golbeck, J. H., *Journal of Biological Chemistry*, 275, 8531-8539 **2000**

31. Rigby, S. E. J., Evans, M. C. W., Heathcote, P., *Biochemistry*, 35, 6651-6656 **1996**

32. Klughammer, C., Klughammer, B., Pace, R. J., *Biochemistry*, 38, 3726-3732 **1999**

33. Johnson, T. W., Zybailov, B., Jones, A. D., Bittl, R., Zech, S., Stehlik, D., Golbeck, J. H., Chitnis, P. R., *Journal of Biological Chemistry*, 276, 39512-39521 **2001**

34. Epel, B., Niklas, J., Sinnecker, S., Zimmermann, H., Lubitz, W., *Journal of Physical Chemistry B*, 110, 11549-11560 **2006**

35. Epel, B., Niklas, J., Antonkine, M. L., Lubitz, W., *Applied Magnetic Resonance*, 30, 311-327 **2006**

36. Mehring, M., Höfer, P., Grupp, A., *Berichte der Bunsen-Gesellschaft-Physical Chemistry Chemical Physics*, 91, 1132-1137 **1987**

37. Gemperle, C. and Schweiger, A., *Chemical Reviews*, 91, 1481-1505 **1991**

38. Goldfarb, D., Epel, B., Zimmermann, H., Jeschke, G., *Journal of Magnetic Resonance*, 168, 75-87 **2004**

39. Angerhofer, A. and Bittl, R., *Photochemistry and Photobiology*, 63, 11-38 **1996**

40. Pushkar, Y. N., Zech, S. G., Stehlik, D., Brown, S., van der Est, A., Zimmermann, H., *Journal of Physical Chemistry B*, 106, 12052-12058 **2002**

41. Rigby, S. E. J., Muhiuddin, I. P., Evans, M. C. W., Purton, S., Heathcote, P., *Biochimica et Biophysica Acta*, 1556, 13-20 **2002**

42. Purton, S., Stevens, D. R., Muhiuddin, I. P., Evans, M. C. W., Carter, S., Rigby, S. E. J., Heathcote, P., *Biochemistry*, 40, 2167-2175 **2001**

43. Bonnerjea, J. and Evans, M. C. W., *FEBS Letters*, 148, 313-316 **1982**

44. Smith, N. S., Mansfield, R. W., Nugent, J. H. A., Evans, M. C. W., *Biochimica et Biophysica Acta*, 892, 331-334 **1987**

45. Rigby, S. E. J., Muhiuddin, I. P., Santabarbara, S., Evans, M. C. W., Heathcote, P., *Chemical Physics*, 294, 319-328 **2003**

46. Forman, A., Davis, M. S., Fujita, I., Hanson, L. K., Smidth, K. M., Fajer, J., *Israel Journal of Chemistry*, 21, 265-269 **1981**

47. Fajer, J., Davis, M. S., Forman, A., Klimov, V. V., Dolan, E., Ke, B., *Journal of the American Chemical Society*, 102, 7143-7145 **1980**

48. Lubitz, W., in Scheer, H. (Ed.), *Chlorophylls*, Boca Raton, CRC Press, 903-944 **1991**

49. Fairclough, W. V., Forsyth, A., Evans, M. C. W., Rigby, S. E. J., Purton, S., Heathcote, P., *Biochimica et Biophysica Acta*, 1606, 43-55 **2003**

50. Timmel, C. R., Fursman, C. E., Hoff, A. J., Hore, P. J., *Chemical Physics*, 226, 271-283 **1998**

51. van Dijk, B., Gast, P., Hoff, A. J., Dzuba, S. A., *Journal of Physical Chemistry A*, 101, 719-724 **1997**

52. Poluektov, O. G., Utschig, L. M., Dubinskij, A. A., Thurnauer, M. C., *Journal of the American Chemical Society* , 127, 4049-4059 **2005**

53. Silakov, A. About the origin of emissive signals in pulse difference TRIPLE spectra. **2006**

54. Höfer, P., Entwicklung von Puls-ENDOR-Verfahren und Ihre Anwendung auf Polyazetylen, Universität Stuttgart, **1988**

55. Epel, B. and Goldfarb, D., *Journal of Magnetic Resonance*, 146, 196-203 **2000**

56. Flores, M., Isaacson, R., Abresch, E., Calvo, R., Lubitz, W., Feher, G., *Biophysical Journal*, 92, 671-682 **2007**

57. Flores, M., Isaacson, R., Abresch, E., Calvo, R., Lubitz, W., Feher, G., *Biophysical Journal*, 90, 3356-3362 **2006**

58. Sinnecker, S., Flores, M., Lubitz, W., *Physical Chemistry Chemical Physics*, 8, 5659-5670 **2006**

59. Schweiger, A. and Jeschke, G., *Principles of pulse electron paramagnetic resonance*, New York, Oxford University Press **2001**

60. Li, Y., van der Est, A., Lucas, M. G., Ramesh, V. M., Gu, F., Petrenko, A., Lin, S., Webber, A. N., Rappaport, F., Redding, K., *Proceedings of the National Academy of Sciences of the United States of America*, 103, 2144-2149 **2006**

61. Schlodder, E., Falkenberg, K., Gergeleit, M., Brettel, K., *Biochemistry*, 37, 9466-9476 **1998**

62. Kulik, L. V., Dzuba, S. A., Grigoryev, I. A., Tsvetkov, Y. D., *Chemical Physics Letters*, 343, 315-324 **2001**

63. Jeschke, G., *Chemphyschem*, 3, 927-932 **2002**

64. Evans, M. C. W., Purton, S., Patel, V., Wright, D., Heathcote, P., Rigby, S. E. J., *Photosynthesis Research*, 61, 33-42 **1999**

65. Muhiuddin, I. P., Rigby, S. E. J., Evans, M. C. W., Amesz, J., Heathcote, P., *Biochemistry*, 38, 7159-7167 **1999**

6. Triplet States in Photosystem I and II

Chl triplet states (^{3}Chl) in photosynthetic reaction centers (RCs) are carefully avoided in nature, since they are dangerous, reactive species. They can convert ground state molecular oxygen to so-called singlet oxygen, a very dangerous cell poison. Hence, in photosystems ^{3}Chl triplet states (here, and in the following chapter, Chl triplet state always means the energetically lowest triplet state) are effectively quenched by energy transfer to carotenoids (Car), which dissipate the excess energy by heat. In addition, already existing singlet oxygen can be converted to its ground state by carotenoids (Figure 6.1).[1-3]

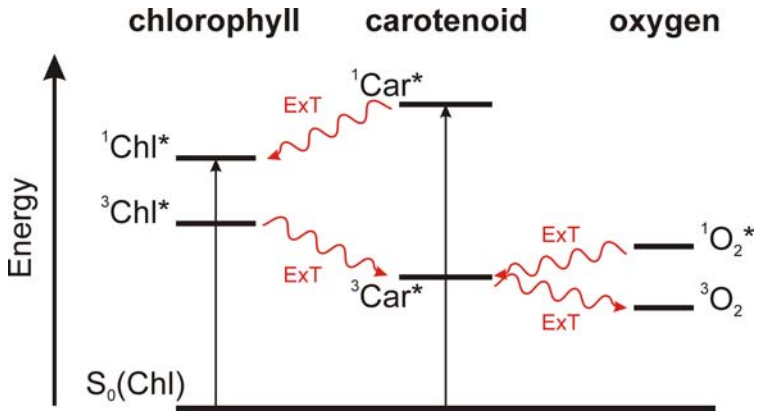

Figure 6.1: Energy transfer between Chls, carotenoids and oxygen in photosynthetic reaction centers. Higher excited states are not shown, because they decay rapidly. Scheme adapted from ref. [4].

On the other hand, the triplet state is an important probe of the electronic structure and function of Chl molecules. [5;6] Since triplet states are paramagnetic, they are accessible by EPR spectroscopy and related techniques like **o**ptically **d**etected **m**agnetic **r**esonance (ODMR).[7] Using EPR spectroscopy, the kinetics of triplet creation and decay can be studied, and the electronic structure of the Chl triplet can be determined, *e.g.* the zero field splitting (ZFS)

tensor, the *g*-tensor (at sufficient high magnetic fields) and the hyperfine (hf) tensors. The knowledge of these parameters is especially interesting, if the triplet state of the electron donor Chl(s) can be selectively generated. It contains valuable information about the excited state of the primary donor Chl(s), from which the electron transfer starts. This information is otherwise not accessible by EPR spectroscopy.

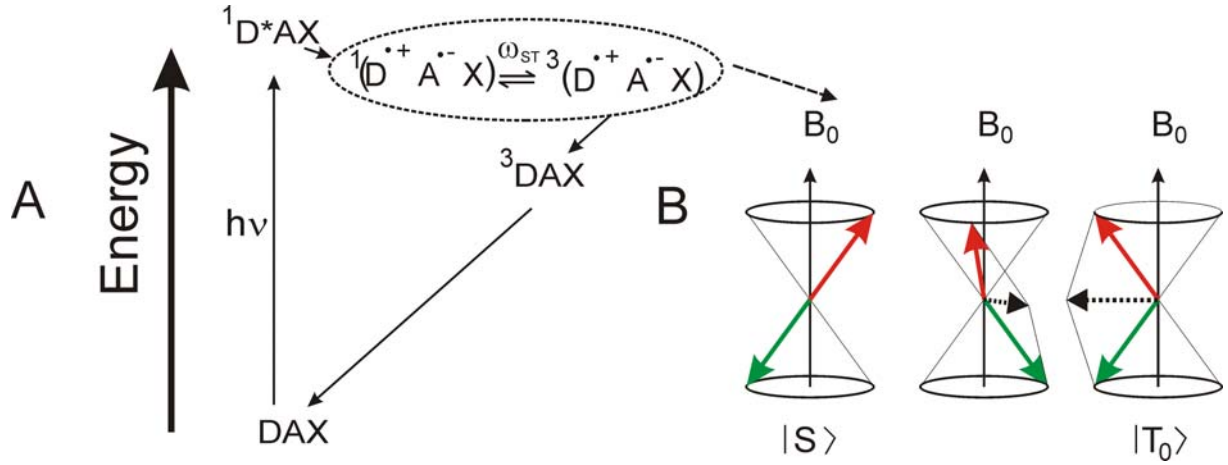

Figure 6.2: Triplet state generation *via* the radical pair mechanism in photosynthetic RCs with blocked electron transfer (from A to X). **A** Schematic energy diagramm of the charge separation and subsequent triplet state generation. D denotes the primary donor, A (primary) acceptor, and X the cofactor following A in the electron transfer chain, which is either reduced or removed. ω_{ST} is the singlet-triplet mixing frequency. **B** Vector diagram of singlet-triplet mixing in spin-correlated radical pairs. The green and the red arrow represent the two unpaired electron spins on D and A, respectively.

As an approximation, the spin density distribution (which is related to the hfccs) in the triplet state can be considered as a superposition of the spin density distribution in two molecular orbitals: the **h**ighest **o**ccupied **m**olecular **o**rbital (HOMO) and the **l**owest **u**noccupied **m**olecular **o**rbital (LUMO). The HOMO is the orbital probed by EPR spectroscopy if the primary donor is singly oxidized (radical cation $D^{\bullet+}$). The LUMO reflects properties of the excited state $^1D^*$, from which the electron transfer starts. The triplet state of the donor Chls in photosynthetic RC can be created if the electron transport to the 'secondary' electron acceptor molecules is blocked (see Figure 6.2 and Eq. 6.1).

$$DAX \xrightarrow{hv} {}^1D^*AX \rightarrow {}^1(D^{\bullet+}A^{\bullet-})X \overset{\omega_{ST}}{\Leftrightarrow} {}^3(D^{\bullet+}A^{\bullet-})X \rightarrow {}^3DAX \qquad (6.1)$$

In the charge separated state, singlet triplet mixing occurs through hyperfine interactions and *g*-value differences of electron donor (D) and acceptor molecules (A) with the rate ω_{ST}. Depending on the state of the RP in the moment when the recombination takes place, the RP can recombine to the singlet or triplet state of the donor molecule D. This special mechanism of triplet generation is called the radical pair mechanism. It leads to the selective population of the T_0 sublevel, and thus to a particular polarization pattern (Figure 6.3).[5;8] The blocking of the electron transfer beyond A can be achieved either by reduction or

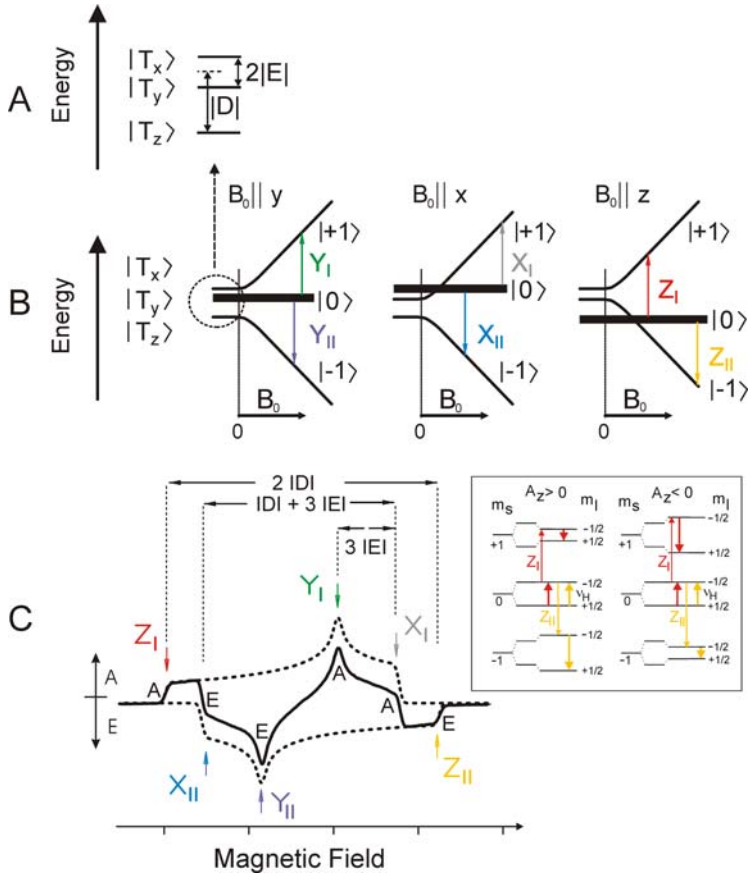

Figure 6.3: Triplet spin energy levels of ^{3}Chl and a spin polarized EPR spectrum. D and E are the ZFS parameters. In ^{3}Chl, D > 0, E < 0. **A** Triplet spin energy levels in zero external magnetic field. **B** Triplet spin energy levels in a strong external magnetic field. The thickness of the lines refers to the population of the respective level. The T_0 level (|0>) is selectively populated due to the radical pair mechanism. The arrows indicate the (allowed) EPR transitions for ZFS axes parallel to the magnetic field. **C** Spin polarized EPR spectrum, corresponding to scheme **B**. *g* is assumed to be isotropic. A denotes absorption, E emission. The observed EPR spectrum (thick line) is the sum of an emissive and an absorptive spectrum (dashed lines). A scheme of EPR and NMR transitions at two specific magnetic fields (corresponding to spectral positions Z_I and Z_{II}) is presented in the box.

by extraction of the cofactor X. The triplet states ^{3}D in photosynthetic RCs are short-lived states which usually decay in the microsecond to millisecond range to the neutral ground state D.[5;9] Hence, time-resolved techniques like transient EPR or pulse EPR are used to investigate these states .[10] [11;12]In triplet states, the particular polarization of the electronic levels leads to an overlap of EPR signals arising from different transitions, which can complicate the analysis of the ENDOR spectra considerably. Depending on the polarization of the excited EPR transition, the ENDOR spectra are also in emission or absorption. On the other hand, their transient nature can be also an advantage, since the signals of the triplet state can be differentiated from stationary signals, and the strong polarization of the electron spin states provides intense signals. In addition, the ZFS allows orientation selection in the ENDOR experiment.[8;13-15] This is not possible if investigating the donor radical cation $D^{\bullet+}$ at standard frequencies like X- or Q-band due to its small *g*-anisotropy.[10;16;17]

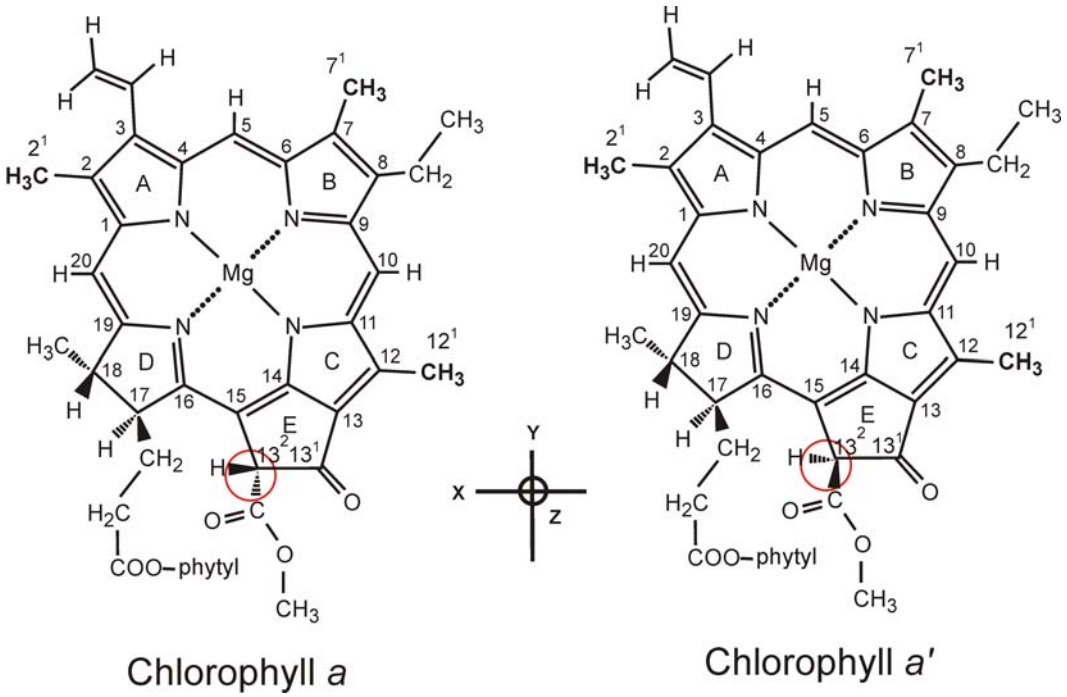

Figure 6.4: Molecular structures of Chl *a* and Chl *a′*, the 13^2 epimer of Chl *a*, and the ZFS principal axes according to refs. [14;18].

For the understanding of the electronic structure of protein bound cofactors, a comparison with model systems *in vitro* is vital, as can be seen in chapters 4 and 5 for the case of the quinone radical anions. As model systems for the Chl triplet states in PS I and PS II, monomeric Chl *a* and Chl *a´* (Figure 6.4) can be studied. The Chl molecules are typically dissolved in a suitable organic solvent, which needs to be a glass to achieve *in situ* light excitation of the sample (*e.g.* by a Laser). Chl *a* and Chl *a´ in vitro* have been already investigated previously by EPR and ENDOR spectroscopy. The *g*-tensor,[19] the ZFS tensor,[14;19;20] and a few ^{1}H hfccs been determined for one spectral orientation (magnetic field parallel to the Z axis of the ZFS tensor).[13;14] It was found that the lines in the ENDOR spectra of ^{3}Chl were not so well resolved as compared to $^{3}P_{680}$, indicating a less defined environment in the organic solvent as compared to the protein.

The mechanism of generation of Chl triplet states *in vitro* is different from the one which is found in photosynthetic RCs. The triplet state is created from the excited singlet state of the respective Chl *via* intersystem crossing (ISC).[5] Due to this mechanism not only the T_0 sublevel is selectively populated. Depending on the orientation of the Chl with respect to the magnetic field, also the T_{-1} and T_{+1} levels can be populated. This results in a different spin polarization pattern as compared to primary donor triplet states. At Z orientation single crystal like ENDOR spectra can be obtained. At X- and Y-orientation, the severe overlap of emissive and the absorptive ENDOR line precludes the analysis of the spectra. No investigations of ^{3}Chl *in vitro* were done. A comparison with other Chl triplet states *in vivo* seemed to be a better approach. A comparison with bacterial donor triplet states is not very promising, since the site of the triplet is chemically quite different (Bchls instead of Chls), and it is also electronically different from the one in PS I.[8;9;21] Thus, a comparison with the donor triplet state $^{3}P_{680}$ of PS II, which seems to be closer to PS I, was performed. It provides strong signals, which allows to optimise the experimental conditions for measurements of $^{3}P_{700}$.

The triplet state $^3P_{680}$ in PS II

Introduction

Photosystem II (PS II) catalyzes the light driven electron transfer from water to plastoquinone.[22;23] The multi protein complex consists of 20 subunits. PS II binds a number of cofactors, among them 35 Chls and 11 carotenoids, two pheophytin molecules, two plastoquinones, two hemes, the Mn_4Ca cluster, and one Fe^{2+}. According to the X-ray structure of *T. elongatus* PS II (currently at 3.0 Å), the central core of PS II, which harbors the electron transfer chain, is formed by 2x5 transmembrane helices, assigned to the protein subunits D1 (PsbA) and D2 (PsbD).[24] The arrangement of these subunits resembles the structure of the L and M subunit of the photosynthetic RC of purple bacteria, and the structure of the C-terminal domain of the large subunits PsaA and PsaB of PS I.[25;26]

The electron transfer chain consists of four Chls, two pheophytins (Ph), two plastoquinones, one redox active tyrosine (Y_Z) and the Mn_4Ca cluster.[27;28] The charge separation is preceded by capturing of light by the antenna system, which is much smaller than the antenna in PS I. The excitation of Chl(s) in the RC leads to a charge separation. The electron is transferred to a mobile plastoquinone, called Q_B, *via* a chain of electron carriers that include a pheophytin and a tightly bound plastoquinone molecule called Q_A (Figure 6.5). After two subsequent electron transfer steps the doubly reduced Q_B^{2-} binds two protons and leaves the binding site as plastohydroquinone. The empty binding site is then refilled by an oxidized plastoquinone from the membrane plastoquinone pool. In each round of the photocycle $P_{680}^{\bullet+}$ is re-reduced by extracting one electron from the Mn_4Ca-cluster with a redox active tyrosine (Y_Z) functioning as the intermediate electron carrier. After four subsequent electron transfer steps, *i.e.* when four positive charges have been accumulated at the Mn_4Ca-cluster, one molecule of oxygen is released.

In principle, each of the four Chls in the RC could represent the primary electron donor P_{680}.[28] Also more than one Chl might be involved as it was found for the BChls in the bacterial photosynthetic RC.[29] The Chls named P_{D1} and P_{D2} are oriented parallel to the membrane (Figure 6.5). Their center-to-center distance is about 8.2 Å, further separated from each other than the respective Chls in PS I[30] or the special pair BChls in photosynthetic reaction centers from purple bacteria.[31;32] The larger distance between these Chls in PS II indicates that they are not so strongly excitonically coupled and therefore may be even regarded as monomeric Chls. The second pair is located at a distance of ~10 Å from the first pair of Chls. The plane of the chlorine head group of these Chls is tilted at an

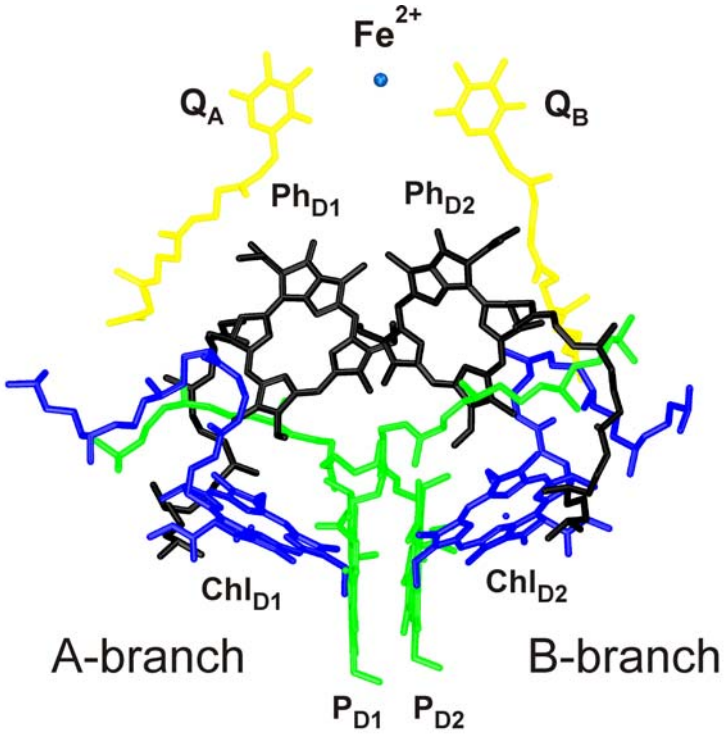

Figure 6.5: Arrangement of some organic cofactors of the electron transfer chain in PS II reaction center (green – Chls P_{D1} and P_{D2}; blue - accessory Chls Chl_{D1} and Chl_{D2}; black – pheophytins Ph_{D1} and Ph_{D2}; yellow – plastoquinone-9/Q_A and Q_B in the A- and B-branch, respectively) according to the 3.0 Å X-ray structure[24] (PDB entry 2AXT).

angle of 30° to the membrane plane. Using EPR spectroscopy on oriented photosynthetic membranes[33] and PS II single crystals,[34] it was shown that the triplet state $^3P_{680}$ at low

temperatures is located on one of the accessory Chls, Chl_{D1} or Chl_{D2}. The distance between $Q_A^{\bullet-}$ and $^3P_{680}$ was determined by pulse EPR (ESEEM) measurements,[35] and revealed that Chl_{D1} is the site where the triplet is localized. In contrast, the long-lived radical cation $P_{680}^{\bullet+}$ is located on P_{D1} and P_{D2}.[28;36] Despite the different location of long-lived radical cation and the transient triplet state, the standard term $^3P_{680}$ for naming the recombination triplet state in PS II is commonly used and will be used in the following.

For investigation of the triplet state $^3P_{680}$, a PS II preparation which contains solely the part of PS II which is involved in the initial charge separation steps is used. This minimizes possible problems caused by other light-induced reactions which may occur in the complete PS II complex. In addition, this minimizes the amount of antenna Chls which are not involved in the charge separation. This provides the possibility of a high concentration of PS II in the sample while still having sufficient transparency at the excitation wavelength (here: 532 nm). On the other hand, it needs to be assured, that the cofactors arrangement is not different in preparations of the whole PS II complex. The D_1D_2cytb_{559} complex[37] fulfills all the conditions stated above.[36;38] The D_1D_2cytb_{559} complex used in this work[39] contains six Chls *a*, two pheophytins *a*, and one or two β-carotenes. It carries no quinones and most probably has no non-heme iron. Thus, the electron transport from the pheophytin molecule (Ph_{D1}) to Q_A is blocked. Upon illumination the spin polarized triplet state $^3P_{680}$ in PS II is created:

$$P_{680}Ph_{D1} \xrightarrow{hv} {}^1P_{680}^{*}Ph_{D1} \rightarrow {}^1(P_{680}^{\bullet+}Ph_{D1}^{\bullet-}) \overset{\omega_{ST}}{\Leftrightarrow} {}^3(P_{680}^{\bullet+}Ph_{D1}^{\bullet-}) \rightarrow {}^3P_{680}Ph_{D1} \qquad (6.2)$$

Results and Discussion

EPR and ENDOR studies at low temperatures

Figure 6.6 shows transient EPR spectra of $^3P_{680}$ at X-band and at Q-band, and Figure 6.7 (Insert) a pulse EPR spectrum of $^3P_{680}$ at Q-band (all at 10 K). They show an AEEAAE

polarization pattern, which is typical for triplet states created by the radical pair mechanism (see also Figure 6.3). The two transient spectra appear almost identical, showing that the ZFS tensor represent the most important magnetic interaction for the EPR spectrum. The transient X-band spectrum has slightly better signal to noise ratio (similar accumlation time.) In the pulse Q-band spectrum somewhat more intensity on some canonical orientations and a more intense emissive Y component is observed. This is in agreement with previous pulse X-band and pulse D-band studies.[14;40] It was previously explained by the stronger influence of relaxation processes on the pulse EPR spectra.[14]

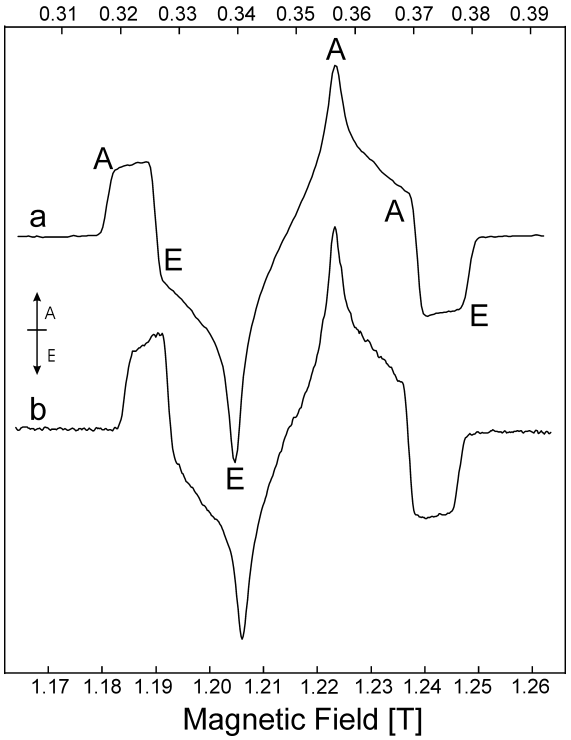

Figure 6.6: Transient EPR spectra of $^{3}P_{680}$ at 10 K. Spectrum **a**: X-band spectrum. Spectrum **b**: Q-band spectrum. A = absorption, E = emission.

Pulse X-band EPR spectra were also recorded and found to be strongly dependent on the interpulse distance τ due to strong modulations arising from the nitrogen atoms coordinating

the central Mg^{2+} ion (data not shown). The ZFS parameters obtained from the simulation of the spectra (|D| = 0.0288 cm^{-1}, |E| = 0.0042 cm^{-1}) resemble those obtained previously, see *e.g.*[14;40;41] The ZFS parameter of $^3P_{680}$ are very similar to those of monomeric Chl *a in vitro*.[14;19] This can be interpreted as a localization of the triplet exciton on a monomeric Chl.[41;42] At 10 K the decay of the EPR signal after the Laser flash is in the range of milliseconds, with the amplitude at Z-orientation decreasing slightly slower than at the other canonical orientations (data not shown).

Pulse Q-band ^1H ENDOR spectra recorded at different field positions are presented in Figure 6.7. Several absorptive and emissive ENDOR lines are resolved. Only at orientations **a** and **b** (Z_I and Z_{II} orientation) pure absorptive or emissive ENDOR lines are observed. The narrow lines observed at these spectral positions also indicate that this is a single crystal like position. Only Chl molecules with its plane perpendicular to the external magnetic field are probed (Figure 6.4). For this orientation a short explanation of the ENDOR spectra of this spin polarized triplet state is given with help of Figure 6.3. Since in $^3P_{680}$ S = 1 and D > 0, ENDOR transitions arising from protons (I = ½; $g_H > 0$) with a hfcc > 0 have at spectral position **a** (Z_I orientation) an ENDOR frequency smaller than the Larmor frequency (lines 1-5), and higher than the Larmor frequency for negative hfcc (lines 6-12). For position **b** (Z_{II} orientation) the situation is reverse. The superposition of absorptive and emissive ENDOR lines at spectral positions **d-g** can be explained by the overlap of the absorptive and emissive EPR spectra (Figure 6.3). A narrow and intense 'matrix' line is observed in all spectra. This is due to the ENDOR transition in the $m_S = 0$ manifold. The ENDOR linewidth of some peaks from weak to medium hfccs was found to be smaller than 100 kHz (*e.g.* line 8). This is already at the limit of the resolution in the ENDOR spectra. Hence, additional high resolution ENDOR spectra with more points and longer RF pulses were recorded. They did not show significantly

improved resolution (data not shown). Therefore, the 'standard' conditions (see chapter 3) were applied for all ENDOR measurements.

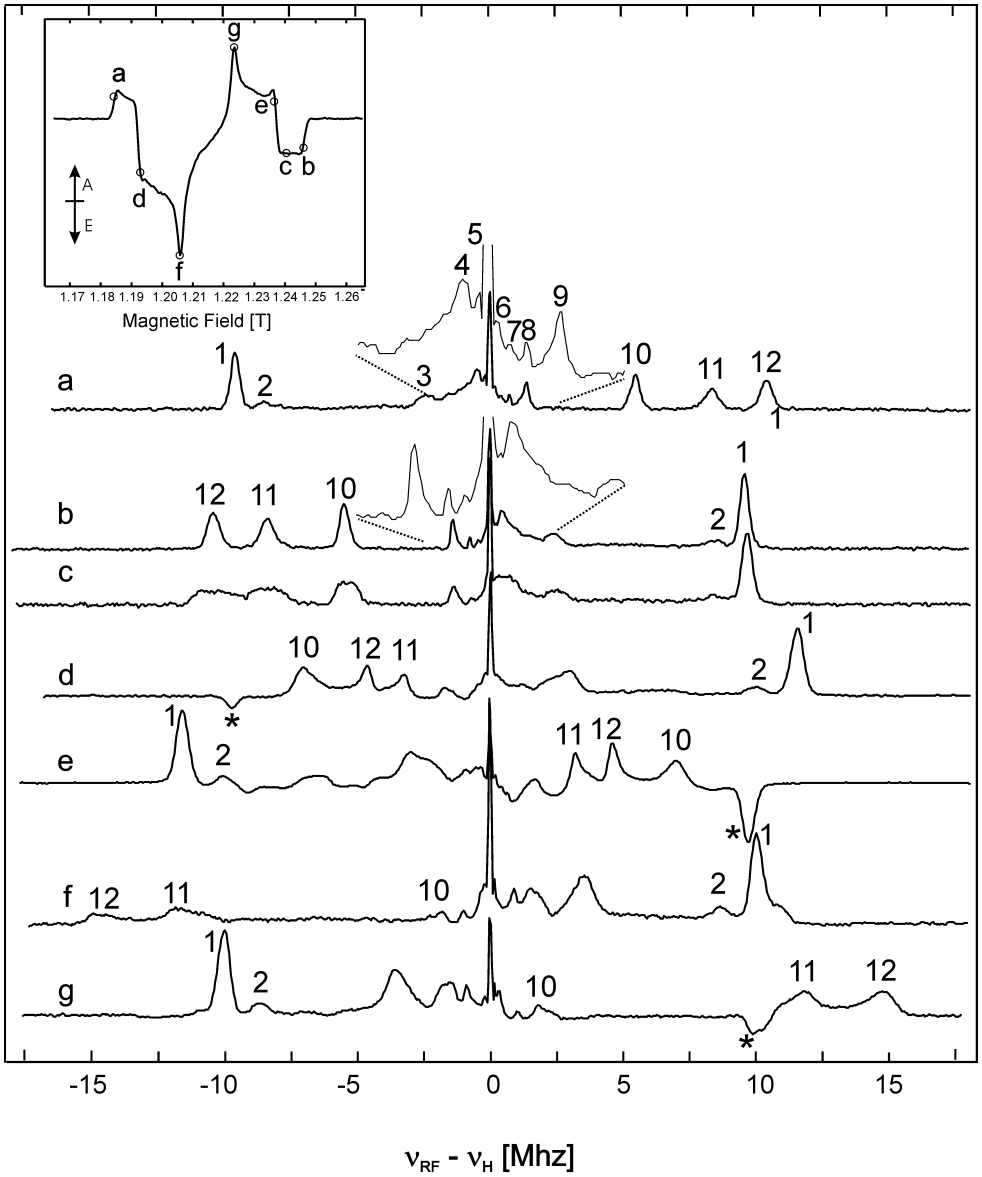

Figure 6.7: Pulse Q-band ^{1}H ENDOR spectra of $^3P_{680}$ at 10 K (DAF = 1 µs, no 'dark' background). Insert upper left corner: Corresponding pulse Q-band EPR spectrum (corrected for 'dark' background). The field positions, at which the presented ENDOR spectra are measured, are marked with letters. For better comparison, all ENDOR spectra are presented as absorptive spectra. The asterisks mark some prominent examples of ENDOR lines with different polarization.

There have been two previous ENDOR studies on $^3P_{680}$: a transient ENDOR study at X-band by Di Valentin *et al.*,[13] and a pulsed (Davies) ENDOR study at X-band by Lendzian *et al.*[14] The hfccs determined in these works are in excellent agreement with the ones determined here

(Table 6.1). Pulse (Davies) ENDOR is usually considered to be better than transient ENDOR for the detection of strongly coupled protons, and less suited for the detection of weak to medium coupled protons (where transient ENDOR is better). However, under the higher resolution conditions used here (long RF and MW pulses), more lines from weakly coupled protons are resolved than in the transient ENDOR study. The ^{1}H hfccs and their tentative assignment is presented in Table 6.1, based on the previous ENDOR studies on $^3P_{680}$,[13;14] hfccs of Chl $a^{\bullet-}$ and Chl $a^{\bullet+}$ in liquid solution[43] and DFT calculations of Chl $a^{\bullet-}$ and Chl $a^{\bullet+}$.[44]

Only the most important hfccs and their assignment are discussed in the following. The assignment of the small hfccs to molecular positions is complicated, since a large number of protons in a ^{3}Chl molecule can exhibit small hfccs.[6;43] The three large negative hfccs (lines 10, 12, 11) arise from the methine protons **5**, **10** and **20** (α-protons). The most prominent positive hfcc (line 1) arise from the methyl group at position **12**.

Table 6.1: ^{1}H hfccs in $^3P_{680}$ in D_1D_2cytb_{559} complexes at low temperature as determined by ENDOR spectroscopy (MHz) and tentative assignment. n.a. means not assigned.

	12 (CH_3)	**2 (CH_3)**	**7 (CH_3)**	**n.a.**	**n.a.**	**n.a.**	**5 (α)**	**10 (α)**	**20 (α)**	**n.a.**	**n.a.**	**n.a.**	
$\mathbf{A_x}$	+9.6	+8.4	+2.4	+3.3/6.5 (broad)	+0.4	+0.2	-5.5	-10.4	-8.4	-1.4	-0.8	-0.5	this work
$\mathbf{A_z}$	+9.5						-5.5	-10.4	-8.4				a
$\mathbf{A_z}$	+9.6				+0.6		-5.4			-1.4	-0.7		b
$\mathbf{A_y}$	+10.0	+8.7	+3.6	+1.6	+0.9	+0.2	-1.8	-14.8	-11.8		-1.0		this work
$\mathbf{A_y}$	+10.0						-1.8	-14.8	-11.8				a
$\mathbf{A_x}$	+11.5	+10.0	+2.9		+1.2		-7.0	-4.7	-3.3	-1.7			this work
$\mathbf{A_x}$	+11.4						-7.1	-4.7	-3.3				a
$\mathbf{a_{iso}}$[c]	+10.4	+9.0	+3.0		+0.8		-4.8	-10.0	-7.8	-1.5			this work
$\mathbf{a_{iso}}$[c]	+10.3						-4.8	-10.0	-7.8				a

[a] from X-band pulse ENDOR at 10 K[14]
[b] from X-band transient ENDOR at 10-20 K[13]
[c] $a_{iso} = \frac{1}{3}\mathrm{Tr}(\mathbf{A}) = \frac{1}{3}(A_x + A_y + A_z)$

The second largest positive hfcc (line 2) could arise from the methyl group at position **2**, but is much larger than expected from the average of the isotropic hfccs in Chl $a^{\bullet-}$ and Chl $a^{\bullet+}$ in liquid solution.[43] Also its intensity is much lower than that of line 1. Slow nuclear relaxation due to hindered rotation of the methyl group has been proposed as an explanation for this behaviour.[14] To investigate this hypothesis, ENDOR experiments were repeated at position **b**, but with a lower repetition rate of 3.3 Hz instead of the 'standard' 10 Hz. Identical ENDOR experiments were also performed at elevated temperature (10 Hz at 30 K, data not shown). In both cases, the relative intensity of line 2 to line 1 stayed approximately the same. The nuclear relaxation might be still too slow at 30 K, demanding higher temperature to observe 'normal' intensity of this ENDOR line. Due to the worse yield and rapid decay of the EPR signal at higher temperatures, ENDOR experiments did not yield a sufficient signal to noise ratio to resolve this issue (data not shown).

The set of hfccs determined for $^3P_{680}$ fits quite well to a monomeric Chl *in vitro*, confirming that $^3P_{680}$ is indeed a monomeric Chl (see also ref. [14]). Small differences indicate an influence of the protein surrounding on the spin density distribution in ^{3}Chl *in vivo* ($^3P_{680}$). The quite narrow lines from the methyl group at position 12 and the three methine protons at the canonical orientations X and Z demonstrate that the ZFS axes are close to collinear with hf tensor principal axes. Thus, the orientation of the ZFS axes presented in Figure 6.4 for Chl *a* *in vitro* is also valid for $^3P_{680}$ (see also ref. [14]).

EPR studies at elevated temperatures

Figure 6.8 presents transient EPR spectra of $^3P_{680}$ recorded at different temperatures at X-band. In the low temperature region the spectra are almost identical to the ones recorded at

10 K. Around 100 K the spectrum starts to change. The amplitude at the Z-orientation decreases and additional features appear in the spectra. At temperatures larger than 200 K, the spectra have very low intensity at the positions of the low temperature Z-orientation. The pattern is quite broad and without the sharp edges observed at low temperatures. The polarization pattern changes from AEEAAE to AEAE. There are also noticeable 'wings'

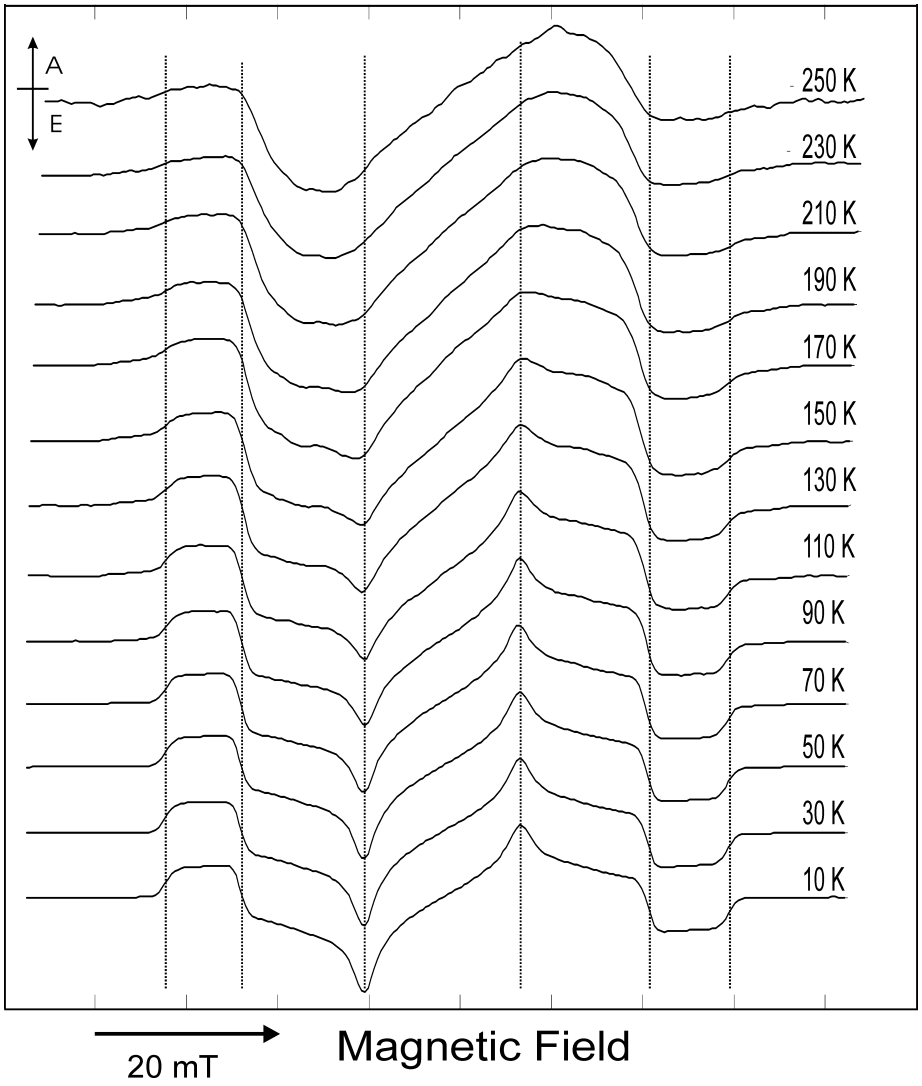

Figure 6.8: Transient X-band EPR spectra of $^3P_{680}$ at different temperatures. The dashed lines indicate the positions of the low-temperature X, Y and Z orientation.

at more extreme field position than the Z-orientations. Similar observations were also made in previous X-band studies on the temperature dependence of $^3P_{680}$.[45;46] Due to the different signal to noise ratio in these studies the detection of the broad 'wings' and the low intensity

Z-peak was sometimes difficult. In these two studies, different interpretations of the spectra were given. Bosch *et al.* explained the observed temperature dependence with selective, anisotropic relaxation of the precursor radical pair.[45] In contrast, Kamlowski *et al.* explained their results as a transition between two triplet states of different electronic origin.[46] In one of the states the triplet is located on a monomeric Chl (corresponding to Chl_{D1}), while in the second one the triplet is delocalized over at least two Chls with non-collinear ZFS axes (corresponding to Chl_{D1} and P_{D1}). These two states are the limiting cases at low and high temperature, while at intermediate temperatures the EPR spectra can be explained in terms of a superposition of the EPR spectra of the two limiting cases. The coefficients of this superposition follow a sigmoidal temperature dependence. Kamlowski *et al.* proposed as an explanation a distribution of activation energies for the delocalization process. In a later study by the same authors, using oriented PS II membrane fragments, Frankenmöller *et al.* found that the orientation of the ZFS axes changes at high temperature, confirming their previous interpretation of delocalization of the triplet exciton at higher temperature.[47] A FTIR study of the $^3P_{680}$ triplet state was also interpreted as a temperature dependent delecolization of the triplet exciton on a second Chl.[48;49] In a recent high-field EPR studie, the temperature dependence was also interpreted as a result of hopping of the triplet exciton.[40] The broad outer wings observed in the EPR spectra at higher temperature were explained in terms of a delocalization of the triplet exciton to a pheophytin (Ph_{D1}) in addition to the two Chls. The model of temperature dependent delocalization of the triplet excition is also strongly supported by a recent DFT study[50], which explained optical spectra of $^3P_{680}$ at different temperatures.[51;52]

It is concluded that at low temperature the triplet excition is located on the Chl_{D1}, while at higher temperature the triplet excition becomes delocalized, populating a second Chl (P_{D1}) and the pheophytin Ph_{D1}.

The triplet state $^3P_{700}$ in PS I

Introduction

According to the X-ray structure P_{700} is a Chl (hetero)dimer, which consists of one Chl *a* molecule (P_B, B-branch) and one Chl *a*′ molecule (P_A, A-branch).[30;53] Chl *a*′ is the 13^2 epimer of Chl *a*, in which the two substituents at the position 13^2 are interchanged (Figure 6.4). The two Chl rings are approximately parallel to each other and overlap at the pyrrole rings A and B (Figure 6.9). The interplanar distance is about 3.6 Å. Both Chls show only a slight deviation from planarity. Both have an axial ligand to the central Mg ion provided by a histidine residue from the two large subunits PsaA and PsaB. There are no hydrogen bonds to the Chl *a* molecule (P_B), but to the Chl *a*′ (P_A) exists a hydrogen bonding network from amino acids and water molecules. The 13^1 keto group carbonyl oxygen is the acceptor of a H-bond from threonine A743. In addition, the carboxy ester oxygen of the 13^2 carbomethoxy group is H-bonded by water. Three other amino acid residues Tyr A603, Ser A607 and Thr A743 are putative hydrogen bond partners of this water molecule. In each of the two branches, two additional Chls are found. These are the accessory Chls and the A_0 Chls. Upon light excitation the excited singlet state of the primary donor Chls is generated. In the subsequent steps several radical pairs are created, including $P_{700}^{\bullet+}A_0^{\bullet-}$ and $P_{700}^{\bullet+}A_1^{\bullet-}$. If the electron transfer beyond the acceptor A_0 is blocked, the triplet state $^3P_{700}$ is formed:

$$P_{700}A_0 \xrightarrow{h\nu} {}^1P_{700}^{*}A_0 \rightarrow {}^1(P_{700}^{\bullet+}A_0^{\bullet-}) \overset{\omega_{ST}}{\Leftrightarrow} {}^3(P_{700}^{\bullet+}A_0^{\bullet-}) \rightarrow {}^3P_{700}A_0 \qquad (6.3)$$

In this work, this has been realized by reduction of the acceptor quinone A_1. The extraction of the phylloquinone by treatment of PS I with organic solvents is also possible and yields

essentially the same EPR spectra[54;55]. At high temperature, the generation of the triplet state $^3P_{700}$ is also possible from the radical pair $P_{700}^{\bullet+}A_1^{\bullet-}$, if the Fe-S clusters are pre-reduced.[56;57]

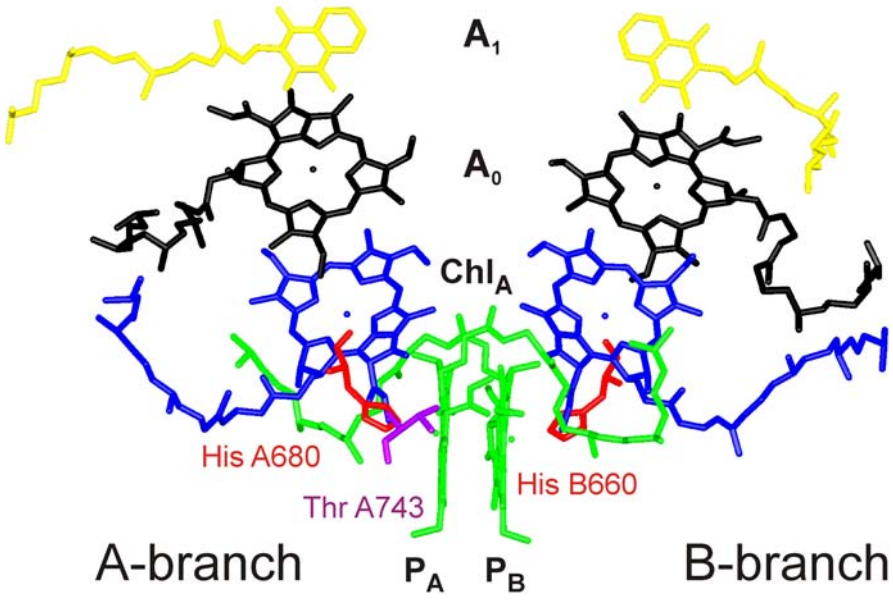

Figure 6.9: Arrangement of organic cofactors in the electron transfer chain of PS I (green – Chls P_A and P_B; blue - accessory Chls Chl; black – A_0 Chls; yellow-VK_1/A_1) according to the 2.5 Å X-ray structure[53] (PDB entry 1JB0).

Previous EPR experiments on oriented photosynthetic membranes at low temperature showed that $^3P_{700}$ is localized on one or more Chl(s) with their plane perpendicular to the membrane.[42] This corresponds to the Chls P_A and/or P_B. A real delocalization as observed in bacterial photosynthetic RC[29] was excluded, since the ZFS parameters are close to those of monomeric Chl *in vitro*, and only slightly smaller than those in $^3P_{680}$.[14;42] At higher temperature the transient EPR spectra change, but in a different way than in case of $^3P_{680}$. The general shape and polarization pattern AEEAAE is maintained, but the |E| value decreased considerably (about 40%), while |D| remained unchanged. In a large intermediate temperature

range no EPR spectra with sufficient signal to noise ratio were obtaind.[54;55] Two models were suggested:

i) slow hopping of the triplet exciton at low temperature, probably on both (parallel) P_{700} Chls P_A and P_B, which becomes faster at higher temperatures

ii) temperature activated hopping of the triplet exciton. The exciton hops rapidly, but asymmetrically between the two dimer Chls.

To experimentally address this problem, several methods were applied, which have shown to be successful in the investigation of the triplet state $^3P_{680}$ in PS II. For the localization of $^3P_{700}$, single crystal EPR measurements were attempted. ESEEM measurements were performed to determine the position of the triplet state within the PS I complex. ENDOR spectroscopy was applied to determine the hfccs of $^3P_{700}$. Temperature dependent transient EPR spectra were recorded with the goal of better signal-to-noise ratio in the intermediate temperature range, enabling the understanding of the temperature dependence of the |E|-value.

Results and Discussion

The measurements conducted on $^3P_{700}$ turned out to be much more complicated than the ones on $^3P_{680}$. The EPR signals of $^3P_{700}$ are much weaker and the accumulation of a stationary background signal ($A_0^{\bullet-}$) occurred under the repetitive light excitation of the samples. These problems were also observed previously.[20] PS I molecules with photoaccumulated $A_0^{\bullet-}$ do not contribute anymore to the $^3P_{700}$ signal (under the illumination conditions used here the 'lifetime' of the $^3P_{700}$ signal is about 60-90 minutes).

EPR and ENDOR studies at low temperatures

Single crystal EPR measurements are not possible with 'normal' PS I single crystals, since it was found that already a short incubation with small concentration of a reductant (*e.g.* sodium dithionite) leads to dissolution of the crystal.[58;59] The generation of reduced PS I crystals was thus attempted with PS I-Ferredoxin co-crystals (in collaboration with the group of P. Fromme).[60] These co-crystals are much more stable at elevated ionic strength of the surrounding solution. However, the measurements on the reduced co-crystals did not show any transient EPR signal of $^3P_{700}$.

The second direct way to obtain structural information is the determination of the distance between $A_1^{\bullet-}$ and $^3P_{700}$ with ESEEM methods. Borovykh *et al.* introduced this method to determine the distance between $^3P_{865}$ and $Q_A^{\bullet-}$ in bacterial photosynthetic RCs.[61] In the case of $Q_A^{\bullet-}$ and $^3P_{680}$ in PS II this method turned out to be also successful.[35] However, in the case of PS I, only strong modulations arising from the radical pair $P_{700}^{\bullet+}A_1^{\bullet-}$ were visible, but no modulation arising from the interaction within the triplet –radical pair were seen.

The investigation of $^3P_{700}$ using ENDOR spectroscopy was more successful; the first ENDOR spectrum of $^3P_{700}$ was obtained (Figure 6.10).

The Q-band pulse EPR spectrum is similar to the one from $^3P_{680}$, showing the typical polarization pattern of a Chl triplet state generated *via* the radical pair mechanism. The |D|- and |E|-values (|D| = 0.0278 cm^{-1}, |E| = 0.0038 cm^{-1}) are slightly smaller than the ones from $^3P_{680}$ (|D| = 0.0288 cm^{-1}, |E| = 0.0042 cm^{-1}). The ENDOR spectra show a worse signal-to-noise ratio than in case of $^3P_{680}$. However, a few lines can be identified and assigned to molecular positions (Table 6.2).

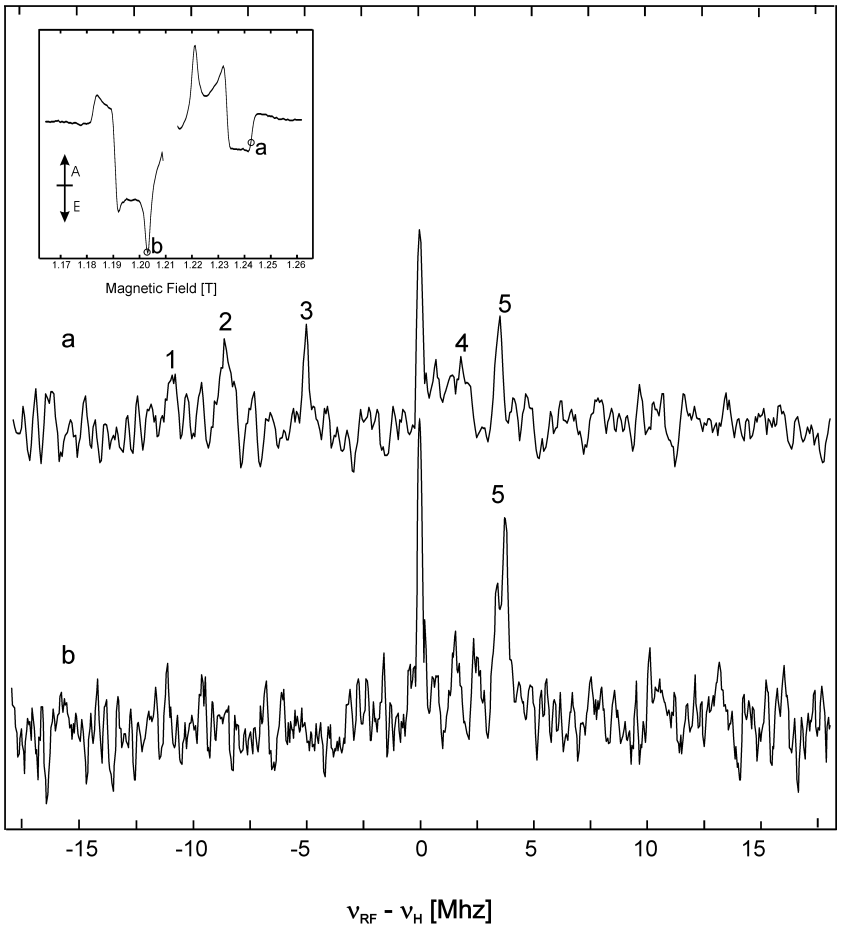

Figure 6.10: Pulse Q-band ^{1}H ENDOR spectra of $^{3}P_{700}$ (DAF = 1 µs, no 'dark' background) at 30 K. Insert in upper left corner: reference pulse Q-band EPR spectrum (spectrum around g = 2 omitted for clarity, there are strong signals due to the radical pair $P_{700}^{\bullet+}A_1^{\bullet-}$). The field positions, at which the presented ENDOR spectra are measured, are marked with letters. For better comparison, both ENDOR spectra are presented as absorptive spectra.

The lines 1 to 3 are associated with negative hfccs, and are assigned to the methine protons (**5**, **10**, **20**). The hfccs are very similar to those in $^{3}P_{680}$. Surprisingly, no ENDOR signals from protons with large positive hfccs are detected. In $^{3}P_{680}$ only one large hfcc from the methyl group at position **12** provided a strong signal. In case of $^{3}P_{700}$, these could be a similar effect as in $^{3}P_{680}$: hindered rotation of the methyl group slows down the nuclear relaxation and thus suppresses the methyl group signal. The presence of three large negative hfccs with similar magnitude than in ^{3}Chl *in vitro*[14] and $^{3}P_{680}$ strongly supports the suggestion that $^{3}P_{700}$ is located on one monomeric Chl at low temperature.

Table 6.2: Comparison of ^{1}H hfccs in $^3P_{700}$ in PS I and $^3P_{680}$ in PS II, as determined at low temperature by ENDOR spectroscopy (MHz) and tentative assignment. n.a. means not assigned.

	12 (CH_3)	**2 (CH_3)**	**7 (CH_3)**	**n.a.**	**5 (α)**	**10 (α)**	**20 (α)**	
$\mathbf{A_z}$	+9.6	+8.4	+2.4		-5.5	-10.4	-8.4	$^3\mathbf{P_{680}}$
$\mathbf{A_z}$			+3.5	+1.7	-5.0	-10.9	-8.5	$^3\mathbf{P_{700}}$
$\mathbf{A_y}$	+10.0	+8.7	+3.6		-1.8	-14.8	-11.8	$^3\mathbf{P_{680}}$
$\mathbf{A_y}$			+3.6					$^3\mathbf{P_{700}}$

The data presented above do not resolve the question if the triplet is located on the monomeric Chl P_A or P_B. On the basis of FTIR measurements on $^3P_{700}$ and $P_{700}^{\bullet+}$, it has been suggested that the triplet is located on P_A.[62] In the $P_{700}^{\bullet+}$-P_{700} difference spectra signals from two Chls were detected, while in the $^3P_{700}$-P_{700} difference spectra only signals from the Chl with lower frequency vibrations of the carbonyl group at position 13^1 and the ester group at position 13^2 were observed (see Figure 6.4, ring E). Since only the Chl P_A shows hydrogen bond interactions to the protein environment and close by water molecules,[53] it has been assigned to the site of the triplet excition. ODMR measurements were performed on PS I of a series of mutants, where the axial histidine ligands to the central Mg^{2+} of P_A and P_B were exchanged for His. The more pronounced effect was found for P_B, and thus it was concluded that P_B carries the triplet excition at low temperature.[63] This contradiction can not be solved on the basis of the present data. However, in future DFT calculations of the triplet state located on P_A or P_B proton hfccs could be calculated. The comparison of the calculated hfccs for the two cases with the hfccs observed experimentally could finally answer this question.

EPR studies at elevated temperatures

Figure 6.11 presents transient EPR spectra of $^3P_{700}$ recorded at different temperatures at X-band. In the low temperature region the spectra are almost identical to the one recorded at 15 K. Above 150 K the spectrum starts to change. The spectral positions X and Y come closer to each other ($(\Delta|E|/\Delta T > 0)$ with increasing temperature, while the spectral position Z stays the same ($\Delta|D|/\Delta T = 0$). This trend continues after increasing the temperature up to room temperature, with the overall polarization pattern being conserved. The |D|- and |E|-values are summarized in Table 6.3. The spectra are very similar to the ones obtained by Sieckmann *et al.*,[54] in the low temperature ($T \leq 50$ K) and high temperature region ($T \geq 280$ K), but show a superior signal-to-noise ratio. In contrast to Sieckmann *et al.*, who did not succeed to record EPR spectra with sufficient signal-to-noise ratio in the intermediate temperature range, the triplet state $^3P_{700}$ could be recorded over the complete temperature range. An explanation suggested by Sieckmann *et al.* about the reason for their difficulties recording EPR spectra in the intermediate temperature range is line broadening. This can be excluded on the basis of the data presented here. Following the argumentation of Sieckmann *et al.*, the temperature dependence of the |E|-value in $^3P_{700}$ can be explained as a result of changes in the localization of the triplet state. At low temperature, the triplet state is localized on a monomeric Chl, while at high temperature the triplet exciton is delocalized over two Chls. Since the |D|-value is not temperature dependent, and taking the orientation of the ZFS-axes in Chls into account (Figure 6.4), the two Chls must have a parallel arrangement of the planes. In case of two parallel Chls like in P_{700}, the |D|-value will not change if the triplet exciton is delocalized on both Chls. But the |E|-value will be effected, if the in-plane ZFS axes differ by the angle of the ZFS axes of the two Chl with respect to each other.[54;55] In the case of the P_{700} dimer, the molecular axes of P_A and P_B (and thus also the ZFS axes) are rotated with respect to each other.[53] Two different mechanisms were proposed by Sieckmann *et al.* to explain the

temperature dependence of the |E|-value. In the first mechanism the rate of the hopping of the triplet exciton between the two Chls increases with temperature, starting from slow hopping at low temperature (spectrum monomeric Chl) to fast hopping at high temperature (triplet delocalized on two Chl). This mechanism is analogous to the line broadening and coalescence phenomena for two interconverting spins at different resonance frequencies.[64] Intermediate hopping rates would result in line broadening at X and Y positions, while narrow lines are observed at slow and high hopping rates. In the EPR spectra, no broadened features at X and Y position were observed in the intermediate temperature range, and the |E|-value continuously decreases with increasing temperature.

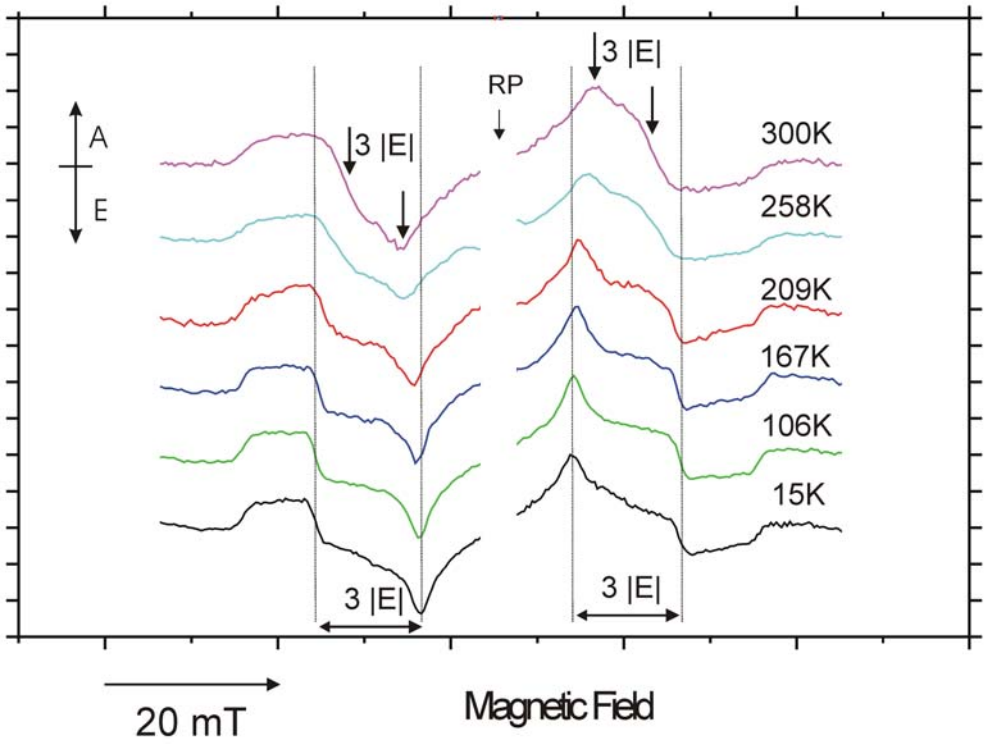

Figure 6.11: Selected X-band transient EPR spectra of $^{3}P_{700}$ at different temperatures. The dashed lines indicate the positions of the low-temperature X, Y and Z orientation.

The slow hopping at low temperature would result in an ENDOR spectrum with two different sets of hfccs of the two Chl (assuming that both Chls have not identical ^{1}H hfccs,

which is highly unlikely considering the differences of the two Chl structures and their environment[53]). This is not observed in the ENDOR spectrum of $^3P_{700}$ (see Figure 6.10 and discussion above). This mechanism proposed by Sieckmann *et al.* clearly does not match the experimental observations and is excluded therefore.

This leaves the second mechanism proposed by Sieckmann *et al.* to be most likely. In this mechanism the excitation hops rapidly but asymmetrically between the two halfs of the dimer, due to two energetically different Chls in the P_{700} dimer. The resulting |E|-value is depending on the population of the two Chls and the angle of the ZFS axes of the two Chls with respect to each other:

$$\left|E^*\right| = \frac{1}{2}\sqrt{1-4p_1p_2\sin^2\alpha}\left(D_{xx}-D_{yy}\right) = \left|E\right|\sqrt{1-4p_1p_2\sin^2\alpha} \qquad (6.4)$$

where $|E^*|$ means the |E| value at a certain temperature, p_1 and p_2 the equilibrium populations of the exciton on one of the Chls, |E| the low temperature value (monomeric Chl) and α the angle between the in plane ZFS axes of the two Chls.[54] At low temperature, the population $p_2 = 0$, and thus $|E^*| = |E|$. With increasing the temperature the population on the second Chl increases, and the distribution becomes more symmetric. When the temperature is high enough compared to the energy gap between the two Chls, the delocalization will be symmetric, with $p_1 = p_2$. In this case, Eq. 6.4 can be written as follows: $\left|E^*\right| = \left|E\right|\cos\alpha$. The assumption of complete delocalization at room temperature delivers an angle $\alpha \sim 55°$. This does not fit to the X-ray structure, if the same ZFS axes are present here as in monomeric Chl *in vitro* or in $^3P_{680}$ in PS II. However, Vrieze *et al*. suggested a rotation of the triplet ZFS axes as compared to Chl *in vitro.*[18] The angle fits well, if the ZFS axes are collinear with the two lines connecting the nitrogen atoms of pyrrol ring A and C, and B and D (Figure 6.4). It has to be mentioned, that in principle, another explanation for the temperature dependence of the

Table 6.3: The ZFS parameters |D| and |E| of $^3P_{700}$ obtained from the transient EPR spectra.

Temperature [K]	|E| [10^{-4}cm^{-1}]	|D| [10^{-4}cm^{-1}]
15	**38 ±2**	**278 ±4**
35	38 ±2	278 ±4
55	38 ±2	279 ±4
70	38 ±2	278 ±4
86	38 ±2	280 ±4
106	**38 ±2**	**280 ±4**
126	37 ±2	280 ±4
147	37 ±2	280 ±4
167	**36 ±2**	**280 ±4**
177	35 ±2	279 ±5
188	35 ±2	280 ±5
198	34 ±2	280 ±5
209	**33 ±3**	**281 ±5**
219	32 ±3	279 ±5
223	32 ±3	280 ±5
228	31 ±3	280 ±6
238	30 ±3	280 ±6
248	29 ±3	281 ±8
258	**27 ±3**	**280 ±8**
268	26 ±3	280 ±8
279	25 ±3	280 ±8
289	23 ±3	278 ±8
300	**23 ±3**	**277 ±8**

|E|-value can be given.[54] The triplet could be localized on one Chl over the whole temperature range. The |E|-value would be reduced at higher temperature because of thermal population of a low lying vibronically excited triplet state of the same Chl, or the spatial spin distribution of the localized triplet state changes as a function of the temperature as result of structural change, *e.g.* due to a phase transition.[55] Considering the extent of the change of the |E|-value, and the structural information available about the two P_{700} Chls (short interplanar distance, differences in the environment of two Chls, which could easily cause an energetic difference between the two Chls), this is quite unlikely.

Conclusions

The short-lived triplet states $^3P_{680}$ of PS II and $^3P_{700}$ of PS I were investigated by transient EPR, pulse EPR and pulse ^1H ENDOR spectroscopy. In case of $^3P_{680}$, previous results concerning the temperature dependence of the EPR spectra were confirmed.[40;45;46] New proton ENDOR lines were detected due to the high resolution of the spectra.

The experiments on the triplet state $^3P_{700}$ in PS I turned out to be much more complicated than for $^3P_{680}$. Attempts to obtain structural information regarding the site of the Chl which carries the triplet exciton at low temperature, using ESEEM techniques and single-crystal EPR, were not successful. However, the first ENDOR spectra of $^3P_{700}$ were recorded and the monomeric nature of $^3P_{700}$ at low temperature could be confirmed. Transient EPR was performed on $^3P_{700}$ over the whole temperature range from helium temperature to room temperature. A more complete set of spectra than in previous studies was obtained.[54;55] It was shown that the temperature dependence of the |E|-value is continuous and not stepwise. One of the mechanisms proposed previously to explain the temperature dependence[54;55] can be excluded on the basis of the data obtained here. Further evidence for the delocalization of the triplet excition at higher temperature can be provided from ENDOR spectra of $^3P_{700}$ with sufficient signal-to-noise ratio at all three canonical orientation. If the ZFS axes are really significantly rotated, the ENDOR lines recorded at spectral positions X and Y should be much broader.

Advanced DFT calculations of the EPR parameters of the triplet states could be of great help for the interpretation of the EPR and ENDOR spectra. With the X-ray structures of PS II[24] and PS I[53] at 3.0 Å and 2.5 Å, respectively, DFT calculations of the Chls proposed to carry the triplet state and their direct environment are possible. For example, in case of $^3P_{680}$ the knowledge of the hfccs can lead to a more complete assignment of hfccs to molecular positions and in case of $^3P_{700}$ to the determination of the site of the low temperature triplet

state. Furthermore, the energy differences between the localization of the triplet state on different Chls (and pheophytin in case of PS II) coud be calculated to understand the effect of temperature dependent triplet localization and delocalization.

References

1. *The Photochemistry of Carotenoids*, Frank, H. A., Young, A. J., Britton, G., and Cogdell, R. J. (Eds.), Advances in Photosynthesis Vol. 8, Govindjee (Series Ed.), Dordrecht, Springer **1999**
2. Frank, H. A. and Cogdell, R. J., *Photochemistry and Photobiology*, 63, 257-264 **1996**
3. Brudvig, G. W., Telfer, A., Moore, T. A., Styring, S., Rutherford, A. W., Fromme, P., Aro, E. M., *Philosophical Transactions of the Royal Society of London Series B-Biological Sciences*, 357, 1431-1440 **2002**
4. Holzwarth, A. R., in Häder, D. P. (Ed.), *Photosynthese*, Stuttgart, Georg Thieme Verlag, 1-20 **1999**
5. Budil, D. E. and Thurnauer, M. C., *Biochimica et Biophysica Acta*, 1057, 1-41 **1991**
6. Angerhofer, A., in Scheer, H. (Ed.), *Chlorophylls*, Boca Raton, CRC Press, 945-991 **1991**
7. Hoff, A. J., in Amesz, J. and Hoff, A. J. (Eds.), *Biophysical Techniques in Photosynthesis*, Advances in Photosynthesis.Vol. 3, Govindjee, Dordrecht, Kluwer Academic Publishers, 277-298 **1996**
8. Lubitz, W., Lendzian, F., Bittl, R., *Accounts of Chemical Research*, 35, 313-320 **2002**
9. Lubitz, W., *Electron Paramagnetic Resonance*, A Specialist Periodical Report.Vol. 19, Gilbert, B. C., Davies, M., and Murphy, D., The Royal Society of Chemistry, 174-242 **2004**
10. Levanon, H. and Möbius, K., *Annual Review of Biophysics and Biomolecular Structure*, 26, 495-540 **1997**
11. Stehlik, D. and Möbius, K., *Annual Review of Physical Chemistry*, 48, 745-784 **1997**
12. Levanon, H., in Amesz, J. and Hoff, A. J. (Eds.), *Biophysical Techniques in Photosynthesis*, Advances in Photosynthesis.Vol. 3, Govindjee, Dordrecht, Kluwer Academic Publishers, 211-234 **1996**
13. Di Valentin, M., Kay, C. W. M., Giacometti, G., Möbius, K., *Chemical Physics Letters*, 248, 434-441 **1996**
14. Lendzian, F., Bittl, R., Telfer, A., Lubitz, W., *Biochimica et Biophysica Acta*, 1605, 35-46 **2003**
15. Lendzian, F., Bittl, R., Telfer, A., Lubitz, W., *Biophysical Journal*, 78, 2253Pos **2000**
16. Möbius, K., *Molecular Crystals and Liquid Crystals*, 394, 1-17 **2003**
17. Möbius, K., *Chemical Society Reviews*, 29, 129-139 **2000**
18. Vrieze, J., Gast, P., Hoff, A. J., *Journal of Physical Chemistry*, 100, 9960-9967 **1996**

19. Poluektov, O. G., Utschig, L. M., Schlesselman, S. L., Lakshmi, K. V., Brudvig, G. W., Kothe, G., Thurnauer, M. C., *Journal of Physical Chemistry B*, 106, 8911-8916 **2002**

20. Lendzian, F. personal communication. **2002**

21. Lendzian, F., Bittl, R., Lubitz, W., *Photosynthesis Research*, 55, 189-197 **1998**

22. Blankenship, R. E., *Molecular Mechanisms of Photosynthesis*, Oxford, Blackwell Science Limited **2002**

23. *Molecular to Global Photosynthesis*, Archer, M. D. and Barber, J. (Eds.), Photoconversion of Solar Energy Vol. 2, London, Imperial College Press **2004**

24. Loll, B., Kern, J., Saenger, W., Zouni, A., Biesiadka, J., *Nature*, 438, 1040-1044 **2005**

25. Schubert, W.-D., Klukas, O., Saenger, W., Witt, H. T., Fromme, P., Krauss, N., *Journal of Molecular Biology*, 280, 297-314 **1998**

26. Grotjohann, I., Jolley, C., Fromme, P., *Physical Chemistry Chemical Physics*, 6, 4743-4753 **2004**

27. Holzwarth, A. R., Müller, M. G., Reus, M., Nowaczyk, M., Sander, J., Rögner, M., *Proceedings of the National Academy of Sciences of the United States of America*, 103, 6895-6900 **2005**

28. Renger, G. and Holzwarth, A. R., in Wydrzynski, T. and Satoh, K. (Eds.), *Photosystem II: The Light-Driven Water:Plastoquinone Oxido-Reductase*, Advances in Photosynthesis and Respiration.Vol. 22, Govindjee, Dordrecht, Springer, 139-175 **2005**

29. Hoff, A. J. and Deisenhofer, J., *Physics Reports*, 287, 1-247 **1997**

30. Fromme, P., Jordan, P., Krauss, N., *Biochimica et Biophysica Acta*, 1507, 5-31 **2001**

31. Deisenhofer, J., Epp, O., Sinning, I., Michel, H., *Journal of Molecular Biology*, 246, 429-457 **1995**

32. Ermler, U., Fritzsch, G., Buchanan, K. S., Michel, H., *Structure*, 2, 925-936 **1994**

33. van Mieghem, F. J. E., Satoh, K., Rutherford, A. W., *Biochimica et Biophysica Acta*, 1058, 379-385 **1991**

34. Kammel, M., Kern, J., Lubitz, W., Bittl, R., *Biochimica et Biophysica Acta*, 1605, 47-54 **2003**

35. Kawamori, A., Ono, T. A., Ishii, A., Nakazawa, S., Hara, H., Tomo, T., Minagawa, J., Bittl, R., Dzuba, S. A., *Photosynthesis Research*, 84, 187-192 **2005**

36. Bittl, R. and Kawamori, A., in Wydrzynski, T. and Satoh, K. (Eds.), *Photosystem II: The Light-Driven Water:Plastoquinone Oxido-Reductase*, Advances in Photosynthesis and Respiration.Vol. 22, Govindjee, Dordrecht, Springer, 389-402 **2005**

37. Nanba, O. and Satoh, K., *Proceedings of the National Academy of Sciences of the United States of America*, 84, 109-112 **1987**

38. Hara, H., Dzuba, S. A., Kawamori, A., Tomo, T., Satoh, K., Iwaki, M., Itoh, S., *Biochimica Biophysica Acta*, 1322, 77-85 **1997**

39. van Leeuwen, P. J., Nieveen, M. C., van de Meent, E. J., Dekker, J. P., van Gorkom, H. J., *Photosynthesis Research*, 28, 149-153 **1991**

40. Paschenko, S. V., Proskuryakov, I. I., Germano, M., van Gorkom, H. J., Gast, P., *Chemical Physics*, 294, 439-449 **2003**

41. Rutherford, A. W. and Mullet, J. E., *Biochimica et Biophysica Acta*, 635, 225-235 **1981**

42. Rutherford, A. W. and Setif, P., *Biochimica et Biophysica Acta*, 1019, 128-132 **1990**

43. Lubitz, W., in Scheer, H. (Ed.), *Chlorophylls*, Boca Raton, CRC Press, 903-944 **1991**

44. Sinnecker, S., Koch, W., Lubitz, W., *Journal of Physical Chemistry B*, 106, 5281-5288 **2002**

45. Bosch, M. K., Proskuryakov, I. I., Gast, P., Hoff, A. J., *Journal of Physical Chemistry*, 100, 2384-2390 **1996**

46. Kamlowski, A., Frankemoller, L., van der Est, A., Stehlik, D., Holzwarth, A. R., *Berichte der Bunsen-Gesellschaft-Physical Chemistry Chemical Physics*, 100, 2045-2051 **1996**

47. Frankemöller, L., Kamlowski, A., Krüger, U., van der Est, A., Stehlik, D. A transient EPR study of the temperature and orientation dependence of the spectrum of 3P680 in Photosystem II, Ziessow, D., Lubitz, W., and Lendzian, F. (Eds.). 939-940Berlin, Technische Universität Berlin. **1998**

48. Noguchi, T. and Berthomieu, C., in Wydrzynski, T. and Satoh, K. (Eds.), *Photosystem II: The Light-Driven Water:Plastoquinone Oxido-Reductase*, Advances in Photosynthesis and Respiration.Vol. 22, Govindjee, Dordrecht, Springer, 367-387 **2005**

49. Noguchi, T., *Plant and Cell Physiology*, 43, 1112-1116 **2002**

50. Raszewski, G., Saenger, W., Renger, T., *Biophysical Journal*, 88, 986-998 **2005**

51. Germano, M., Shkuropatov, A. Y., Permentier, H., de Wijn, R., Hoff, A. J., Shuvalov, V. A., van Gorkom, H. J., *Biochemistry*, 40, 11472-11482 **2001**

52. Germano, M., Shkuropatov, A. Y., Permentier, H., Khatypov, R. A., Shuvalov, V. A., Hoff, A. J., van Gorkom, H. J., *Photosynthesis Research*, 64, 189-198 **2000**

53. Jordan, P., Fromme, P., Witt, H. T., Klukas, O., Saenger, W., Krauss, N., *Nature*, 411, 909-917 **2001**

54. Sieckmann, I., Brettel, K., Bock, H., van der Est, A., Stehlik, D., *Biochemistry*, 32, 4842-4847 **1993**

55. Sieckmann, I., Untersuchung von funktionalen Molekülen im ladungsgetrennten Zustand des Photosystem I mit zeitauflösender Elektronenspinresonanz-Spektroskopie, Phd Thesis Technische Universität Berlin, **1993**

56. Polm, M. and Brettel, K., *Biophysical Journal*, 74, 3173-3181 **1998**

57. Setif, P. and Brettel, K., *Biochimica et Biophysica Acta*, 1020, 232-238 **1990**

58. Fromme, P. and Witt, H. T., *Biochimica et Biophysica Acta*, 1365, 175-184 **1998**

59. Teutloff, C., Untersuchungen zur Bindung des sekundären Akzeptors in Photosystem I mit Methoden der EPR-Spektroskopie, Phd Thesis Technische Universität Berlin, **2004**

60. Fromme, P., Bottin, H., Krauss, N., Setif, P., *Biophysical Journal*, 83, 1760-1773 **2002**

61. Borovykh, I. V., Kulik, L. V., Dzuba, S. A., Hoff, A. J., *Journal of Physical Chemistry B*, 106, 12066-12071 **2002**

62. Breton, J., *Biochimica et Biophysica Acta*, 1507, 180-193 **2001**

63. Krabben, L., Schlodder, E., Jordan, R., Carbonera, D., Giacometti, G., Lee, H., Webber, A. N., Lubitz, W., *Biochemistry*, 39, 13012-13025 **2000**

64. Abragam, A., *The Principles of Nuclear Magnetism*, London, Oxford University Press **1961**

7. Summary and Outlook

Summary

In this work most attention was devoted to the investigation of two important cofactors of the electron transfer chain in PS I. They are the 'primary' electron donor P_{700} (Chl *a*/Chl *a*′ heterodimer) and the 'secondary' electron acceptor A_1 (phylloquinone, vitamin K_1). EPR was used as spectroscopic tool. Advantage was taken of the higher resolution of EPR spectra and sensitivity at elevated magnetic fields. These were combined with the use of multiple resonance techniques like ENDOR and TRIPLE spectroscopy. This all allowed to elucidate the proton hf tensors of these cofactors. Furthermore, DFT calculations were performed[1] to facilitate an assignment of the hf tensors to molecular positions.

Studies on quinone model systems

It is a very demanding task to unravel the electronic structure of a protein bound cofactors and to understand the specific influence of the protein on redox potential and the electronic structure. Therefore, phylloquinone and several related quinones were investigated *in vitro* prior to the experiments on the quinone in PS I. The redox potential of the quinone in the A_1 binding site was compared to the redox potential of quinones in solvents with different polarity (instead of VK_1 the simpler and smaller quinone BQ was used). The *g*-tensors of $BQ^{\bullet-}$ in frozen solutions of solvents of different polarity were also determined. In general it can be concluded, that the very low redox potential and the high g_x-value of VK_1 ($VK_1^{\bullet-}$) in the A_1 binding site of PS I can be explained in terms of a apolar protein environment, in agreement with previous studies.

[1] All DFT calculations were performed by Dr. S. Sinnecker (MPI für Bioanorganische Chemie, Mülheim/Ruhr).

ENDOR and TRIPLE experiments were performed (exp is performed, spec is used) spectroscopy was performed on the phylloquinone in a protic solvent (isopropanol). The hf tensor principal components for all protons visible in the ENDOR spectra were determined for the first time. The DFT calculations predicted the hf tensors of the quinone protons with high precision. The combination with a COSMO continuum model for solvation further improved the agreement with the experimental results. Hydrogen bonding to the quinone radical anions was studied in detail. It was shown for 'higher substituted' quinones like $VK_3^{\bullet-}$ and $VK_1^{\bullet-}$ that some of H-bonds do not lie in the plane of the quinone. This is in contrast to what is observed for simpler model quinones like $BQ^{\bullet-}$ and $NQ^{\bullet-}$. Hydrogen bond lengths were estimated both from the dipolar couplings of the respective protons using the point dipolar model and from nqccs using the empirical formulas. The distances obtained by these two methods are very similar for the quinone radical anions investigated (1.77 ± 0.05 Å) and agree with the distances obtained by the DFT calculation. However, the DFT calculations were found to be less precise in the prediction of the hf tensors of the protons H-bonded to the quinone than of the quinone protons.

The electron acceptor A_1

Both the stationary radical anion $A_1^{\bullet-}$ (photoaccumulated) and the spin-correlated radical pair $P_{700}^{\bullet+}A_1^{\bullet-}$ of PS I from *Thermosynechococcus elongatus* were investigated in detail. In addition, PS I isolated from the *Synechocystis menB* mutant was used for substitution of the quinone with VK_3 (VK_3-h_8 and VK_3-d_8) in the A_1 binding site. Under the experimental condition used in this work, only the A-branch A_1 is reduced. This holds both for stationary $A_1^{\bullet-}$ and for $A_1^{\bullet-}$ in the RP $P_{700}^{\bullet+}A_1^{\bullet-}$. The hf tensor of the methyl group protons was determined with high precision for $A_1^{\bullet-}$ in PS I from *T. elongatus* and in PS I from the *menB* mutant. In the latter the quinone was substituted with VK_3-h_8. For the first time, ENDOR lines

of the α-protons of the second (benzene) ring were assigned. Only one H-bond to $A_1^{\bullet-}$ was detected experimentally. Furthermore, the DFT calculations showed that the presence of only one H-bond can account for the significant asymmetry in spin density distribution observed experimentally. The H-bond direction is close to g_x and is slightly out of plane. The length of the of H-bond was estimated from the dipolar coupling to be 1.64 Å, in agreement to the length of 1.66 Å obtained in the DFT calculations. This corresponds to a short and strong H-bond, similar to the H-bond lengths found in bacterial photosynthetic RCs. Furthermore, it was demonstrated further that DFT calculations using the simplified structural model with only one H-bonded residue can at a basic level explain the ENDOR spectra. This indicates that H-bond interaction is indeed the crucial factor for the explanation of the spin density distribution in $A_1^{\bullet-}$.

Triplet states in photosystems I and II

The short-lived triplet states $^3P_{680}$ of PS II and $^3P_{700}$ of PS I were investigated. In case of $^3P_{680}$, previous results concerning the temperature dependence of the EPR spectra were confirmed. New proton ENDOR lines were detected due to the high resolution and the improved signal-to-noise ratio of the spectra.

The first ENDOR spectra of $^3P_{700}$ were recorded and the monomeric nature of $^3P_{700}$ at low temperature could be confirmed. Transient EPR experiments were performed on $^3P_{700}$ over the whole temperature range from low temperature to room temperature. A more complete set of spectra than in previous studies was obtained. It was shown that the temperature dependence is continuous and not stepwise. From this it was concluded that the triplet exciton is located at low temperature on one of the dimer Chls, while at high temperature the triplet exciton is delocalized over both Chls of the P_{700} dimer.

Outlook

The use of higher magnetic field in combination with advanced multiple resonance techniques like ENDOR and TRIPLE spectroscopy turned out to be very successful for the investigation of quinone radical anions. The good agreement of the DFT calculations on these systems with the experimental results provides confidence that it can be used also for other quinones in different protein binding sites. Hence, this approach of combining high resolution spectroscopy with the state of the art DFT calculations should be continued and applied to other systems.

For study of A_1 the assignment of the smaller hfccs could be achieved by use of perdeuterated PS I substituted with protonated quinones. The substitution of selectively deuterated quinones in the A_1 binding site would also be helpful. DFT calculations could be extended by including more amino acids residue from the environment to achieve a better agreement of the hf tensors of the weakly coupled protons.

For the case of $^3P_{700}$, ENDOR spectra with sufficient signal-to-noise ratio recorded at all three canonical orientations would provide important knowledge about the orientation of the ZFS axes in $^3P_{700}$. If the ZFS axes are really significantly rotated as compared to $^3P_{680}$ or ^{3}Chl *in vitro*, the ENDOR lines should be much broader. Further knowledge about the triplet states could be obtained by DFT calculations of the Chls, which are suggested to carry the triplet state. The knowledge of the calculated hfccs can lead to a more complete assignment of hfccs to molecular positions in case of $^3P_{680}$ and in case of $^3P_{700}$ to the determination of the site of the low temperature triplet state. Furthermore, the energy differences between the localization of the triplet state on different Chls in PS I could be calculated to understand the effect of temperature dependent triplet delocalization.

8. List of abbreviations

A_0	‘primary’ electron acceptor in photosystem I
A_1	‘secondary’ electron acceptor in photosystem I
a_{iso}	isotropic hyperfine coupling
A, A_i	hyperfine tensor, principal values
ACN	acetonitrile
ADP, ATP	adenosine diphosphate, adenosine triphosphate
AN	acceptor number
AQ	anthraquinone
B_0, B_1, B_2	static magnetic field, microwave field, radiofrequency field
β_e, β_N	Bohr magneton, nuclear magneton
β–DM	n–dodecyl–β–D–maltoside
BChl	bacteriochlorophyll
BQ	1,4-benzoquinone
Chl *a*, *b*	chlorophyll *a*, *b*
CT	charge transfer
CW	continuous wave
D, D_i	zero field splitting (ZFS) tensor, principal values
D, E	zero field splitting (ZFS) parameters
DFT	density functional theory
DME	dimethoxyethane
DMF	*N*,*N*-dimethylformamide
DMSO	dimethylsulfoxide
E_m	midpoint potential
ENDOR	electron-nuclear double resonance
EPA	electron pair acceptor
EPD	electron pair donor
EPR (also: ESR)	electron paramagnetic resonance (electron spin resonance)
ESE	electron spin echo
ESEEM	electron spin echo envelope modulation
$E_T(30)$	solvent polarity parameter (Dimroth and Reichardt)
E_T^N	normalized solvent polarity parameter (Dimroth and Reichardt)

EtOH	ethanol
F_X, F_A, F_B	[Fe_4-S_4] clusters in PS I (electron acceptors)
Fc	ferrocen
Fd	ferredoxin
FSE	field swept echo
$\boldsymbol{g}$, g_i	(electronic) *g*-tensor, principal values
g_N	nuclear g-value
H; H_{EZ}, H_{DD}, H_{EX}, H_{NZ}, H_{hfi}, H_{nq}	spin Hamiltonian operator; electron zeeman, electron-electron dipolar, electron-electron exchange, nuclear zeeman, hyperfine interaction, nuclear quadrupolar coupling terms of the spin Hamiltonian
hf	hyperfine
hfi	hyperfine interaction
hfc, hfcc(s)	hyperfine coupling, hyperfine coupling constant(s)
$\vec{I}$	nuclear spin operator
IP	isopropanol, 2-propanol
J	exchange coupling
m_S, m_I	magnetic quantum number of an electron, nucleus
MeOH	methanol
MQ	menaquinone
MTHF	2-methyl-tetrahydrofuran
ν_{MW}	microwave frequency
ν_N	Larmor frequency of a nucleus
ν_{RF}	radiofrequency
NADP+, NADPH	nicotinamide adenine dinucleotice; oxidized, reduced
NHE	normal hydrogen electrode
NMR	nuclear magnetic resonance
P_{680}	‘primary donor’ pigments of PS II absorbing around 680 nm
P_{700}	‘primary donor’ pigments of PS I absorbing around 700 nm
P_{MW}, P_{RF}	microwave power, radiofrequency power
PQ_9	plastoquinone-9
PS I, PS II	photosystem I, photosystem II
PsaA, PsaB, ..	protein subunit A, B, .. of photosystem I
PsbA, PsbB, ..	protein subunit A, B, .. of photosystem II

Q_A, Q_B	‘primary’, ‘secondary’ electron acceptors in type II photosynthetic reaction centers (*e.g.* PS II)
ρ	spin density
RP	radical pair
RC	(photosynthetic) reaction center
$\vec{S}$	electron spin operator
tert-ButOH	*tert*-butanol
THF	tetrahydrofuran
TRIPLE	electron-nuclear-nuclear triple resonance
VK_1	vitamin K_1, phylloquinone
VK_3	vitamin K_3, menadione

9. Acknowledgement

I like to thank Prof. Dr. Wolfgang Lubitz for providing me the possibility to work in his group at the Max-Volmer-Laboratorium at the TU Berlin and later in his group at the Max-Planck-Institut für Bioanorganische Chemie in Mülheim an der Ruhr. His constant support and interest in my work contributed much to this thesis.

Prof. Dr. Peter Hildebrandt was so friendly to be the second reviewer of this thesis.

At the Max-Volmer-Laboratorium in Berlin, I especially thank Dr. Christian Teutloff, which introduced me to EPR and ENDOR spectroscopy and helped me a lot. Prof. Dr. Robert Bittl and Dr. Friedhelm Lendzian were always helpful when problems in the EPR laboratory occurred. I thank them and Dr. Eberhard Schlodder for many discussions about of photosystem I. For the support and discussions regarding molecular biology and biochemistry of *Chlamydomonas reinhardtii*, I thank Dr. Heike Witt and Claudia Schulz. Unfortunately, the growth of the mutants was too much disturbed to allow isolation of PS I in sufficient amount for spectroscopic investigations.

At the Max-Planck-Institut für Bioanorganische Chemie in Mülheim an der Ruhr I enjoyed a fruitful collaboration with Drs. Boris Epel and Mikhail L. Antonkine on the $A_1^{\bullet-}$ project and on the studies of the quinone model systems *in vitro*. In addition, the latter one also spent some time for the proofreading of this thesis. Dr. Sebastian Sinnecker did all the DFT calculations presented in this work, despite his tight schedule. I thank him very much. Gudrun Klihm and Frank Reikowski keep EPR spectrometers in Mülheim running. Especially Gudrun Klihm helped me a lot to maintain the legendary ‘Thanner I’ and did many measurements for the joint project with Prof. Dr. Jim Allen on the primary donor of bacterial photosynthetic reaction centers. Christoph Laurich did a really good job in the electrochemistry part of the

model quinone project. Dr. Eberhard Bothe supplied his setup for the electrochemical work presented in this thesis. Inge Heise prepared the fully deuterated benzoquinone.

A collaboration was built up with the working group of Prof. Dr. Alfred Holzwarth at the Max-Planck-Institut für Bioanorganische Chemie, which resulted in several joint publications. Michael Reus was very helpful in growing several *Chlamydomonas reinhardtii* and S*ynechocystis* strains.

The group of Prof. Dr. Petra Fromme (formerly TU Berlin, now Arizona State University), especially Dr. Joachim Frank and Dr. Jan Kern (TU Berlin), provided me photosystem I from *Thermosynechococcus elongatus*.

Herbert Zimmermann from the Max-Planck-Institut für Medizinische Forschung in Heidelberg was so kind to provide fully deuterated naphthoquinone and vitamin K_3.

The phylloquinone extracted PS I complexes from *Synechocystis* sp. PCC 6803 kindly provided by the group of Prof. Dr. Art van der Est (Brock University, Canada).

I am grateful to Prof. Dr. Wade Johnson (Susquehanna University, USA) and Prof. Dr. J. H. Golbeck (The Pennsylvania State University, USA). They provided me a clone of *menB26 Synechocysti*s sp. PCC 6803, which was essential for the quinone substitution experiments performed in this work.

Dr. Holger Strauss and Prof. Dr. Peter Schmieder kindly provided the cells from *Synechocysti*s sp. PCC 6803.

Furthermore, I would like to thank all people which I had the pleasure to work with and which were not explicitly mentioned here. Special thanks goes to my family for continuous support.

10. List of Publications

Teile der vorliegenden Arbeit wurden bereits veröffentlicht

1. B. Epel, J. Niklas, S. Sinnecker, H. Zimmermann, W. Lubitz
Phylloquinone and Related Radical Anions Studied by Pulse Electron Nuclear Double Resonance Spectroscopy at 34 GHz and Density Functional Theory
Journal of Physical Chemistry B 110, 11549-11560 **2006**

2. B. Epel, J. Niklas, M. L. Antonkine, W. Lubitz
Absolute Signs of Hyperfine Coupling Constants as Determined by Pulse ENDOR of Polarized Radical Pairs
Applied Magnetic Resonance 30, 311-327 **2006**

3. J. Niklas, B. Epel, M. L. Antonkine, S. Sinnecker, W. Lubitz
The Electron Acceptor A_1 of Photosystem I. A Pulse Q-band EPR, ENDOR and TRIPLE Study
In preparation

Weitere Publikationen

1. H. Witt, E. Schlodder, C. Teutloff, J. Niklas, E. Bordignon, D. Carbonera, S. Kohler, A. Labahn, W. Lubitz
Hydrogen Bonding to P700: Site-Directed Mutagenesis of Threonine A739 of Photosystem I in *Chlamydomonas reinhardtii*
Biochemistry *41, 8557-8569* ***2002***

2. M. G. Müller, J. Niklas, W. Lubitz, A. R. Holzwarth
Ultrafast Transient Absorption Studies on Photosystem I Reaction Centers from *Chlamydomonas reinhardtii*. 1. A New Interpretation of the Energy Trapping and Early Electron Transfer Steps in Photosystem I
Biophysical Journal 85, 3899-3922 **2003**

3. A. Remy, J. Niklas, H. Kuhl, P. Kellers, T. Schott, M. Rögner, K. Gerwert
FTIR Spectroscopy Shows Structural Similarities between Photosystems II from Cyanobacteria and Spinach
European Journal of Biochemistry 271, 563-567 **2004**

4. A. R. Holzwarth, M. G. Müller, J. Niklas, W. Lubitz
Charge Recombination Fluorescence in Photosystem I Reaction Centers from Chlamydomonas reinhardtii
Journal of Physical Chemistry B 109, 5903-5911 **2005**

5. A. R. Holzwarth, M. G. Müller, J. Niklas, W. Lubitz
Ultrafast Transient Absorption Studies on Photosystem I Reaction Centers from *Chlamydomonas reinhardtii*. 2. Mutations near the P700 Reaction Center Chlorophylls Provide New Insight into the Nature of the Primary Electron Donor
Biophysical Journal 90, 552-565 **2006**